Steuerungs- und Regelungstechnik

Sabrina Rechkemmer

Lifetime modeling and model-based lifetime optimization of Li-ion batteries for use in electric two-wheelers

Band 48

**Berichte aus dem
Institut für Systemdynamik
Universität Stuttgart**

LIFETIME MODELING AND MODEL-BASED LIFETIME OPTIMIZATION OF LI-ION BATTERIES FOR USE IN ELECTRIC TWO-WHEELERS

Von der Fakultät
Konstruktions-, Produktions- und Fahrzeugtechnik
der Universität Stuttgart
zur Erlangung der Würde eines Doktor-Ingenieurs (Dr.-Ing.)
genehmigte Abhandlung

vorgelegt von

Sabrina Rechkemmer

geboren in Heilbronn

Hauptberichter:	Prof. Dr.-Ing. Dr. h.c. Oliver Sawodny
Mitberichter:	Prof. Dr.-Ing. Kai Peter Birke
2. Mitberichter:	Prof. Dr.-Ing. Weimin Zhang
Tag der mündlichen Prüfung:	27. Mai 2020

Institut für Systemdynamik der Universität Stuttgart

2020

Berichte aus dem
Institut für Systemdynamik
Universität Stuttgart

Band 48

Sabrina Rechkemmer

Lifetime modeling and model-based lifetime optimization of Li-ion batteries for use in electric two-wheelers

D 93 (Diss. Universität Stuttgart)

Shaker Verlag
Düren 2020

Bibliographic information published by the Deutsche Nationalbibliothek
The Deutsche Nationalbibliothek lists this publication in the Deutsche Nationalbibliografie; detailed bibliographic data are available in the Internet at http://dnb.d-nb.de.

Zugl.: Stuttgart, Univ., Diss., 2020

Printed in Germany.

ISBN 978-3-8440-7445-1
ISSN 1863-9046

Shaker Verlag GmbH • Am Langen Graben 15a • 52353 Düren
Phone: 0049/2421/99011-0 • Telefax: 0049/2421/99011-9
Internet: www.shaker.de • e-mail: info@shaker.de

同济大学
TONGJI UNIVERSITY

博士学位论文

电动两轮车的锂离子池寿命建模及其优化研究

姓　　名：　Sabrina Kathrin RECHKEMMER（凯琳）

学　　号：　1590015

所在院系：　机械与能源工程学院

学科门类：　工学

学科专业：　机械工程

指导教师：　张为民，Prof. Oliver SAWODNY

二〇二〇年五月

同济大学
TONGJI UNIVERSITY

A dissertation submitted to

Tongji University in conformity with the requirements for

the degree of Doctor of Engineering

Lifetime modeling and model-based lifetime optimization of Li-ion batteries for use in electric two-wheelers

Candidate:	Sabrina Kathrin RECHKEMMER
Student Number:	1590015
School/Department:	School of Mechanical Engineering
Discipline:	Engineering
Major:	Mechanical Engineering
Supervisor:	Prof. Weimin ZHANG
	Prof. Oliver SAWODNY

May, 2020

VORWORT

Die vorliegende Arbeit entstand während meiner Zeit als wissenschaftliche Mitarbeiterin am Institut für Systemdynamik (ISYS) an der Universität Stuttgart sowie an der School of Mechanical Engineering (SME) an der Tongji University Shanghai im Zuge des Joint PhD Programms. Die Arbeiten wurden dabei in Kooperation mit Bosch (China) Investment Ltd. in Shanghai durchgeführt. Aufgrund der besonderen Konstellation der interkontinentalen und interinstitutionellen PhD Kooperation möchte ich mich an erster Stelle bei allen drei beteiligten Institutionen bedanken, welche mir diese wunderbare Möglichkeit gegeben haben. Allen voran natürlich bei Prof. Oliver Sawodny und Prof. Weimin Zhang, welche den Joint Ph.D. schnell und unkompliziert ins Leben gerufen haben, sowie bei Dr. Markus Kneifel, welcher den engen Anwendungs- und Industriebezug durch die Beteiligung von Bosch in Shanghai hinzugefügt hat. Zudem danke ich Prof. Birke vom Institut für Photovoltaik der Universität Stuttgart für die freundliche Übernahme des Mitberichts und Prof. Reuss für die Übernahme des Vorsitzes.

Des Weiteren geht mein Dank an alle, die mich bei der Erstellung dieser Arbeit sowohl in Deutschland als auch China unterstützt haben.
Für die viele Hilfe beim Zurechtfinden an der Tongji und dem Überwinden der organisatorischen Hürden danke ich den Beratern für ausländische Angelegenheiten an der SME, Ada, Hanna, und natürlich aktuell Fei. Mein Dank geht insbesondere auch an meinen dortigen Doktorvater Prof. Weimin Zhang, welcher sich sehr für mich eingesetzt hat. Neben meinem Betreuer möchte ich mich beim gesamten Promotionskomitee an der Tongji bedanken, das mich so freundlich begrüßt und mir bei der Promotion geholfen hat, auch wenn ich aufgrund der abwechselnden Aufenthalte hin und wieder eine Sonderbehandlung benötigte. Für die Hilfe bei der Durchführung des PhD und den vielen praktischen Hinweisen danke ich auch Dongdong Li und Dr. Jiabin Sun, welche neben ihrer PhD auch noch auf meine achten mussten.
Wesentliche Impulse sowie das Anwendungsszenario wurden dabei durch Bosch gegeben. Hier möchte ich mich bei allen Kolleginnen und Kollegen vor allem in der Abteilung CR/RTC2-AP in Shanghai aber auch bei den vielen intialen Anlaufstellen in Renningen und Ludwigsburg bedanken. Besonders hervorheben möchte ich dabei Dr. Xiaoyun Zang, welche mir in Shanghai mit Rat und Tat zur Seite stand, sowie Dr. Alexander Boronka, der immer wieder die richtigen Hinweise und Impulse gab um die Arbeit auszurichten und voranzubringen. Für das Zustandekommen des Projektes und die organisatorische und fachliche Betreuung geht mein besonderer Dank insbesondere auch an Dr. Markus Kneifel und Dr. Peter Fischer.
In diesem Zusammenhang möchte ich meinem Doktorvater Prof. Sawodny nochmals für das entgegengebrachte Vertrauen auch durch dick und dünn, die Unterstützung und den Freiraum danken. Und natürlich bedanke ich mich auch bei allen Kolleginnen und Kollegen am ISYS, welche mich in meiner Zeit begleitet haben: Im speziellen möchte ich Dr. Julia Sachs für die Einführung ans ISYS und die ersten Impressionen, Patric Skalecki für das Korrekturlesen und die interessanten Einblicke in den Betonstraßenbau, Bernhard Rolle für die viele Unterstützung und sprachlichen Tipps, Dr. Eckard Arnold

für die vielen Hinweise zur Optimierung, Prof. Zeitz für die vielen Kommentare und Anmerkungen, sowie allen Beteiligten der Automotive und Optimierungsgruppe für die angeregten Diskussionen danken. In diesem Zusammenhang geht auch ein großer Dank an Joachim Endler, Gerlind Preisenhammer und Corina Hommel, welche uns am ISYS den 'Verwaltungskram' immer gut abgenommen haben.

Und zuletzt danke ich natürlich auch allen Freunden, Bekannten und Beteiligten, welche zwar nicht direkt mit dem Projekt Kontakt hatten, aber mich seelisch, moralisch, durch Diskussionen und Korrekturlesen unterstützt haben: meiner Familie für das Vertrauen, meinem Freund Laurentiu für die Geduld, Motivation und den Rückhalt, sowie Zhuoqi Zeng und Michael Wunderlich für die vielen Erfahrungen in China, die anregenden Diskussionen und Übersetzungen.

Stuttgart, im Juni 2020

Sabrina Rechkemmer

KURZZUSAMMENFASSUNG

Elektrofahrzeuge (EVs) und elektrische Hybridfahrzeuge (HEVs) sind durch das wachsende Umweltbewusstsein in den vergangenen Jahren zunehmend ins Rampenlicht gerückt. Im Zusammenhang mit batteriebetriebenen Elektrofahrzeugen (BEVs) hat der Übergang von Blei-Säure hin zu Li-Ionen Batterien die Nutzerakzeptanz unter anderem durch die höhere mögliche Reichweite erhöht. Li-Ionen Batterien bieten eine höhere spezifische Energie- und Leistungsdichte wodurch bei geringerem Gewicht eine größere Reichweite erzielt werden kann. Jedoch bleibt die Batterielebensdauer weiterhin eines der Kernprobleme. Im Bereich der E-Mobilität ist China durch seinen wachsenden und flexiblen Markt eines der Vorreiterländer. Obwohl zumeist konventionelle EVs mit vier Rädern untersucht werden, sollte der Markt für elektrische Zweiräder (E2Ws) nicht vernachlässigt werden. Durch das partielle Verbot von konventionellen Mopeds prägen E2Ws schon heute das Stadtbild in Chinas Metropolen wie z.B. Shanghai und Peking.
Diese Arbeit behandelt dabei die Lebensdauervorhersage von Li-Ionen Batterien sowie die Anwendbarkeit dementsprechender Modelle für die Optimierung der Betriebs- und Ladestrategie. Dazu wird eine modellbasierte Optimalsteuerung entworfen. Im Zentrum stehen typische Anwendungsszenarien für E2Ws in Shanghai. Die Ergebnisse lassen sich jedoch auch generalisieren und auf EVs sowie verschiedene Anwendungsfälle und Fahrverhalten übertragen. Ein realistisches Fahrverhalten muss zunächst hergeleitet werden um die typische Nutzung eines E2W widerzuspiegeln. Da die meisten der vorhandenen genormten Fahrzyklen für vierrädrige Fahrzeuge und Abgastests entworfen sind, wird zunächst eine Testkampagne zur Datenerfassung in Shanghai durchgeführt um die lokalen Gegebenheiten zu erfassen. Auf Basis einer Umfrage zum Nutzerverhalten wird ein Anwendungsbeispiel, welches sich als tägliche Fahrt zur und von der Arbeit ergibt, hergeleitet. Flottendaten werden erfasst um typische Fahrzyklen abzubilden. Darauf basierend wird ein typischer Fahrzyklus für E2W in Shanghai entworfen, welcher zwischen den zwei dominanten Leistungsklassen der E2W in Shanghai unterscheidet. Ein Vergleich der entworfenen Fahrzyklen zu vorhandenen Zyklen zeigt die Eigenheiten der leistungsschwachen E2W in Shanghai auf.
Im nächsten Schritt wird der E2W selbst charakterisiert und modelliert. Der Antriebsstrang besteht dabei vor allem aus drei Komponenten: dem elektrischen Motor, der Leistungselektronik und der Batterie. Modelle des Motors sowie der Leistungselektronik werden zusammen mit der Interaktion des Fahrzeugs und der Straße benötigt um die aufgenommenen typischen Fahrzyklen in ein Leistungsprofil umzuwandeln, welches die Belastung der Batterie widerspiegelt. Dies wird beispielhaft anhand einer Permanentmagneterregten Synchronmaschine (PMSM) sowie einer statischen Kräftekonvertierung, welche die Motordynamik vernachlässigt, gezeigt. Unterschiedliche Abstraktionsgrade werden benötigt, da für die Optimierung oftmals eine Abwägung zwischen Genauigkeit und Komplexität getroffen werden muss. Für Simulation und Verifikation werden komplexere Modelle verwendet. Das Hauptaugenmerk dieser Arbeit liegt auf der Untersuchung und Modellierung der Li-Ionen Batterie aus Systemsicht. Das Wachstum der sogenannten Solid-Electrolyte Interphase (SEI) Schicht wird als dominanter

Alterungsprozess erläutert sowie verschiedene Modelldarstellungen hinsichtlich ihrer Anwendbarkeit in Simulation und Optimierung verglichen. Auch wenn oftmals nur von Li-Ionen Batterien gesprochen wird, so werden damit jedoch verschiedene Elektrodenmaterialien zusammengefasst, wodurch sich Unterschiede im Alterungsverhalten ergeben und diese betrachtet werden müssen. Da in der Literatur jedoch nur wenig Daten zu verschiedenen Zellchemien verfügbar sind, wird eine Alterungskampagne aufgesetzt um die Charakteristiken einer Lithium Mangan Oxid Zelle (LMO) zu untersuchen. Dazu werden die Ergebnisse der kalendarischen und zyklischen Tests erläutert und mit anderen Zellchemien verglichen. Im Anschluss werden ein sogenanntes Single Particle Modell als Repräsentant der elektrochemischen Modellierung sowie ein vereinfachtes elektrisches Ersatzmodell eingeführt, verbessert und an die Zellergebnisse angepasst. Auf Basis dessen und der Motormodellierung wird das sich ergebende Antriebsstrangmodell kurz dargestellt.
Im nächsten Schritt wird der zuvor beschriebene Fahrzyklus mit dem Modell des Antriebsstrangs kombiniert und für die modellbasierte Optimierungsstrategie aufbereitet. Dazu wird ein entsprechender Anwendungsfall definiert und das Optimierungsproblem aufgestellt. Da das größte Optimierungspotential während des Ladevorgangs und der Lagerung identifiziert wurde, wird eine kombinierte optimale Lade- und Betriebsstrategie beschrieben. Die Optimierungsergebnisse werden hinsichtlich verschiedener Fahrzyklen sowie der Sensitivität zum zugrunde liegenden Alterungsmodell und der Zellchemie verglichen. Die Gültigkeit der Ergebnisse wird mithilfe weiterer Zelltests validiert und mit Simulationsergebnissen verglichen, welche zeigen, dass eine Verlängerung der Lebensdauer erzielt wird. Anschließend wird eine heuristische Betriebsstrategie abgeleitet, welche auch online auf dem Steuergerät des E2W implementiert werden kann.
Insgesamt wird im Zuge dieser Arbeit damit ein neuer Fahrzyklus für E2W in Shanghai vorgestellt, der Alterungsvorgang von Li-Ionen Zellen untersucht und modelliert, eine Alterungskampagne und ein Alterungsmodell für LMO Zellen beschrieben, sowie eine optimale Lade- und Betriebsstrategie auf Basis eines realistischen Fahrszenarios in Shanghai hergeleitet.

ABSTRACT

Electric vehicles (EVs) and hybrid electric vehicles (HEVs) have received increased attention over the last years as a result of the growing environmental awareness. In the context of battery electric vehicles (BEVs), the transition from lead-acid to Li-ion batteries increased user acceptance of BEVs as the driving range could be extended. Compared to lead-acid batteries, Li-Ion batteries offer a higher specific energy and power density, which result in the extension of the range. However, battery lifetime remains a key issue. In the field of e-mobility, China is one of the pioneering countries due to its growing and flexible market and its expertise in battery production. Although conventional four-wheel EVs are mostly being studied, the market for electric two-wheelers (E2W) should not be neglected. Due to the partial ban of conventional two-wheelers, E2Ws already shape the cityscape in China's metropolises such as Shanghai and Beijing. This study deals with the lifetime prediction of Li-ion batteries and the applicability of such models to optimize the operation and charging strategy. A model-based optimal control is therefore designed. The focus is on typical application scenarios for E2Ws in Shanghai. The results, however, can also be generalized and transferred to EVs as well as various application cases and driving conditions. A realistic driving behavior must first be derived to reflect the typical use of an E2W. Since most of the existing standardized driving cycles are designed for four-wheeled vehicles and exhaust emission tests, a data acquisition campaign is conducted to capture the local conditions in Shanghai. On the basis of a user behavior survey, a typical use case is derived for a daily commute to and from work. Fleet data is collected to represent typical driving cycles. Based on this, a typical driving cycle for E2W is designed in Shanghai, which distinguishes between the two dominant power classes of E2W in Shanghai. A comparison between the derived driving cycle and other cycles highlights the special characteristics of E2Ws in Shanghai due to their lower power.
The next step is to characterize and model the E2W. The powertrain consists mainly of three components: electric motor, power electronics and battery. Models of the electric motor and power control in combination with vehicle-to-street characteristics are required to convert the recorded typical driving cycles to equivalent power profiles. This is illustrated by implementing a permanent magnet synchronous machine (PMSM) model in addition to a static force conversion which neglects motor dynamics. Different degrees of abstraction are required, as optimization often requires a balance between accuracy and complexity. More complex models are required for simulation and verification. The main focus of this study is to investigate and model a Li-ion battery from a system perspective. The growth of the so-called Solid-Electrolyte Interphase (SEI) layer is discussed as a dominant aging process. In addition, different model representations are compared regarding their applicability in simulation and optimization. Although the term Li-ion battery is commonly used, different electrode compositions exist within Li-ion batteries and cell chemistry specific effects need to be considered. Since there is not much data available on different cell chemistries in the literature, an aging campaign is initiated to investigate the characteristics of a lithium manganese oxide (LMO) cell.

Results for calendar and cycle aging are presented and compared to further cell chemistries. Subsequently, a so-called single particle model representing an electrochemical modeling as well as a simplified electrical equivalent circuit model will be introduced, improved and adapted to the cell results. Based there-on and the motor modeling, the resulting powertrain simulation model is briefly presented.
In a next step, the previously described driving cycle and powertrain models are incorporated into a model-based optimization strategy. A proper use case is defined and an optimization problem is formulated. Since the greatest optimization potential was identified during charging and storage, a combined optimal charging and operating strategy is described. The optimization results, with regard to different driving cycles as well as the sensitivity to the underlying aging model and cell chemistry, are compared. The validity of the results is proven by further cell tests and compared with simulation results, which show that an extension of the lifetime is achieved. A heuristic operating strategy is then derived, which can also be implemented online on the E2W control unit.
In the course of this thesis a new driving cycle for E2W in Shanghai is presented, the aging process of Li-ion cells is investigated and modeled, an aging campaign and an aging model for LMO cells are described, and an optimal charging and operating strategy based on a realistic driving scenario in Shanghai is derived.

扩展摘要

近年来，由于环保意识的增强，电动汽车（EV）和混合电动汽车（HEV）受到越来越多的关注。在电池电动车（BEV）的背景下，铅酸电池过渡到锂电池，使得续驶里程进而扩大，用户也因此越来越接受电池电动车。与铅酸电池相比，锂离子电池具有更高的比能量和功率密度，一方面在相同的功率下重量更轻，另一方面在相同重量下可以实现更长的续航里程。但是，电池寿命仍然是关键问题。在电动汽车领域，中国由于其不断发展的灵活市场和在电池生产方面的专业知识而成为领先国家之一。尽管大多数研究仍专注于传统四轮电动汽车，但电动两轮车（E2W）的市场不可忽视。由于中国对部分两轮车的禁令，电动两轮车已成为中国大都市，如上海和北京的城市景观之一。

本研究涉及锂离子电池的寿命预测以及此类模型在实际使用状态下用于操作优化和充电策略的适用性。研究重点关注上海电动两轮车的典型应用场景，研究结果同样可以被普遍化并运用到电动汽车以及各种驾驶条件与应用案例中。模型优化基于所有涉及部分的准确且高效的模型计算以及应用场景的精确定义。如图1课题大纲所示，设置了数据收集活动以获取背景信息和用于研究分析的数据库。行驶数据可以用于生成上海市电动两轮车的典型驾驶工况。车辆模型包括电机模型、电机控制器模型、尤其是电池电模型和老化模型。仿真架构是优化电池寿命的基础，基于此提出了一种最佳的充电和存储策略。此外，可以使用更复杂的模型来验证所获得的优化结果。最终推导出可在线实施的启发式算法。

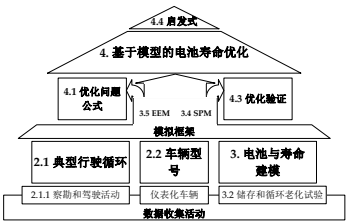

图 1: 工作大纲.

首先必须得出符合现实的驾驶行为，以反映如图2所示的E2W的典型应用。由于大多数现有的标准驾驶运行工况都是针对常规车辆和废气排放测试而设计的，因此在上海开展了数据采集活动以获取符合当地条件的数据。文中还说明了为什么需要收集数据，可以使用哪些类型的数据以及数据收集方法如何影响驾驶运行工况特性。这篇文章提出了三种数据收集方法：民意调查，智能手机和E2W实车测试。

图 2: E2W.

根据对用户行为的调查，得出了一个典型用例，即每天上下班通勤。然后，使用智能手机收集用于通勤的驾驶数据。没有选择特定的测试路线，而是明确了测试区域和通勤模式。数据按照不同的速度分类成不同的E2W类型。根据在标准中的定义，典型的E2W外观和市场份额，文章确定了E2W的三个类别：电动自行车，自行车式电动踏板车（BSES）和踏板车式电动踏板车（SSES）。基于智能手机的速度跟踪和仪器化的E2W的比较表明，这两种方法均适用于数据收集。智能手机的优势在于，更多的人可以参加，他们可以使用自己的E2W，因此可以降低成本。但是，传感器质量通常较差，采样率低，并且确切的驾驶条件可能未知。本课题引入了一种方法，以抵消智能手机对驾驶循环的电量预测能力比较低的弱点。

在此基础上，设计了在上海的E2W的典型行驶运行工况，这个工况区分上海E2W的两种主要功率等级。此外，使用了四种驾驶循环构建方法来构建驾驶运行工况并比较了它们的适用性。结果，使用马尔可夫链构建的驾驶运行工况被用作上海E2W运行工况（SE2WC）。由于上海E2W的功率较低，将得出的行驶运行工况与其他运行工况进行比较，突出显示了文章得出的运行工况的特殊特性。

表1列出了SE2WC在BSES和SSES两种车型下的典型特征，并和通用的全球统一摩托车排放认证循环工况（WMTC）进行了比较。结果表明，上海的E2W驾驶与常用的WMTC相比具有不同的特征：SE2WC的行程通常更长，速度和加速，减速比WMTC更低。这些本地化的驾驶运行工况将被用于确定典型的电池负载和应用场景。

表 1: 行驶周期的关键特征.

评价标准	单位	WMTC	BSES SE2WC	SSES SE2WC
距离	km	3.77	4.61	9.44
持续时间	s	600	1149	1704
平均速度	km/h	23.0	14.4	21.4
最大速度	km/h	50.0	32.3	40.4
(平均)加速度	m/s^2	0.57	0.39	0.50
(平均)减速	m/s^2	-0.61	-0.41	-0.45

下一步是将E2W特征化和建模。动力总成主要由三个部分组成：电动机，电力电子设备和电池。将已记录的典型驾驶循环工况转换成等效的功率曲线需要用到电机的模型、逆变器的模型、以及车辆到马路的物理特征模型。本文实现了永磁同步电机（PMSM）的模型，该模型因其相对较低的重量，紧凑的设计和高效率而经常用于E2W。PMSM由三相电流驱动，但通常使用转子磁链定向的dq模型进行建模和控制。文章介绍了模型方程式和控制方案。另外，提出了忽略电动机动力学的静态动力转换。由于优化通常需要在准确性和复杂性之间取得平衡，因此需要不同程度的抽象。可以使用更复杂的模型进行仿真和验证，并可以为诸如优化运行之类的复杂任务导出简化的模型。

这项课题的主要重点之一是从系统角度对锂离子电池进行研究和建模。老化过程可以归类为活性材料的损耗（LAM），比如石墨材料的体积变化；和锂存量的损耗（LLI）。LLI是由诸如电解质分解，钝化层的形成和锂镀层之类的副反应产生的。LAM的发生主要是由于在操作过程中机械应力引起的裂纹和溶解。负极表面的固体电解质界面（SEI）层的增长是电池老化的主要因素。总之，老化过程导致容量损失和电池电阻增加。此外，可以分析电池的差分电压曲线的变化确定老化过程。

尽管通常使用术语"锂离子电池"，但锂离子电池中存在不同的电极成份，并且需要考虑电池化学特有的作用。由于文献中关于不同电池化学性质的数据很少，本文基于老化运动研究了锂锰氧化物（LMO）电池的特性。本文介绍了日历老化和循环老化的结果，并将其与其他化学成分的电池进行了比较。

此外，本文比较了如图3所示的不同模型表达形式，以及它们在仿真和优化中的适用性。电池的电压和电流特性可以用等效电路模型（EEM）表示。此类EEM与经验老化关系一起用于对老化进行建模。文章引入了一个更精确而且计算量尚可的电化学模型，即所谓的单粒子模型（SPM），并与EEM进行了比较。EEM通常由三部分组成：代表电流-电压特性的等效电路，集总参数热模型和经验老化模型。根据LMO老化测试和其他化学材料的电池测试，评估了不同类型的老化模型及其质量。

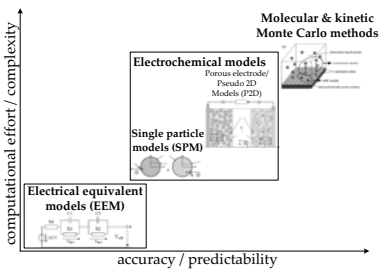

图 3: 各种电池建模方法综述.

另一方面，SPM不仅可以模拟电流，电压和温度的影响，还可以描述导致浓度变化，运输过程和化学反应的内部过程。因此，与EEM相比，它提供了更深刻的信息并可以描述更多的老化效应。由于需要求解几个偏微分方程和代数方程，该模型适用于仿真，但很难集成到大多数优化方案和算法中。

因此，它用于验证EEM获得的结果。本文展示了整个车辆动力总成仿真环境。电机，电力电子逆变器和电池的模型在不同的细节层次上组合在一起，从忽略电动机动态特性的快速近似老化到包括逆变器开关效应和电化学电池模型的电动机模型。图4展示了仿真环境的结构。

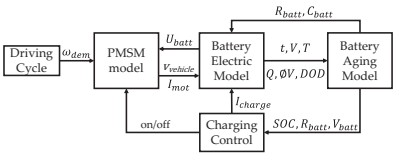

图 4: 整体仿真模型.

下一步，将先前描述的驾驶运行工况和动力总成模型合并到基于模型的优化策略中。定义了合适的用例并构建了优化问题。根据前面所述的调查结果和数据收集的结果，通勤上班被选为上海E2W的主要出行原因。如图5所示，本文确定了日常通勤驾驶循环作为应用场景。将基于驾驶路径，用户驾驶行为和电池模型的充电曲线作为自由度来优化电池寿命。通勤驾驶循环包括早上驾车去上班的电池放电过程、工作时间电池的存储过程、晚上下班回家的第二次放电过程和夜间电池存储和充电过程。

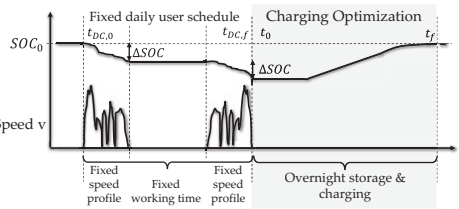

图 5: 全天的优化架构.

由于最大的优化潜力是在充电和存储过程中，因此本文描述了一种组合的最佳充电和操作策略。一天的最佳充电策略，对于整个电池寿命也是最佳的。在行驶过程中，根据驾驶运行工况，电池会在一定程度上放电。夜间充电曲线对应了使成本函数（这里的成本函数是电池老化）最小化的最优控制策略。由于每天的通勤路线差别不大，对于一天来说是优化的充电策略，对于整个电池生命周期来说也是延缓老化的最优策略。在整个优化策略中，根据采用的驾驶运行工况，电池在一天的行驶过程中，被放电到一定程度。夜晚，能够决定什么时候充电和充多少电的智能充电系统会将其充电至初始SOC。该智能充电系统可以基于下一章节描述的优化结果调整它的充电策略。优化本身可分解为两个步骤：充电曲线优化和初始SOC或目标SOC优化。为了优化充电曲线，假定初始SOC是固定的。然后，运行优化以识别最能保护电池的充电时间和电流曲线。在各种SOC级别上重复此过程，以确定节省电池寿命最多的SOC。文章使用SQP（顺序二次规划）算法解决优化问题。

作为第一个结果，图6显示了给定SOC为60%和80%时的典型最佳电流曲线。在所有优化的充电轨迹中都可以观察到普遍的总体趋势：在保持温度和老化约束的同时尽可能晚地对电池充电。这是合理的，因为电池会随着SOC和温度的升高而加速老化。

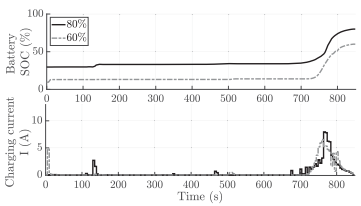

图 6: 典型最佳电流曲线。

其次，在特性图中的优化结果如图7所示。由于优化的目标是使电池容量损耗最小、也就是老化最慢，可以看到，初始SOC的最佳选择决定于实际的放电深度（DOD）。对每个DOD的初始SOC的最佳选择由一个标记突出显示。对于低的DOD，最小老化不会在出现在可能最小的SOC和未充满电的情况下。例如，如果20%的DOD能够满足日常通勤的需要，大约65%的初始SOC是最佳选择。正如预期的那样，老化随着DOD的增加而增加。此外，对于较大的DOD，最佳初始SOC值接近100%。

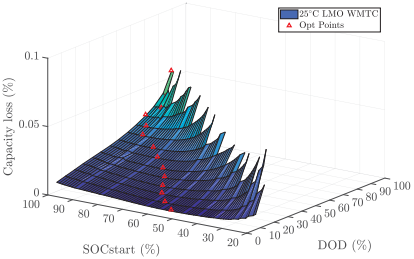

图 7: 不同的DOD和初始SOC的优化结果。

下一步，不同的优化结果将会基于以下几个方面进行比较：不同的运行工况，温度以及对潜在老化模型和化学物质的敏感性。结果表明，不同的运行工况和温度不会显着影响最佳SOC。但是，老化模型和电池化学物质的选择都对优化结果有影响。所计算出来的最优的初始SOC和充电曲线用来验证优化结果和基本假设，这个假设是，即这种全天优化能够代表整个生命周期的工况。

因此，所描述的全天放电曲线可以用来进行LMO电池的放电循环。这里，我们评估了三种情况：使用最优初始SOC和充电曲线进行充电；基于最佳初始SOC和驱动后直接进行常规恒流（CC）充电的组合的半最佳策略；以及进行100%SOC的常规充电。结果显示在图8中。通过使用较低的初始SOC，已经可以实现大多数容量节省。

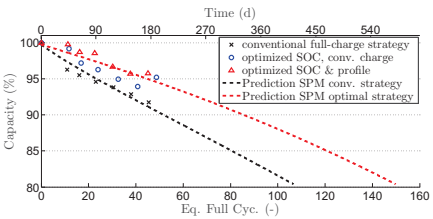

图 8: 验证电池单元测试和SPM预测.

在大约39个等效的完整周期（等于150天）之后，传统、组合和最佳策略的平均容量损失分别为7%，5.5%和5%。这相当于通过降低初始SOC，减少了21%的老化，额外的8%的减少是通过调整充电时间和充电曲线实现的。SPM老化模型的结果可用于生命周期的预测。如果将电池寿命的结束时间定义为剩余容量的80%（EOL80），则常规循环使用的电池将在400天（1.1年）后到达寿命终点。如果采用最佳充电策略，SPM预测电池在580天（1.6年）后达到其EOL80标准。总体而言，结果表明，优化的策略能够将电池使用寿命延长半年。

最后，我们提出了一种启发式操作策略，该策略也可以在线用在计算能力较低的E2W控制单元上。基于多项式函数和查找表，可以估算出优化策略。

简而言之，我们在此篇论文中：

- 评估了上海E2W的驾驶特性，提出了一个新的上海E2W的运行工况，并引入各种详细的车辆模型将运行工况转换成用于精确里程预测的功率曲线；
- 基于LMO电芯的完全老化测试研究了锂离子电池的老化过程并建立了老化模型；
- 提出了简化的电化学模型，调整后用于被评估的LMO电池，并对模型进行了改进，可用于仿真和验证；

- 将等效电模型与经验老化方程式结合起来，以进行快速老化计算，并作为优化架构的基础；
- 基于上海的实际驾驶情况得出了最优的充电和操作策略，并通过全新的电芯测试验证了它在电池老化性能上优于常规策略和半优化策略；
- 推导了可在线实施的启发式算法。

EXTENDED ABSTRACT

Electric vehicles (EVs) and hybrid electric vehicles (HEVs) have received increased attention over the last years due to the growing environmental awareness. In the context of battery electric vehicles (BEVs), the transition from lead-acid to Li-ion batteries has improved the user acceptance of BEVs by extending their range. In comparison to lead-acid batteries, Li-ion batteries offer a higher specific energy and power density thus a longer range can be achieved at a lower weight. However, battery lifetime remains a key issue. In the field of e-mobility, China is one of the pioneering countries due to its growing yet flexible market and its expertise in battery production. Although conventional four-wheeled EVs are predominantly being investigated, the market for electric two-wheelers (E2W) should not be neglected. Due to the partial ban of conventional two-wheelers, E2Ws already have shaped the cityscape in China's metropolises such as Shanghai and Beijing.

This study deals with the lifetime prediction of Li-ion batteries and the applicability of such models to optimize the operation and charging strategy under realistic application cases. The focus is on the typical application scenarios for E2Ws in Chinese urban areas such as Shanghai. The results can however also be generalized and transferred to EVs as well as various application cases and driving conditions. Model-based optimization is based on accurate yet computationally efficient models of all relevant parts and a precise definition of the application case. The work outline is presented in Fig. 9. It shows that data collection campaigns are set up to obtain background information and a database for the study. A typical driving cycle for E2W in Chinese urban areas can then be generated from the driving data.

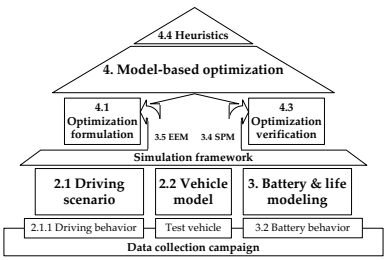

Figure 9: Work outline

A vehicle model comprising a motor, power electronics and, in particular, a battery electric model and an aging model is developed. This simulation framework is used as the basis to optimize the battery lifetime. An optimal charging and storage strategy is presented. In addition, more complex models can be used to verify the achieved optimization results. In the end, heuristics for online implementation are derived.

A realistic driving behavior must first be derived to reflect the typical use case of an E2W, as shown in Fig. 10. Since most of the existing standardized driving cycles are designed for conventional vehicles and exhaust emission testing, a data acquisition campaign is conducted in Shanghai to capture local conditions. In this context it is also demonstrated why data needs to be collected, which types of data collection are available, and how the data collection methods influence driving cycle characteristics.

Figure 10: E2W.

Three approaches for data collection are presented: conducting a survey, using smartphone and instrumented E2W measurements. On the basis of a survey on user behavior during a daily commute to and from work, a typical use case is derived. Then, driving data for commuting is collected using smartphones. No specific test route is selected, but a test area and profile. The data is clustered into speed profiles representing different E2W types. According to their standards, typical E2W appearance and market share, three classes for E2W are identified: e-bikes, bicycle-style electric scooters (BSES), and scooter-style electric scooter (SSES). The comparison between smartphone-based speed tracking and an instrumented E2W indicates that both methods are suitable for data collection. Smartphones have the advantage that more people can participate in a campaign where the participants use their own E2W. Thus the cost and effort can be reduced. However, the sensors are commonly less accurate, lower sampling rates are often selected, and the exact driving conditions might be unknown. A method to counter the lower energy predictions of driving cycles, obtained by smartphones, is introduced.

Based on this, a typical driving cycle for E2W in Shanghai is designed, which distinguishes between the two dominant power classes of E2W in Shanghai. Furthermore, four driving cycle construction methods are used to construct driving cycles and compare them for their applicability. As a result, the constructed driving cycles using Markov chains are used for the Shanghai E2W Driving Cycle (SE2WC). A comparison of the derived driving cycle to other cycles emphasizes the special characteristics of E2Ws in Shanghai due to their lower power. Table 2 illustrates the key characteristics of the SE2WC for BSES and SSES in comparison to the Worldwide Harmonized Motorcycle Emissions Certification Cycle (WMTC), which is commonly used. Results show that E2W driving in Shanghai has different characteristics than the commonly used WMTC. Trips of the SE2WC are much longer and the speed as well as the acceleration and deceleration are lower than for the WMTC. These localized driving cycles can then be used to determine typical battery load and usage scenarios.

Table 2: Key characteristics of driving cycles.

Criteria	Unit	WMTC	BSES SE2WC	SSES SE2WC
Distance	km	3.77	4.61	9.44
Time	s	600	1149	1704
Avg. Speed	km/h	23.0	14.4	21.4
Max. Speed	km/h	50.0	32.3	40.4
(Avg.) Accel.	m/s^2	0.57	0.39	0.50
(Avg.) Decel.	m/s^2	-0.61	-0.41	-0.45

The next step is to characterize and model the E2W itself. The powertrain consists mainly of three components: electric motor, power electronics and battery. Models of the electric motor and power control in combination with vehicle-to-street characteristics are required to convert the recorded typical driving cycles to equivalent power profiles. This is illustrated by implementing a permanent magnet synchronous machine (PMSM) model, which is often used in E2Ws due to its relatively low weight, compact design and high efficiency. The PMSM is operated by a three-phase current, but commonly modeled and controlled using a rotor-fixed dq-model. Model equations and a control scheme are introduced. In addition, a static force conversion which neglects motor dynamics, is presented. Different degrees of abstraction are required as optimization often requires

a balance between accuracy and complexity. More elaborate models can be used for simulation and verification. Simplified models can be derived for complex tasks such as optimization runs.

The main focuses of this study is to investigate and model the Li-ion battery from a system perspective. Aging processes can be differentiated into the loss of active material (LAM), for example due to volume changes of graphite, and the loss of lithium inventory (LLI). LLI results from side effects such as electrolyte decomposition, the formation of a passivation layer and lithium plating. LAM mainly occurs due to mechanical stress-induced cracking and dissolution during operation. The growth of the so-called Solid-Electrolyte Interphase (SEI) layer at the surface of the negative electrode is described as a dominant aging process. In summary, aging processes result in a loss of capacity and increase in the resistance of the cell. Furthermore, changes in the differential voltage curve of a cell can be analyzed.

Although the term Li-ion battery is commonly used, different electrode compositions exist within Li-ion batteries and specific cell chemistry effects need to be considered. Since there is only little data on different cell chemistries available in the literature, an aging campaign is initiated to investigate the characteristics of a lithium manganese oxide (LMO) cell. Results for calendar and cycle aging are presented and compared to additional cell chemistries.

In addition, different model representations, as summarized in Fig. 11, are compared regarding their applicability in simulation and optimization. Voltage and current characteristics of a battery (cell) can be represented by an electrical equivalent circuit model (EEM). Such an EEM combined with an empirical aging relation is implemented to model aging. A more accurate yet still computationally manageable electrochemical model, a so-called single particle model (SPM), is introduced and compared with the EEM. An EEM typically consists of three parts: an electrical equivalent circuit representing current-voltage characteristics, a lumped parameter thermal model and an empirical aging model. Different types of aging models and their quality are evaluated based on the LMO aging tests and other cell chemistries. On the other hand, an SPM models not only current, voltage and temperature effects, but also describes internal processes leading to concentration shifts, transportation processes, and chemical reactions. Therefore, it provides a deeper insight and can describe more aging effects than an EEM. Since several partial differential and algebraic equations need to be solved, this model is suitable for simulations but hard to integrate into most optimization schemes and algorithms. It is therefore used to verify the results obtained by the EEM.

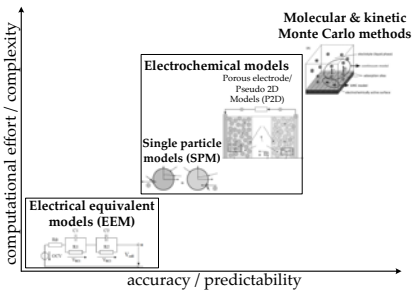

Figure 11: Overview of different battery cell modeling approaches.

A complete vehicle powertrain simulation environment is then presented. Models of the motor, power electronics, and battery are combined in different levels of detail, ranging from a fast aging approximation neglecting motor dynamics up to a motor model including inverter switching effects and an electrochemical battery model. Fig. 12 presents the structure of the simulation environment.

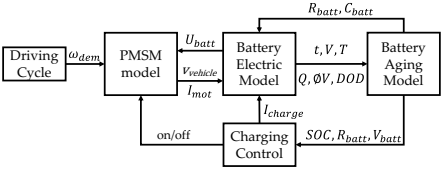

Figure 12: Overall simulation model.

The driving cycle and powertrain models are incorporated into a model-based optimization strategy. A proper use case is defined and an optimization problem is formulated. Commuting to work is selected as the main travel purpose of E2Ws in Shanghai based on the previously described results of the survey and data collection campaign. A daily driving routine is identified to optimize the battery lifetime by adapting the charging scenario as shown in Fig. 13. This is based on the driving profile, user behavior, and battery model. The commuting cycle consists of a discharge due to driving to work in the morning, a storage phase during working hours, a second discharge phase driving back home as well as an overnight storage and charging time.

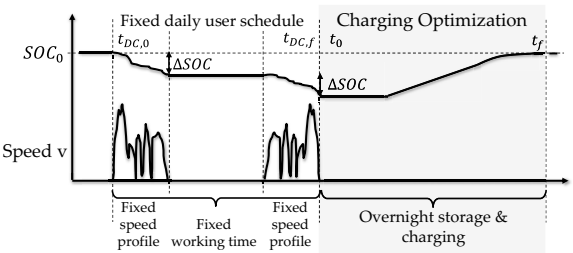

Figure 13: Optimization framework for one day.

Since the highest potential was identified during charging and storage, a combined optimal charging and operating strategy is described. In this case, the overnight charging profile corresponds to the optimal control which should be selected to minimize the cost function, which is the battery aging. A charging strategy, which is optimal for one day, also offers lifetime-saving potential over the entire battery lifetime, since the daily routine only differs slightly. In the optimized setup, the battery is discharged to a certain extent during driving, depending on the driving cycle applied. It is assumed that the battery is recharged to its initial state of charge (SOC) overnight by a charging system which can decide when and how much to charge. Such an intelligent charging system adapts its strategy according to the optimization results presented in the next paragraph. The optimization itself is decomposed into two steps: charging profile optimization and initial or target SOC optimization. A fixed initial SOC is assumed to optimize the charging profile. The optimization is then realized to identify the most battery-protecting charging time and current profile. This procedure is repeated at various SOC levels to identify the most battery lifetime saving SOC. The optimization problem is solved using an SQP (sequential quadratic programming) algorithm.

As a first result, Fig. 14 displays typical optimal current profiles for a given SOC of 60% and 80%. A general trend can be observed in all optimized charging trajectories: The battery is commonly charged as late as possible while maintaining the temperature and aging constraints. This is consistent with theory since aging increases with an increase in SOC and temperature.

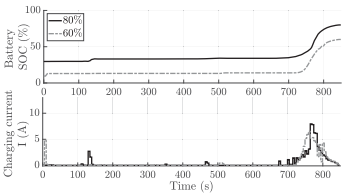

Figure 14: Exemplary optimal charging profile.

Secondly, the optimization results are shown in a characteristic map in Fig. 15. As the aim is to minimize capacity loss, which equals aging, the initial SOC is optimally chosen, which depends on the actual depth of discharge (DOD). The optimal choice of the initial SOC for each DOD is highlighted by a marker.

For low DOD, minimum aging is not achieved at the minimally possible initial SOC and full charge. For example, an initial SOC of approximately 65% is the optimal choice if 20% DOD are achieved by driving the daily commuting cycle. As expected, aging increases with higher DOD. Furthermore, the optimal initial SOC value shifts closer to 100% for larger DODs.

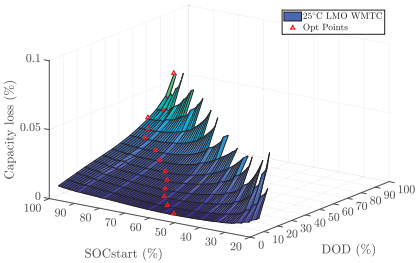

Figure 15: Optimization results for different DOD and initial SOCs.

In a next step, optimization results are compared with regard to different driving cycles, temperatures, as well as the sensitivity to the underlying aging model and cell chemistry. Results indicate that different driving cycles and temperature do not significantly influence the optimal SOC. However, the optimization is sensitive towards both the choice of the empirical aging model and cell chemistry.

The obtained optimal initial SOC and charging profile are used to validate the optimization results and the basic assumption that such a one-day optimization is able to represent the whole lifetime. Therefore, LMO cells were cycled using the described one-day profile. Three scenarios are evaluated: charging using the optimal initial SOC and charging profile, a semi-optimal strategy based on a combination of the optimal initial SOC as well as a conventional constant current (CC) charge directly after driving and conventional charging to 100% SOC. Results are displayed in Fig. 16. Most

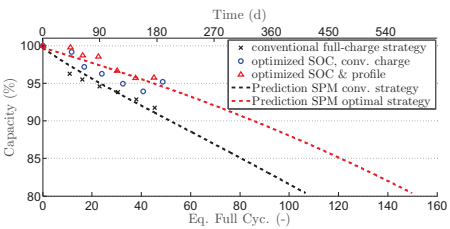

Figure 16: Validation cell tests and SPM prediction.

of the capacity saving potential can already be achieved by using a lower initial SOC for cycling. After approximately 39 equivalent full cycles, which equals 150 days, capacity loss is in average respectively at 7%, 5.5%, and 5% for the conventional, combined and optimal strategy. This corresponds to 21% less aging by decreasing the initial SOC and an additional 8% by adapting the charging time and profile. Results of the SPM aging model can be used for lifetime prediction. When the end of lifetime of the cell is defined at 80% remaining capacity (EOL80), the conventionally cycled cells reach a lifetime of 400 days (1.1 years). In case of the optimal charging strategy, the SPM predicts that the cells reach their EOL80 criteria after 580 days (1.6 years). Overall, results show that the optimized strategy might be able to improve the lifetime by half a year. This corresponds to a lifetime extension of 45%.
Finally, a heuristic operating strategy is presented, which can also be implemented online on the E2W control unit where less computing power is available. Based on polynomial functions and lookup tables, the optimized strategy can be approximated.

To summarize the research done for this thesis

- driving characteristics of E2Ws in Shanghai are evaluated, a novel driving cycle for E2W in Shanghai is presented and converted to a power profile for an accurate range prediction using a vehicle model incorporating different levels of detail;
- the aging process of Li-ion cells is investigated through a thorough cell aging campaign based on LMO cells and aging models are described;
- a simplified electrochemical model (single particle model) is presented, adapted to the evaluated LMO cell, improved and used for simulations and verification;
- an electrical equivalent model is combined with improved empirical aging equations for fast aging calculations and is used as a basis for the optimization framework;
- an optimal charging and operating strategy based on a realistic driving scenario in Shanghai is derived and validated against a conventional and an semi-optimal strategy using additional realistic cell tests;
- and heuristics for online implementation are deduced.

CONTENTS

ABBREVIATIONS

Abbrev.	Description
AC	alternating current
ACADO	Toolkit for Automatic Control and Dynamic Optimization
BEV	battery electric vehicle
BMS	battery management system
BOL	begin of life(time)
BOT	begin of test
BSES	bicycle-style electric scooters
CAN	Controller Area Network
CC/CV	constant current/constant voltage
CEMDC	Centre for Environmental Monitoring Motorcycle Driving Cycle
CM	closest match (approach)
CNY	Chinese yuan
CONV	conventional (full charge) charging strategy
CONV-SOC	conventional charging strategy but using the optimal initial SOC
CPE	constant phase elements
CR	charge rate
CVT	continuously variable transmission
C&C	Cut and Clip (approach)
DAE	differential algebraic equation
DC	direct current
DCR	discharge rate
DDP	discrete dynamic programming
DFT	discrete Fourier transform
DOD	depth of discharge
DOF	degree of freedom
DVA	differential voltage analysis
EEM	electrical equivalent model
efc	equivalent full cycle
EIS	electrochemical impedance spectroscopy
EOL	end of life(time)
EOT	end of test
EUR	Euro
EV	electric vehicle

E2W	electric two-wheeler
E2WME	E2W measurement equipment
FFT	fast Fourier transform
FTP-75	American EPA Federal Test Procedure
GDP	gross domestic product
GPS	global positioning system
HEV	hybrid electric vehicle
HPPC	Hybrid Pulse Power Characterization
ICA	incremental capacity analysis
ICE	internal combustion engine
IMU	inertial measurement unit
KHM	Kaohsiung Driving Cycle
kMC	kinetic Monte Carlo (method)
LAM	loss of active material
LCO	lithium cobalt oxide, $LiCoO_2$
LFP	lithium iron phosphate oxide, $LiFePO_4$
LLI	loss of lithium inventory
LMO	spinel lithium manganese oxide, $LiMn_2O_4$
LTO	lithium titan oxide
LXO	lithium-x-oxide with x representing different materials such as Ni, Mn, Co, ...
MC	Markov chain (method)
MOSFET	metal–oxide–semiconductor field-effect transistor
MTPA	Maximum torque per ampere
MW	Moving window (method)
NCA	blend of lithium oxide with nickel, cobalt and aluminum, $Li(NiCoAl)O_2$
NEDC	New European Driving Cycle
NMC	blend of lithium oxide with nickel, manganese and cobalt, $Li(NiMnCo)O_2$
OCV	open circuit voltage
ODE	ordinary differential equation
OPT	optimal SOC & charging strategy
OS	operating system
PDE	partial differential equation
PDOP	position dilution of precision
PE	polyethylene
PHEV	plug-in HEV
PI	proportional and integral part of controller
PMSM	permanent-magnet synchronous machine

PWM	pulse width modulation
P2D	pseudo-two-dimensional (model)
P3D	pseudo-three-dimensional (model)
QC/T 759	City driving cycle for vehicle testing
QP	quadratic program(ming)
RC	resistor-capacitor network
RLC	resistor-inductance-capacitor network
RMSE	root mean square error
SEI	solid electrolyte interphase (layer)
SE2WC	Shanghai E2W cycle
SME	smartphone measurement equipment
$SOC_{(o)(start)}$	(initial) state of charge
SOH	state of health
SPM	single particle model
SQP	sequential quadratic program(ming)
SPMSM	surface-mounted PMSM
SSES	scooter-style electric scooters
SVM	space vector modulation
TMDC	Taipei Motorcycle Driving Cycle
US	United States
WLTP	Worldwide harmonized light vehicles test procedures
WMTC	Worldwide harmonized motorcycle emissions certification cycle
XPS	X-ray photoelectron spectroscopy
XRD	X-ray diffraction
ZARC	parallel connection of a resistor and CPE

1

INTRODUCTION

With the rise of the world population and the economic boom of China, the demand for energy and standard of living increased likewise. As a result, emissions due to electricity production, industry and traffic contribute to the increase in air pollution. In China alone CO_2 emissions of approximately 7.54 tons per capita were recorded in 2014 in comparison to the world average of 4.97 [247]. Although the emissions were in 2014 still lower than the emissions in Germany (8.9 tons per capita), the strict politics in Germany led to a decrease of CO_2 emissions while the industry in China still hungers for energy. With a GDP of 12.2 trillion US$ in 2017 in China and a population of 1.39 billion as reported by [99, 247], this trend is likely to continue. Road traffic significantly constitutes to the amount of emissions [268]. The transportation sector accounted for about 851.2 million tons of CO_2 in China alone in 2016. This was only surpassed by electricity and heat production (4,386 million) and manufacturing industries and construction (2,850 million) [99]. In contrast to the latter two, which are commonly located outside or in the outskirts of a city, road traffic is a main issue within large cities and affects the daily life of millions of people living in the metropolises.

In recent years, much attention has been given to the development of hybrid electric vehicles (HEVs) and pure electric vehicles (EVs) to counter emissions due to traffic. Especially EVs are promoted as an emission-free solution to improve the standard of living within crowded cities. Still, the electric energy for such EVs is mostly provided by fossil fuels such as coal and oil electricity plants making them not totally emission-free. In China, political measures were taken to increase the attractiveness of HEVs and EVs. In addition, the partial ban of motorcycles and mopeds with an internal combustion engine (ICE) led to an immense growth of electric two-wheeler (E2W) sales in China's large cities. Still, many manufacturers of EVs and E2Ws face similar issues hindering the success of most e-mobility concepts: EVs are, on the one hand, regarded as environmental friendly and a clean solution for the future. On the other hand, they are only attractive for short distances as low energy storage potential and long recharging times are the main disadvantages. Therefore, many researches focus on the development of new and improved energy storage technologies. One possibility is the use of high energy batteries for energy storage. With the change from lead-acid to Li-ion technology, higher power at less weight is available. This sustains the attractiveness of EVs and E2Ws. One main issue still remains, though. Replacing a battery is very costly and for E2W, the battery even is the most expensive part. In most cases, the battery has to be replaced after 1 to 2 years as its capacity has decreased below 80%, which marks a battery's end of lifetime [272]. Lifetime can, on the one hand, be increased by the design and chemistry of the battery. This typically leads to a loss in power or energy storage.

On the other hand, battery lifetime strongly depends on the operating conditions. Li-ion batteries which are stored at low state of charge (SOC) have a much longer lifetime than the ones stored at high SOC. For cycling similar behaviors can be observed. So besides increasing the lifetime by chemical improvements, also operation restraints and driving optimization can prolong the battery lifetime.
This research focuses on the second approach. If, by proper operation and charging, the lifetime of an existing battery can be improved, EVs and E2Ws might become increasingly attractive. In this context, it is important to look not only at the battery itself but the whole powertrain, vehicle type, and operation condition since the battery experiences different stress depending on the use case. In addition to increasing the lifetime, other optimization goals, such as range extension, might be handled and improved the same way. In total, this will help the customers to get an environmental friendly form of transportation, the manufacturers to increase the approval and decrease both the initial and maintenance cost of EVs and E2Ws, and sustain the environment, as batteries can be used longer and less disposal of batteries is necessary.

1.1 STATE OF THE ART

1.1.1 E-mobility in China

Roadmaps for the development and standardization of electric mobility have been presented in Germany [154, 155], and similarly standards for EVs are developed and updated in China [197, 198]. At the same time, financial and political incentives have been set up to promote EVs. As a result, research has focused on improving HEVs and pure EVs over the last years and the numbers of EVs have increased. Although EVs are particularly in focus in Germany and in China, the influence of E2Ws should not be underestimated. In Germany the class of electric pedelecs, low-power E2W with an electric motor which is only allowed to assist during pedaling, is the most common E2W type and experienced a drastic rise in recent years. Still, also fully electrical two-wheelers are developing [26, 89]. Due to laxer regulations and favorable traffic conditions, the E2W market in China shows different characteristics [273]. Although most E2Ws do have pedals and show similarities to conventional bicycles, they can also be – and in reality are mainly – operated solely by the electric motor [246].
In 2016 annual E2W sales in China totaled more than 30 million whereas the sales in the rest of the world summed only up to 3 million [151]. In Germany, merely 535 thousand E2W were sold most of which were pedelecs. In total, approximately 120 million E2W were in operation in China in 2015 and more than 200 million are estimated for 2018 [151, 272]. The increasing popularity of E2W can also be seen in the change of transportation means over the last decades. Whereas in 1995 bicycles accounted for about 39% of the daily trips in Shanghai and E2W only for less than 3%, people stated that in 2014 they used the E2W already in more than 20% of the trips and only 7% of the trips were done on a bicycle [80].

The popularity and success of E2W can be accounted to different factors. On the one hand, they are agile and able to maneuver through heavy traffic, lightweight, and come with an efficient powertrain structure. In addition, E2W are cheap and easy to ride as they require no license and are treated like bicycles [272]. They require minimal parking

space, have a low noise and emission characteristic, and low operation and maintenance costs [45, 46, 103]. Recent advances in technology further improved the cost effectiveness and performance. Although most E2W are still operated by lead-acid batteries, the market share of Li-ion batteries is expected to rise, and has already risen, due to reduced cost of Li-ion batteries. Whereas in 2016 more than 95% were still operated by lead-acid batteries, current research, as introduced in section 2.1.1.3, indicates that the proportion has already changed.
On the other hand, politics enforced a ban of combustion engine mopeds and motorbikes in most larger cities to counter the air pollution [246]. This, in addition to the often crowded and delayed public transportation, makes E2Ws very attractive for short distances of approximately 10 km as required in urban traffic and commuting scenarios. However, after an initial drastic increase in E2W numbers, another issue arose which led to campaigns against E2W [46, 272]. E2W drivers were hard to control and often neglected traffic rules thus leasing to an increase in traffic accidents. In addition, chaotic parking and resulting sidewalk or road congestions became a problem, especially since the rise of shared-bike companies. Nevertheless, China is the largest supplier of E2W worldwide with a market share of more than 92% [151] and new markets open up especially in India.

As a result, driving conditions of E2W in China differ from western countries. The urban traffic scenario with low-power E2Ws leads to complex driving characteristics, which need to be investigated. For optimization purposes, a scenario is required to identify the system, which needs to be covered, and especially its boundaries. A battery intended for the use in an E2W might have another operation area (power range, acceleration demands) than that of an EV. Varying powertrain setups and components might lead to different operation strategies. This effect is intensified by different street, environmental and driving conditions. A driver in Europe might drive in another way than a driver in China, e.g. due to regulations and traffic. Therefore it is useful to get an understanding of driving cycles for E2W in China.
There are some internationally used drive cycles, but they are typically developed for cars (higher power/speed) for American or European conditions. Examples are the New European Drive Cycle (NEDC [234]), which is a synthetic drive cycle for vehicles, and the World Motorcycle Test Cycle (WMTC [235]), which is intended to measure fuel consumption and emissions in motorcycles. Both are not designed for electric vehicles and require higher power than typical E2W are able to provide. The Chinese city driving cycle for vehicle testing (QC/T 759 [194]) is used to evaluate city buses and passenger cars in dynamometer performance tests. However, it has the drawback that no localized driving cycle was recorded and it is only valid for four-wheelers. Other studies propose two-wheeler driving cycles for Asia but they are unverified, mostly intended for emission measurements, and recorded with combustion engine motorcycles of higher power [47, 230–232].

1.1.2 E2W modeling

Focusing more closely on the EV and E2W in particular, these typically consist of four main powertrain components: electric motor, power electronics, transmission, and battery. For E2Ws as used in Asian countries such as China, these components are generally relatively simple since cost reduction is one of the most important factors for E2W design. In most cases the design of the powertrain can be reduced to a battery pack (either

lead-acid or Li-ion), motor controller, and electric motor. The transmission is either done using a constant transmission ratio for externally attached motors or not present at all for in-wheel motors. Most E2Ws in China use an in-wheel motor due to their relatively low power and the simple motor design.

For the context of this work, a permanent-magnet synchronous motor (PMSM) is used. PMSMs are often found in E2Ws due to their relatively low weight, compact design and high efficiency. In the Chinese market most E2W nowadays are designed for a nominal power between 200 W and 750 W with a maximum speed of 20 km/h to 50 km/h [45, 46, 103, 246, 266]. Many studies have been conducted for modeling of PMSM. The principle of operation is well understood and different levels of detail for implementation exist. PMSM are synchronous motors with permanent magnets fixed to the rotor. The stator coils are usually powered by a three phase current. For the use with constant current power sources like batteries the constant current has to be transformed to a three phase current using a voltage source inverter and control scheme. There are two main PMSM designs: in-wheel PMSM usually come with an outer rotor design while inner rotor designs are often attached to the wheel using a gearbox. For control purposes the PMSM is typically not described in the natural three phase system (abc-system), but transformed to a rotor-fixed two-phase system (dq-system) known as Park's transformation [112, 116, 172]. This is possible as the three axes are not independent from each other, and in a second step the static world coordinate system can be transformed to a rotating reference frame. In the rotating reference frame, the currents and voltages are constant in steady state. This simplifies the control and cascade control schemes can be implemented to control the current and speed in separate loops. The description of the PMSM in dq-coordinates is relatively simple and requires little parameters. Various studies exist, which introduce more detailed processes, by including e.g. saturation, coupling effects between d- and q-axis, losses and other nonlinearities. Especially for motor design, three-phase models are also used [214]. This requires a good knowledge of control but offer a more detailed analysis of e.g. component sizing.

For the actuation of the electric motor, power electronics and a control strategy are required. However, most AC motors are supplied by a direct current (DC) source. In case of EVs, a battery is used as DC power source. For conversion from DC to a three-phase AC, inverters are used. Nowadays, most inverters used for EVs are three-phase inverters. Electric motors such as the PMSM are supplied by three phase currents with 120° phase difference. The most important inverter control schemes are either pulse width modulation (PWM), hysteresis control, as well as space vector modulation (SVM). Also a variety of power electronics and control strategies exist. For E2W application typically a voltage-fed three phase inverter is used together with an intercircuit capacitor to transform the constant battery current to three phase motor currents. If a detailed analysis is required the switches have to be modeled (e.g. MOSFETs). Otherwise, the switching behavior can be assumed to be ideal. Control strategies for dq-control are separated into constant torque and field-weakening control schemes for the velocity control loop. Much literature is available on control schemes [101, 113, 116, 146, 147, 181, 223, 233]. Examples are PI-control, vector control, direct torque control or maximum torque per ampere control. Other schemes take use of predictive current control as described in [146]. A good overview of the main PMSM modeling and control schemes is given in [116].

1.1.3 Li-ion batteries

In addition to the electric motor, power electronics, and transmission, the battery plays an important role in an EV and E2W since the battery is commonly the most expensive part of an E2W.

Technology

Two main battery types are used for low-power E2Ws in Asia: lead-acid and Li-ion. Meanwhile lead-acid batteries have been the standard for the last decades, Li-ion batteries are emerging [46, 151, 272]. Li-ion batteries provide a higher gravimetric and volumetric energy density. Therefore, a smaller and lighter Li-ion battery can replace a lead-acid battery of the same power and capacity. Lead-acid batteries on the other hand are still cheaper and their system behavior is well-researched. As cost is the most important factor for the E2W market in Asian countries, many E2W still use lead-acid batteries. Li-ion cells provide output voltages of about 3.2 V for lithium iron phosphate ($LiFePO_4$, LFP) cells and 4.2 V for lithium manganese oxide ($LiMn_2O_4$, LMO) or lithium nickel manganese cobalt oxide ($Li(Ni_xMn_yCo_z)O_2$, NMC) cells depending on the SOC and exact chemistry used [117, 118, 169, 238]. Lead-acid cells provide only about 2.4 V. The structure and operation behavior of Li-ion cells is shortly introduced. Li-ion cells come in various shapes, sizes, and properties. They can either be distinguished by their recharge-ability, with primary cells being non-rechargeable and secondary being rechargeable, material type, e.g. LFP, LMO, and NMC, appearance, e.g. cylindrical, prismatic, and pouch cells of various sizes, and cell capacity to name a few. In the following, only secondary Li-ion batteries with a graphite negative electrode are examined.

The major components of a Li-ion cell are the negative electrode, separator, and positive electrode. The negative electrode is commonly composed of graphite due to its low voltage potential of approximately 0.1 V against metallic lithium. Recently, research focuses also on lithium alloys such as LiTiO (LTO) as negative electrode material due to its increased stability. However, the material is still very expensive compared to graphite electrodes and offers a lower usable voltage range due to its higher potential against lithium ($\approx$1.5 V) [118]. Various Li compounds are used for the positive electrode. For example, $LiCoO_2$ (LCO), $LiFePO_4$ (LFP), $LiMn_2O_4$ (LMO), $Li(NiCoAl)O_2$ (NMC), and $Li(NiMnCo)O_2$ (NCA) are used. These materials have all in common that Li-ions are used to transport charge between the electrodes. The electrodes' active materials are commonly attached to thin foils of the current collector using binders. Copper is typically used as current collector of the negative electrode and Aluminum for the positive electrode. The current collectors have the task to transport the electrons to and from the active materials to close the electric circuit. The separator material can be microporous membranes, fabrics or films such as polyethylene (PE)-based microporous membrane separators [227]. A separators task is to mechanically separate and insulate between the electrodes, to hold the liquid electrolyte and to enable a flow of Li-ions while preventing electrons to pass. Lithium salts in an organic solvent are widely used as electrolyte. Much research focuses on improving the electrolyte by adding various additives to improve its stability and every manufacturer uses its own special recipe. For details it is referred to [117, 118, 153, 256].

Fig. 1.1 provides an overview of the most common cell shapes. Cylindrical cells as displayed in Fig. 1.1 (a) are widely available and used in the standardized size of 18650

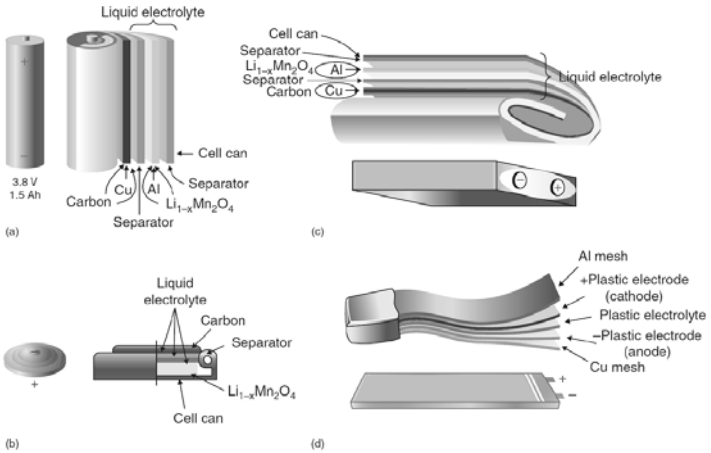

Figure 1.1: Different cell shapes: (a) cylindrical, (b) coin, (c) prismatic, (d) pouch. Adapted from [117]

cells. In this shape, the positive and negative electrode as well as the separator are rolled up. The current collectors, in this case copper for the graphite negative electrode and aluminum for the LMO positive electrode, are combined at the top or bottom and form the cell contacts. Typical 18650 cells offer a voltage of 3.2 V to 4.2 V and capacity of 1.5 Ah to 2.5 Ah depending on the chemistry. Prismatic cells (c) are either also rolled up or consist of different separate layers of electrode-separator-electrode layers. Flat cells, often also labeled as pouch cells if the housing is not solid, are similar built. In Fig. 1.1 (d), plastic electrodes are used. Coin cells (b) are commonly used for the development of new cells or for aging analysis. They typically only consist of one layer of negative and positive electrode together with a separator.

A battery typically consists not only of one cell but many connected in series or parallel to achieve higher output voltages or a higher capacity and output current. The cells are arranged together in battery packs. For larger batteries, they are arranged in modules first and the modules are combined to packs. As every cell is reacting slightly different, battery management systems (BMS) are applied to battery packs. Their main task is to ensure that every cell remains a safe state during charging and discharging. Depending on the battery type and application, BMS monitor voltage, current, and temperature of the cells.

Meanwhile SOC detection has been quite simple for lead-acid batteries as the electrolyte indicates the SOC, Li-ion cells have no means to directly measure a parameter which corresponds to the SOC. Their SOC can be estimated based on the charge throughput (ampere counting) starting from a fully charged cell. However, due to measurement noises and other inaccuracies during current measurement, results of the charge throughput deviate over time. Further, voltage can be used as a SOC indicator. By measuring the open circuit voltage (OCV), the voltage the cell settles to if no current is applied for a long time, of a cell at various SOC, a dependency between voltage and SOC can be drawn. However, voltage varies strongly based on the applied current. Therefore, voltage can

only be used as an SOC indication after long storage periods. Applying a Kalman filter to predict and update the SOC can help to increase the accuracy by combining ampere counting and voltage measurements with a cell model. Still, research about this topic is ongoing.
Another peculiarity of Li-ion cells is their charging behavior. Li-ion cells are quite sensitive to overcharging as the electrolyte decomposes. Further, the voltage profile during charging shows a steep increase for high voltages. Most suppliers provide a maximum cell voltage for charging to avoid electrolyte decomposition. Even though the maximum voltage is reached, the cell is not yet fully charged. Therefore, the charging process is separated into a constant current (CC) charging until the cut-off voltage is reached and a constant voltage (CV) charging until the current decreases below a certain level. As the constant voltage charging takes quite a long time to charge the cell, various other charging strategies have been proposed and used to achieve fast charging. For example, multistage CC with varying current, boost charging, pulse charging, or sinusoidal ripple charging have been used [109, 127].

Operating Principle

The operating principle of a Li-ion cell is depicted in Fig. 1.2. Almost all cyclizable Li-ions are present in the positive electrode consisting of Li-metal compounds such as LFP and LMO for a discharged cell. Once a charging current is applied, a voltage difference between the electrodes is generated forcing Li^+ to be decalated from the host lattice of the positive electrode. Likewise, the corresponding electrons migrate from the positive electrode over the current collector and charger connections to the negative electrode. Decalated Li^+ dissolves into the electrolyte, where a solvation sheath is built up around the positive ion. The Li^+ migrates then through the separator material to the negative electrode due to the potential difference and diffusion. The solvation sheath breaks up at the negative electrode's surface and Li^+ is intercalated into the graphite layers of the negative electrode. Typically, a solid electrolyte interphase layer is present at the surface of the negative electrode. This layer is built up due to overlapping potential areas of the negative electrode and the electrolyte. Side products are formed during this reaction leading to an initial reduction of Li^+. However, the side products form a protective layer preventing further electrolyte to reach the negative electrode material. After this layer has been built up, Li^+ can still migrate through it to reach the negative electrode and intercalate into the graphite layers. This process is reversed during discharge.

The occurring reactions can be separated into negative electrode and positive electrode reactions. For graphite-based negative electrodes, the reaction results in:

$$C_6 + xLi^+ + xe^- \underset{\text{discharge}}{\overset{\text{charge}}{\rightleftharpoons}} Li_xC_6 \tag{1.1}$$

Reactions occurring at the positive electrode depend on the positive electrode's material. For the case of LFP, it can be written as:

$$LiFePO_4 \underset{\text{discharge}}{\overset{\text{charge}}{\rightleftharpoons}} Li_{1-x}FePO_4 + xLi^+ + xe^- \tag{1.2}$$

If LMO is used, the reaction results in:

$$LiMn_2O_4 \underset{\text{discharge}}{\overset{\text{charge}}{\rightleftharpoons}} Li_{1-x}Mn_2O_4 + xLi^+ + xe^- \tag{1.3}$$

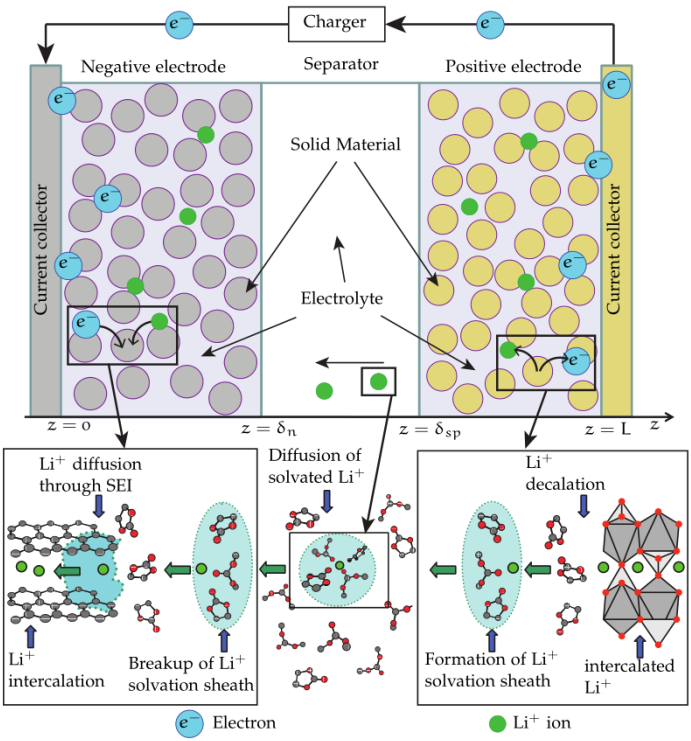

Figure 1.2: Overview of a Li-ion cell and operating principle. Derived from [56, 139, 252, 263].

The overall reaction can, for the example of LMO, be written as:

$$\mathrm{LiMn_2O_4 + C_6} \underset{\text{discharge}}{\overset{\text{charge}}{\rightleftharpoons}} \mathrm{Li_xC_6 + Li_{1-x}Mn_2O_4}\,. \tag{1.4}$$

Aging

Although Li-ion batteries have been used for over 20 years now, some of the processes occurring in the cells are still under research. The complexity of Li-ion battery modeling is mostly due to many different cell chemistries (LFP, LMO, NMC) existing and many are still in development. Even if a cell is labeled as one chemistry, every manufacturer uses its own recipe. For example, electrode composition, electrolyte, additives, and even housing and form (round, prismatic, pouch cell) influence aging. Furthermore, cell manufacturers improve their cell design continuously. Each cell chemistry has different advantages and disadvantages, like LFP being safer than manganese based systems, LMO being durable and having a low cost or NMC having a high energy density and output power. The basic processes – like transport of ions, chemical main reactions

and electron exchange – are well described in literature, but especially for reactions and interactions leading to aging of the cell many questions are still open.

Cell aging itself occurs due to chemical reactions, transport processes, ion intercalations, external stress and their synergy. These processes lead to a loss of lithium inventory and active material. Side reactions such as electrolyte decomposition, passivation layer formation and lithium plating induce a loss of cyclizable lithium. Active material is lost when the material gets damaged, for example due to cracking and dissolution reactions due to volume changes [12, 36, 37, 163, 240]. Although mainly interactions on the electrodes' surface and electrolyte lead to aging effects, also current collectors, binders and additives might interact [163]. One of the main aging mechanisms in cells with a graphitic negative electrode is accounted to the growth of a passivation layer on the surface of the negative electrode. This is commonly labeled as Solid-Electrolyte Interphase (SEI) layer [12, 17, 36, 37, 163, 165, 262].
An SEI layer forms as the graphite at the negative electrode's surface reacts with electrolyte components due to a negative potential being applied. The positive electrode comprising lithium also reacts with the electrolyte forming an SEI, but this effect is negligible compared to the passivation effect of the SEI on the graphite surface. A decomposition at very low and high voltages occurs as the electrolyte is thermodynamically unstable in these voltage ranges. During the first cycles, this SEI layer is built up so that no further side products can form. Ideally, Li-ions can pass through the SEI layer and electrons cannot by being immediately consumed. However, due to electrical and mechanical stress during charge and discharge, the SEI layer can be damaged. During repair processes, the SEI layer consumes further Li-ions. Occurring processes are, for example, summarized in [239]. Electrolyte decomposition leads to the formation of an SEI. Graphite exfoliation results from cracks formed by gas and solvent co-intercalation. In addition, the growth of the SEI layer, SEI porosity changes, corrosion effects at the current collector, and lithium plating induce changes.
Aging can commonly be separated into three phases: initial fast degradation during formation (SEI layer build-up), slower degradation during regular lifetime, and drastic drop of cell capacity and power at end of lifetime. Initially, the SEI layer grows and leads to a capacity loss and resistance increase as Li-ions are constantly consumed and the SEI thickness adds to the cell's electrode resistance. Once the cell is close to its end of life, which is commonly defined after reaching 80% of the cell's initial capacity or a doubling in resistance, the aging characteristic changes. A rapid loss in capacity and resistance increase is observed. Whereas the growth of the SEI is predominantly responsible for aging before the end of life criteria is reached, lithium plating accounts for the rapid degradation after end of life [209, 257]. Due to the manifold lithium metal compounds used as positive electrode material, it is hard to formulate occurring reactions and interactions exactly. Time consuming accelerated aging test campaigns are required to determine the exact aging characteristics.

For aging analysis, different methods are available. Capacity and resistance changes can be recorded based on charge throughput and voltage drop [36, 68]. Further, variations and peculiarities of the OCV and differential voltage can be used to detect further effects. Differential curves show the effects of so called phase transitions or phase equilibria [29, 64]. Electrochemical impedance spectroscopy (EIS) can be used as a non-destructive method to examine and allocate cell aging processes to different reactions [17, 95]. The electrical properties of the cell are described by using an impedance diagram over dif-

ferent applied frequencies. In addition, cells can be decomposed and half-cell measurements provide additional information. Evaluations under an electron microscope reveal the electrodes' structure in detail.

Modeling

Various approaches yielding different accuracy and complexity have been described in literature and can be used for simulation and analysis of battery cells. In the simplest case, electrical equivalent circuits together with empirical aging models can be used as described in [28, 52, 170, 178, 205, 245]. These are referred to as electrical equivalent models (EEMs). In most automotive tasks, aging behavior is even neglected. EEMs aim on reproducing the observable results of a cell, like voltage and current for system modeling and capacity increase and resistance loss in the case of aging effects.
EEMs typically consist of three elements: a base model to represent the current-voltage characteristics of the cell, a thermal model to represent heating and cooling, and an empirical aging model. The base model typically consists of either a resistor in series with an ideal voltage source, which reflect the static battery behavior, over various resistors and capacitors in parallel, often labeled as RC-elements and in total as Randles circuit [181], to e.g. more complex RLC-circuits as described in [39]. Electrical equivalent models have the advantage that they have a relatively low complexity and computation times compared to e.g. electrochemical models, which often involve partial differential equations. They usually require less knowledge about the cells' chemistry and therefore use less parameters which are easier to obtain. A lumped parameter thermal model is added to include temperature variations due to (dis-)charging. Empirical aging equations use available measures such as current, voltage, and temperature and derived values such as SOC, charge throughput, cycle number, and depth of discharge (DOD) to model capacity loss and resistance increase [28, 52, 170, 205, 245].

On the other hand electrochemical models of various modeling depth are designed to resemble cell internal processes including transport of ions, concentration flows, and chemical reactions [13, 59–62, 164, 179]. Inside electrochemical models, molecular models such as Kinetic Monte Carlo methods [106, 145, 191] offer the highest accuracy but require also the highest computation power and system knowledge. Pseudo two dimensional (P2D) or porous electrode models use simplified expressions of the electrodes and reactions [129]. Single particle models (SPMs) [4, 5, 71, 134, 170, 175, 176, 199] are one dimensional models which neglect different concentrations in the solution and merely model the electrodes as one particle where diffusion and intercalation occurs. Three and two-dimensional electrochemical models offer the highest accuracy but computation time increases likewise. Multiphysics models as presented in [7, 11, 91, 130, 140] combine molecular models with other electrochemical and electrical approximations to reduce the complexity. In addition, SPMs offer a good tradeoff between accuracy and computation time and provide insight to inner cell mechanisms. Still, most electrochemical models do not consider aging. Especially more complex and coupled electrochemical models used for cell design only require to run some cycles and aging influences can be neglected. Lifetime simulations are commonly done by SPMs, as they are still computable over a long time horizon. SPMs include a simpler version of the transport phenomena as well as assume the electrodes to be representable by one single particle instead of modeling a large amount of active material and composite grains. For a detailed comparison it is referred to [180]. Various approaches have been presented to further simplify SPMs by approximating the partial differential equations (PDEs) to

ordinary differential equations (ODEs). They are based on Pade approximation [141], orthogonal decomposition [40], and many other simplification methods [27, 129].

1.1.4 Optimal operation of EVs/E2Ws

Optimization can either be conducted at component layer, where, for example, the motor efficiency is increased by constructive measures [6, 261], or at the system level, where the interaction between all components can be analyzed. In this context, the identification of degrees of freedom (DOF) for the optimization is an essential step. Considering HEVs, the switching and transition between conventional and electric engine provides a good optimization potential. In the case of pure EVs, this essential DOF is not available. Still, power distribution between different electric engines can be used as DOF if more than one is installed in a vehicle [58, 77, 259]. Likewise, different power sources such as a battery and supercapacitor [42, 259] can be utilized as an additional DOF for optimization.
If only one motor and battery are available, the optimization commonly relies on an adaption of the speed profile [148]. In this context, predictive operation strategies which look ahead on the driven route offer a potential for range extension and optimal use of the energy storage [92]. However, such a control and optimization strategy generally inflicts a power restraint. The acceleration and speed are limited, which negatively affects the drivers and their driving experience. On the other hand, an overall operation strategy can be defined which optimizes not or not solely the operation and driving of the vehicle but also the storage and charging phases.

Battery lifetime & charging optimization

The role of charging profile optimization has received increased attention in recent years. Following the argumentation provided in [187], one large research topic comprises charging time optimization and charging station distribution. As the number of charging stations is still limited, these studies focus on minimizing charging time or the optimal use of the existing infrastructure [123, 208]. Other approaches focus on minimizing electricity cost [96] or analyzing the charging pattern [241]. However, in most cases battery aging is neglected or only used as an additional optimization goal. Battery charging optimization regarding lifetime and charging time based on power grid operation was presented in [19]. An electrochemical aging model was used to describe the influence of battery degradation. The authors in [72, 226] proposed a charging management with respect to user requirements and lifetime. The charging profile for different scenarios is improved using a semi-empirical aging equation and an EV thermal model. In comparison to conventional charging, the presented optimized charging is able to reduce aging. Moreover, temperature was identified as a key aging factor. [2, 3] as well as [131] present an optimal battery charging strategy regarding time-to-charge, energy loss and temperature increase. They draw the conclusion that the commonly used constant current constant voltage (CC-CV) charging strategy is close to the optimal strategy. However, they only use a very basic electrical equivalent model and full charge scenarios. Research findings in [264] present an optimized charging strategy regarding temperature rise and charging time. Aging effects are only taken into account by analyzing the polarization voltage to determine the maximum charging current.

Optimization setup

There are various approaches to realize an optimization. One choice is between model-free and model-based approaches. Model-free optimization schemes directly use process data without deeper knowledge of the underlying system and can thus be applied to many different problems. They typically rely on extensive tests on a realistic system such as data driven methods. However, measurement outliers and noise might have a strong impact on the optimization outcome. In comparison to model-free optimization strategies, a model-based optimization can use predictions and results of the underlying model to improve its results. This typically leads to an increased performance, both in terms of faster convergence rates and higher accuracy. In other words, fewer model evaluations are required to find the optimal solution, and the optimization results can also be valid in between or outside of the sampled space (generalization through interpolation, extrapolation). In addition, a model adds a deeper knowledge of the system itself and possible bottlenecks. On the other hand, the underlying model is required to accurately reflect reality. For complex processes it might be difficult to obtain such a model globally or at least locally with sufficient accuracy. Furthermore, changes of the model must be known or the optimization result will deviate from reality.

For the purpose of this thesis, model-based optimal control schemes are desired which aim to find an optimal trajectory of one or more control inputs. Indirect methods approximate the necessary optimality conditions and the resulting boundary-value problem needs to be solved numerically. A non-linear approximation of the optimization problem is used in direct methods. This problem can be solved by different discretization methods such as collocation or sequential quadratic programming (SQP) [33]. SQP for example converges usually quite fast to an optimal solution and can deal with many states, but on the other hand is strongly dependent on the initial conditions, solves partly linearized sub-problems of quadratic structure, cannot deal with non-continuous states and is only able to find the local solution. In addition, dynamic programming such as discrete dynamic programming (DDP) [20, 63] can be used to determine the operational strategy. DDP has advantages when dealing with discrete signals and is able to converge to the globally optimal solution of the discretized problem but suffers from high computation time, need of discretization, and the chosen discretization grid and can thus typically handle only a small-scale problems. An optimization can be set up to minimize one objective or many (Pareto-front). Once a problem formulation has been established, a solver can be chosen that fits the requirements best. Depending on the model structure, optimization method, solver, and available hardware, the optimization framework can be implemented offline or online.

1.2 AIM OF THE WORK

The overall objective of this work is the model-based optimization of the lifetime of Li-ion batteries in a realistic operation scenario. This comprises the analysis of a realistic scenario, in this case the operation of a E2W in China, the setup of a simulation framework including models of all relevant components, a detailed analysis of Li-ion cells and their aging behavior, the determination of realistic degrees of freedom for optimization, and the actual realization of the optimization framework to improve battery lifetime. Three main steps are necessary for a methodological and model-based optimization

approach: data collection, simulation, and optimization. This thesis is structured accordingly as visualized in Fig. 1.3.

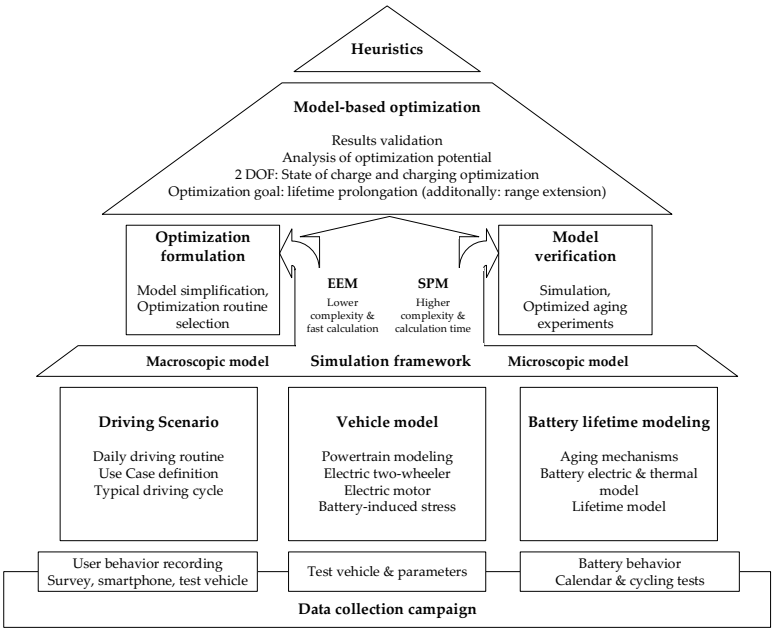

Figure 1.3: Work outline.

Starting from the bottom to the top, the framework illustrated in Fig. 1.3 is based on real-world or experimental data to sustain the theory and models. If no or an insufficient data basis is available, a data collection campaign is required to gain a detailed understanding of the occurring processes. In the case of E2W battery lifetime optimization, optimization input data and data to sustain the E2W model is required. The first comprises details about a typical use-case of E2W and a corresponding typical or representative driving cycle. The latter is, due to its complexity and the focus on battery lifetime, separated into a vehicle powertrain model, which comprises the force interaction between the street and the wheels, the electric motor, and the transmission, and a battery (lifetime) model.

The determination of a driving scenario requires a thorough understanding of the use-case. Data about typical user behavior can be collected through surveys or driving behavior and route recording. Latter can, in this specific case, be separated into speed tracking via smartphone and by providing a test vehicle which is equipped with additional measurement equipment. As a result, a daily driving routine can be identified leading to a typical driving cycle. For the synthesis of a driving cycle, the previous descriptions can be aggregated into three main questions which need to be answered at first:

- What is a realistic use-case for E2W operation and battery lifetime optimization in China?
- Does an applicable driving cycle exist and, if not, how can a suitable driving cycle be identified?
- And finally, how does a typical E2W driving cycle in Shanghai look like and what are its characteristics?

The second pillar focuses on the establishment of a vehicle model starting from vehicle to environment interaction over motor modeling to power electronics, control, and transmission. The motor model relies on available motor parameters and its operation and control strategy. Data provided by a test vehicle can be used to validate the vehicle model by measuring battery current and voltage. Questions associated to this task can be summarized to:

- How can a typical driving cycle be converted into a power profile which the battery has to supply and how is it affected by the driver?
- Which powertrain components are relevant for an E2W and how are the components modeled?
- What does a typical power profile for E2W operation, which the battery has to supply, look like and what are its implications on the battery?

The third foundation of the simulation framework is built up by the battery model. The term "Li-ion battery" is commonly used to describe all batteries where the positive electrode comprises lithium metal. However, different positive electrode chemistries such as LFP, LMO, and NMC exist and they differ in their voltage level, capacity, stability, and also in the extent of some degradation effects. As a result, the cells' aging behavior has to be analyzed for one specific cell type at first. A test campaign consisting of storage (calendar) and cycle aging tests can be used to determine aging influences. In a next step, similarities and differences to other cell chemistries might be derived to gain a battery model, which is not only valid for one specific cell type and manufacturer but can be adapted to other cell types, too. Four key questions for battery (lifetime) modeling can be formulated, which guide through this topic.

- How do Li-ion cells age and which factors influence the extent of aging?
- Which measures exist to characterize a new cell and how can the performance of a cell be evaluated?
- Which modeling approaches exist to describe the aging of a cell and can these models be adapted to a new cell type?
- Is the complexity of the models manageable for lifetime simulations? Which trade-off between accuracy and complexity is necessary?

The last question introduces a central dilemma when dealing with lifetime simulations: A long time horizon of at least one year needs to be simulated to get an idea of the aging behavior over time. On the one hand, models should be as accurate as possible to represent reality. On the other hand, this leads to very complex models which are hard to solve in a time-efficient manner. As a result, a simulation framework is derived which covers both microscopic and macroscopic models. The first approach aims at rebuilding the real process as close as possible while the latter generalizes or neglects more effects

to reduce model complexity and calculation time. In the case of Li-ion batteries, molecular and electrochemical models can be viewed as microscopic representations whereas electrical equivalent and empirical models belong to a macroscopic scale.
When dealing with models of different timescales, it has to be shown that the accuracy loss at the transition from a detailed and complex to a more general model is tolerable enough for the desired output. On the other hand, microscopic models can be used to validate macroscopic models and to verify that the simplifications made are reasonable. In addition, cell aging experiments are used to sustain the statements.

Once suitable models, which offer a reasonable tradeoff between accuracy and complexity, have been implemented and validated, an optimization framework can be derived. The central aim of this study is the lifetime prolongation of the battery under a realistic use-case. Once the DOFs, with which the lifetime can be influenced, and the optimization algorithm have been identified, the optimization can be conducted. In the end, optimization results need to be checked and justified. In this case, additional aging experiments with a conventional and an optimized strategy are used to back-up the results. However, in reality, control devices in an E2W cannot handle the complex calculations necessary for an advanced optimization scheme. Therefore, a transfer of the optimization results to the limitations of the real application is required. Simplifications often result in heuristic rules or characteristic maps which can be implemented on the control device and calculated online. In summary, key questions for optimization are formulated.

- Which DOFs exist for optimizing the battery lifetime?
- How can the models be adapted and integrated into an optimization formulation?
- How does the optimized strategy look like and which factors influence it?
- Are the optimization results valid? Does the optimal strategy really perform better?
- Can the results be implemented online and on a control device where computation time and power play an important role?

In contrast to other researches, this approach focuses on battery lifetime instead of charging time and incorporates the overall system. Modeling and optimization approaches are combined with a practical use-case to close the gap between theory and practice. In particular, aims are

- to provide an overview of the E2W use-case in Shanghai as well as an E2W driving cycle and typical battery stress,
- to provide a deeper insight into Li-ion aging processes for a LMO cell and analyze the cell's aging behavior,
- to improve aging models both on a microscopic and macroscopic scale,
- to identify optimization potential for E2W operation,
- to derive a novel charging optimization strategy for E2Ws, which can also be used for EVs,
- and to propose heuristic rules for an optimal strategy which can also be implemented on a control device.

1.3 OUTLINE

The outline is motivated through and based on the framework provided in Fig. 1.3. Chapters 2.1, 2.2, and 3 elaborate the three main pillars of identifying an appropriate driving scenario as model and optimization input, a vehicle model for conversion of the speed profile of the driving cycle to a load or power profile applied to the battery, and a battery lifetime model including a description of aging mechanisms.

Chapter 2 introduces the use-case of E2W in Shanghai and the powertrain conversion starting from the speed profile over motor and power electronics modeling to the power input for the battery. EV and E2W specific driving cycles and scenarios are evaluated for their applicability to urban traffic in Shanghai in section 2.1. The term of E2W is further specified and research goals for determining a novel Shanghai driving cycle are set. The collected driving and user behavior data as well as different cycle synthesis methods are evaluated. The resulting driving cycle is compared to similar official and unofficial driving cycles to highlight similarities and differences. A vehicle model is then described in section 2.2. Model equations of a PMSM are shortly introduced for different modeling depths. These are combined with a proper control scheme to convert the speed to a power profile which is applied to the battery. The dynamic vehicle model is compared to a force-based static conversion regarding accuracy and complexity in section 2.3. Measurements on an E2W show the plausibility of the models.

Chapter 3 introduces battery and lifetime modeling. Basics of Li-ion cells are elaborated into detail as the accuracy of the battery model significantly affects the optimization results. Aging processes, lifetime analysis methods, and modeling approaches are presented. Accelerated aging tests for the evaluated LMO cell are described and results analyzed. Starting from an initial characterization, regular capacity and resistance measurement results are described. Besides, differential voltage analysis is conducted to gain more insight into aging processes. Calendar cell aging effects due to variations in storage time, temperature, SOC are evaluated. Furthermore, influences of DOD, charge rate, average voltage, and chemistry variations are studied. Findings are incorporated into two modeling approaches: a single particle model (SPM) and an electrical equivalent model (EEM). At first, model equations for an SPM are introduced and improvements are proposed to incorporate cell specific effects. A motivation of model simplifications is provided leading to similar empirical aging descriptions as used in EEMs. Likewise, an EEM model is presented and improved. Results are validated using the aging test results as well as literature data. EEM and SPM are compared to identify the accuracy loss due to simplification. Based on the battery model and the motor and power electronics model, an overall simulation framework consisting of different modeling depths is introduced.

This simulation framework can be used as basis for or validation of the model-based optimization framework described in chapter 4. The optimization problem is defined and delimited at first leading to an optimal charging strategy based on a typical driving profile. Results are presented for both the charging profile and the optimal choice of the initial SOC. Influences of different effects such as varying driving cycles, aging models, cell chemistries and temperatures are evaluated. Optimal results are validated against a conventional strategy by using the simulation framework and additional cell tests. Finally, an online implementation using heuristics is proposed. Chapter 5 summarizes the key findings and concludes the topic.

2

DRIVING SCENARIO AND VEHICLE MODEL

2.1 DRIVING SCENARIO

In the context of this work, the optimization framework described previously requires realistic estimates of the battery stress in order to improve battery lifetime and to prove the validity of the approach. Battery stress generally depends on the vehicle, environment, and driving profile. If the vehicle and the environment are known, the driving profile can be converted into a battery load cycle. The driving cycle itself varies depending on the driver, the route traveled, and the general application scenario. For each scenario, a driver- and route-related optimal result must thus be calculated separately. In order to ensure better comparability, a generalized driving cycle is desirable and can be seen as a feasibility study for the optimization approach. A statement about battery lifetime for a localized market can be obtained using a typical driving cycle which represents the average driver and driving behavior. If the optimization approach provides solid results, it can easily be adapted to improve the battery lifetime for user-specific driving cycles.

Driving cycles play an important role in the analysis and design of vehicles. They contribute to the development of common test standards for different vehicles and allow a more definite comparison. Many standardized driving cycles are already available for different purposes, for example see [18] for an overview. Most driving cycles focus on emission testing of vehicles such as the New European Driving Cycle (NEDC [234]), the American EPA Federal Test Procedure (FTP-75 [237]), or the Worldwide Harmonized Light Vehicles Test Procedures (WLTP [236]). For two-wheeled vehicles (two-wheelers), the worldwide harmonized motorcycle emissions certification cycle (WMTC [235]) can be used. However, all those standard driving cycles are designed for vehicles with an ICE and not for EVs. With the growing importance of EVs, first studies on EV driving cycles are also available [34]. However, these driving cycles were developed in the United States (US) or Europe and represent driving conditions in these countries.
The Chinese city driving cycle for vehicle testing (QC/T 759 [194]) has been presented for the Chinese market. It provides operating cycles for city buses and passenger cars for dynamometer performance tests. Since a synthetic profile is described, it cannot be used to create a realistic power and current profile [21]. Further studies aim at providing localized driving cycles but they are also designed for emission testing of conventional cars [104, 137, 258] or electric vehicles [82, 265]. There is no official test profile available for two-wheelers in the Chinese market.

A closer look at the Asian market reveals that one of the main means of transportation are two-wheelers, such as motorcycles or scooters with relatively low power [16, 45, 103,

246]. In Europe or America, the conditions and amount of two-wheelers, especially electric ones, is quite different [88]. In order to capture the different behaviors, localized driving cycles can be utilized. Unofficial driving cycles for motorcycle traffic in Asian cities include the Taipei Motorcycle Driving Cycle (TMDC [232]), Kaohsiung Driving Cycle (KHM [231]), and Centre for Environmental Monitoring Motorcycle Driving Cycle (CEMDC [230]). They concentrate mainly on two-wheeler traffic in Asian cities such as Taipei, Kaohsiung, and Hanoi. However, these cycles are based on two-wheelers using an ICE and not on E2W. As a result, different characteristics such as acceleration and power might occur for electrically driven two-wheelers.

This chapter aims to show what a realistic E2W use-case could look like for battery lifetime operation in large Chinese cities such as Shanghai. Based on this, it is investigated how such a typical driving cycle can be converted into a battery load profile and which level of detail is required for vehicle and powertrain modeling.

2.1.1 Data Collection

As a first step, it is examined whether an appropriate E2W driving cycle exists for Shanghai and, if not, how a driving cycle can be identified. In this context, it is also demonstrated why a data collection is necessary, which data collection methods are available, and how these methods influence the driving cycle characteristics. As a result, a typical E2W driving cycle in Shanghai is described and analyzed.

A reliable driving cycle for use in the optimization is to be developed since optimization results are expected to depend on the applied driving cycle. Thus, using an appropriate cycle increases the quality and validity of the optimization itself. In particular, differences and/or similarities to car driving cycles, which were already conducted in China, and to existing two-wheeler driving cycles in Europe, America and Asia may be of interest. In addition, driver-specific effects, e.g. due to the aggressiveness level of the driver, as well as the typical battery operating range can be detected when recording a large data set of driving data.

2.1.1.1 E2W classification

Before suitable driving cycles for E2W in China can be identified and analyzed, a common classification of E2Ws in Asia and China in particular must be defined. According to the definitions in the standards [193, 195, 196, 198], further literature such as [16, 45, 246], typical E2W appearance, and E2W market share, four classes for E2W are used in the following sections: e-bikes, bicycle-style electric scooters (BSES), scooter-style electric scooter (SSES), and electric motorcycles. Characteristics of these classes are displayed in 2.1 and summarized in Table 2.1.

The terms BSES and SSES are used in order to distinguish them more closely from e-bikes or pedelecs as known in the European and American market. For the context of this paper, e-bikes are standard bikes upgraded with a battery and motor. Their power ranges up to 240 W continuous power with manual pedaling being possible. The purely electrically driven top speed is about 20 km/h. BSES on the other hand are characterized by a bicycle-like appearance, but show more distinct moped features such as steering wheel, footrest, and seats for one to two people. Using battery voltages of 24 V to 48 V, they are typically designed for a power level of 350 W and top speed of 32 km/h for

(a) (b) (c) (d)

Figure 2.1: E2W definitions: (a) e-bike ($\leqslant$ 240 *W*), (b) BSES ($\leqslant$ 400 *W*), (c) SSES ($\approx$ 500 *W*), and (d) electric motorcycle ($\geqslant$ 1 kW). [255]

Table 2.1: E2W classification used.

E2W type	e-bike	BSES	SSES	el. motorcycle
Power (kW)	$\leqslant$0.24	$\approx$0.35	0.4–1	$\geqslant$1
Top speed (km/h)	$\leqslant$20	$\approx$32	$\approx$40	$\geqslant$40
Battery voltage (V)	$\approx$24	24–48	48–60	$\geqslant$60

the Chinese market. SSES on the other hand look like common scooters or mopeds. In China, their power level varies from 400 W up to 1000 W with a typical value of 500 W at 60 V and a top speed of about 40 km/h [16, 45, 246]. If the power exceeds 1 kW or larger speeds than 40 km/h are possible, the vehicles are treated as electric motorcycles. In order to separate electric motorcycles from low-power E2W, the term E2W is particularly used to describe the second. If no tighter definition is given, both BSES and SSES are denoted by the term E2W. E-bikes and electric motorcycles are not part of this study.

2.1.1.2 Determining an applicable driving cycle

Although most official driving cycles are designed for vehicles with combustion engines and are mainly used for emission measurement, these might be used for the urban E2W driving in Shanghai. They are therefore assessed for their applicability to the given scenario. The Tables 2.2 and 2.3 compare the described driving cycles and show whether they can meet the traffic condition requirements of EVs and low-power E2Ws in Chinese cities such as Shanghai. Decision criteria as to whether available driving cycles can be used for the use case of an Asian city EV driving cycle are described below. Since the driving cycle should represent the driving of an EV or E2W in Asian urban environments, decision criteria are whether the driving cycle represents

- urban or city driving,
- the Asian market and traffic situation,
- an official driving cycle,
- EVs, and
- naturalistic driving behavior.

Since the nominal power of E2Ws is significantly lower than that of conventional motorcycles, further criteria need to be introduced to determine whether a two-wheeler driving cycle is suitable for the given E2W use case. These are that the

- top speed of the driving cycles should be less than 40 km/h and
- the nominal motor power less than 500 W.

Table 2.2: Decision matrix for available car driving cycles.

Driving cycle	Weight (%)	NEDC	FTP-75	WLTP	QC/T 759
City driving	30	1	1	1	1
Asian market	30	0	0	0.5	1
Official cycle	10	1	1	1	1
EV	10	0	0	0	0
Naturalistic	20	0	1	1	0
Weighted Sum (%)	100	40	60	75	70

Table 2.3: Decision matrix for available two-wheeler driving cycles.

Driving cycle	Weight (%)	WMTC	TMDC	KHM	CEMDC
City driving	20	1	1	1	1
Asian market	20	0	1	1	1
Official cycle	5	1	0	0	0
E2W	15	0	0	0	0
Naturalistic	10	1	1	1	1
Speed $\leqslant$ 40 km/h	15	0	0	0	0
Power $\leqslant$ 0.5 kW	15	0	0	0	0
Weighted Sum (%)	100	25	50	50	50

In the present case, the driving cycles for cars and two-wheelers are analyzed separately. By selecting different weights for the presented criteria, focus is laid on the given scenario. The driving cycle has to represent city driving and should represent the Asian market well. Since realistic driving conditions are desired for optimization, the driving cycle should be a naturalistic one. EVs are commonly designed to offer a similar performance to vehicles with ICEs, at least in urban traffic. Both are assumed to have a similar driving behavior. Therefore, the driving cycle does not necessarily have to be designed for an EV. Official cycles would ensure an increased reliability of the cycle. The weights are chosen according to this line of thought, but can of course be chosen differently for other purposes. Table 2.2 shows that WLTP and QC/T759 meet the criteria with a match of about 70 %. The WLTP, with a fit of 75%, might thus be used as driving cycle for EVs in Chinese urban traffic.

On the other hand, Table 2.3 shows the weighing and criteria chosen to find a suitable driving cycle for two-wheelers. None of the presented driving cycles for two-wheelers is able to fulfill the speed and power requirements for Chinese urban traffic. In addition, the cycles are all designed for conventional motorcycles and not for E2W. With a maximum fit of 50 %, these driving cycles are likely to show a different driving behavior than the one desired.
In summary, the WLTP might be used to estimate EV driving conditions in Shanghai but no driving cycle can represent E2W urban driving. Thus, a data collection campaign to identify a suitable driving cycle which is able to predict the driving behavior of an E2W driver in urban traffic in China is required.

2.1.1.3 E2W data collection campaign in Shanghai

A typical and representative driving cycle for E2Ws in China is thus developed as also published in [183, 185]. A test campaign under different circumstances, such as different cities, rural areas, environmental conditions, and background of the drivers, would be out of scope of this work. Therefore, Shanghai was selected as a representative Chinese city (also classified as tier 1 city), where many E2Ws are used due to their benefits. First, the test campaign is motivated and described in the next section. Subsequently, the quality and accuracy of the speed tracking equipment is analyzed. Finally, results of the test campaign are discussed in section 2.1.1.4.

Test campaign setup

Typically, steps for deriving a new driving profile include the selection of a suitable test route, data acquisition, and cycle construction. Since no detailed information about the operation of E2Ws in Shanghai is available, the development process is extended to first identify a typical operation profile. Initially, general information about driving distances and times is collected by means of a survey. Therefore, 40 employees of a company situated in the test area were asked to fill in this survey. Since the background of these participants might be similar and their responses might not reflect the average behavior of E2W drivers in Shanghai, a further 157 survey answers were collected at a local metro station. Based on the results, commuting to and from work is selected as typical scenario for E2W usage.
Then, smartphones are used to record travel data for commuting. An office area mixed with residential areas in the west of Shanghai is selected as test field, whereby no specific test route is initially selected. The data is then clustered into speed profiles representing the two different E2W types, BSES and SSES. Typical driving cycles are generated using different driving cycle construction methods. In the end, a representative real test route is selected based on the recorded data. On this representative route test drives with a test E2W are carried out. The obtained data are first compared with the data recorded by the smartphone test campaign to evaluate the quality of the smartphone data. In addition, the data collected with the test E2W on this representative test route are correlated with the constructed driving cycles.

Survey
The main objective of the survey is to determine typical distances traveled on an E2W, journey times, usage intentions, and E2W power. The survey consists of 7 questions regarding age and gender of the driver, driving frequency, reason(s) for driving, trip distance and time, E2W power, and battery type. Age and gender indicate the user group, driving frequency and reason indicate the main scenario, trip distance and time determine typical daily mileage for the scenario under consideration, E2W power provides an indication of whether BSES or SSES are used, and the battery type can be used to verify the overall validity of the sample based on market share of lead-acid and li-ion batteries. In total, the survey provided around 200 answers and can be assumed to give a good overview of E2W usage.

Smartphone data collection
If E2W position and speed need to be recorded over time and the accuracy requirements of the obtained data lie within the scope of conventional GPS recorders, a smartphone can be used for data recording. Data acquisition by a smartphone app is a simple yet effective method to generate a large amount of test data. Nowadays, many people

(a) Sketch **(b)** Test E2W

Figure 2.2: Test E2W style.

own a smartphone with GPS functionality which can be used for tracking purposes. Anyone willing to participate can use their own phone and E2W. On the other hand, many different brands and operating systems (OS) exist. Thus, the accuracy of the obtained data and the implementation of the algorithms might pose some challenges. To motivate many people to participate and to keep the installation and operation effort low, available smartphone applications were selected.
17 employees from a company located in the test area participated in the smartphone data collection campaign and recorded their route on an E2W during one-week test period. More than 100 trips were recorded and evaluated.

Test E2W data collection
The test E2W is a typical e-scooter operating on Chinese streets. The E2W comes in a moped-like appearance as presented in Fig. 2.2. With a nominal power of 500 W and battery voltage of 60 V, the E2W has a maximum speed of 45 to 50 km/h. The battery consists of 5 12 V lead acid cells. The in-wheel motor is most likely a PMSM. The test E2W is equipped with standard measurement equipment including an IMAR IμVRU IMU and GPS including barometer, Vector GL1000 data logger as well as voltage, current, and throttle measurement. The 500 W E2W is used to generate more driving data, to check if the smartphone data are sufficient to get an overview of the driving behavior, validate the derived typical driving cycles, as well as to get information about the driver behavior. More detailed information about the test E2W is provided in Table A.1 in Appendix A.1.1.
On top of GPS location and derived velocity, the test E2W can provide more accurate acceleration data as well as information about throttle actuation and current demand. The E2W is mainly used for validation purposes of the smartphone-based data collection. Thus, only 8 trips of 2 test drivers were recorded during the initial campaign.

The results from the survey, smartphone and test E2W data acquisition are then used to find a representative test route for the test E2W. As some background information about test drivers and test E2Ws is missing for the smartphone tests, drives on the equipped test E2W provide a deeper understanding of a typical profile on the test route under well-known conditions. For this purpose, one test driver conducted a further 8 rides on the selected test route.

Test equipment analysis

These representative drives are also used for a detailed analysis of the test equipment. Smartphone data collection has advantages over equipping a test E2W, but there are some drawbacks, which have to be considered. The brand and type of the smartphone

determine the available sensors and accuracy. Most smartphones offer GPS and acceleration information with a suitable accuracy for tracking but record it at a low sampling rate to save energy. The selected basic tracking apps thus only record the GPS position and speed in an interval of 1 s. No information from the smartphone's accelerometer or gyroscope could be recorded and speed was calculated based on the GPS position. The quality of the GPS signal depends on the position of the smartphone during a ride, the quality of the sensor used, and the tracking app. Therefore, smartphone measurements might show some data failures if no GPS signal is available, data inconsistencies or inaccuracies if the signal quality is poor due to high buildings or bridges blocking the satellite signal, or app recording errors. Due to the measurement equipment and data logger on the test E2W, data can be recorded at higher frequencies, which is reported to lead to higher accuracy. Assuming motor dynamics of about 100 Hz together with the vehicle drag and inertia, typical meaningful movements occur at 10 Hz or below. With a recording frequency of 1 Hz as done in the smartphone apps, some vehicle dynamics might not be recorded. Frequencies above 10 Hz on the other hand are prone to measurement noise and do not resemble the vehicle dynamics, as described in [135]. Therefore, a recording frequency of 10 Hz is chosen for the test E2W.

The validation test drives on the E2W are used to evaluate if the lower recording frequency and the less professional sensors of smartphones have a significant impact on the quality of the recorded driving cycles. The trips were recorded with the app on a smartphone as well as with the GPS and IMU on the test E2W. In addition, the battery voltage, battery current, and E2W throttle signal were measured to get a realistic estimation of the energy consumption during the drive. The results showed that smartphone data needs to be preprocessed to identify outliers, data failure, and other inaccuracies due to improper use of the app and the generally less powerful GPS signal. On the other hand, the raw GPS signal of the test E2W also needs to be filtered as it shows a superimposed noise signal due to the fluctuations of the position signal by about 5 m. Energy differences mostly result from lower accelerations as a result of the recording frequency. Energy underestimation on a specific test route seems to be static. Therefore, a lower frequency data might also be used. In this case, more accurate energy estimations can be achieved by increasing the smartphone energy prediction by some percent. A detailed analysis can be found in Appendix A.1.2.
In general, energy predictions might vary depending on the recording frequency and device but do not necessarily lead to false dynamics estimations. Results from smartphone tracking with 1 Hz resemble, in this case, all relevant dynamics and provide sufficient information for determining a driving cycle.

2.1.1.4 Data collection results

As a next step, the results obtained by survey, smartphone and test E2W data collection can be evaluated. Key characteristics are identified in the following. Fig. 2.3 separates the results into the total count (black), the 16 survey answers of the smartphone test campaign only (gray), the 24 answers of other company employees (light grey), and an additional 157 survey data sets collected at a local metro station (white). In total, the survey shows that the majority of the participants is between 25 and 30 years old (70 %) with more female (69 %) than male participants. Most participants drive an E2W on a daily basis (83 %) and use it to commute to and from work (86 %). Approximately 62% of the E2Ws offer a nominal power of 250 W to 499 W. Another 30% state a power lower

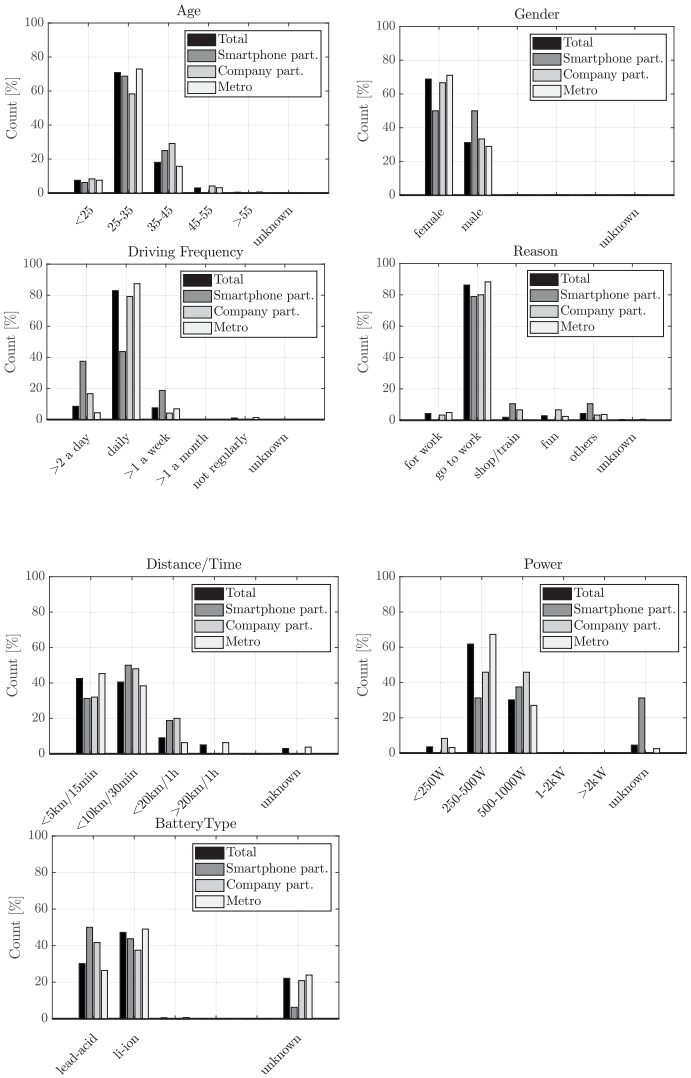

Figure 2.3: Survey results in total, obtained by smartphone test campaign participants, further participants from the same company, and metro answers.

than 1 kW and some even drive an E2W with a power lower than 250 W. One surprising result is the high amount of Li-ion E2Ws (44%). One explanation might be that the

Table 2.4: Overview of key characteristics obtained by different data collection methods.

		Data Collection Method		
Criteria	Unit	Survey	Smartphone	Test E2W
Distance	km	0-20	1-20	3.5-16
Time	min	0-60	2-54	25-45
Power	kW	0.2-1	0.2-1	0.5
Max. Speed	km/h	-	20-50	40
Avg. Speed	km/h	-	20	21
Avg. Distance	km	6.4	6.5	7.9
Avg. Stop Time	%	-	12.1	22.7

participants have newly bought their E2Ws or – as Li-ion E2Ws are still expensive and relatively new in the Chinese market – that they were not sure about the battery type used by the E2W. As summarized in Table 2.4, average traveled distance is about 6 km.

Accordingly, the majority of the smartphone test participants is between 25 and 35 years (69 %) and 35 and 45 years (25 %) old. In contrast to the other survey data, 37% of the smartphone test participants drive their E2W more than twice a day. The main purpose is also commuting to and from work (79%). Power levels also vary between 250 and 1000 W. However, almost one third of the participants did not know their E2W's power. The 8 female and 9 male participants recorded trips with distances ranging from 1 km up to 20 km and trip times between 2 and 54 minutes. Both survey and smartphone data show good accordance as displayed in Table 2.4. This shows that the smartphone data obtained during one week reflect the overall driving attitude of the participants. Data are also collected using the test E2W during that time. Based on answers of more than 200 survey participants, commuting to and from work is selected as main scenario for E2W operation. Further, the survey shows that most E2Ws driven in the urban area of Shanghai have a power lower than 500 W and no power larger than 1 kW was recorded. This corresponds to the local regulations for E2Ws.

In Fig. 2.4, key characteristics of the recorded trips are shown for speed, time, distance, and acceleration clusters. As expected, the graphs indicate that BSES drive at lower speeds than SSES. About half of the BSES trips end after 10 minutes and less than 5 km, SSES trips vary between 10 and 50 minutes with an average distance of 10 km. Most BSES have an average speed of about 15 km/h. Average speed of SSES varies slightly more, with about 37 % driving at 25 km/h. Acceleration distributions show a similar behavior, with SSES tending to accelerate and decelerate slightly stronger.

Table 2.5 provides an overview of the key characteristics. For the data recorded by smartphone, the overall test results (including the trips which do not fit into BSES or SSES classes but show no inconsistencies), BSES, and SSES test results are displayed. In average, BSES trips take about 17 min to cover a distance of 4.46 km at an average speed of 14.3 km/h. SSES drive about 10.2 km in 25 min at a speed of 20.8 km/h. The power of the E2Ws seems to correlate with the traveled distance and time. Likewise, a lower power leads to lower accelerations.

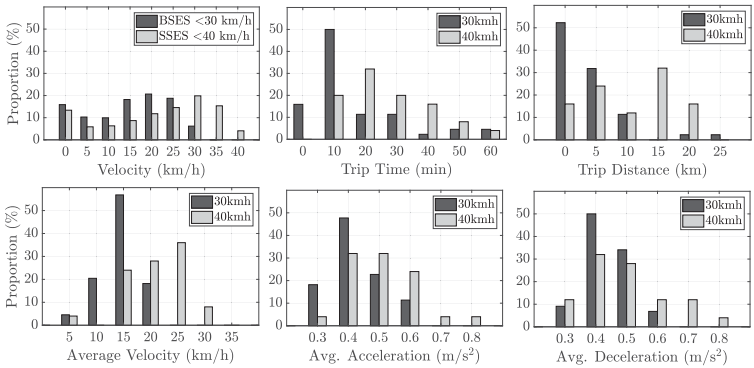

Figure 2.4: Velocity, time, distance and acceleration distributions for trips classified into BSES ($v < 30$km/h) or SSES ($30\,\mathrm{km/h} \leqslant v < 40\,\mathrm{km/h}$).

Table 2.5: Key characteristics of Shanghai data collection campaign.

Criteria	Unit	Smartphone		
		Overall	BSES	SSES
Distance	km	6.54	4.46	10.23
Time	s	1266	1046	1549
Avg. Speed	km/h	17.7	14.3	20.8
Max. Speed	km/h	35.8	28.6	39.9
Avg. Stop Time	%	12.1	12.0	10.7
Avg. Accel.	m/s^2	0.40	0.43	0.50
Avg. Decel.	m/s^2	-0.39	-0.44	-0.49
Energy	Wh/km	20.6	19.1	23.4

2.1.2 Driving Cycle

2.1.2.1 Driving cycle synthesis

Various methods for the generation of driving cycles exist. Driving cycles can be taken from real recordings or be synthesized. Synthesized driving cycles can again be separated into cycles where velocity changes only stepwise or naturalistic driving cycles with many velocity variations, often labeled as modal and transient cycles [34].
Methods for constructing naturalistic driving cycles include best fits of existing driving cycles [232], cut and clip approaches as presented in [231] and [230], where start-stop microtrips are extracted and randomly put together, stochastic methods using Markov chains [76, 93, 120, 126, 212, 213], optimization based on typical repeating routes each day as described in [22], stochastic [210], and many other mixed approaches [24, 34, 104, 271]. In the following, four methods, namely closest match, moving window, Cut and Clip, and Markov chains, are shortly introduced and evaluated following the argumentation provided in [183].

Closest match and moving window

The simplest method chooses one of the existing driving cycles, which fits the average values of all trips best. For this approach, some key characteristics are selected and weighted to generate an overall cost function, for which the minimum is chosen as best choice. For all presented approaches the same criteria and weighing was used:

$$F = \frac{3}{10}\Delta v_{avg} + \frac{2}{10}\Delta a_{avg} + \frac{2}{10}\Delta s_{end} + \frac{1}{10}\Delta t_{end} + \frac{1}{10}\Delta v_{max} + \frac{1}{10}\Delta t_{stop} \tag{2.1}$$

Here Δs_{end}, Δv_{avg}, Δa_{avg}, Δt_{end}, Δv_{max}, Δt_{stop} are the difference in the trip distance, average velocity, average acceleration, end time, maximum velocity, and stop time, respectively. The values are given in % to the average value. For further detail refer to [232]. The weights are chosen according to the main purpose of the driving cycle to represent typical driving speeds and accelerations as well as distances for estimation of power consumption and typical stress. Especially for the Cut and Clip and Markov chain construction, only profiles with a deviation of less than 15 % of each of the before mentioned parameters as well as acceleration, deceleration, idling, and cruising phases are taken into account.

One of the main disadvantages of finding the closest match of an existing track is that the trip has to exactly fit the average distance and/or length. By assuming this, trips with a higher match for other key characteristics such as average velocity, which are simply too long, are neglected. So one possible extension of this approach can be labeled as moving window method. If a driving cycle should cover a given distance or time, then the fit can be increased by choosing a window size, which exactly represents this distance or time. Trips which are shorter than this distance or time window can be prolonged by adding the same trip multiple times at the end of the trip and then applying the window. This approach is especially interesting, if only a part of the driving cycle, which has the closest match to the average values of all driving cycles, needs to be chosen. Starting from the first value in the data set, the window moves through the measurement data to find the best fit.

Cut and Clip

A drawback of the previous approaches is that different trips cannot be combined to improve the result. A trip usually consists of not only one driving period but many start/stop situations in between, for example due to traffic lights. It is possible to split all trips into those microtrips and combine them later on to generate a new driving cycle. That way, naturalistic driving behaviors can be used to generate new trips. Those microtrips can then be randomly put together to get different trip lengths. This method has, for example, been described in [231] and [230]. In the following sections, it is referred to as Cut and Clip approach (C&C).

Markov Chains and Monte Carlo Simulation

Markov Chains together with a Monte Carlo simulation are described in detail in [76, 93, 120, 212] and will only be shortly introduced. The method focuses on randomly generating naturalistic driving cycles. A new velocity profile is obtained by analyzing and clustering recorded trips by velocity, acceleration, or slope transition probabilities. In case a Markov process is used, the following state solely depends on the current state or on a limited number of previous states. In this case, only the current state is considered. The probability P for the transition from state x_i to x_j can be written as

$$P_{ij}(X_{k+1} = x_j | X_k = x_i) \tag{2.2}$$

if the Markov property holds. By choosing many (quasi-)random variables X_1, X_2, X_3, ..., a discrete-time Markov chain is built up. Depending on the applied method, the selection of these variables can be completely random or based on some additional relations. In this case, a random walk implementation, also known as Markov Chain Monte Carlo method [23] or more accurately as Metropolis-Hastings algorithm, is applied. Using this implementation, the transition probability of each row has to sum up to 1 as it represents all probabilities on how to get from the current state to a next state: $\sum_j P_{ij} = 1$.

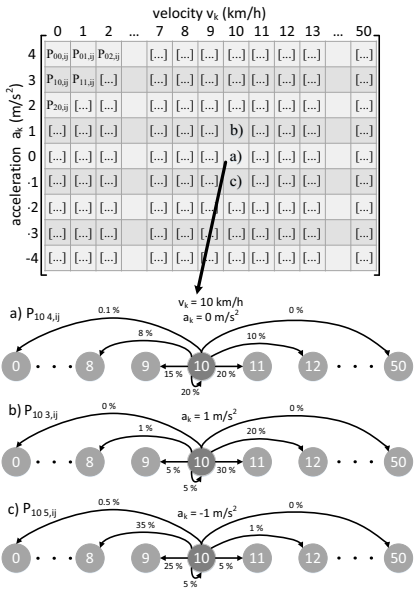

Figure 2.5: Markov chain construction with matrix structure of the current step on the top and the probability of some matrix entries $P_{i_1 j_1, i_2 j_2}$ on the bottom.

In the given case, the states are velocity v and acceleration a leading to a two-dimensional Markov chain.

$$P_{i_1 i_2, j_1 j_2}(v_{k+1} = v_{j_1}, a_{k+1} = a_{j_2} | v_k = v_{i_1}, a_k = a_{i_2}) \,. \tag{2.3}$$

For example, it is recorded how often the velocity will go from 10 km/h to 11 km/h or 9 km/h or any other velocity value in the next time instance. Fig. 2.5 shows an example of the construction process. At the top, the matrix structure with the current acceleration and velocity clusters is displayed. Each matrix cell itself contains the probabilities for the next velocity and acceleration. This is shown for the cases a), b) and c), where the current velocity is 10 km/h. For different current accelerations of 0 (a), 1 (b) or -1 m/s² (c), the probabilities differ. The values in the bubbles indicate the velocity states v_{k+1}, while the arrows represent the probability of changing from one velocity class to the next in this iteration. The acceleration a_{k+1} is not displayed for simplicity. For instance, it is more likely that a vehicle will be faster in the next time instance if the current acceleration is positive.

In the presented case, the velocity values are clustered into groups of 0.1 m/s (0.36 km/h). The same applies to the acceleration values with a step size of 0.4 m/s². A step size of 0.4 m/s² can be seen as sufficiently small since the main information of the acceleration classification is whether the driver accelerates or decelerates. The probability values are then recorded in a matrix indicating velocity and acceleration steps. For each of the matrix cells, the probability of switching from the current speed and acceleration pair to the next is stored. Hence each cell contains a speed-acceleration matrix. The current velocity and acceleration are used to define the transition to the next velocity, which can be represented by a Markov process.

A new naturalistic driving cycle is synthesized by randomly selecting the next velocity, whereby the velocity transition is obtained by evaluating Markov chains. Thus a random variable X_k between zero and one is drawn for each second t_k of the driving cycle. The first probability value of the corresponding row entry of the probability matrix $P_{i,j}$ which is larger than the selected random variable X_k is selected as proposed following state x_{k+1}. This state can then be subjected to a plausibility check. For example, if the vehicle dynamics are limited, the resulting acceleration between the state x_k and the proposed following state x_{k+1} can be evaluated. If the acceleration is larger than the vehicle dynamics allow, another random number between zero and one is drawn and the previous draw is discarded. This is continued until a suitable candidate is found. Thus a driving cycle is constructed once suitable states and therefore velocities have been determined for all time instances.

However, due to the stochastic approach, not every generated velocity profile fits well to the average values of the desired driving behavior. Therefore, not only one but many driving cycles are constructed this way to generate many samples. In every iteration, the characteristics of the driving campaign are compared to the characteristics of the newly generated driving cycle using the evaluation criteria in (2.1). If the current constructed cycle has a lower deviation to these, it is saved. Otherwise it is discarded. The iteration ends either if the deviation between the desired and actual characteristics are sufficiently low, for example less than 10%, or if 20.000 driving cycle candidates have been constructed and evaluated. Since the actual driving cycle length is freely configurable at the beginning, this approach has the advantage that driving cycles of different length or time can be easily designed.

As a remark, the above-mentioned methods are typically based on speed data obtained from one data collection method, in this case speed data. When using professional test equipment, data from different sensors might be available, which can be fused to increase the accuracy. For example, a Kalman filter can be used to fuse GPS, IMU, and magnetometer data. In this study, however, only one sensor is available during the smartphone test campaign. The reference data is measured using three sensors for a limited number of drives. These drives were conducted on a test route that best matched the average results of the data collection. Since the aim is to improve a typical rather than an actual driving cycle for Shanghai E2Ws, the reference data might be used to estimate typical higher frequency dynamics. Such a method for offline sensor data fusion based on the frequency spectrum is discussed in Appendix A.1.3.

2.1.2.2 Driving cycle analysis

Driving cycles are constructed based on the available data. First, separate driving cycles for BSES and SSES are introduced, which are able to highlight characteristics for

a low-power and medium-power E2W. In addition, a combined driving cycle, which is synthesized using all available data (both BSES and SSES), is presented. This combined driving cycle is primarily used for optimization purposes as described in chapter 4. It is able to represent both characteristics of BSES and SSES. The validation cell tests in chapter 4.4 are also based on this cycle to make general statements about aging for E2W in Shanghai.

Fig. 2.6 presents the results for the designed driving cycles for (a) BSES and (b) for SSES. The recorded driving cycle with the closest match to the average values is displayed first. Although end time and distance can be closely matched to the average values of all trips, the resulting driving profiles can only partially reflect the average characteristics. It is therefore difficult to generate driving profiles of different lengths flexibly. The same applies to the profiles obtained by the moving window approach, although this method already corresponds closer to the key characteristics obtained by the data collection. Due to the fixed length of the window, the method does not necessarily lead to a trip with zero speed at the end. In the case of BSES, this approach leads to a concatenation of a shorter trip. The trips obtained by the C&C as well as the Markov chain method together with Monte Carlo simulation are more relevant for driving cycle synthesis as they are able to construct driving cycles of varying length.

Although the construction methods lead to different driving cycles, similarities can be observed for some of the general properties. For BSES, the cycles generated by closest match, moving window, and Markov chains show that almost no phases exist with a constant speed. Acceleration and deceleration phases alternate and the speed varies between 10 km/h and 30 km/h. In contrast to closest match and moving window, the driving cycle generated by Markov chains shows larger phases at a lower speed of about 10 km/h. The C&C approach, on the other hand, results in a driving cycle which also shows phases with almost constant speed. As all driving cycles represent the overall characteristics of the collected data, these can be seen as different driving scenarios for BSES in Shanghai which show influences of the traffic and driver behavior.
The driving cycles designed for SSES correlate closer to each other. Phases with a constant maximum speed alternate with stop phases. The motor power clearly limits the maximum speed, which lies in all cases at about 35 km/h to 40 km/h. If the speed needs to be reduced, it either drops to 10 km/h the driver has to stop completely. The characteristic behavior of SSES in Shanghai thus seems to be more consistent.

Fig. 2.7 displays the resulting combined driving cycle using the C&C based on all collected data. It consists of three driving and stop phases. After an acceleration phase at the beginning, the driver is most likely stuck in traffic in front of a crossing. Afterwards, the driver accelerates fast to approximately 35 km/h until the next full stop due to a crossing. The last driving phase continues for about 15 min with larger fluctuations in the speed. This resembles a typical speed profile during rush hour, where the driver adapts its speed profile to traffic. Overall, the driving cycle includes all relevant driving conditions observed in Shanghai, with a low speed phase due to traffic lights, a high speed section with almost no traffic, and a long cruising phase with traffic. It is therefore suitable for a generalized consideration of E2W traffic and battery load in Shanghai and is referred to as combined Shanghai E2W cycle (SE2WC) in the following.

Comparison of constructed driving cycles
Table 2.6 provides an overview of the key characteristics of the constructed driving cycles

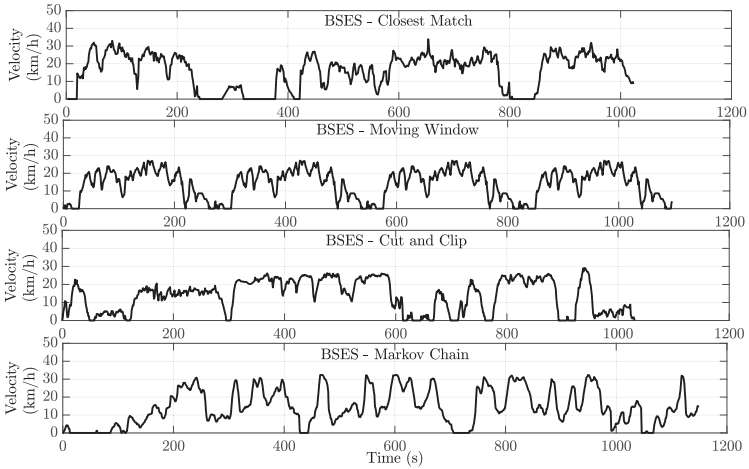

(a) BSES

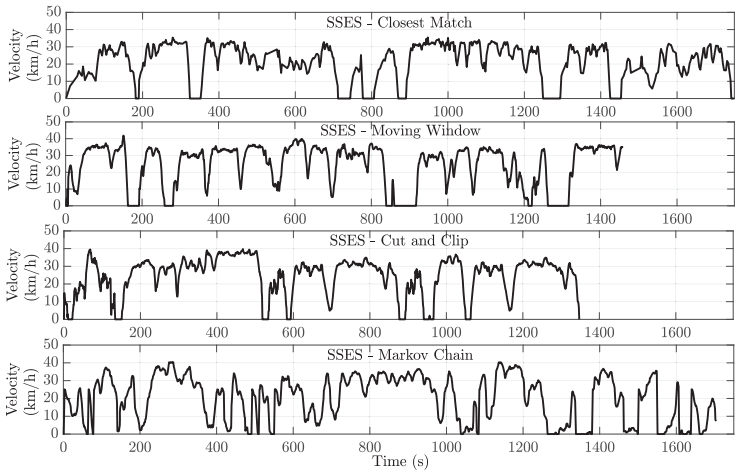

(b) SSES

Figure 2.6: Generated driving cycles for BSES (a) and SSES (b) obtained by the four different methods. The profile obtained by closest match to the existing trips is shown on the top, the moving window and C&C approach in the middle and the constructed driving cycle using Markov chains at the bottom.

and the averages obtained by the data collection campaign. Besides distance, time, and average and maximum speed, further key characteristics are displayed. For average acceleration and deceleration calculation, only values greater than 0.1 m/s^2 are taken

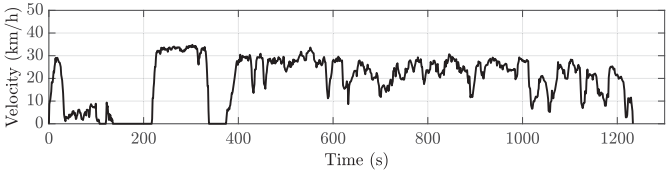

Figure 2.7: Combined driving cycle constructed using the C&C approach.

into account to adapt for measurement noise. For BSES both the C&C and Markov chains construction approach show a close fit to the average data obtained by data collection. Deviations lie within 15 % for the designed average parameters. The Markov chain approach shows longer cruising and shorter acceleration and deceleration times. In this case, the C&C approach yields slightly improved results, as many microtrips could be obtained. For SSES, on the other hand, the C&C approach deviates by 18% from the average speed and by 20% from the average acceleration. The Markov chain approach provides more accurate results with only 3% and no deviation, respectively. As already observed for the BSES case, the Markov approach leads to longer cruising and less accelerating times for SSES. Nevertheless, both methods are able to construct driving cycles which represent the driving behavior of BSES and SSES in Shanghai. The Markov chain approach is more flexible and is able to construct completely new but realistic driving cycles. However, it requires many iterations to find a suitable driving profile due to its stochastic nature. The C&C approach offers a faster calculation speed if driving data with many start and stop situations is available. Otherwise, the Markov chain approach provides more precise results even though the computational effort is high. In the following, the driving cycles obtained by the Markov chain approach are referred to as BSES SE2WC and SSES SE2WC.

The combined SE2WC is able to represent distance, trip time, top speed, and average speed with less than 10 % deviation. The SE2WC shows larger acceleration and deceleration values than the average of the recorded data. Deviations occur as the C&C approach is only able to use existing microtrips of the recorded driving cycles. E2W types and thus power levels differ, as introduced in chapter 2.1.1.1. As a result, the variance of the acceleration is quite high and most microtrips show either a higher or lower average acceleration. Approximately 100 trips were recorded and approximately 500 microtrips could be extracted. This leads to a limited number of new driving cycles which can be generated using C&C. The driving cycle shows only two stop phases and a long driving phase at the end. Since the speed varies while driving, the phase is not classified as cruising phase but consists of many acceleration and deceleration phases. This behavior may be due to the fact that the driver tried to avoid stopping, but often had to accelerate due to traffic and intersections. Overall, the initial driving cycle represents an average driving behavior but can be improved by separating the recorded data into BSES and SSES drives as mentioned above.

2.1.2.3 Comparison to other driving cycles

The synthesized driving cycles for BSES and SSES in Shanghai can be compared to other two-wheeler driving cycles to highlight similarities and differences. Taiwanese cycles

Table 2.6: Key characteristics of obtained BSES, SSES, and combined driving cycle.

Criteria	Unit	BSES Data	BSES C&C	BSES Mark. SE2WC	SSES Data	SSES C&C	SSES Mark. SE2WC	Combined Data	Combined C&C SE2WC
Distance	km	4.46	4.49	4.61	10.23	9.74	9.44	6.54	6.68
Time	s	1045	1030	1149	1549	1347	1704	1266	1233
Avg. Speed	km/h	14.3	13.9	14.4	20.8	24.6	21.4	18.9	19.4
Max. Speed	km/h	28.6	29.1	32.3	39.9	39.8	40.4	33.8	34.8
Idling	%	12.0	11.7	12.9	10.7	8.3	10.5	10.7	10.2
Cruising	%	27.5	28.9	34.8	26.3	29.9	33.0	31.6	29.3
Accelerating	%	31.4	30.3	27.6	34.7	30.3	27.3	28.5	28.5
Decelerating	%	29.1	29.0	24.8	28.3	31.5	29.6	29.2	32.0
(Avg.) Accel.	m/s^2	0.43	0.42	0.39	0.50	0.40	0.50	0.44	0.48
(Avg.) Decel.	m/s^2	-0.44	-0.43	-0.41	-0.49	-0.41	-0.45	-0.44	-0.51

such as the TMDC by [232] and KHM by [231] and the CEMDC as described in [230] for Hanoi in Vietnam are used for comparison. Part 1 of the WMTC with reduced speed is included as an official test cycle. The speed profile of the unofficial driving cycles is displayed in Fig. 2.8. The speed profiles of the Markov chain constructed SE2WC for BSES and SSES can be taken from Fig. 2.6.

In Table 2.7, key features of the different driving cycles are listed. Driving cycles were generated using Cut and Clip (C&C), naturalistic (N), Closest Match (CM), and Markov approaches and are compared to the recorded BSES and SSES data. TMDC, KHM and WMTC show many start and stop situations with only short or no cruising phases in between. CEMDC shows longer cruising and less idling times than TMDC and KHM. During cruising, the speed shows larger fluctuations, which indicates slow down and acceleration due to traffic. Average accelerations for TMDC are much higher than for the other cycles.
If comparing the driving behavior of the Shanghai data collection campaign to other known driving cycles, two main differences can be detected. At first, both BSES and SSES driving cycles show longer cruising phases as displayed in Fig 2.6. Meanwhile the SSES data shows similarities to the CEMDC, the BSES data has much lower average and maximum speeds. With a top speed of 32 km/h for the BSES SE2WC and 28.6 km/h for all recorded BSES trips, BSES drive much slower than two-wheelers presented in WMTC, KHM, TMDC, and CEMDC. Average speed is with 14.3 km/h also much lower. This together with lower average accelerations of about 0.43 m/s^2 than WMTC (0.57 m/s^2), KHM (0.58 m/s^2), and TMDC (0.80 m/s^2) indicates that the power level of the BSES is lower than for those cycles. Only CEMDC (0.42 m/s^2) shows similar average accelerations but a too high average and maximum speed of 21 km/h and 41 km/h respectively. With an average trip distance of 4.46 km, BSES drivers drive only half the distance of SSES drivers (10.23 km). SSES driving shows similarities to the CEMDC cycle. Still, the top speed of about 40 km/h is lower than for the presented non-electrical scooter cycles. With an idling phase covering 10.7% of the whole trip and 26.3% cruising phase, the SSES has a slightly different driving behavior than the CEMDC.
In total, the CEMDC is similar to the SSES SE2WC due to similar distance, time, and speed but CEMDC has shorter cruising and idling times as well as lower average ac-

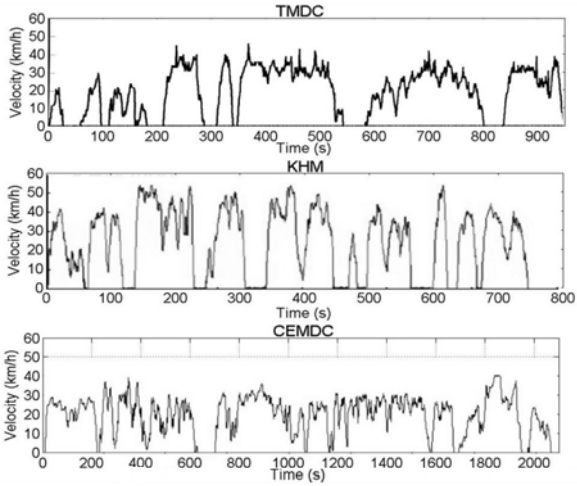

Figure 2.8: Driving cycles for E2W presented in literature: TMDC [232], KHM [231], and CEMDC [230]. As there are no speed and time values available for the cycles presented in literature, the figures are directly taken from the relevant publications. For the KHM, also only a time period of about 800 s was published.

Table 2.7: Key characteristics and comparison of different driving cycles and data collection campaigns.

Criteria	Unit	WMTC (part 1)	KHM	TMDC	CEMDC	Shanghai BSES Data	BSES SE2WC	Shanghai SSES Data	SSES SE2WC
Type/ Method	-	N	C&C	CM	C&C	rec	Markov	rec	Markov
Distance	km	3.77	6.57	5.11	11.51	4.46	4.61	10.23	9.44
Time	s	600	1126	950	2061	1046	1149	1549	1704
Avg. Speed	km/h	23.0	21.0	19.4	21.0	14.3	14.4	20.79	21.4
Max. Speed	km/h	50.0	55.0	45.0	41.0	28.6	32.3	39.9	40.4
Idling	%	17.5	27.7	19.5	7.7	12.0	12.9	10.7	10.5
Cruising	%	21.8	8.7	18.7	21.0	27.5	34.8	26.3	33.0
Acceler- ating	%	31.2	32.6	31.5	36.9	31.4	27.6	34.7	27.3
Deceler- ating	%	29.5	31.0	30.3	34.3	29.1	24.8	28.3	29.6
(Avg.) Accel.	m/s^2	0.57	0.58	0.80	0.42	0.43	0.39	0.50	0.50
(Avg.) Decel.	m/s^2	-0.61	-0.61	-0.83	-0.46	-0.44	-0.41	-0.49	-0.45

celerations. TMDC shows too high average accelerations indicating two-wheelers with higher power. KHM and WMTC show too high maximum speeds and accelerations, although they are lower than in the TMDC. For BSES, none of the presented cycles is able to represent the driving behavior. BSES show a lower maximum and average speed as well as accelerations.
As a result, novel and representative driving cycles for E2W in Chinese urban areas have been developed, which can now be used to generate an accurate driving behavior and battery load estimation for the optimization. As a next step, the speed profile needs to be converted to a battery load profile using a vehicle model.

2.2 VEHICLE MODEL

For a suitable modeling of the battery life, not only the battery itself but also its control and load must be modeled. In the E2W, the battery supplies the necessary current and voltage for the operation of the electric motor. An electric motor model can be separated into three main components: electrical motor model, load (powertrain) model, and power electronics, which consists of a power converter (inverter) and control scheme. Corresponding model approaches are discussed in the next sections. The description follows the argumentation presented in [112, 115, 116, 184].

2.2.1 Permanentmagnet Synchronous Machine (PMSM)

The considered electric motor is a permanent magnet synchronous motor (PMSM). PMSMs are often used in low power E2W due to their relatively low weight, compact design and high efficiency. A PMSM belongs to the class of synchronous machines. In contrast to asynchronous machines, the rotor runs synchronously with the rotating stator field. However, an excitation field must also be generated in the rotor. In the case of the PMSM, this is done by permanent magnets, but for other synchronous machines this field can also be generated by an excitation winding. The stator coils of PMSMs are usually powered by a three phase current. For the use with constant current power sources such as batteries the constant current has to be transformed to a three phase current using an voltage source inverter and control scheme. There are two main PMSM designs: in-wheel PMSM usually come with an outer rotor design while inner rotor designs are often attached to the wheel using a gearbox. For modeling purposes both designs can be handled similarly. They usually differ in the number of poles p and slots s, with the number being higher for outer rotor designs, and the need of a transmission. In the following, the transmission's influence will be neglected, since it is assumed that its influence can be covered by a loss factor μ_{tm}.

An exemplary in-wheel outer rotor PMSM as used in E2Ws is shown in Fig. 2.9 (a). The casing is opened to show the coils and magnets. The wheel tire would be attached to the outer rotor and the wheel axle to the inner stator. The electronic circuit for inducing the three phase current is located at the bottom. Rotor and stator parts are described and highlighted in Fig. 2.9 (b). The copper coils are wrapped around the pole shoes. Isolation between the pole shoe and coils prevents the three phases to interfere with each other and fixes their position. Permanent magnets are attached to the surface of the rotor. As a result, the presented PMSM can be labeled as a surface-mounted PMSM (SPMSM).

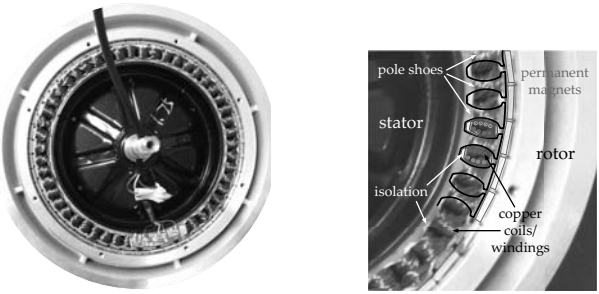

(a) Motor **(b)** Detail view

Figure 2.9: Typical in-wheel motor design (a) and detail view (b).

The PMSM equations are shortly introduced in the following. For a detailed description and derivation it is referred to Appendix A.2 and [114, 116, 172]. The considered PMSM is operated by a three-phase current. The electrical behavior of the PMSM can be reproduced by means of series-connected resistors R_s and inductance L of the stator coils. Using Ohm's ($u(t) = R \cdot i(t)$) and Faraday's law ($u_{ind}(t) = -\frac{d}{dt}\psi(t) = -\frac{d}{dt}[L(t)\,i(t)]$) with u being the voltage, R resistance, i current, and ψ the flux, the voltage $u(t)$ over each of the three phases can be calculated. The rotating three-phase system is then commonly transferred into a stationary two-phase system using the dq-transformation. The dq-transformation, often also referred to as Park's transformation, converts the stator-fixed coordinate system into a rotor-fixed one. As a result, the general PMSM voltage equations

$$\begin{aligned} u_d &= R_s\, i_d + \frac{d}{dt}\psi_d - \omega_{el}\,\psi_q \\ u_q &= R_s\, i_q + \frac{d}{dt}\psi_q + \omega_{el}\,\psi_d \end{aligned} \tag{2.4}$$

are obtained with the electrical angular velocity ω_{el} and rotor angle Θ_{el}:

$$\omega_{el} = \frac{d}{dt}\Theta_{el} = \frac{d}{dt}\Theta_{mech}\,p\,. \tag{2.5}$$

The subscripts d and q stand for the direct- and quadrature axis, respectively.

In addition to the electrical behavior, the mechanical speed and load attached to the motor needs to be considered. See, for example, [114, 116] for a detailed model derivation. Assuming no losses, the torque generated by the motor has to be equal to the motor's rotational inertia and the torque of the load attached to the motor T_{load}. The motor inertia can be calculated from the rotational energy if the inertia J is assumed constant. The differential equation of the angular speed can then be formulated as

$$\frac{d}{dt}\omega_{el} = \frac{p^2}{J}\frac{3}{2}\left(\psi_d\, i_q - \psi_q\, i_d\right) - \frac{p}{J}\,T_{load}. \tag{2.6}$$

The load torque T_{load} itself can be calculated by taking the forces resulting from the rolling friction F_r, the drag resistance F_w, the slope force F_s, and the acceleration force F_a into account.

$$T_{load} = (F_r + F_w + F_s + F_a)\,r_{wheel}\,. \tag{2.7}$$

The forces can be calculated as shown in (2.8) with rolling resistance c_r, vehicle mass m, gravitational constant g and slope angle α.

$$\begin{aligned} F_r &= c_r\, m\, g\, \cos(\alpha)\,, & F_w &= \frac{1}{2} c_w\, A_{front}\, \rho_{air}\, v^2 \\ F_s &= m\, g\, \sin(\alpha)\,, & F_a &= (m + m_{add})\, a \end{aligned} \tag{2.8}$$

Further parameters are the drag coefficient c_w, effective front area of the vehicle A_{front}, air density ρ_{air}, velocity v, additional mass m_{add}, acceleration a, and wheel radius r_{wheel}.

If nonlinear effects such as hysteresis and saturation are negligible or when the accuracy demands are less strict, the general equations in (2.4) can be simplified. The fluxes are assumed to be independent of each other and using the inductance law and derivatives

$$\begin{aligned} \psi_d &= L_d\, i_d + \psi_{PM}\,, & \frac{d}{dt}\psi_d &= L_d \frac{d}{dt} i_d \\ \psi_q &= L_q\, i_q\,, & \frac{d}{dt}\psi_q &= L_q \frac{d}{dt} i_q \end{aligned} \tag{2.9}$$

the system equations can be simplified. Variable ψ_{PM} denotes the flux induced by the permanent magnet. As a result, the simplified PMSM equations in state space representation become

$$\begin{aligned} \frac{d}{dt} i_d &= \frac{1}{L_d}\, (u_d - R_s\, i_d + \omega_{el}\, L_q\, i_q) \\ \frac{d}{dt} i_q &= \frac{1}{L_q}\, (u_q - R_s\, i_q - \omega_{el}\, L_d\, i_d - \omega_{el}\, \psi_{PM}) \\ \frac{d}{dt} \omega_{el} &= \frac{p^2}{J} \frac{3}{2}\, [\psi_{PM}\, i_q + (L_d - L_q) i_d\, i_q\,] - \frac{p}{J}\, T_{load}\,. \end{aligned} \tag{2.10}$$

Although the basic model equations are easy to implement and, for example, sufficiently accurate for a basic simulation, they cannot represent all effects, especially at the boundaries. For example, saturation effects and cross-coupling occur, which lead to varying inductances. Accordingly, the derivatives that occur are no longer trivial. The main focus of this study is on battery-related effects and only little motor data for parametrization is available. Thus a highly accurate motor model is not required and the presented PMSM equations can be used.

In addition to the before mentioned electrical and mechanical models, the properties of a PMSM change with temperature. In particular the coil resistance R_s is influenced by temperature changes. In particular, temperature changes in a coil can be modeled depending on a reference temperature T_{ref}, the coil resistance R_s and a parameter which depends on the coil material.

$$R_s(T) = R_s(T_{ref})\, (1 + \alpha_{Cu}\, (T - T_{ref}))\,. \tag{2.11}$$

In (2.11), the parameter α_{Cu} represents the heating properties of a copper coil corresponding to a temperature difference. According to the law of conservation of energy, the change of temperature in a body is given by the internal storage capacity (m_c, $c_{p,c}$), heat generation Q_g, and heat dissipation Q_d.

$$m_c\, c_{p,c}\, \frac{dT}{dt} = Q_g - Q_d \tag{2.12}$$

The temperature rise is assumed to result only from ohmic losses in the coils. Then, the generated heat can be written as

$$Q_g = I_{mot}^2 \, R_s(T) \, p \, . \tag{2.13}$$

Commonly, a PMSM within an E2W is located in the back wheel. As a result, the stator with the excitation coils lies inside and the permanent magnets are attached to the surrounding rotor. Heat dissipates both through the wheel spokes and the rotor. It is assumed that the heating of the coils and surrounding stator iron is the same and both can be described by a single temperature T_{coil}. The generated heat within the coils is therefore either directly dissipated to the surrounding the air or transferred to the permanent magnets and the iron parts of the rotor with temperature T_{rotor}. The overall heat transfer can be described by (2.14).

$$\begin{aligned} Q_{coil,rotor} &= \frac{T_{coil} - T_{rotor}}{R_{coil,rotor}} \quad \text{with } R_{coil,rotor} = \frac{L_{coil,rotor}}{k_{coil,rotor} \, A_{coil,rotor}} \\ Q_{coil,air} &= \frac{T_{coil} - T_{air}}{R_{coil,air}} \qquad \text{with } R_{coil,air} = \frac{1}{h_{coil,air} \, A_{coil,air}} \, . \end{aligned} \tag{2.14}$$

Variable $R_{coil,rotor}$ represents the thermal transfer resistance, $L_{coil,rotor}$ the average distance between stator and rotor, $k_{coil,rotor}$ the thermal conductivity, for example through the air gap, permanent magnets to the iron, and $A_{coil,rotor}$ the effective heat transfer surface. Heat dissipation to the air can be simplified as described in [162] by approximating the heat transfer coefficient $h_{iron,air}$ in dependence on the surrounding air as

$$h_{iron,air} \approx (12 \, \sqrt{v_{air}} + 2) \, . \tag{2.15}$$

The tangent surfaces can be calculated from the inner (r_{in}) and outer radius r_{out} through $A_{x,y} = 2\pi r^2 l_{mot}$. It is assumed that no heat is generated at the rotor iron ($Q_{g,rotor} = 0$). Heat can be transferred to the coils and the surrounding air. Similar to (2.14), the rotor heat transfer can be described by (2.16).

$$\begin{aligned} Q_{rotor,coil} &= \frac{T_{rotor} - T_{coil}}{R_{rotor,coil}} \quad \text{with } R_{rotor,coil} = R_{coil,rotor} \\ Q_{rotor,air} &= \frac{T_{rotor} - T_{air}}{R_{rotor,air}} \qquad \text{with } R_{rotor,air} = \frac{1}{h_{rotor,air} \, A_{rotor,air}} \end{aligned} \tag{2.16}$$

Finally, the heat equations for both stator and rotor result in

$$\begin{aligned} m_c \, c_{p,c} \, \frac{dT_{coil}}{dt} &= I_{mot}^2 \, R_s(T) \, p - \frac{T_{coil} - T_{rotor}}{R_{coil,rotor}} \\ m_c \, c_{p,c} \, \frac{dT_{rotor}}{dt} &= 0 - \left(\frac{T_{rotor} - T_{coil}}{R_{rotor,coil}} + \frac{T_{rotor} - T_{air}}{R_{rotor,air}} \right) \, . \end{aligned} \tag{2.17}$$

In total, the thermal model needs to be coupled to the PMSM electrical behavior as shown in Fig. 2.10. Temperature is marked by $Temp$ instead of T to distinguish it more closely from torque T. Air temperature $Temp_{air}$ and the resulting motor current flowing through the coils I are input parameters to the thermal model and the coil resistance due to temperature changes R_s is fed back to the PMSM electrical and mechanical model.

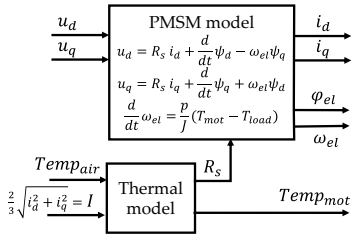

Figure 2.10: PMSM model equations & thermal model.

2.2.2 Power electronics and control

In the next step, the state space representation given in (2.10) needs to be combined with a control scheme to get a suitable motor model which is used for different levels of accuracy. A controller usually consists of an inverter, motor control scheme, and a three phase to two phase conversion. The control scheme regulates either speed or torque by controlling the underlying current at first in constant torque and field weakening area. Conversion from the direct current provided by the battery into a three phase current for the motor is the task of an inverter.

Various methods can be applied to model power electronics. Starting from more accurate models, using three-phase inverters including e.g. MOSFET switching characteristics and field weakening control, to simple models, which control the dq-current without need of an inverter, many different approaches exist [108, 146, 147, 172, 228]. In this context, cascade control is often applied as a simple yet efficient way to control the motor currents. The system can be separated in an underlying current control and a speed controller. Due to the design of the dq-axis system the d- and q-currents are constant values if the PMSM is operated in steady state. This allows for a simple control strategy, such as a PI-control.

Cascade control and inverter
For a basic PMSM with no reluctance, the d-axis typically resembles the axis in the direction of the sum of the magnetic fields of the permanent magnets. Therefore, the d-axis can be assumed to have no influence on generating force. If it is assumed that no flux-weakening is necessary, which comes typically into effect only at large motor speeds, the current $i_d(t)$ should be zero to minimize losses.
For one of the basic control schemes of direct torque control, by assuming $i_d = 0$ for all times, operation in steady state and a negligible reluctance torque ($L_d = L_q$), the behavior between torque T and current i_q becomes $T = \frac{3p}{2}\psi_{PM} i_q$. Fig. 2.11 provides an overview of such a cascade controlled PMSM using a current and speed controller. The demanded motor speed ω_{dem} is transformed to an equivalent current demand in q-direction $I_{q,dem}$ whereas $I_{d,dem}$ is set to 0. A load model calculates the vehicle response and feeds the resulting torque to the PMSM model.

Apart from torque control, other approaches can be derived, which e.g. allow maximum torque-per-ampere (MTPA) or maximum efficiency as seen in [101, 113, 223, 233]. In this study, a basic control strategy is sufficient to motivate the conversion of a recorded E2W

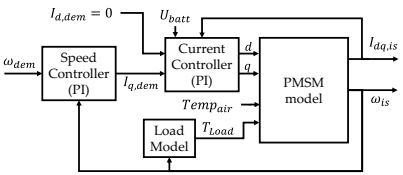

Figure 2.11: Overview of cascade control scheme for PMSM by neglecting inverter dynamics.

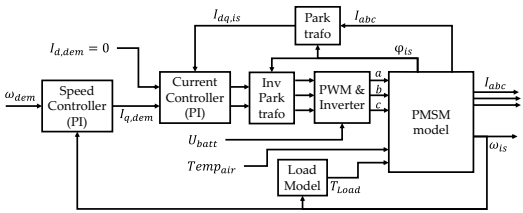

Figure 2.12: Overview of cascade control scheme for PMSM.

speed into a battery power profile. Although MTPA is often used in real applications, the differences in the power and current profile between $i_d = 0$ and MTPA control are rather small. Additional small current and voltage deviations do not lead to significant battery stress as the internal battery dynamics smoothen the current. The motor is typically only operated in the constant torque area and field weakening operation is not described here.

The power electronics is extended by an inverter which switches the voltage on and off on different lines to mimic an alternating voltage. The result should commonly resemble a sinusoidal AC voltage, which can be applied to the three phases of the PMSM. One switching method is known as pulse width modulation (PWM). This method varies the time between the on and off status of the voltage and current. Due to the motor dynamics and inertia, the motor smoothes this signal. If the switching frequency is high enough, typically around 1 kHz and higher, a sinusoidal voltage is produced. For details see [115, 116].

Model depth of detail

Two models are derived to account for different depths of detail. Once a cascade control scheme with an outer speed control and inner current control loop where the inverter behavior is neglected as visualized in Fig. 2.11. Second, a cascade control of the PMSM model in combination with a PWM and an ideal voltage fed inverter as shown in Fig. 2.12. Both control schemes are based on the previously described dq PMSM motor model.

In the first case, no conversion of the three-phase to the two-phase dq-system is required. This simplification is only possible for simulation, where both control and PMSM are modeled in the dq-system. The outer control loop takes the angular speed demand of the motor ω_{dem} and the actual motor speed ω_{is} as input and provides the control input

for the current controller. The output of the speed PI controller equals a torque demand T_{dem} and is converted into a current demand $i_{d,dem}$ as visualized in Fig. 2.13. The current in d-direction $i_{d,dem}$ is set to zero as operation in torque control and not field-weakening area is defined. Both currents $i_{d,dem}$ and $i_{q,dem}$ are separately controlled using PI controllers. The resulting voltages $u_{d,dem}$ and $u_{q,dem}$ are then fed into the PMSM model equations presented in Fig. 2.10 together with the temperature of the surrounding air $Temp_{air}$ and load torque T_{load}. This together with the torque demand due to vehicle to environment interactions results in a current in d- and q-direction as well as an actual motor angular speed.

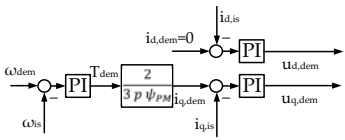

Figure 2.13: Speed and current controller setup.

If the influence of inverter dynamics should be investigated or the model scheme should be applied to a real motor setup, a conversion of the two-phase to three-phase system is often required. In this case, the previous scheme is extended by using the Park transformation and an inverter model as visualized in Fig. 2.12. PWM is used for modulation and an ideal switching behavior of the three-phase inverter is assumed. Inside the PMSM model, a conversion from three-phase back to the two-phase dq-model is required before the PMSM model equations can be applied. In addition, the actual battery voltage U_{batt} can be input to the inverter as a limit. Both of these model and control architectures can be used in a next step to get a realistic representation of battery stress.

2.3 EXTRACTING LOAD CYCLE FROM DRIVING CYCLES

The typical driving cycle(s) introduced in chapter 2.1.2.2 should be used to model motor power demands and therefore typical battery load and stress. As optimization basis, a vehicle dynamic model and battery model are required. The vehicle model has the task to transform the driving cycle into a current profile, which is then applied to the battery model. The derived driving cycles need to be converted to equivalent power demands. Two different approaches are described in the following two sections, which convert the speed to a power or current/voltage profile. First, section 2.3.1 describes a basic setup where motor dynamics are neglected and the speed profile of the driving cycle is converted into a current profile using a power estimation for the vehicle model only. Second, the PMSM model and power electronics are added to model powertrain-specific effects into more detail in section 2.3.2. In principle, different complexity and therefore accuracy levels of PMSM and control can be used. The cascade control scheme comprising the PMSM model but neglecting inverter dynamics presented in Fig. 2.11 is used as reference. Although the more complex cascade control scheme including inverter switching is closer to the real setup, the accuracy gain in contrast to the additional simulation time is insignificant. Due to the switching frequency of at least 1 kHz,

simulation time increases drastically. In addition, a transformation from the two-phase to three-phase system, which serves as the input for the inverter, is not required for simulation setups.

2.3.1 Static conversion

Analogous to the load torque calculation for the motor forces in (2.7) and (2.8), the calculation is based on the forces acting on the E2W body and wheels. The mechanical power P_{mech} is equal to the applied forces F times the vehicle velocity v. The applied forces are calculated based on rolling friction F_{roll}, drag F_{drag} and slope F_{slope} forces, and acceleration force F_a. Using the electric motor efficiency η, the electrical power P_{el} can be calculated. Additionally, a power offset P_{con} of 20 W is added to account for additional consumers such as controllers, interfaces, and lights. No additional force due to slope is assumed during the drive as the test area in Shanghai can be assumed to be flat.

$$P_{mech} = F \cdot v \tag{2.18}$$

$$= \left(\underbrace{m\, c_r\, g}_{F_{roll}} + \underbrace{\frac{1}{2} c_w\, \rho_{air}\, A_{front}\, v^2}_{F_{drag}} + F_{slope} + \underbrace{m\, a}_{F_a} \right) v \tag{2.19}$$

$$P_{el} = \frac{1}{\eta} P_{mech} + P_{con} \tag{2.20}$$

Table A.2 provides an overview of the used vehicle parameters. These were initially estimated based on typical E2W masses and appearance. Later on, these parameters were adapted to the test E2W described before. An overview of the vehicle and motor parameters is given in Appendix A.1.1.

The battery current is determined based on the battery voltage U_{batt} and electrical power P_{el}:

$$I_{batt} = \frac{P_{el}}{U_{batt}}\,. \tag{2.21}$$

As a battery consists of many cells, the cell voltage and current are calculated based on the amount of cells in parallel N_p and serial N_s.

$$I_{cell} = \frac{I_{batt}}{N_p}\ ,\ U_{cell} = \frac{U_{batt}}{N_s} \tag{2.22}$$

For example, 16 cells connected in serial and 2 in parallel of the used 12 Ah LMO cell with a nominal voltage of 3.7 V lead to a battery setup of 60 V and 24 Ah.

2.3.2 Conversion using powertrain model

If motor dynamics are included in the model, the vehicle speed has to be converted to an equivalent angular speed of the motor at first. The angular motor speed is influenced by the wheel radius r_{wheel} and transmission factor n of the actual E2W setup. Using the circumference of the wheel, the angular speed of the wheel w_{wheel} and motor w_{mot} can be calculated.

$$w_{wheel} = \frac{v_{E2W}}{2\,\pi\, r_{wheel}} \qquad w_{mot} = n\, w_{wheel} \tag{2.23}$$

The demanded angular motor speed w_{mot} is used as control input. The outer cascade loop controls the speed of the motor to match the desired speed. The inner loop, which shows faster dynamics, controls the two-phase currents. In this case, i_d should be zero and i_q controlled according to the desired speed respectively torque. In reality, typically a torque control instead of a speed control is used. Then the throttle signal is the input to the control loop.

Interactions of the transmission, wheel and street conditions to the PMSM's speed and torque output are modeled in a load model. The load torque introduced in (2.7) and (2.8) is used. In addition, the force resulting from the rolling friction F_r is extended by a term to reduce the rolling resistance to zero at very low speeds.

$$F_r = c_r \, m \, g \, \cos(\alpha) \, \tanh(2\,v) \tag{2.24}$$

An overview of the PMSM and vehicle parameters is given in Table A.3 and A.4 in Appendix A.1.1, respectively.

2.3.3 Comparison and verification

Both the simplified static conversion and the model including the motor dynamics are fed with typical speed profiles. The resulting current profiles are presented in Fig. 2.14 for the SSES SE2WC and in Fig. 2.15 for the combined SE2WC (a) and the WMTC (b). A positive current corresponds to a discharge of the battery.

Fig. 2.14 (a) provides an overview of the driving cycle. The range between 150 s and 450 s is enlarged in (b). Both the static and motor-based battery current calculation lead to similar characteristics and show only small differences. First, the signal of the PMSM simulation shows a small time offset. This results from the motor and powertrain inertia, which induces a small delay of the cascade controller in the simulation model. Second, the static force conversion leads to larger peaks and fluctuations in the current signal. Since the driving cycle is typically sampled at 1 s intervals, the speed does not increase or decrease continuously, but jumps between values. Due to the motor dynamics and limited motor power, the PMSM simulation results in a smoother current signal. In addition, the PMSM simulation shows a slightly higher current at low speeds. This can be explained by the holding torque as no mechanical brake is implemented.

The same small differences between the static and motor-based battery current estimation can be seen if other driving cycles are used as shown in Fig. 2.15. The WMTC profile in Fig. 2.15 (b) shows larger maximum accelerations and speeds than the previous cycles. As a result, the maximum capable motor torque is exceeded. The simulation model including motor dynamics is only able to follow the speed trajectory with some delay. As the WMTC is designed for conventional motorcycles, which offer a higher power than the 750 W PMSM can provide, this difference is reasonable.
In all three cases, a constant average voltage of 60 V is assumed for the static conversion. The simulation model including the motor dynamics takes the voltage obtained by a battery model of the LMO cell described in chapter 3 as input. A current profile is used for testing as the test equipment requires a current input and does not allow for power input. Overall, both approaches show good accordance in the typical speed area of low-power E2Ws and only differ if the profile requires a higher motor power.

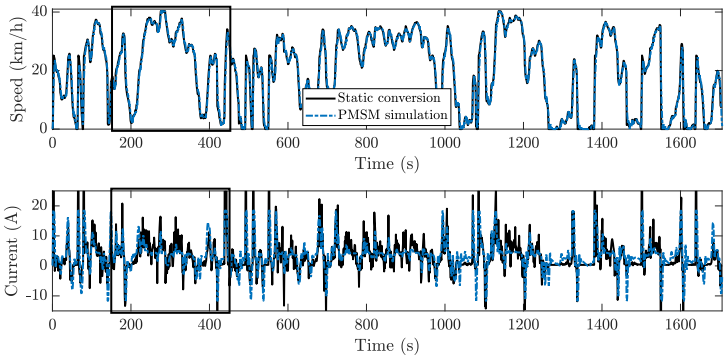

(a) SSES SE2WC

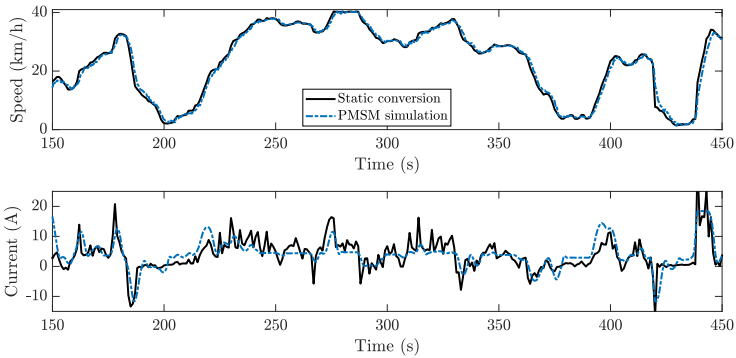

(b) Detail view

Figure 2.14: Comparison of speed and current obtained by static and whole powertrain conversion for SE2WC for SSES. (a) Overview (b) Detail view.

Verification at experimental E2W

In a next step, results are verified using the experimental E2W. Fig. 2.16 compares an exemplary speed, current, voltage, and throttle profile recorded during one test drive on the E2W. The recorded speed profile is then used as input for the vehicle and motor model described before. In addition, a battery model of the LMO cell described in chapter 3 is used to get a realistic voltage drop. The resulting current and voltage profile of the simulation (blue dashed line) is compared to the test drive (black line).
The experimental E2W uses a lead-acid battery instead of a LMO cell, which is used for the battery model of the simulations. Therefore, differences in battery resistance and capacity are expected. The measurement equipment records discharge currents by positive values. No negative currents can be measured due to limitations of the test

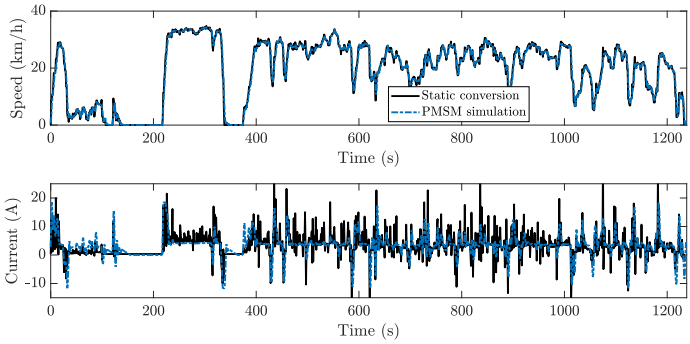

(a) Combined SE2WC

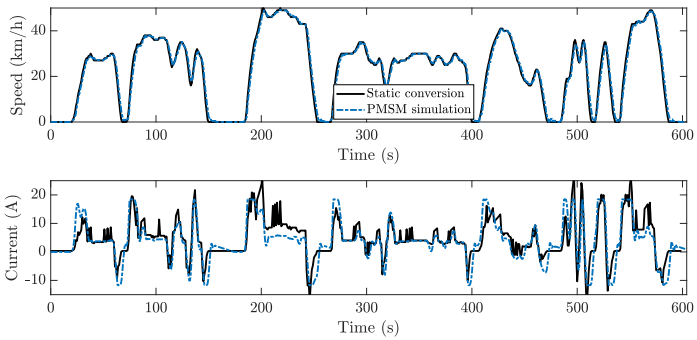

(b) WMTC

Figure 2.15: Comparison of speed and current obtained by static and whole powertrain conversion for the combined SE2WC (a) and WMTC (b).

equipment. Still, regenerative braking effects can be observed as peaks in the voltage profile. The lead-acid battery shows an initial voltage of about 64 V for the presented test drive. The initial SOC of the LMO battery is set to 65% to match this voltage level. The remaining parameters are set to the same values as given in Appendix A.1.1.

Fig. 2.16 (a) provides an overview of the speed, current, voltage, and throttle signal recorded on the test route. The speed profile can in general be accurately tracked in the simulation. Current and voltage characteristics show similar trends for both measurement and simulation. Differences in the current profile occur for negative currents and during areas where the speed remains almost constant. The measured current (black line) shows no negative values as the test equipment is not able to record negative currents. Still, negative currents, which correspond to regenerative braking, occur also in the experimental E2W and the effects can be observed in the voltage profile. The mea-

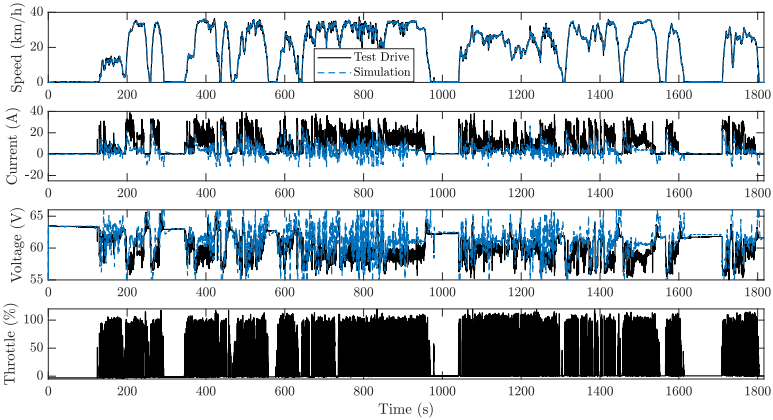

(a) Verification drive

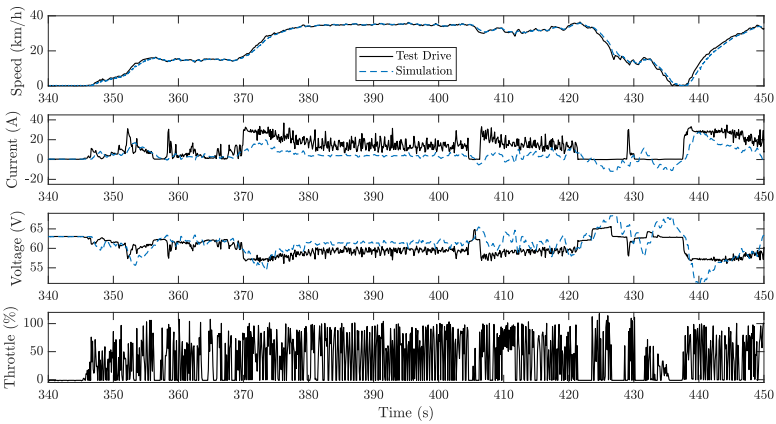

(b) Detail view

Figure 2.16: Comparison of speed, current, voltage, and throttle recorded during a test drive and simulation model. (a) overview of driving cycle, (b) detail view for 240 s to 450 s

sured current shows larger fluctuations, in particular during constant speed areas. This effect is highlighted in Fig. 2.16 (b), where the time area between 340 s and 450 s is shown in detail.

In contrast to the simulation, the test E2W is controlled by a torque demand and not by speed. The torque demand is provided by the driver as a throttle signal. The lower plot of Fig. 2.16 (b) displays the recorded throttle signal, which takes values between 0 (no acceleration) and 100% (maximum torque and acceleration requested). In most E2W in China the throttle handle is very sensitive. This together with the relatively low

power of the E2W leads to an on/off switching characteristic with either full throttle or no throttle. As a result, also the current and voltage shows strong fluctuations, even if an almost constant speed in maintained.
The effect of the different battery types – lead-acid for the experimental E2W and Li-ion used in the simulation – can be especially recognized in the voltage profile. Larger voltage drops are recorded for the experimental E2W than simulated. This leads to the assumption that the lead-acid battery has a higher internal resistance than the Li-ion battery used in this study. In addition, the current in the simulation is lower if a constant speed is maintained. This might result from differences in the E2W weight and motor characteristics as well as the neglected slope force. Slope information could not be included since the altitude signal was too disturbed due to buildings blocking the satellite view during the trip. The model also leads to more and longer recuperation phases than recorded on the test E2W. This can be seen especially in the voltage signal in Fig. 2.16 (b) in between 420 s and 440 s. For example, the measured voltage signal shows a relatively constant recuperation area in between 423 s and 427 s. This leads to the assumption, that recuperation of the test E2W is only enabled if no torque is demanded by the driver for some time. Then, the E2W recuperates at a specific constant current or power. The simulation, on the other hand, adapts its recuperation current to follow the speed input since it is designed as a speed and not torque control.

In summary, the simulation provides reasonable results and differences to the experimental setup can be accounted to the torque instead of the speed control strategy and different characteristics of the lead-acid battery.

3

BATTERY AND LIFETIME MODELING

The optimization of the battery lifetime requires a sound knowledge of the operation conditions, the powertrain components, and, in particular, the battery and its aging characteristics. The influence of a power profile on battery performance and especially on aging is thus described in this chapter. The battery aging model forms the basis for the optimization. Realistic results can only be achieved if the battery model is able to accurately predict the effects of different influencing factors. Therefore, battery aging processes and lifetime modeling are described in detail.

First, basic concepts of Li-ion cells are introduced. Section 3.1 provides an overview of Li-ion cell operation, performance evaluation, aging mechanisms, and state of the art lifetime modeling techniques. Although most graphite-based cells exhibit similar aging processes, the specific aging effects are more pronounced in some positive electrode materials. Furthermore, there are variations in cell behavior as different cell manufacturers use different additives and electrolyte compositions. Aging tests for one selected cell type are described and conducted in section 3.2 in order to gain a sound understanding of relevant aging processes. The test results are then analyzed in section 3.3. One electrochemical and one electrical equivalent model are introduced in section 3.4 and 3.5, respectively. Both models are suitable for predicting the lifetime of a battery cell. However, they show a different model complexity and accuracy as they have different levels of detail. A comparison of the models and their different strengths is given in section 3.6. In the end, the overall simulation model for the entire powertrain is described in section 3.7. Models of the electrical engine, powertrain control, and battery including the lifetime prediction are presented in various levels of detail.

In summary, four key questions will be answered in this chapter:

- How do Li-ion cells age and which factors influence the extent of aging?
- Which measures exist to characterize a new cell?
- Which modeling approaches exist to describe the aging of a cell and how does the performance change over lifetime? Can these models be adapted to a new cell type?
- Are the models suitable for lifetime simulations and is their complexity sufficient to implement them in optimization routines? Which tradeoff between accuracy and complexity is necessary?

3.1 LI-ION CELL

Li-ion cells are on the rise and replace lead-acid cells in an increasing number of applications. Although Li-ion batteries are still more expensive than lead-acid batteries, they offer advantages in voltage, energy, and weight. With an approximately two times higher voltage than aqueous batteries and a gravimetric specific energy of up to 240 Wh/kg, Li-ion batteries offer an up to six times higher energy content at the same weight than lead-acid batteries [118, 238]. Before a detailed analysis of Li-ion cells and their lifetime is provided, some general terms are introduced describing the state of the art of Li-ion cell aging, tests, and modeling approaches.

3.1.1 Aging processes

Aging theory/processes
Aging processes typically result from different chemical processes, transport processes, external stress, and their interactions. Although mainly interactions on the electrodes' surface and electrolyte lead to aging effects, also current collectors, binders and additives might interact [163]. Aging processes can be categorized into loss of active material (LAM), for example due to volume changes of graphite, and loss of lithium inventory (LLI). LLI results from side reactions such as electrolyte decomposition, formation of a passivation layer, and lithium plating. LAM mainly occurs due to mechanical stress-induced cracking and dissolution during operation. For example, volume and structural changes occur [12, 36, 37, 163, 240, 253]. Aging mechanisms are commonly separated for negative and positive electrode although similar effects occur.

One of the main aging mechanisms in cells with a *graphitic negative electrode* (Li_xC_6) is accounted to the growth of a passivation layer on the surface of the negative electrode. This is commonly labeled as Solid-Electrolyte Interphase (SEI) layer [12, 17, 36, 37, 163, 165, 166, 204, 215, 238]. An SEI layer forms as the graphite at the negative electrode's surface reacts with electrolyte components due to a negative potential being applied. The positive electrode comprising lithium also reacts with the electrolyte forming an SEI, but this effect is negligible compared to the passivation effect of the SEI on the graphite surface. A decomposition at very low and high voltages occurs as the electrolyte is thermodynamically unstable in these voltage ranges. During the first cycles, this SEI layer is built up preventing further side products to form. It is commonly assumed to be separated into a smaller more stable inorganic layer and a porous organic layer consisting of various side products formed by the salts and solvents in the electrolyte as well as Li-ions [17, 166, 215, 238]. Ideally, Li-ions can pass through the SEI layer and electrons cannot by being immediately consumed. However, due to electrical and mechanical stress during charge and discharge, the SEI layer can be damaged. During repair processes, the SEI layer consumes further Li-ions. Occurring processes are, for example, summarized in [239] as electrolyte decomposition leading to the formation of an SEI, graphite exfoliation due to cracks formed by gas and solvent co-intercalation, SEI growth and porosity changes, corrosion effects at the current collector, and lithium plating. These processes can be further enhanced due to ions formed by the cathode material (e.g. Mn^{2+} dissolution at low and high voltages for LMO). Lithium plating commonly occurs once the negative electrode potential vs Li/Li^+ drops below 0 V [132, 253]. In total, the SEI layer grows and leads to a capacity loss and resistance increase

as Li-ions are constantly consumed and the SEI thickness adds to the cell's electrode resistance.

Although various interactions and reactions occur during this process, it is often assumed that the migration of Li-ions through the SEI is the rate-determining process of the aging reaction and can be modeled to represent the whole reaction kinetics as described in [166, 173, 176, 215]. Various factors such as the exact electrolyte composition, the additives, and the electrode materials influence the formation of the SEI. Further important measures are the electrode thickness, the distance between both electrodes (separator thickness), and differences in the electrode surface areas [127].

Li-ions are formed at the (positive) lithium electrode and move from it to the graphite electrode due to the potential difference. They migrate through the SEI at the graphite electrode and interact with the graphite. Besides negative electrode effects, degradation also occurs at the *positive electrode*. It commonly consists of lithium metal oxide materials. However, the exact metal used can vary. For example, LiFePO4, LiCoO2, LiMn2O4, Li(MnNiCo)O, Li(NiCoAl)O are used. Similarly to the negative electrode, the active material (lithium metal oxide) changes, for example due to structural changes (phase transitions). Further, an SEI forms at the positive electrode, electric and mechanic connections between current collector, binder, and active material might loosen, and LAM occurs as Li-ions might interact with the negative electrode [239, 240].

Aging can commonly be separated into three phases: initial fast degradation during formation (SEI layer build-up), slower degradation during regular lifetime, and drastic drop of cell capacity and power at end of lifetime. For example, [209] and [257] describe the transition to the nonlinear aging which marks the definite EOL. In this stage, lithium plating occurs as the SEI grows into the pores of the negative electrode. This effect appears especially at low temperatures as well as at high SOC and currents, where only little Li intercalation is possible [132].

Aging influences

The described aging mechanisms lead to a degradation of the cell. This degradation can be accelerated or decelerated by changing the environmental conditions and stresses applied to the cell. The effect of these aging influences as reported in literature is shortly introduced. First effects of capacity fade of Li-ion cells were reviewed in [12]. They examined different mechanisms leading to capacity loss such as overcharge, electrolyte decomposition, film formation at positive and negative electrode, electrode dissolution, and phase changes. A first battery model using these capacity fade mechanisms is described, which forms the basis for further improvements. [36] were one of the first to analyze calendar aging of LCO and $LiNiO_2$ cells. In [37], Broussely et al. furthermore provided a first overview of the main aging mechanisms during storage and cycling. They reported that the growth and stability of the SEI layer is the main aging phenomena. As a result, the capacity decreases with cycle number but the loss rate itself also decreases. This leads to the characteristic square-root like capacity decrease. [217] reviews different early literature and determines common aging effects. They conclude that reversible and irreversible effects occur, temperature is the most dominant aging accelerator, and an increase in voltage leads to a faster capacity loss during storage. Calendar aging for LFP cells is also shown in [107]. They observed that capacity decreases strongly with higher temperature and less with SOC. [207] analyzes NMC cells for calendar aging effects. A linear time dependency is obtained. In addition to an increase in

aging with temperature and SOC, it is assumed that the time interval between checkup measurements might influence the lifetime. Especially for storage or cycling scenarios where only a small capacity loss occurs, the checkup measurements, where the cell is fully charged and discharged at least once, might play an important role in capacity decrease.

[70] compares calendar aging results of NMC, LMO-NMC, NCA, and LFP cells. It is derived that cells containing manganese react more severely to high temperatures. LFP cells show a long calendar life and are less prone to temperature changes. In [109], calendar aging results are presented for NCA, NMC, and LFP cells. Additionally, half-cell measurements are described. Generally, the lower the SOC the lower the aging. [109] detected that some SOC areas, for example 30% to 60%, showed only small differences in capacity fade. Although the different cell types showed similar trends, differences in the extent of aging were detected. The NMC cells reacted more severely to temperature and a high SOC. Whereas the resistance increased with growing SOC for NCA and NMC cells, LFP cells showed almost no increase. [218] demonstrated that a stored LMO-NMC cell ages much faster at 100% SOC than at 90% SOC. The loss of cyclizable lithium, the decomposition of the electrolyte and the loss of active cathode material are seen as main aging causes. Cells with a low SOC also showed a loss of cyclizable lithium, but less than those with a high SOC. Likewise, cycle aging for a LMO-NMC cell is described in [219]. [78, 79] showed that aging increases exponentially with growing charge rate for LCO cells. A critical CR is identified at 1 C at which degradation increases drastically. The unit C describes the current normed to the maximum cell capacity. For example, 1 C for a 12 Ah cell represent a CR of 12 A but only 2 A for a 2 Ah cell. Further, they showed that exceeding the maximum voltage leads to a severe increase of the degradation. In addition, [102] evaluated a NMC cell at different temperatures during cycling. Temperatures above 45°C lead to significantly larger capacity loss and resistance increase.

[142] discussed the influence of a vehicle-to-grid strategy and presented results for a LFP and NMC cell. Calendar and cycle aging tests were conducted, cycling only to a full charge at various DOD and CR. [86] compared different NMC, LFP, and LMO cells for EVs under alternating (seasonal) temperatures. Additionally, the NMC cell comprises a LTO electrode instead of graphite. [86] concluded that the lifetime of the LMO cell is very short and the NMC/LTO cell shows almost no capacity decrease. Furthermore, [43] showed that micro-cycles, very shallow cycles but with high CR, have no significant influence on aging of high-power NMC cells. A detailed analysis of current ripples on battery lifetime is also provided in [35]. No significant influence of AC frequencies on the aging is observed for high-power NMC cells. However, a slightly larger influence is observed for high energy cells. As most tests are conducted with a static charge and discharge current, [201] compared static cycling with more realistic dynamic profiles. Tests for a LFP cell indicated that static cycling as done in accelerated aging tests overestimates the capacity loss compared to more realistic dynamic scenarios. Likewise, [97] validated their NMC aging model results based on a dynamic WLTP profile. This shows that it is important to validate such results using a realistic profile.
[138, 207] analyzed a NMC cell at various temperatures, current rates, DODs and SOCs. They concluded that the influence of SOC and DOD decreases at high temperatures. Very low temperatures of about 0°C are leading to a large capacity loss due to lithium plating. [121] examined the initial capacity increase observed under some conditions.

LFP calendar and cycle aging tests show similar results as described before. A theory is introduced that relates the initial capacity increase to one electrode being larger than the other one in round cells. [1] compared the influence of different fast charging methods on temperature increase and aging. Using LFP cells, they stated that dynamic fast charging profiles perform better than a static CC-CV charging. In [216] and [168] further thermal effects due to non-uniform distributions and abuse were examined. [81] additionally stated that the choice of electrolyte additives alters the cell degradation process. For example, volume changes of a NMC pouch cell can be reduced by a proper choice of electrolyte and additives. An overview of aging mechanisms and influences is also given in [163].

In summary, following parameters, general relationships, environmental influences and operating conditions are reported to effect aging and their main influence is described:

- time — aging increases either linear or square root like over time, used as main aging influence factor for storage scenarios
- temperature — very high (>45°C) and low (<0°C) temperatures are harmful to the cell
- SOC or voltage — high SOC and voltage levels lead to a stronger degradation
- charge throughput/ cycle number — similar influence as time and is commonly used as main aging influence for cycling
- DOD — higher DOD typically lead to stronger degradation
- charge rate (CR) — high CRs (above the defined limit by the manufacturer) lead to lithium plating, a risk of overcharging and therefore cell failure
- discharge rate (DCR) — less influential than CR and depends on the cell type (high energy or high power cell)
- micro-cycles — very shallow cycles do not significantly influence aging and similar aging processes occur as for storage
- overcharge or undercharge — leads to lithium plating or electrode dissolution and thus rapid aging
- test procedure — static charge/discharge scenarios overestimate realistic stress scenarios; too many checkup measurements might induce additional stress
- charging profile — dynamic charging profiles show advantages over CC/CV charging
- cell chemistry — some materials react stronger to specific effects such as manganese reacting stronger to high temperatures
- mechanical abuse — cell damage and failure due to misuse or mechanical stress during assembly and operation

Since a spinel LMO cell is being investigated, LMO-specific effects are briefly discussed. LMO cells show additional mechanisms for capacity fade, which do not or only attenuated occur in other cell chemistries. In addition to electrochemical degradation reactions that lead to the formation of the SEI layer, manganese ions (Mn^{2+}) dissolute from the positive electrode of spinel LMO at very low and high voltages. This dissoluted man-

ganese is transported from the positive to the negative electrode through the electrolyte and leads to an increased formation of side products, especially at high voltages [12, 70, 243, 250]. For example, [243, 244] observed an increased Mn^{2+} content for voltages above 4.1 V and below 3.2 V vs. Li/Li^{+}. Furthermore, volume changes caused by a cubic-to-tetragonal phase shift, often referred to as Jahn-Teller distortion, lead to a higher degradation and accelerate the process of manganese dissolution. During charging, a LMO positive electrode undergoes three main phase transitions as reported in [12, 159, 160]. These phases are characterized by the Li-ion content in the $Li_yMn_2O_4$ lattice. A cubic and tetragonal phase can be observed for $1 < y < 2$, one cubic phase for $y > 0.6$, and two cubic phases for $y < 0.6$. Changes between these phases are reported to result in rapid voltage changes, in particular at approximately 2.96 V, 3.94 V, and 4.11 V vs Li/Li^{+}. Especially during the first phase transition from cubic to tetragonal, a volume change of approximately 6.5% occurs, which results in additional battery stress and degradation [12, 159, 160, 250]. In summary, a LMO positive electrode exhibits additional aging effects which lead to a higher degradation at both very low and high voltages.

3.1.2 Aging measurement/analysis methods

After general aging processes and influences are identified, suitable test methods need to be derived to measure and quantify these effects. Various test methods have been proposed and some of the commonly used and practicable methods are shortly introduced in the following sections.

3.1.2.1 (Accelerated) Aging test

Aging can either be evaluated by observing the real application or by laboratory tests. Evaluating the performance of cells in an E2W or EV during regular use is difficult since the operation conditions are often hard to determine and cannot be varied. Therefore, laboratory aging tests are often used to simplify the setup and to generate predefined test conditions. For example, cells are typically used instead of whole batteries, tests are conducted in a test chamber to maintain a defined environmental condition and special test equipment is used to apply a given current or voltage profile to the cells and to measure and record all relevant electrical parameters. Accelerated aging tests, which are often used in practice, further try to accelerate aging effects by adding additional stress to the cells. In most cases a higher temperature is used, which leads, according to the Arrhenius law, to faster reaction rates and therefore faster cell degradation. Other measures to speed aging up are applying higher currents or reducing relaxation intervals in between cycles. A drawback of such accelerated aging tests is that the results might lead to false conclusions as other side effects, which are normally not observed under non-stress conditions, might occur.

Tests are commonly either done for storage or operating conditions or a combination of both. Storage is often referred to as calendar and operation as cycle aging conditions. Calendar aging tests can either be performed at open or closed circuit conditions. In the first case, cells are at first charged or discharged to their predefined voltage or SOC level. Cells are then stored without interacting with them leading to a slight decrease of voltage over time due to self-discharge. The latter case involves the cells to remain connected to the charging equipment. If the cell voltage differs from its set value, it is slightly charged. This way, the same cell voltage is maintained during the whole test

period. Open-circuit scenarios have the advantage that they resemble realistic storage scenarios where a voltage decrease due to self-discharge occurs. After each 20 to 50 days, cells are typically characterized by several charge and discharge cycles leading also to a reset to the defined voltage. As a drawback, voltage specific effects might not be clearly recognizable. The voltage characteristic curve is typically relatively flat between 20% and 90% SOC and a small voltage change might lead to differences in SOC. Further, self-discharge might lead to a too low voltage level and thus might harm the cell. On the other hand, closed circuit conditions have the advantage that the same voltage level can be maintained throughout the whole test period and voltage-specific effects can be clearly seen. However, a constant charge, even if only a very small current is applied from time to time, does not resemble a real storage scenario. In the end, the choice of the calendar aging test scenario depends on the intended use case of the tests. If a realistic storage scenario including self-discharge is intended, an open circuit scenario might provide improved possibilities. In the case of HEVs, closed circuit conditions might be advantageous as they are more similar to a charge sustaining scenario.

Cycle aging tests can either be performed by simulating a realistic operation scenario or by repeating the same cycle for many times. Applied discharge and charge profiles can either be realistic, synthetic or consist of constant current/constant voltage phases. A variety of different tests are available depending on the intended use case. Commonly, full discharge and charge scenarios with 1 C rate are applied. Variations in charge rate, DOD, SOC, and charging profile are possible as well as changing environmental conditions. Furthermore, in the context of HEVs or PEVs, charge sustaining and charge depleting is distinguished. In both cases, reference performance tests are done at fixed intervals to determine the current performance of the cells in terms of capacity and resistance changes or similar measures.

3.1.2.2 Capacity and resistance

The state of health (SOH) of a cell is often characterized by the loss in total cell capacity and resistance increase. The main reason for capacity loss is the loss of lithium which can be used for cycling. A loss of cyclizable lithium occurs for example when lithium is consumed or bound by the SEI layer or other side reactions such as lithium plating. Resistance increase results mostly from corrosion and degradation of the electrodes and SEI layer growth. Both processes are not directly correlated such that each aging process has to be discussed and described separately. However, in most cases it can be assumed that the end of life (EOL) criteria for the capacity loss will be reached before the one defined for resistance increase.

With capacity loss, the total ampere-hour throughput for one discharge process will decrease leading to e.g. a smaller range for electric vehicles. With resistance increase, the power capability of the cell decreases. This leads to less performance in terms of short-time dynamic behavior, leading e.g. to higher – though reversible – voltage drops. Typically, the EOL of a battery is defined either by a capacity loss of 20% to 30% or a resistance increase by 100% (doubling of resistance). In this study, EOL is reached when the capacity drops below 70% of the initial capacity (30% capacity loss) or resistance doubles.

Both capacity and resistance vary depending on the measurement method and specifications. Therefore, it is important to define a common scheme for capacity and resistance

measurements. A cell's capacity can be determined based on ampere-counting during a full charge and discharge cycle. For example, a cell is at first fully charged to its maximum voltage using CC-CV charging. The cell is then fully discharged until the lower cutoff voltage is reached. The integral over the current is then the total cell capacity $C_{cell} = \int_{t=0}^{t=T_{end}} I\,dt$. In this case, a high discharge current leads to a large immediate voltage drop. In contrast to scenarios where a low discharge current is used, the lower cutoff voltage is reached before the cell is fully discharged. As a result, a low discharge current leads to larger capacity values than a high one. Most suppliers provide information about the discharge rate used for capacity determination on their data sheets. Commonly, a discharge rate of 1 C is used to determine the capacity of cells. A charge or discharge rate (CR) using the unit C can be converted to a current I using the nominal capacity C_n of the cell: $I = CR \cdot C_n$. In case a cell has a nominal capacity of 10 Ah, 1 C corresponds to 10 A. Likewise, 0.5 C corresponds to 5 A and 2 C to 20 A.

Similarly, resistance varies depending on the measurement method. A cells resistance changes as electrode and electrolyte properties change due to chemical reactions and transport processes. In a simplified way, a cell's electric properties might be represented by an electrical equivalent circuit consisting of one series resistance and one or more RC-elements – parallel connected resistors and capacitors – connected in series. The series resistance represents then the static cell resistance and the added elements resemble the dynamic voltage changes. A detailed description of this analogy is provided in section 3.5 and the equivalent structure is also introduced in the context of EIS measurements in section 3.1.2.4. As a result, different resistance values are obtained at different SOCs, temperatures, and measurement methods.

Resistance is commonly calculated based on the voltage drop observed when applying a current to the cell. One profile for performance and resistance evaluation is the Hybrid Pulse Power Characterization (HPPC) test [49, 50]. It defines a specific discharge and charge pulse pattern to evaluate the power and resistance of a battery. The HPPC is applied in 10% SOC intervals to the battery. Resistance can be calculated based on charge or discharge pulses. For discharge, a 10 s discharge pulse of 1 C or higher is used. The resistance can then be calculated based on the 10 s voltage drop as $R_{10s} = \left|\frac{V_{10s} - V_{0s}}{I_{10s} - I_{0s}}\right|$. Similarly, the charge resistance can be obtained. The duration of the pulse and the measurement influences the results due to changing resistance values as explained before. It is therefore important to define the duration and maintain it constant during the tests.

Besides capacity and resistance other parameters such as power and energy capability/fade can be evaluated. However, as they are closely linked to capacity and resistance measures and can be calculated based on these values, only capacity and resistance is measured. A detailed description of the test setup and test execution is provided in chapter 3.2.

3.1.2.3 Differential curves

In addition to the determination of aging on the basis of capacity and resistance changes, some aging effects and influences can be seen in an analysis of the differential curve during charging and discharging. Differential curves show the effects of so-called *phase transitions* or *phase-equilibria*. Incremental capacity analysis (ICA) and differential voltage analysis (DVA) can be used for analysis. For ICA, changes of the charge throughput are depicted over the voltage range leading to a dQ/dV or dSOC/dV curve. DVA draws

voltage changes over the charge throughput (dV/dQ or dV/dSOC). The electrodes typically undergo changes in the lattice structure during a charge and discharge process since Li-ions are inserted into (intercalated) or removed from the electrode lattice. The electrode potential typically changes only very little if the current lattice structure is maintained but increases or decreases rapidly if the structure is changed. Thus, characteristic stages are obtained which can be seen in the ICA or DVA. Peaks in a DVA curve indicate phase equilibria whereas peaks in the ICA curve indicate phase transformations as can be seen based on the defining equations. Depending on the effect to be shown, either ICA or DVA can be used.

DVA and ICA curves can be recorded for both full cells and half-cells. Half-cell measurements have the advantage to record effects of one electrode only. Therefore, characteristics resulting from the negative (graphite) electrode and positive (lithium metal oxide) electrode can be separated. First observations for manganese dioxide are reported in [158–160]. Other studies expanded the analysis to other cell chemistries such as NCA [29–31], NMC [32, 69], LMO-NMC [64, 65, 248], and LFP [122]. On the other hand, full cell or battery voltage measurements of DVA and ICA are also possible. Although the voltage characteristics show combined effects of both positive and negative electrode, their position and amplitude can indicate positive and negative electrode effects. A measurement of the cell voltage or the battery voltage is typically available in vehicles and differential curves can be used to estimate aging effects during operation.

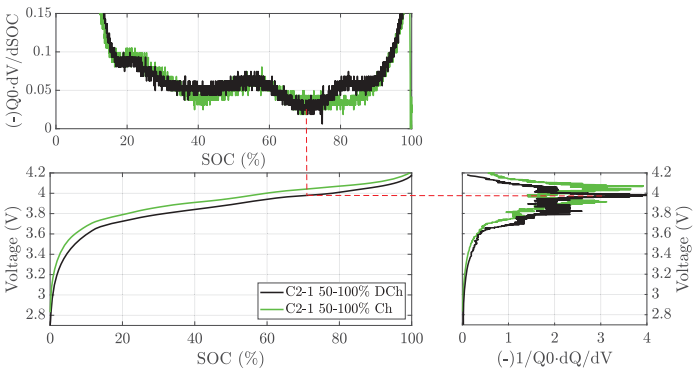

Figure 3.1: Overview of representation forms of differential curves analysis for a 0.1 C discharge (black) and charge (green). Top left: DVA. Bottom right: ICA. Bottom left: OCV voltage characteristics.

OCV, DVA and ICA correlate closely to each other as depicted in Fig. 3.1. The upper plot shows a typical DVA plot using the normalized dV/dSOC over SOC characteristic. The lower right plot shows the corresponding ICA using the normalized dQ/dV over voltage. The voltage characteristic on the lower left, which draws voltage over SOC, can be used to relate the DVA to the ICA. The characteristics are presented for a 0.1 C discharge (black) and charge (green) for a LMO cell. It can be seen that, for example, the valley at about 70% SOC in the DVA corresponds to a peak at about 4 V in the ICA as marked by the dashed line. Furthermore, the positions of the peaks and valleys

differ slightly depending on whether they are recorded for a discharge (black) or charge (green). This can be accounted to the applied current which induces a small voltage drop through the cell's resistance. In this case, charge and discharge voltages lie about 0.09 V apart. The voltage difference increases to approximately 0.14 V for 0.2 C and 0.32 V for 1 C.

The cell voltage can be seen as a superposition of the cell potential at the negative and positive electrode [64, 111]. If half-cell measurements are available, characteristic effects of the total cell voltage can be accounted to the positive and negative electrode. Changes or shifts in the voltage or differential voltage curve occur due to material or phase changes in the electrodes, for example due to an increase in the lithium content (lithiation) or, likewise, delithiation. In general, the graphite electrode shows five stages of Li-intercalation, where four of them can be clearly seen in the voltage curve [57, 64, 65]. Transitions between these stages can be observed by plateaus in the voltage characteristic as shown in Fig. 3.2. Details about the process are described in [57, 91, 94, 100] and are summarized here. Li-ions are intercalated into the graphite structure starting from a fully discharged cell ($0 < x < 0.05$). Initially, only some Li-ions are intercalated at approximately every fourth slab (stage IV or 4L, where L indicates the disordered liquid-like manner of the intercalation) or less in a liquid-like manner. Once the stoichiometry of Li-ions x in Li_xC_6 increases to about 0.1, which corresponds to a half-cell potential of approximately 0.2 V against Li/Li^+, the intercalation structure changes to every third slab being filled by Li-ions (stage III or 3L). A voltage plateau is observed once such a stage transition occurs. Stage II is often separated into two phases where every second slab is filled either with a higher or lower in-plane density [94]. The disordered stage 2L is often present at a stoichiometry of around 0.3. At about $x = 0.5$, the electrode shows an ordered in-plane density and is thus often labeled 2. These stage transitions continue until almost 1 Li-ion is surrounded by 6 C-atoms (Li_1C_6, stage I or 1). The phase transitions between these stages can be observed as peaks in the ICA. Since the voltage variations are relatively small for the graphite electrode (0 V-0.3 V) in contrast to the positive electrode (2.7 V-4.2 V), these peaks can mostly be seen in positive electrode materials, which exhibit a flat voltage curve such as $LiFePO_4$ [91], or in half-cell measurements. Commonly, the peak corresponding to the stage transition from stage 2L to stage 2 is the most dominant peak [57].

In addition, transitions of different positive electrode materials such as LFP, LMO, NCA, and NMC lead to different half-cell potentials of the positive electrode. Typical characteristics for a LMO chemistry are reported in [64, 225]. [160] showed that three distinct regions occur corresponding to three peaks I, II, and III at about 4.1 V, 3.95 V, and 2.86 V in the ICA of a LMO cell. A NMC cell shows two characteristic peaks at 3.4 V and 3.6 V as well as a broader but lower peak in between 3.7 V and 4 V as described in [64, 192, 206]. If blended electrodes are used, they show the characteristics of both materials. For example, [64, 249] examined a LMO-NMC cell using ICA. They reported that five negative electrode phase transformations occur, which, in combination with two LMO specific and two NMC specific transitions, lead to the characteristic peaks. As their properties and transition types vary, these are not described into detail. Section 3.3.1.3 and 3.3.3 present a detailed analysis of the voltage characteristics of the studied LMO cell as well as extensions to a LMO-NMC cell.

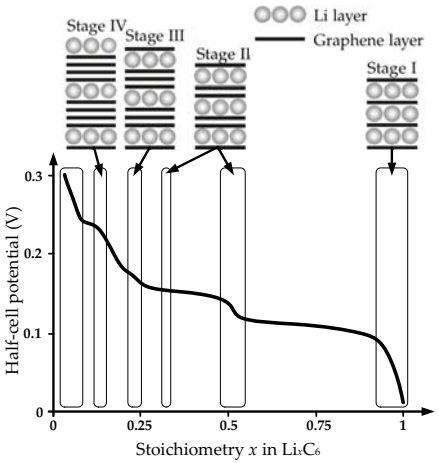

Figure 3.2: Half-cell potential of natural graphite with correlating stage transitions. Adapted from [91, 100, 189]

3.1.2.4 EIS

Electrochemical impedance spectroscopy (EIS) can be used as a non-destructive method to examine and allocate cell aging processes to different reactions. The electrical properties of the cell are described by using an impedance diagram over different applied frequencies. It is therefore sometimes also called AC impedance spectroscopy. A sinus excitation with a very low amplitude is applied to the cells. The response gives hints about the internal electrical structure. By applying sinus curves of different frequency, the response can be drawn in a Nyquist plot to identify resistances, capacities and inductances inside the cell with different time constants. As a drawback, the method requires relatively expensive measurement equipment and a complex data analysis. Although in-situ measurements are possible, EIS measurements are often not conducted in real applications such as in vehicles. Comparable estimates of electrical parameters can be obtained from pulse tests such as the HPPC, which are easier to implement. The EIS method and its application to Li-ion cells is described in literature. Details can be found in [8, 9, 17, 81, 95, 219, 239, 240]. Results and interpretations are shortly summarized.

If a voltage $u(t) = \hat{U} \sin(\omega t)$ with angular frequency ω is applied to the cell, a current response is measured as $i(t) = \hat{I} \cos(\omega t + \phi)$ with ϕ being the phase shift. The resulting impedance Z can then be described by

$$Z = \frac{u(t)}{i(t)} = |Z| \frac{\sin(\omega t)}{\cos(\omega t + \phi)} \tag{3.1}$$

and be separated into a real $\mathrm{Re}(Z) = Z' = |Z| \cos(\phi)$ and imaginary part $\mathrm{Im}(Z) = Z'' = |Z| \sin(\phi)$. The latter two can be drawn in a Nyquist plot to illustrate the electrical properties of a cell. Fig. 3.3 (a) depicts an ideal EIS curve for a Li-ion cell. The Nyquist plot is often separated into five parts which can be correlated to electrical components.

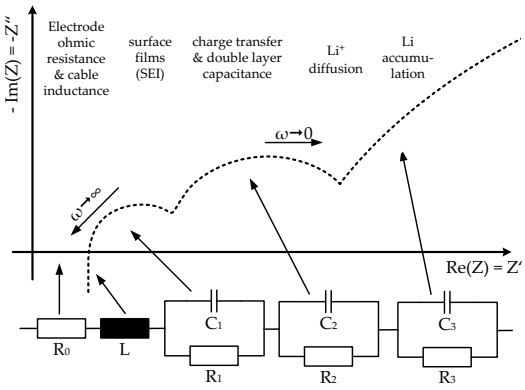

(a) Impedance spectra and RLC electrical equivalent

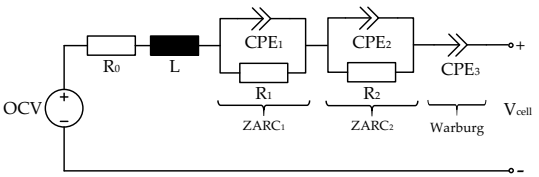

(b) RL-ZARC-Warburg electrical equivalent representation

Figure 3.3: (a) Overview of typical/ideal impedance spectra obtained by EIS and electrical circuit representation according to [8, 17]. (b) Electrical equivalent representation using, for example, ZARC and Warburg elements

A series resistance can be used to describe the electrodes' ohmic resistance. This results in a frequency-independent offset on the real axis Z'. In addition, an inductance is measured. This occurs in particular when long cables are attached to the cell to measure the EIS. For ω against ∞ the inductance leads to an imaginary part of ∞. The first semi-circle corresponds to the formation of surface films such as the SEI. In some cases the particle-current collector contacts are interpreted as semi-circle [219]. These processes are quite fast and are observed at high angular frequencies within an EIS measurement. The corresponding semi-circle can be modeled as a parallel connection of a resistor R and capacitance C, in short called RC-elements, or by more complex structures such as constant phase elements (CPEs), ZARC or Warburg elements as shown in Fig. 3.3 (b). A ZARC element consists of a parallel connection of a resistor and constant-phase element. The constant-phase element is similar to a capacitor if the introduced depression factor is 1. It acts like a resistor if the depression factor is 0. It is able to model also non-ideal semi-circles. The second semi-circle is often accounted to the charge transfer of the double layer capacitance. Slower processes, which result in a large third semi-circle, which is here depicted as line, are due to Li^+ diffusion and, finally, Li-accumulation. A

Warburg element behaves similar to a series connection of a resistor and a RC-element and can be used to model the almost linear increase at the end, which resembles the Li diffusion and accumulation [9]. Electrical equivalent models use the described electrical components to estimate the voltage and current response of the cell and are introduced in section 3.5.

3.1.2.5 Further methods

In addition to the previously introduced methods, many other different non-destructive and destructive methods exist to evaluate cell structure, electrochemical parameters, and chemistry. For example, cell disassembly and separation of anode and cathode can be used to get more information about the cell aging process. Destructive methods are typically only used at the end of the lifetime or to analyze general cell aspects. Half-cell measurements combined with morphological and structural analysis such as X-ray diffraction (XRD) and X-ray photoelectron spectroscopy (XPS) provide detailed results of the cell materials. Observations under an electron microscope can help to identify the status of the cell degradation and to correlate it to different aging effects and electrode coatings/layers. Further, slow potential scan rate cyclic voltammetry can be used to determine reduction and oxidation processes. It is referred to [12, 17, 81, 219, 254] for more details.

3.1.3 Influence of Li-ion chemistry

When dealing with Li-ion batteries and cells, different electrode materials can be used for the positive and negative electrode, resulting in different cell properties such as lifetime, degradation, and safety. Although a negative electrode composed of LTO offers advantages in calendar and cycle life as no SEI layer is built up, graphite is widely used in Li-ion batteries due to its lower price, wider voltage range, and longer experience with this material. For the positive electrode, on the other hand, a variety of compositions exist with different advantages and disadvantages. One of the first commercialized cells consisted of a lithium cobalt oxide ($LiCoO_2$, LCO) positive and graphite negative electrode. LCO offers a high working voltage, energy and capacity. Limitations occur due to the high cost of cobalt, low thermal stability and sensitivity to high currents. Olivine LFP with graphite as negative electrode exhibits a lower specific energy than LCO but has an increased thermal stability and cycle life. Further, cost is reduced as no cobalt is used. On the other hand, it offers a much lower specific energy than LCO and offers a relatively low working voltage range. It is commonly used in applications where weight is less important and a long calendar and cycle life is required and higher temperatures might occur. Spinel LMO ($LiMn_2O_4$) in combination with a graphite negative electrode outperforms LFP in the context of specific energy and can also achieve higher specific power while still being a relatively cheap material. In addition, manganese is relatively environmental friendly. However, cycle life, especially at high current rates, is worse than for LFP due to reactions with the electrolyte and manganese dissolution. Blends of nickel, manganese, and cobalt (NMC) as positive electrode material offer a relatively high specific capacity and energy. Such blends have the advantage that they are cheaper than LCO due to their lower cobalt content – but more expensive than LMO – and have a longer cycle life compared to LMO. Such blends try to incorporate the positive effects of the blended materials while reducing negative and side effects. NMC cells are, therefore, often used in automotive applications. In addition, blends of nickel, cobalt, and

Table 3.1: Comparison of performance of Li-ion chemistries derived from [118, 149, 177, 269]. (- poor, o neutral, + fair, ++ good)

Criteria	Capacity	Energy	Power	Thermal stability	Safety	Cycle life	Cost
LCO/g	+	++	o	o	o	o	-
LFP/g	+	o	+	++	++	++	++
LMO/g	o	+	+	o	+	-	+
NMC/g	+	++	+	o	+	o	o
NCA/g	++	++	+	-	o	+	o
LXO/LTO	+	o	+	++	++	++	-

aluminum (NCA) are extensively researched due to their high capacity and energy. In contrast to manganese based cells, cycle life is improved. However, this comes at the cost of thermal stability. If properly operated and cooled, NCA cells are also a good choice for automotive applications. Substituting the graphite negative electrode with LiTiO (LTO) in the before mentioned cell composites, drastically improves calendar and cycle life as well as safety in terms of thermal stability. The main cause of aging in graphite-based cells is the formation of the SEI layer. As the potential of LTO is about 1 V higher than that of graphite against lithium, no SEI layer is formed as the electrolyte does not react with the negative electrode. However, this also leads to a lower working voltage of LTO based cells and therefore a lower specific energy. In addition, LTO is more expensive than graphite and the cost of such cells is still very high. [117, 118, 153]

Table 3.1 gives an approximate rating of the cells according to specific performance criteria. For clarity, a cell using LCO as positive electrode material and graphite as negative one is abbreviated as LCO/g. As the positive electrode material matters less for LTO negative electrodes, these cells are summarized as LXO/LTO with X standing for Co, Mn, or any other positive electrode compounds. Although NMC and NCA are mostly studied and focused on in automotive applications due to their higher specific energy than LFP and longer cycle life than LMO, LMO cells are used in E2W due to their lower price and less environmental issues than cobalt-based materials and higher specific energy and therefore lower weight than LFP cells.

3.1.4 Difference cell and pack

Previous descriptions focused on properties and definitions of single cells. However, both voltage and capacity, which can be provided by a single cell, are bound by physical limitations due to the used material. For Li-ion cells, voltage levels of 3.4 V (LFP) to 4.2 V (LMO) against graphite can be achieved with a specific capacity of approximately 120 mAh/g to 200 mAh/g [153]. As a result, cells need to be connected into modules or packs to achieve higher voltage levels of 48 V to 60 V for E2W or even higher voltages for EVs. A battery pack consists either of modules of cells or of strings of parallel cell connections or parallel strings [44, 53]. If cells are grouped into modules at first, one module might comprise a series of cells or parallel cell connections. An arrangement in modules has the advantage that the module can be equipped with a management unit for cell diagnosis and balancing as well as for easier replacement of faulty modules. An overview of Li-ion batteries for HEV and BEVs is also presented in [169].

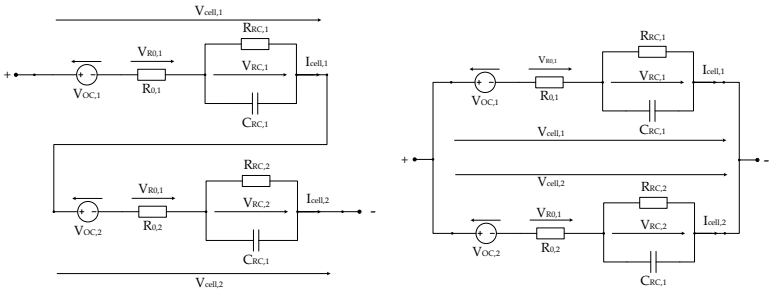

(a) Serial **(b)** Parallel

Figure 3.4: Serial (a) and parallel (b) cell connection using a first order Randles circuit representation.

Fig. 3.4 visualizes the serial and parallel connection of two cells using an electrical equivalent circuit representation. In the given case, a first order Randles circuit is used consisting of a voltage source which represents the cell's OCV, a series resistance R_o, and a RC-element. The battery voltage and current can be calculated as

$$\text{Serial}: V_{mod,s} = n_s\, V_{cell} \qquad I_{mod,s} = I_{cell} \qquad C_{mod,s} = C_{cell} \tag{3.2}$$

$$\text{Parallel}: V_{mod,p} = V_{cell} \qquad I_{mod,p} = n_p\, I_{cell} \qquad C_{mod,p} = n_p\, C_{cell} \tag{3.3}$$

$$\text{with } V_{cell} = V_{OC} + V_{R_o} + V_{RC} \tag{3.4}$$

and the number of cells connected in series or parallel in a battery module $n_{s/p}$. The subscript $cell$ stands for a single cell, and mod for a module of cells. The module capacity C_{mod} behaves exactly as the module current with the capacity increasing by the number of cells connected in parallel and remaining the same if cells are connected in serial.

The connection of single cells into battery modules and packs does not only influence cell voltage, current, and capacity but also aging. Although most aging studies focus on observing aging on cell level, additional effects might come into effect on battery pack level. Temperature gradients occur due to the packed cell setup. If a battery is only cooled on its outer surface area, cells inside are cooled less as the direct convection to the cooling air or liquid is not available. The uneven temperature distribution within a cell is even enhanced due to cell to cell variations. Slightly different cell resistances and capacities might lead to imbalanced resistive losses and currents. In addition, cell contacts and interconnections might increase the total resistance of some cells and induce uneven battery stress [41, 53, 66, 74, 133, 167, 251]. Likewise, the BMS and passive and active cell balancing schemes influence the aging of single cells and the battery itself.
For example, a control oriented battery pack model is introduced in [53]. A battery module and pack model is described using a combination of an EEM together with empirical aging equations. Different parallel and serial connection schemes are described and influences of temperature and cell to cell variations analyzed. Results show that cells within a battery pack age faster than single cells. The worst cell in the pack ages approximately 15% faster than a single cell. Furthermore, a multiscale battery model is

presented in [67]. This model comprises different levels of detail, starting from electrochemical cell and half-cell modeling over cell to cell variations in a battery pack up to BMS effects and balancing. In [66], cell to cell variations are analyzed into detail. Cell to cell variations of SOC, SOH, capacity, and rate capability within $\pm 5\%$ and ohmic resistance within $\pm 15\%$ were examined. The authors conclude that cells connected in parallel are less affected by these variations than in serial connections. Furthermore, [133] infer that cell degradation is influenced by uneven current distribution and thermal gradients in battery cells. They show that the degradation rate increases by approximately 5% in a parallel connection of 6 tightly packed cells if a thermal gradient is present in comparison to a uniform temperature distribution. On the other hand, [41] concluded that capacity fade of a single cell and battery pack are almost similar. Deviations only occur for resistance but can be traced back to an increase in contact resistances of the cells in the battery pack. The internal cell resistance remains the same as in the tests of the single cells. As a result, cell simulations can be also used for aging evaluation of battery packs as long as the cells are properly cooled in a battery pack and contact resistances are minimized.

In summary, cell to cell variations occur in a battery pack and influence the aging characteristics. For typical cell to variations, a cell in a battery pack ages up to 15% faster than a single cell. As the SOH of a battery is determined by the worst performing cell, a battery ages up to 15% faster than a cell for the given setup. In a heuristic approach, a cell model can be used to estimate battery aging by multiplying the cell SOH by 1.15. This value is, of course, only an estimate and a battery might still degrade faster or slower depending on the actual architecture as well as cell to cell variations.

3.1.5 Modeling approaches

Various battery models and modeling approaches have been described in literature. They can roughly be classified in 4 groups:

- Molecular models such as kinetic Monte Carlo (kMC) methods.
- Electrochemical models (porous electrode models, pseudo-3D and 2D models, single-particle models (SPMs)).
- Electrical equivalent models (EEMs) coupled with empirical aging relations.
- Data-driven approaches (neural-networks, Bayesian networks, and Vector machines).

In addition, multiphysics models combine molecular, electrochemical, and empirical approaches.

These approaches are shortly introduced and classified by their complexity with respect to computation time and number of parameters, predictability, validity, and application scope. Molecular models described, for example, by kinetic Monte Carlo simulations, offer the highest predictability [106, 145, 164, 191]. They describe cell-specific and cell-internal effects based on a molecular or atomistic scale and incorporate stochastic effects. Due to their high complexity and computational effort, they are used for cell design and short-term simulations. Multiphysics models are typically used when different modeling depths are required. They might incorporate very accurate yet complex kMC models for processes occurring at the electrode particles together with simpler electrochemical

Table 3.2: Comparison of battery cell modeling approaches.

Model/ Criteria	Complexity	Parameters	Predictability	Validity	Inner states	Scope	Purpose
kMC	very high	many	very high	high	known	molecule /cell	design
multi-physics	very high	many	very high	very high	known	cell & battery	design & analysis
porous electrode	high	many	high	high	known	cell	design
SPM	medium	medium	medium to high	medium	known/ averaged	cell	analysis & simulations
EEM	low to medium	little	low to medium	low	unknown	cell & battery	(lifetime) simulations

transport processes or empirical models to get an overall cell and sometimes also battery pack model [7, 11, 91, 130, 140, 191, 251].

Electrochemical models rebuild kinetics and transport processes. These are based on chemical reaction rates, thermodynamics, diffusion, and migration effects. A commonly used approach is the Doyle-Fuller-Newman model incorporating the porous electrode theory [61, 62]. The porous electrode theory can either be applied to a three-dimensional or pseudo-3D (P3D) model, simplified into pseudo two-dimensional (P2D) models or even into one-dimensional models such as single particle models (SPMs). Electrochemical models result in partial differential equations (PDEs) together with differential algebraic equations (DAEs), which require suitable solvers and computational power. Such models are commonly used for cell design and simulations of a few seconds up to one full charge-discharge cycle. Due to their lower complexity, SPMs can also be used for lifetime simulations.

In contrast to electrochemical models, electrical equivalent models (EEMs) rely on electrical equivalent circuits and mainly resemble the observed or measurable effects such as voltage, current, and SOC changes of the battery. The cell's electrical behavior is modeled using a simplified electrical circuit representation. A comparison of different models and their application can be found in [73, 211]. Model parameters and structure are commonly based on empirical observations and adapted to measurement data. If an aging estimation is included in the EEM, it is commonly based on observations of capacity and resistance changes and fitted to measurement data using basic empirical relations, which are sometimes motivated by physical properties.

Furthermore, data-driven approaches such as neural-networks, Bayesian networks, and vector machines have gained in importance. These approaches rely on a large data set which can be used for training and validation. Based on the data and basic structural assumptions, relations between the input (features) and output (labels) variables are identified. As a drawback, the identified model structure remains unknown and overfitting might occur if too little data are available. As data-driven approaches vary in their predictability and computational effort, these are not analyzed in detail. Fig. 3.5 and Table 3.2 provide a qualitative overview of the different model types, their complexity, parameters, predictability, validity, knowledge about inner cell states, scope, and main purpose.

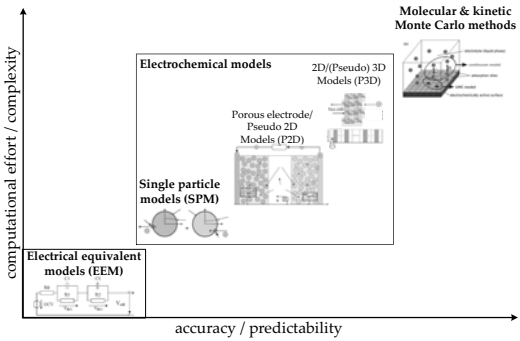

Figure 3.5: Qualitative overview of accuracy and complexity for different electrochemical models and electrical equivalent models (adapted from [180]).

For the context of lifetime simulations and optimization, an SPM, as a simplified version of a porous electrode model, and an EEM offer a good tradeoff between complexity and accuracy and are further investigated. Within electrochemical models, mass transfer can me modeled by the concentrated solution theory which leads to diffusion, migration, and convection based on the potential difference in the cell. Furthermore, kinetics are governed by chemical reaction rates, thermodynamics, and charge transfer, which is assumed to follow a Butler-Volmer kinetics. These relations can either be applied to a P3D models, simplified into P2D models or even into one-dimensional models depending on the effects which should be resembled. In this context, P2D models use already simplified expressions of the electrodes and reactions [15, 48, 124, 129, 260]. Within 1D models, SPMs further simplify the cell structure [4, 5, 71, 134, 170, 175, 176, 199]. They neglect or average different concentrations in the solution and merely model the electrodes as one particle where diffusion and intercalation occurs. In addition, different model simplifications and order reduction methods have been described focusing e.g. on Pade approximation [141], orthogonal decomposition [40], and many other simplification approaches [27, 129]. Aging effects such as SEI layer growth, side reactions, and current shifts are directly represented in the equations of electrochemical models. They mainly differ in their extent and depth of modeling different aging processes. Aging processes result from chemical processes, transport processes, external stress, and their interactions as described in section 3.1.1.

A first cell model incorporating aging effects based on electrochemical relationships is presented in [165] and improved in [12]. A Butler-Volmer expression is used to describe the side reaction by introducing the exchange current density. If irreversible reactions occur, the expression simplifies to a Tafel kinetics. The cell kinetic overpotential is separated into solid and electrolyte phases. The porous electrode theory is applied to model the material balance. Transport processes inside the cell can be modeled as a combination of diffusion and migration processes. Aging effects are related to SEI growth and lithium plating. Nowadays, most models are based on the Doyle-Fuller-Newman model, which introduces some simplifications to generalize the model [61, 62]. Due to

the large amount of different electrochemical models, they are not introduced in detail. A detailed description of an SPM is provided in section 3.4.

On the other hand, empirical aging models were developed on the basis of electrical equivalent models. In contrast to electrochemical models, no cell internal information such as concentrations and layer thickness is available. As a result, aging relations can only rely on measures which can be observed such as voltage, current, temperature, and time. EEMs, which are used for aging estimation, typically consist of three elements: a base model to represent the current-voltage characteristics of the cell, a thermal model to represent heating and cooling, and an empirical aging model [9, 53, 73, 152, 205, 211]. The latter is sometimes also referred to as semi-empirical or physically-motivated empirical model since the equations are partially based on general physical relationships. The base model is commonly described using a Randles circuit with RC or constant phase elements such as ZARC or Warburg elements. These are able to represent the current-voltage characteristics as introduced in section 3.1.2.4 [73, 211]. A lumped parameter thermal model approach is used to describe temperature changes. Resistive losses are modeled as main cause of heat generation. Convection leads to heat transfer between cells and the surrounding air or liquid. Empirical aging equations use available measures such as current, voltage, and temperature as well as derived values such as SOC, charge throughput, cycle number, and DOD to model capacity loss C_{loss} and resistance increase R_{inc}. Changes of the cell resistance and capacity over time need to be fed back to the electrical base model.

As the EOL criteria for capacity loss is commonly reached before the EOL criteria for resistance, most studies focus on accurately estimating aging influences on capacity. The following sections focus on ampere-counting empirical equations. Since they require little background information and result in simple expressions, they are commonly used in applications where low computation power is available, such as battery management systems, or where calculations have to be run repeatedly, such as optimizations.
A first empirical aging model for calendar aging was described in [28] for a LiNiCoO cell. It was observed that aging propagates with a square-root-like time dependency. Bloom et al. used a temperature T and time t dependent power law to represent calendar aging as shown in (3.5). In (3.5), A is a parameter with no direct physical representation, E_a the activation energy, R the gas constant and z the power factor. Parameter z is set to 0.5 as it represents the SEI layer growth.

$$C_{loss} = A \exp\left(\frac{-E_a}{RT}\right) t^z \tag{3.5}$$

Subsequently, researchers examined other time dependencies by either varying the factor z, for example to 0.75, or introducing further time dependencies, such as a mixed square root and linear time [68, 205]. Additionally, influences of the parameter A on voltage or SOC were evaluated. For example, linear [205], power law [68, 170], or exponential [83] relations were described. In some cases, also the exponential temperature influence is simplified by using an polynomial expression [161].

Based on the approach by [28], [245] set up a cycle aging model by introducing an ampere-hour throughput dependency instead of the time dependency for LFP cells. Further, charge rate CR was regarded as an additional stress factor with the severity factor b:

$$C_{loss} = A \exp\left(\frac{-E_a + b\,CR}{RT}\right) (Q_{Ah})^z \tag{3.6}$$

[69, 205] and [105] used this knowledge to derive a more complex empirical aging model based on calendar and cycle aging results of NMC cells. For example, voltage V and depth of discharge (DOD) dependencies were included as shown in (3.7).

$$\begin{aligned} C_{loss} = a_1 (V + a_2) \exp\left(\frac{-E_a}{RT}\right) t^{z_1} \\ + \left(b_1 (\varnothing V + b_2)^2 + b_3 \, DOD + b_4\right) Q_{Ah}^{z_2} \end{aligned} \tag{3.7}$$

Focusing more on HEVs, other influences on the minimum state of charge SOC_{min} and operation mode $Ratio$ were used in [52] as shown in (3.8).

$$\begin{aligned} C_{loss} = \left(a + b \, Ratio^c + d \, (SOC_{min} - SOC_0)^e\right) \\ \cdot \exp\left(\frac{-E_a}{RT}\right) (Q_{Ah})^z \end{aligned} \tag{3.8}$$

$Ratio$ is defined between 0 and 1 depending on the time proportion of discharge (pure electric driving) and charge sustaining in a plug-in HEV. A $Ratio$ of 1 indicates a pure discharge with no charge sustaining. The cell model is extended to a battery pack model in [53].

In (3.7), calendar and cycle aging are integrated in one aging equation. Other approaches switch between calendar and cycle aging, using two separate equations. In case of calendar aging [170] introduced Eq. (3.9) and for cycle aging equation (3.10) using NCA and LFP cells. As seen before, calendar aging progresses with time and cycle aging with charge throughput. Stress factors include SOC and temperature for calendar aging as well as current and temperature for cycling. Capacity degradation is modeled by a SOC-dependent parameter A, which is determined through test and taken from a lookup table. The same parameter is a function of the current I for cycle aging.

$$C_{loss,cal} = A(SOC) \exp\left(\frac{-E_a}{RT}\right) t^z \tag{3.9}$$

$$C_{loss,cyc} = A(I) \exp\left(\frac{-E_a + \alpha|I|}{RT}\right) (Q_{Ah})^z \tag{3.10}$$

Although labeled similarly, all parameters for calendar and cycle aging result in different values, which have to be recalculated for every cell chemistry by doing extensive accelerated aging tests. Similar approaches are described in [86]. Instead of charge throughput, they use cycle numbers to estimate cycle aging. In addition, [86, 156] propose an on-board estimation and update of the empirical parameters. Further empirical equations are proposed in [97, 224]. These mainly differ in their kind of coefficients and polynomial terms to describe the influence of aging factors. Various publications are available which describe further improvements of specific effects such as varying temperatures [161] or load profiles [221].

So, in general, the presented ampere-counting empirical aging equations formulate similar dependencies, observing a square root time and/or charge throughput influence. Many papers account this to a side reaction taking place to build up the SEI. Furthermore, an Arrhenius-like temperature influence with an unknown activation energy is used. Voltage or SOC are described to influence calendar aging and DOD to effect cycle aging.

3.2 (ACCELERATED) AGING TESTS

3.2.1 Aging test setup

Although the main aging processes of Li-ion cells are well known as described in chapter 3.1.1, the extent of aging and ancillary effects differs depending on the cell chemistry as introduced in chapter 3.1.3. A good data basis of cell data and tests is necessary to identify an aging model. Various cell tests have been described in literature. However, often only a limited set of cell tests and data are examined and even less presented. Many studies such as [36, 107, 109, 219] present only data for calendar aging. Others such as [102, 142, 190] present only full-charge scenarios. However, a model used for lifetime optimization has to be able to evaluate both calendar and (realistic) cycling scenarios as well as various SOC, DOD, temperatures, and charge rates. The cell chemistry is chosen based on cell properties and, due to the high cost pressure in the E2W market, especially based on the price. Based on the comparison of different cell chemistries in Table 3.1 and market experience, LMO is selected as suitable candidate.

At first available Li-ion cell data are analyzed and evaluated on whether they can be used to parametrize a lifetime model for E2Ws. Criteria are whether

- the cell tests are conducted for the required LMO cell chemistry,
- various maximum SOCs were evaluated and presented,
- various DODs were evaluated and presented,
- cells were tested at different temperatures,
- the charge rate has been changed,
- both calendar and cycle test were conducted,
- a realistic scenario (realistic in-operation profile) has been evaluated,
- and whether test results were presented.

Evaluated data sources were [69, 205] (S1), [52, 53, 141] (S2), [68] (S3), [105] (S4), [138, 207] (S5), [190] (S6). A decision matrix on the applicability of cell tests on the given scenario is presented in Table 3.3.
[69, 205] present a calendar and cycle aging campaign for NMC cells. In [52, 53, 141], cycle aging tests for a LMO-NMC cell are described. The research focuses on plug-in hybrid electric vehicles (PHEVs) and introduces charge depletion and charge sustaining modes instead of calendar and continuous discharge cycle aging. As a result, the data cannot directly be compared to cell tests for electric vehicles. A high power 6 Ah NMC pouch cell is analyzed in [68]. Results for calendar aging at three different temperatures and cycle aging with 20% DOD are shown. A HEV profile is used to discharge and charge the cells by applying varying currents. Further, only 20% DOD is presented. [105] describe tests for a 10 Ah NMC cell, which can be used for EV applications. Temperature and SOC is examined for calendar aging. Various cycle tests were conducted with 1 C but only a few are described. A 2.15 Ah NMC cell is described in [138, 207]. A test campaign for calendar aging at various SOC and temperatures as well as cycling at different DODs and charge rates is conducted. Similarly, [190] describe calendar aging tests at different temperatures and SOC for a NMC cell. For cycling only full charge scenarios are evaluated using different DODs and CRs. However, both studies presented

Table 3.3: Available Li-ion cell data and their fitness for model parametrization.

Data source	Weight (%)	S1	S2	S3	S4	S5	S6
LMO	20	0	0.5	0	0	0	0
SOC variation	15	1	1	1	1	1	1
DOD variation	15	1	0.5	0	1	1	0.5
Temp. variation	5	1	1	1	1	1	1
CR variation	10	0.5	0.5	0.5	0	1	1
cal. and cyc.	10	1	0.5	1	1	1	1
real scenario	5	1	1	1	0	0	0
results described	20	0.5	0.5	0.5	0.5	0.5	0.5
Weighted Sum (%)	100	65	62.5	60	55	65	60

by [138, 207] and [190] were only presented in 2017.
In total, a thorough test campaign for pure LMO cells with both calendar and cycle aging tests using various SOC and DOD ranges could not be identified. Likewise, data are only partly presented in the publications and cannot directly be extracted. Access to a larger database with cell tests such as shared in the Freedom Cooperative Automotive Research (FreedomCAR [157]) is also not possible. As a result, accelerated aging tests using a common E2W LMO cell were designed and conducted as described in the next section and published in [188]. The cell tests can be used to generate more reliable data and to validate optimization results.

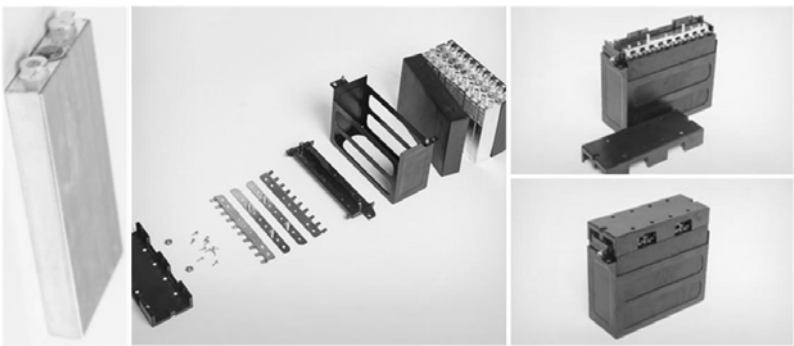

Figure 3.6: Cell assembly and module setup as shown on the supplier website [171].

The tested LMO cells were selected based on a market research for possible E2W batteries in China. No exact information about cell chemistry and composition is available as the cells are commercial LMO cells. The prismatic cells provide a nominal capacity of 12 Ah in a voltage range of 2.7 V to 4.2 V. Charging is specified by the supplier to a maximum current of 12 A (1 C) and discharging up to 24 A (2 C). Fig. 3.6 shows the investigated LMO cell and battery module. The prismatic cells consist of alternating electrode and separator foils. In contrast to the often used 18650 cells, they offer a more advantageous heat distribution and a larger surface area for heat dissipation. As a draw-

Table 3.4: Cell data as provided in data sheet.

Cell Batch	A1 & A2	B
Chemistry	LMO	LMO-NMC
	graphite	graphite
nominal voltage (V)	3.7	3.7
nominal capacity (Ah)	12	13
voltage range (V)	2.7 - 4.2	2.7 - 4.2
max. discharge rate	2 C	2 C
dimensions (mm)	18 x 66 x 133	18 x 66 x 133
working temperature	0 to 45 (Charge)	0 to 45 (Charge)
(°C)	-20 to 45 (Discharge)	-20 to 55 (Discharge)
nominal cycle life	2000 (1C to 60%)	2000 (1C to 80%)

back, the cells need to be put under pressure to maintain a close contact between the foils and are more difficult to manufacture [240].

Initially, 29 cells were purchased for a first accelerated aging test campaign. Subsequently, a second batch consisting of 12 cells of the same cell type was purchased one year later. Finally, a third batch of 6 cells was purchased for the validation tests. The three batches are denoted by A1, A2, and B. A distinction is necessary as the supplier improved their cells every year. The differences between the first and second batch were rather small. However, the supplier changed its cell chemistry from pure LMO to a blend of LMO and NMC for the third batch. Due to the limited space and test channels, not all cell tests could be conducted at the same time. Further, observations made during the initial test round led to the need to perform additional tests to get a thorough understanding of the cell and aging. Therefore, new cells had to be purchased. Changes in the cell chemistry mainly lead to an increase in the initial capacity and decrease of resistance. Still, a similar aging behavior is observed as described in the following sections and the tests can be used to improve the understanding of the LMO chemistry. Table 3.4 gives an overview of the cell characteristics provided in the datasheet.

In total, 3 test runs were conducted. Besides using the batch classification A1, A2, and B, cells are labeled according to their test run and the number of the cell. For the second test run, the index "2-" is added before the cell number. The index "v-" is used to label the third (validation) test run. For example, cell 01 is the first cell of the first test run, 2-01 the first cell of the second test run, and v-01 the first cell of the validation tests. A distinction is necessary as 2 cells of batch A1 and A2 were used for the validation tests later on (see Table 3.12).

3.2.2 Test schedule

An Arbin BT2000 battery test equipment and temperature chamber by Vötsch are used for the accelerated aging tests. The temperature chamber by Vötsch allows cells to be stored on two levels. The outside and operation terminal is shown on the left of Fig. 3.7 and Fig. 3.8 displays the cell setup inside the chamber. As shown on the right side of Fig. 3.7, the Arbin BT2000 is set up to offer in total 12 channels for aging tests, 6 with -100 A to 100 A range and 6 with -50 A to 50 A. With a voltage range in between 0 and

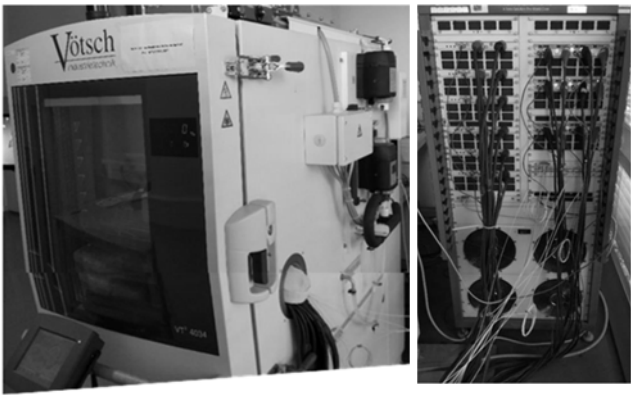

Figure 3.7: Temperature chamber (left) and battery cycler (right) used for testing.

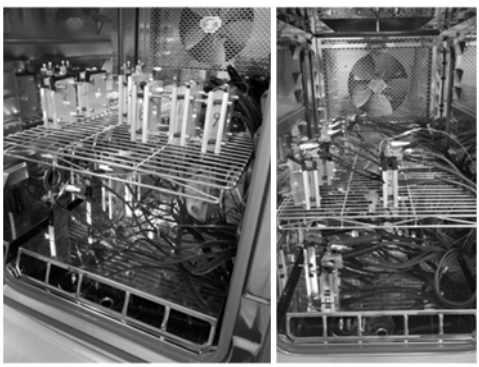

Figure 3.8: View inside of the temperature chamber and cell connections.

5 V, a maximum power of 500 VA and 250 VA is available. Temperature measurement for each channel can be included using temperature sensors. For all measurements, a constant temperature of 25 °C is maintained by the temperature chamber unless specified otherwise.

As a full aging characterization of the LMO cells is desired, both calendar and cycle tests are conducted. The cells were stored at open circuit conditions at room temperature for calendar aging tests. Cycle aging tests consist of a repeated charging and discharging of the cells with a predefined constant charging and discharging rate or a charging and discharging profile. Test scenarios are defined based on the SOC of the cell. The SOC is defined based on the ampere hours being discharge-able from an initial full constant current (CC) and constant voltage (CV) charged cell with 1 C discharge rate. The CV phase cut-off voltage is set to 0.05 C (0.6 A). For example, the storage condition of 50% SOC is achieved by an initial full CC/CV charge followed by a 6 Ah discharge with 1 C

discharge rate (if the initial capacity was 12 Ah). The same accounts for cycling, which is always based on the charge throughput corresponding to the DOD. After the check-up measurements every 3 weeks, the measured remaining capacity was used then to adapt the SOC range to that. If the capacity decreased from 12 Ah to 11.5 Ah, 50% SOC would correspond now to 5.75 Ah.

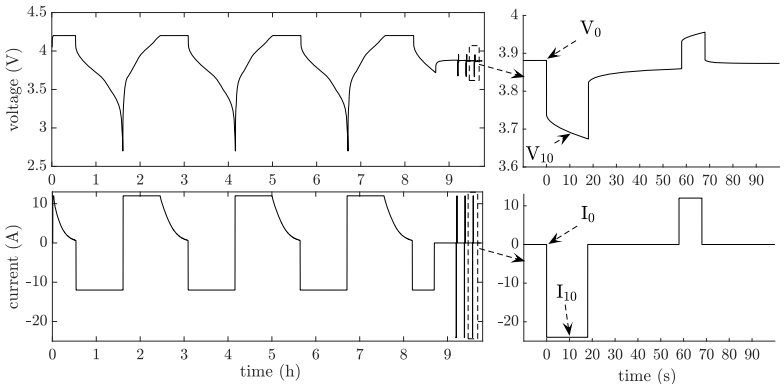

Figure 3.9: Exemplary initial and checkup measurement to determine capacity and resistance. The pulses used for resistance measurement are enlarged on the right.

Before the cycling or calendar aging tests begin, all cells are subject to initial characterization. This consists at first of capacity and resistance measurements. The cell is fully charged using CC/CV charging as defined before. Afterwards, the cell is fully discharged with 1 C until the lower cut-off voltage of 2.7 V is reached. This procedure is repeated three times without a rest time in between. The largest capacity value of the three iterations is used as the cell's 1 C capacity. Afterwards, the cell is discharged to 50% SOC and a 18 s 2 C discharge is applied. After 40 s of rest, the cell is charged for 10 s with 1 C and then rested for 40 s. This procedure is also repeated three times. The discharge resistance after 10 s R_{10s} is used to describe the cell's resistance as shown in Fig. 3.9 and calculated by (3.11).

$$R_{10s} = \frac{V_{0s} - V_{10s}}{I_{0s} - I_{10s}} \tag{3.11}$$

A complete capacity and resistance measurement consisting of three complete discharge cycles and three resistance pulses at 50% SOC is shown on the left. One resistance pulse is enlarged on the right.

As a next measurement, the open circuit voltage (OCV) is determined over the SOC by discharging at a low discharge rate. As discharge rate 0.2 C (2.4 A) and 0.1 C (1.2 A) are used. Lower discharge rates do not add any information as the voltage resolution of the test equipment is limited. The cell is at first CC/CV charged, rested for 1 hour and then discharged using the defined discharge rate corresponding to 10% SOC (for a 12 Ah cell this would be 1.2 Ah). Further, for some cells a stepwise OCV versus SOC measurements are conducted to identify a more ideal OCV at 10% SOC intervals. At the same time, the resistance at different SOCs is recorded. One exemplary measurement

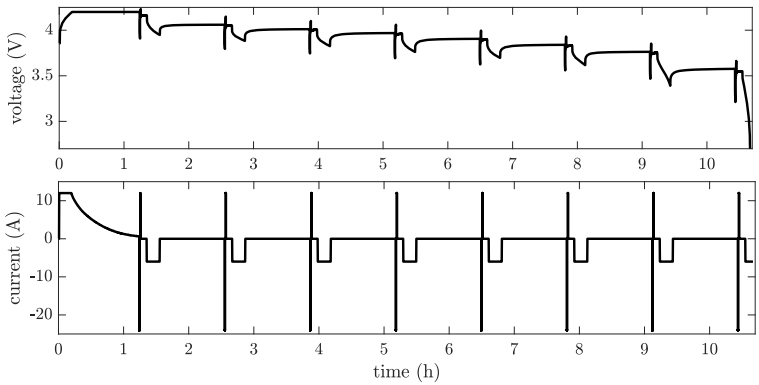

Figure 3.10: Exemplary initial OCV over SOC measurements.

is shown in Fig. 3.10 for voltage (top) and current (bottom). These initial tests are done at 25 °C. Some cells are also subject to further small tests, for example, to determine the influence of clamping on temperature.

In an interval of about three weeks, the cycling and calendar tests were stopped and the remaining capacity and resistance evaluated in the same way as described for the initial characterization. Therefore, the cells were fully charged and discharged three times with 1 C at 25 °C. Afterwards, tests were continued. The first test round started in January 2016, the second one in January 2017, and the validation test in December 2017. Cells were stored for 350 days. Cycling was continued until the EOL criteria was reached or the test time exceeded one year. Validation tests were conducted over a period of half a year. A test matrix is constructed to evaluate cell characteristics in the whole operation range. The cell tests were differentiated into calendar (storage) and cycling tests.

Storage temperature, SOC, and duration are commonly described as main aging influence for *calendar aging* [28, 36, 69, 97, 105, 107, 109, 205, 207, 219]. Aging propagates linearly between minimum and maximum SOC as for example described in [205]. Deviations from the linear aging increase over SOC are reported for low and high SOC [69]. The test matrix presented in Table 3.5 is built up to cover these effects. Only relevant test conditions should be recorded as the amount of channels on the test equipment is limited. The influence on temperature on calendar aging is well known to propagate with an Arrhenius law. Therefore, only one reference test at 45°C was conducted. As a drawback, temperature effects can only be predicted well as long as the Arrhenius-law approximation is valid. This is commonly true for temperatures greater than 10°C and below the maximum specified cell temperature. Other tests were run at 25°C. The SOC grid is finer at low (5%-20%) and high SOC (90%-100%) to capture nonlinear effects occurring there. In between a linear behavior is expected as described in literature [52, 69, 205].

During *cycling*, different DODs, average SOCs, charge and discharge rates, charge throughput, temperature, and duration have an influence on lifetime. In contrast to calendar aging, these influences are harder to describe due to more complex processes

Table 3.5: Test matrix for calendar aging tests.

Cell SOC (%)/ Temp.	5	20	50	90	100
25°C	x	x	x	x	x
45°C			x		

Table 3.6: Test matrix for cycle aging tests.

DOD (%)/ Avg. SOC (%)	20	50	70	85	95
20	x				
30		x			
35	x				
47.5				x	
50	x	x			
52.5					x
65			x		
75		x			
90	x				

occurring. Commonly DOD and average SOC as well as charge throughput are used to describe the main aging influences. Further, a high charge rate is said to have a significant influence on aging. Table 3.6 shows the test matrix for the criteria DOD and average SOC. Different DOD are important as the model should be able to accurately represent different driving characteristics. The DOD of EVs or E2Ws varies depending on the route, distance, and driving style. A good coverage of the whole SOC area is also important for charging optimization. As aging typically decreases with a decrease in SOC, a full charge might not be good for the cell. Therefore, the cell aging behavior at different maximum SOC should be covered.

Additionally, charge and discharge rates were varied. Variations in aging over discharge rate are important to characterize possible negative influences of high accelerations while driving. Charging optimization requires information about lifetime variations due to high charge rates. Charge rates of 0.5 C, 1 C, and 3 C and discharge rates of 1 C, 2 C, and 3 C were evaluated for 25-75%. Further, a typical driving cycle is used instead of constant discharging. A driving cycle results in varying charge (recuperation) and discharge rates during cycling. Aim is to determine whether a realistic profile shows similar characteristics to a constant discharge scenario and might be identified by its average discharge current or other simplified characteristics.

Validation tests are used to verify the optimization results. As described later in chapter 4.2, two DOFs can be identified for the optimal charging: maximum SOC and the charging current and start time itself. Therefore, a derived optimal charging strategy is compared to a conventional charge and a partially optimal charging using the optimal SOC but a conventional charging current profile.

Ideally, at least 3 cells should be tested under every scenario to have a statistical measure and to be fail safe even if one cell shows abnormal behavior. Due to the limitation of space and test equipment, most tests were conducted with 2 cells and some with 1 or 3 cells. The assignment of cells to test conditions is shown in Table 3.7 to 3.9. Cells showing a similar initial capacity and resistance were grouped and assigned to the same test condition to minimize cell-to-cell variations.

Table 3.7: Cell test specification (cell type A1).

Cell number	T (°C)	SOC (%)	CR/DCR (C)
01	25	30-100	1/1
02	25	30-100	1/1
03	25	50-100	1/1
04	25	50-100	1/1
05	25	25-75	1/2
06	25	25-75	1/2
07	25	25-75	1/1
08	25	5-55	1/1
09	25	80-100	1/1
10	25	80-100	1/1
11	25	10-30	1/1
12	25	25-75	1/1
13	25	25-45	1/1
14	25	25-45	1/1
15	25	40-60	1/1
16	25	40-60	1/1
17	25	5-100	1/1
18	25	20	-
19	25	100	-
20	25	50	-
21	25	50	-
22	25	20	-
23	25	100	-
24	25	5-100	1/1
25	25	5	-
26	25	90	-
27	45	50	-
28	45	50	-
29	-	-	-

Table 3.8: Cell test specification (cell type A2).

Cell number	T (°C)	SOC (%)	CR/DCR (C)
2-01	25	50-100	1/1
2-02	25	50-100	1/1
2-03	25	5-90	1/1
2-04	25	5-90	1/1
2-05	25	25-75	1/1
2-06	25	25-75	1/1
2-07	25	5-100	1/profile
2-08	25	5-100	1/profile
2-09	25	25-75	3/1
2-10	25	25-75	1/3
2-11	25	25-75	0.5/1

Table 3.9: Cell test specification (cell type B, cells 3 and 4 are from prior batches).

Cell number	T (°C)	SOC (%)	CR/DCR (C)
v-01	25	61-100	0.5/profile
v-02	25	61-100	0.5/profile
v-03 (A1)	25	61-100	0.5/profile
v-04 (A2)	25	43.5-82.5	opt/profile
v-07	25	43.5-82.5	0.5/profile
v-08	25	43.5-82.5	0.5/profile
v-09	25	43.5-82.5	opt/profile
v-10	25	43.5-82.5	opt/profile

3.3 CELL ANALYSIS

The test results are evaluated. At first, an initial characterization is provided to show the uniformity and variance of the cells and test rounds. Subsequently, capacity loss and resistance increase is analyzed separated in calendar and cycle aging tests. This is supplemented by a differential voltage analysis.

3.3.1 Initial characterization

3.3.1.1 Initial capacity and resistance variation

All purchased cells were subject to initial capacity and resistance tests as described before. Table 3.10 to 3.12 provide an overview of the measured capacity for a 1 C discharge, resistance determined based on the voltage drop during a 10 s 2 C discharge, and the internal resistance measured directly at the cell current collector contacts.

A difference between R_{10s} and R_i results from the test equipment and test method. The battery cycler has relatively large cable clamps as seen in Fig. 3.8. An additional metal contact needs to be attached to the cell contacts to be able to attach the cable clamps to the cell electrodes. Therefore, the measured resistance by voltage drop corresponds not only to the cell's internal resistance but also to the cell cycler's internal resistance and clamping devices. In average, the clamps add a resistance of about 6.8 mΩ to the cell internal resistance of about 2.7 mΩ leading to a R_{10s} of about 9.5 mΩ.

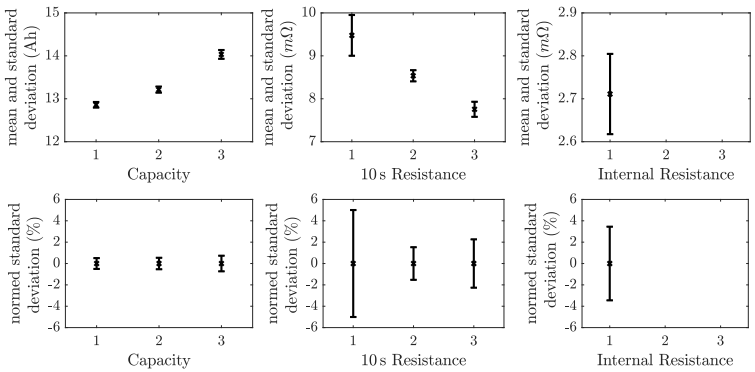

Figure 3.11: Average and standard deviation (top) and normed standard deviation (bottom) of batches A1 (1), A2 (2), and B (3) for capacity (left), 10 s resistance (middle), and internal resistance (right).

Fig. 3.11 provides an overview of the capacity and resistance values for the different batches A1 (1), A2 (2), and B (3). The top plots show the mean value of the capacity is increasing starting from about 12.9 Ah for A1 over 13.2 Ah for A2 to 14.03 Ah for the last batch. At the same time, the resistance calculated based on the 10 s voltage drop decreases from 9.5 mΩ over 8.5 mΩ to 7.8 mΩ. The internal resistance from one current collector to the other is only recorded for the first batch and lies at about 2.7 mΩ.

Table 3.10: Initial cell characterization (cell type A1).

Cell number	Capacity (%)	10 s Res. (mΩ)	internal Res. (mΩ)
01	12.88	9.76	2.70
02	12.95	9.34	2.65
03	12.80	9.68	2.80
04	12.85	9.60	2.70
05	12.85	9.23	2.70
06	12.96	9.26	2.73
07	12.64	8.74	2.80
08	12.66	8.31	2.76
09	12.67	8.72	2.72
10	12.68	9.03	2.96
11	12.62	8.72	2.76
12	12.66	8.62	2.87
13	12.91	9.33	2.57
14	12.92	9.83	2.74
15	12.87	9.92	2.78
16	12.88	9.92	2.69
17	12.83	9.96	2.64
18	12.90	10.33	2.81
19	12.83	10.04	2.83
20	12.90	10.13	2.76
21	12.89	9.96	2.85
22	13.02	10.25	2.70
23	12.80	10.13	2.76
24	13.03	9.75	2.63
25	12.88	9.92	2.70
26	12.93	10.67	2.84
27	13.00	10.17	2.64
28	12.94	9.92	2.69
29	13.17	5.59	1.84

Table 3.11: Initial cell characterization (cell type A2).

Cell number	Capacity (%)	10 s Res. (mΩ)	internal Res. (mΩ)
2-01	13.28	8.64	-
2-02	13.33	8.26	-
2-03	13.41	8.24	-
2-04	13.27	8.43	-
2-05	13.12	8.68	-
2-06	13.18	8.45	-
2-07	13.15	8.13	-
2-08	13.44	8.52	-
2-09	13.01	8.91	-
2-10	13.08	8.86	-
2-11	13.08	8.77	-

Table 3.12: Initial cell characterization (cell type B, cells 3 and 4 are from prior batches).

Cell number	Capacity (%)	10 s Res. (mΩ)	internal Res. (mΩ)
v-01	14.02	7.72	-
v-02	13.76	7.78	-
v-03 (A1)	9.46	10.03	-
v-04 (A2)	12.61	10.02	-
v-07	13.93	7.59	-
v-08	14.01	7.62	-
v-09	14.38	7.40	-
v-10	14.10	8.42	-

The different cell batches were purchased over a period of 3 years with about 1 year difference in between. The results indicate a steady improvement of the cell by the supplier. A larger capacity deviation is observed especially between batches A2 and B. This corresponds with the chemistry change from pure LMO to LMO-NMC.

The bottom plots of Fig. 3.11 present the standard deviation normed to the maximum value. Whereas the capacity values show only a small deviation of below 2%, the initial resistance varies more. The first batch A1 shows a variation of about 10%, batch A2 of about 5% and B of about 3%. The large variation in resistance of the first batch can partly be accounted to the measurement environment for example due to the additional clamps. The internal resistance, measured directly between the current collectors, shows already a lower standard deviation of about 7%. Another reason might be that the cells were stored longer than usual both at the supplier and before the tests could be started. The cells of the first test round were therefore grouped according to their initial capacity and resistance to further minimize cell-to-cell variations.

3.3.1.2 SOC vs OCV and stepwise resistance

The cell resistance further changes depending on the cell's SOC. Fig. 3.12 depicts the resistance at BOL for selected cells of the first test round (top), second test round (middle), and validation tests (bottom). The resistance recorded in 10% SOC steps is shown. Two plots are displayed per test round for the batches A2 and B for improved clarity.

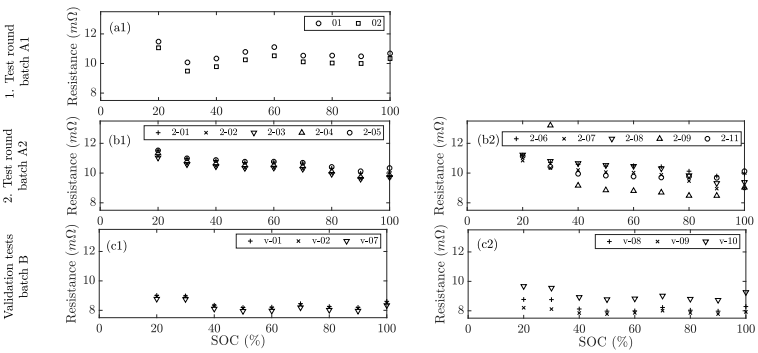

Figure 3.12: Resistance values of tested cells obtained at 10% SOC intervals.

A comparison of cell 01 and 02 of the first test round at BOL is shown in Fig. 3.12 (a1). Results at BOL are only shown for cells 01 and 02 as a stepwise SOC-OCV test was only conducted for these two cells due to limitations of the test equipment at the beginning of the tests. As a result, SOC tests had to be split into three measurements (100-70%, 60-30%,20%-0%). This might be a reason for the piecewise increasing or decreasing resistance values.

In general, the resistance value varies over SOC. The largest resistance value is obtained at low SOC. Most cells show a decrease in resistance the higher the SOC. Resistance varies less in the area between 40% and 60%. The standard deviation of the cell resistance over the SOC range lies below 5%. Due to the resistance variation a comparison

of resistance values needs to be conducted at the same SOC. Resistance is determined at 50% SOC during the tests to eliminate these deviations.

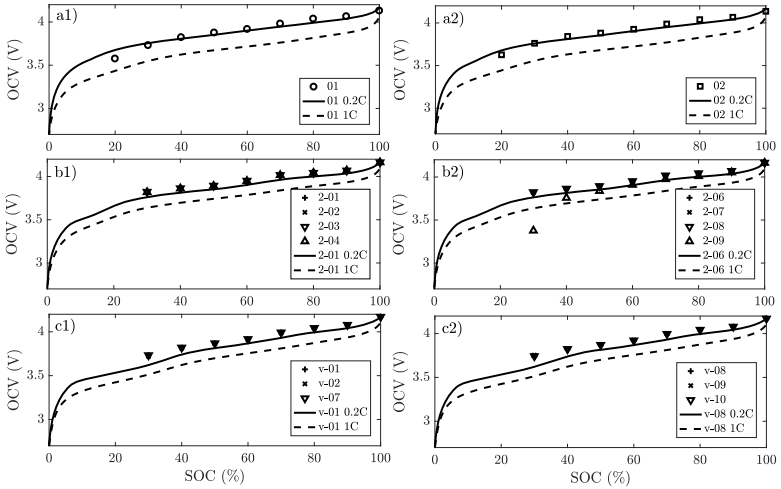

Figure 3.13: OCV values of tested cells obtained at 10% SOC intervals (markers). Further, exemplary voltage curves measured at 0.2 C (solid line) and 1 C (dashed line) discharge rate are shown.

The initial tests are also used to determine the cell's OCV. Typically, the OCV at a specific SOC can only be obtained after all cell internal reactions due to charge or discharge processes have reached a steady state. On the one hand, this can be done by a stepwise discharge followed by a rest period. In the given tests, a rest period of at least 1 h was necessary until almost no voltage changes were recorded. As a drawback, this procedure is very time consuming especially if a fine SOC resolution is required. On the other hand, an estimate of the OCV can be obtained by reducing the discharge rate to a very low level. The cell voltage converges then to the steady-state OCV. Fig. 3.13 displays the voltage measured at 10% SOC intervals after 1 h rest for the first (top), second (middle) and validation (bottom) tests. A comparison with the results of a continuous discharge with 0.2 C (2.4 A) and 1 C (12 A) is provided for selected cells.

The measured voltage for a 1 C discharge deviates from the OCV as seen in Fig. 3.13. A discharge with 0.2 C is already able to predict the OCV more accurately. Lower discharge rates of 0.1 C or 0.05 C could further improve the result but increase the measurement duration. Additionally, the voltage resolution of the test equipment is limited. Too small voltage changes cannot be recorded. A 0.2 C discharge is, therefore, used to describe the changes in (open circuit) voltage and DVA or ICA. A small deviation in the 0.2 C discharge voltage can be observed at low SOC for cell batches A1 and A2 in comparison to batch B. A characteristic bend in voltage can be observed for the first two batches at about 20% SOC. Batch B shows this characteristic bend already at about 40% SOC. Batch A1 and A2 consist of cells with a pure LMO positive electrode, batch B is already

a mixture of LMO-NMC. The voltage drop at about 40% SOC can be accounted to the NMC component of the electrode. The following chapter describes initial differences in terms of DVA and ICA. A detailed analysis of the differences for the three batches is provided in chapter 3.3.3, where DVA and ICA curves are compared over lifetime.

3.3.1.3 Initial DVA and ICA

Especially during a slow charging process with a constant current, which is the state of the art in most EVs if no fast charging is necessary, differential voltage curves can be recorded without adding extra stress to the battery and cells. These curves provide insights about phase transitions and cell chemistry specific effects if no half-cell measurements are available when cells cannot be decomposed. They are therefore useful to analyze cell specific effects, especially regarding the positive electrode material [29, 32, 64, 69, 158].

OCV, DVA, and ICA are used to identify further differences between the three cell batches A1, A2 and B. Fig. 3.14 (a) displays the voltage characteristics of a discharge with 0.2 C. The low rate voltage analysis shows that batches A1 (black) and A2 (dashed green) deviate only slightly in between 10% and 30% SOC. Cells of batch A2 show a larger bend in voltage starting from about 20% SOC. Batch B (grey) shows this voltage drop already at about 40% SOC. This is elucidated in Fig. 3.14 (b) and (c) for DVA and ICA, respectively. A DVA is conducted by differentiating voltage over SOC (dV/dSOC). Further, results are normed by the cells' initial capacity Q0 to achieve a higher degree of comparability. Similarly, results for an ICA are shown for differential charge throughput over voltage (dQ/dV). Results are also normed to the initial capacity Q0. Changes of phases and phase transitions can result from changes of the negative or positive electrode as well as electrolyte and separator adaptions. However, it is assumed that little material adaptions occur in the graphite negative electrode, electrolyte and separator. As a result, changes in the voltage characteristic are in the following sections mainly correlated to changes in the positive electrode material.

For batch A1, two phase transitions at about 3.85 V and 4 V can be detected in the ICA. They result from a combination of the negative electrode and positive electrode potential. The negative electrode potential is assumed to show 5 peaks in the ICA which correspond to the stage transitions introduced in section 3.1.2.3. [29–32] show that half-cell measurements of the negative electrode lead to 4 peaks in the DVA, which indicate phase equilibria at approximately 60%, 25%, 20% and 15% SOC for a NCA cell. Likewise, [64, 65] evaluated the ICA of a NMC-LMO cell and correlated its peaks to both negative and positive electrode stage transitions. They concluded that peaks result from a combination of negative and positive effects. Narrow negative electrode peaks lie at approximately 3.45 V, 3.52 V, and 3.55 V. Broader peaks, which correspond to the negative electrode stages 1, 2 and 2L, are said to appear in between 3.6 V and 3.8 V as well as 3.9 V and 4.15 V.

The peaks of A1 do only partly overlap with the negative electrode peaks. This means that they can mainly be traced back to the positive electrode material of an LMO cell. For example, [160] reported that three distinct regions occur corresponding to three peaks I, II, and III at about 4.1 V, 3.95 V, and 2.86 V in the ICA of a LMO cell. Peaks I and II are in this case shifted by about 0.1 V due to the lower discharge current. Peak III cannot be recognized as it lies outside of the safe operation range (minimum voltage

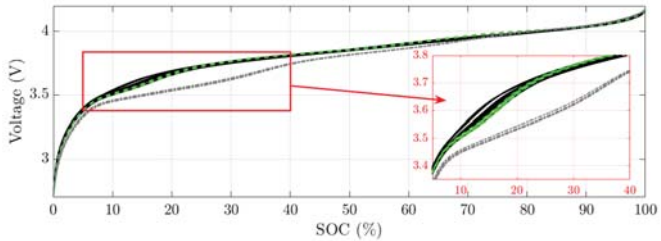

(a) OCV 0.2 C

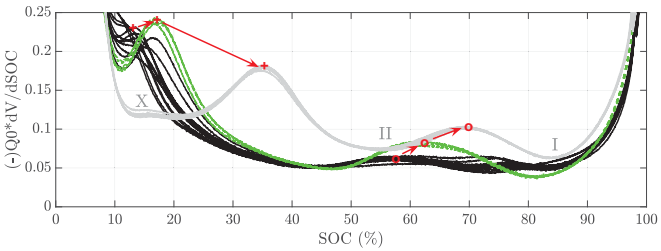

(b) DVA 0.2 C

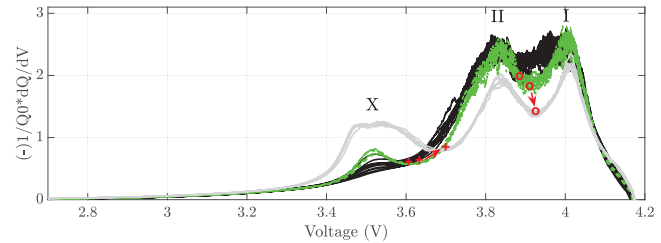

(c) ICA 0.2 C

Figure 3.14: OCV, DVA, and ICA of batch A1 (black), A2 (green dashed), and B (light grey) for a 0.2 C discharge normed to the maximum cell capacity Q_0.

2.7 V). This voltage limit is set by the manufacturers to prevent an irreversible damage of the cell, which occurs when reaching this phase transition. In accordance with [12], the phase transitions can be accounted to a cubic/cubic two-phase reaction, a cubic one-phase reaction, and a cubic/tetragonal two-phase reaction, respectively. Further, batch A2 shows a third distinct peak at about 3.5 V, which becomes even broader for batch B. Also batch A1 shows a small peak at about 3.5 V, also less distinct. This peak, in the following denoted by X, does not correspond to a typical LMO behavior. However, taking the development of the cell into account, the peak arises most likely from a small amount of another positive electrode material besides pure LMO. Other similar studies showed that this peak seems to be less distinct than the peaks I and II. For example,

[70] record the discharge ICA of a LMO cell at 1 C and report no distinct third peak at voltages lower than 3.8 V. This is also sustained by the results in [125] where two main peaks are described in a pure NMC cell. The peak in the C/25 charge curve at 3.60 V was accounted to the stage transition in the NMC positive electrode and the smaller one at 3.47 V to the graphite stage. In a study by [87] three peaks at about 4.1 V, 3.9 V and 3.65 V are observed in a commercial LMO cell. The peaks occur at higher voltages since a C/3 charge is used to determine the ICA. They demonstrated that these three peaks are also visible in half-cell tests against Li metal. Thus, they concluded that the positive electrode is not composed of pure LMO, but probably of a mixture of LMO and small amounts of LCO. As the manufacturer of the examined LMO cell experimented with NMC, the third peak can be accounted to the negative electrode for batch A1 and A2, but also to an increase in the NMC content of the LMO cell, especially for batch B.

The characteristic position of the peaks is, for example, described in [70], where a comparison of a LMO, NMC, NCA, and LFP study is provided. These characteristic peaks were also examined in [64] for a LMO-NMC cell. They reported that 5 negative electrode phase transformations occur, which, in combination with 2 LMO specific and 2 NMC specific transitions, lead to the characteristic peaks. They indicated that LMO induced peaks occur at 4.1 V and 3.9 V and one NMC induced peak an be identified at about 3.5 V, respectively. Likewise, [248] examined a commercial 2.15 Ah 18650 NMC-LMO cell and evaluated the ICA at 0.04 C. They accounted the peaks at 4.04 V and 3.90 V to the peaks resulting from a intercalation of Li-ions into LMO combined with a plateau of NMC and deintercalation of the negative electrode. The two dominant peaks at a lower voltage of 3.60 V and 3.45 V result from Li intercalation into NMC combined with the transformation of the negative electrode structure from stage II to stage I (LiC_{12} to LiC_6). Results of the ICA for cell batch B indicate that peak X might be separated into two peaks at approximately 3.49 V and 3.55 V. These reports match the observed voltage characteristics well with the observed peaks I and II for LMO and X for NMC.

Phase transitions result in peaks in the ICA or valleys in DVA. These limit the three phase regions corresponding to I, II, and X. The phase transition at approximately 3.75 V for batch B can be accounted to a change in NMC as reported by [64]. The second transition at approximately 3.9 V for batch B describes the transition between the two LMO phase equilibria. These two dominant phase transitions and their shift over the different batches are marked by a red + and o, respectively. A shift of these transitions might indicate changes in the material, in this context especially of the positive electrode. For example, the DVA reveals the amount of capacity which can be accounted to a distinct phase. Likewise, a ICA shows the voltage span of a distinct phase. Whereas less than 10% of the cell's total capacity can be accounted to NMC for batch A2 (and less than 5% for A1), NMC makes about 30% for batch B. This leads to the assumption that the positive electrode of batch B consists to 1/3 of NMC and 2/3 of LMO.

The 0.2 C DVA and ICA were only evaluated at the beginning and end of the tests. In between cycling, checkup tests were conducted with 1 C discharge and charge to assess the cell's capacity. These tests can also be used to evaluate 1 C the DVA and ICA characteristics. Fig. 3.15 (a) and (b) visualizes the differences between a DVA and ICA recorded at a 0.1 C, 0.2 C and 1 C discharge using cell batch B. The curves were recorded at the end of test (EOT) and not at the beginning but are shown here as a reference. Fig. 3.15 (c) and (d) furthermore shows the differences between a DVA and ICA recorded at a 0.2 C and 1 C discharge for cell batch A2 at the BOL. No 0.1 C discharge characteristic was

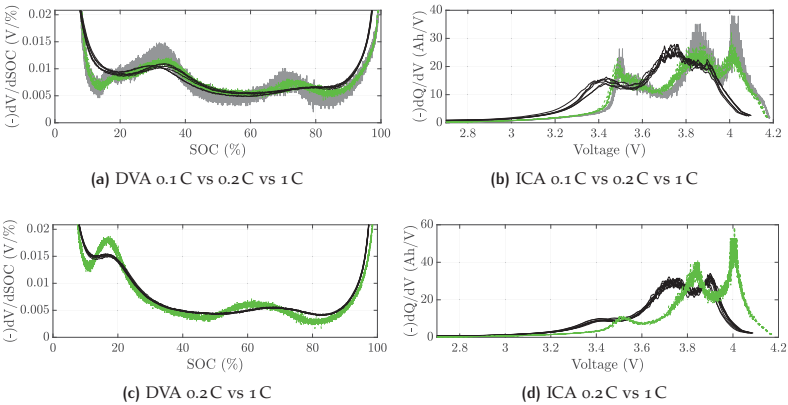

(a) DVA 0.1 C vs 0.2 C vs 1 C

(b) ICA 0.1 C vs 0.2 C vs 1 C

(c) DVA 0.2 C vs 1 C

(d) ICA 0.2 C vs 1 C

Figure 3.15: DVA (a,c) and ICA (b,d) obtained at different DCRs. (a) shows the differences in the DVA of a 0.1 C (grey), 0.2 C (green dashed) and 1 C discharge (black) for batch B at EOT and (b) the same for an ICA. Likewise, DVA (c) and ICA (d) at BOT of batch A2 are shown for 0.2 C (green dashed) and 1 C (black).

evaluated for this batch at the BOL. In both cases, the DVA and ICA are not normalized to the maximum capacity q_0 to show differences in the cells' total capacities.

Similar characteristic peaks and valleys appear for 0.1 C, 0.2 C and 1 C. Whereas 0.1 C and 0.2 C show almost no differences, the 1 C curve differs mostly in the amplitude and sharpness of the peaks and valleys. A voltage offset appears in the ICA whereas the start and end point of the SOC characteristic (DVA) is mostly independent of the discharge rate. This voltage offset can be accounted to the ohmic resistance of the cell. According to Ohm's law, the larger the current, the larger the voltage loss over a resistor. As a result, the curves recorded at 0.1 C and 0.2 C show an initial offset of about 0.09 V to the one recorded at 1 C. Besides a series resistance, the electrical representation of a cell comprises several RC-elements as introduced in section 3.1.2.4. These result in an additional voltage difference of about 0.2 V. In total, the peaks obtained by a 0.1/0.2 C and 1 C lie approximately 0.12 V apart. Lower peak amplitudes and a more smoothed curve can be explained likewise as intercalation processes occur faster and stage formation within the electrodes is less dominant.

As a next step, Fig. 3.16 provides an overview of the 1 C DVA (c) and ICA (d) of the three cell batches A1 (black), A2 (green) and B (grey). Cells 3, 4, 5, and 6 of batch A1 are displayed as dashed black lines as they show a lower peak at approximately 3.4 V. These cells were used for some initial tests and a lower peak might indicate that they are already slightly pre-aged. Although 0.2 C characteristics display phase transitions and equilibria sharper, 1 C characteristics can be used to identify the general behavior of the three dominant peaks in the ICA. 1 C discharge curves show that the peak X at about 3.4 V becomes more elevated for batch B as already seen for the 0.2 C curves. The large voltage offset of the ICA of batch A1 can be explained by the larger resistance of the initial cell batch and the measurement procedure. Initially, capacity was determined by

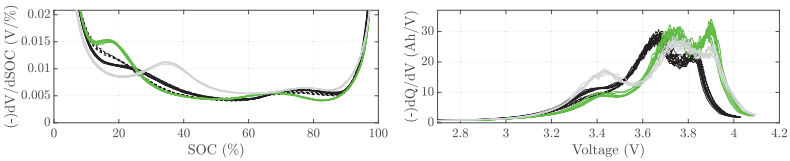

(a) DVA 1 C **(b)** ICA 1 C

Figure 3.16: DVA (a) and ICA (b) of batch A1 (black), A2 (light green) and B (light grey) for a 1 C discharge. Cells 3, 4, 5, and 6 of batch A1 are displayed as dashed black lines.

a single 1 C discharge and charge. Later tests repeated this procedure 3 times and used the second discharge for evaluation. The cell shows a slightly lower resistance after the first full charge as the cell is evaluated in operation and has less time to settle. 1 C and 0.2 C discharge curves are used in section 3.3.3 to describe aging effects.

3.3.1.4 Influence of cell clamping

The cell manufacturer reported that the cells show a significantly longer lifetime when being put under pressure by clamping. Besides reducing negative effects due to expansion during aging, the clamping device leads to an improved heat convection. This can be seen in Fig. 3.17, where one cell with clamping device and one without were cycled with 1 C charge and 2 C discharge. Temperature sensors were attached to both cells at the same position. The clamping devices provide a larger surface for heat convection leading to a lower surface temperature of the clamped cell. After about 3200 s, the temperature sensors got lose and the test was shortly stopped. Therefore, the current is zero for a short time and the temperature drops abruptly. The temperature sensors were not calibrated. Therefore, the ambient and cell temperature differ at the beginning. The clamped cell shows an increase of about 5 °C during cycling meanwhile the temperature for the cell without clamping varies by 10 to 15 °C. In total, both the reduction of expansion and temperature might result in the significantly higher lifetime when being clamped. All described cell tests were done in a clamped state. This resembles the real application, as cells are connected in series and parallel to form modules and in the end a battery setup. The module and battery housing typically affix the cells and provide a clamped setup.

3.3.2 Capacity and resistance changes

Fig. 3.18 provides an overview of the test campaign results for calendar aging displayed over storage time in days. Likewise, results for different cycling scenarios are displayed in Fig. 3.19, 3.20, and 3.21 over equivalent full cycles (efc). Efcs are used instead of time or cycles as a cell cycled with only 20% DOD performs much more cycles in the same time than a cell with 100% DOD. Cell cycles are converted to efcs based on the charge throughput. In this case, one full cycle corresponds to a charge throughput of 2 times 12 Ah. Remaining capacity is presented on the left and resistance on the right. For a clearer comparison of different scenarios, capacity and resistance are displayed in % to the initial value. Cells were stored at 25°C if not specified otherwise. Scenarios with more than one cell are combined to get an average capacity loss and resistance increase.

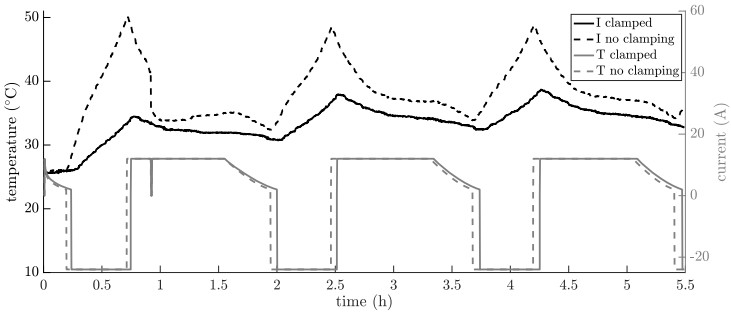

Figure 3.17: Temperature differences for clamped and unclamped cells.

A combined consideration is helpful to identify influences of DOD, SOC, and CR. Furthermore, cell-to-cell variances can be filtered out. Single cell results can be found in Appendix B.1.1. Every combined scenario is presented by its mean and standard deviation. Values for standard deviation have to be taken with care, especially for scenarios where only 2 cells or less were recorded. In these cases, the value does not describe a large enough sample to be reliable. Still, standard deviation is provided as a measure of cell-to-cell variations within this scenario.

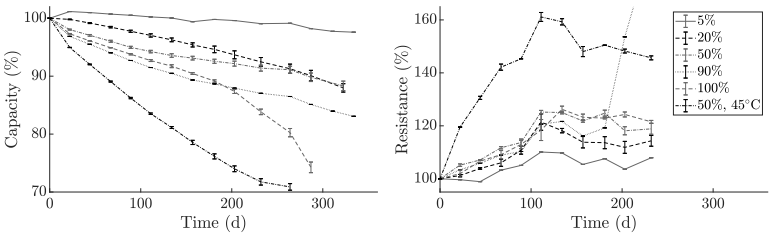

Figure 3.18: Overview of calendar cell aging results for capacity (left) and resistance (right).

Calendar aging

An increase in capacity loss with an increase in storage SOC and temperature is clearly visible in Fig. 3.18. Cell 25 with a storage SOC of 5% shows a small capacity loss of 2% over the 340 days of storage at open circuit conditions. Further, a small capacity increase is observed at the beginning. Cells tested at 20% (18&22) and 50% (20&21) show a larger capacity loss. Initially, the 20% SOC cells age slower than the 50% cell. However, after about 250 days, both cells show a similar capacity loss. After 340 days about 88.3% of the initial capacity remain. The cell stored at 90% SOC loses about 17% of its initial capacity after 340 days. The cells stored at 100% SOC show a similar aging behavior at the beginning. However, after about 180 days of storage, the cell capacity starts to decrease increasingly. The cells lose 30% of their initial capacity within 310 days. A rapid capacity decrease might indicate lithium plating, which occurs especially at high SOC and for overcharging. In general, capacity loss increases the higher the SOC.

A similar trend can also be seen for resistance increase. Resistance increases over storage

duration. However, after an initial linear increase, the resistance seems to settle at a constant value. Only the cell stored at 90% SOC shows a rapid increase in resistance after 200 days. No similar capacity changes are detected. One possible reason might be a contact loss of the clamps of the test equipment.

Besides SOC also temperature seems to have a strong influence on capacity loss. The cells stored at 50% SOC and 45°C lose 30% of their initial capacity after 270 days whereas the cells stored at the same SOC and 25°C lose only about 10%. Similar results can also be seen for resistance increase where the cell stored at 45° shows a 3 times higher resistance increase. Generally, cells tested under the same storage condition showed a similar trend. It can therefore be assumed that the cell behavior is representative for the examined cell type. Section 3.5 provides a deeper analysis of the aging effects and introduces an empirical relation representing the influence of SOC and temperature on calendar aging.

Cycle aging

Influences on capacity and resistance are less distinct for cycle aging. Effects are accounted to average SOC, DOD, charge/discharge rate (CR/DCR), and temperature. Cycle aging results are separated into different scenarios to identify relationships. Fig. 3.19 analyzes the influence of different average SOCs if the DOD is kept constant. The influence of different DODs at 50% average SOC as well as various full charge scenarios with different DODs are presented in Fig. 3.20. Further, Fig. 3.21 shows the influence of different charge and discharge rates.

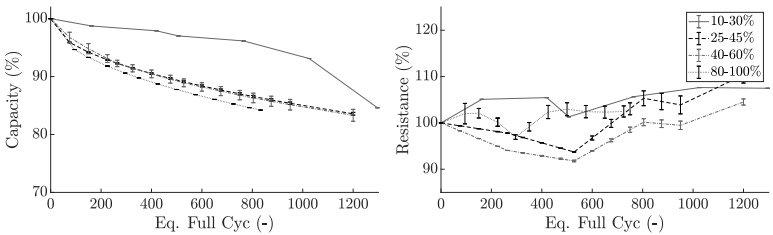

(a) 20% DOD and various average SOC, 1C/1C, 25°C, combined

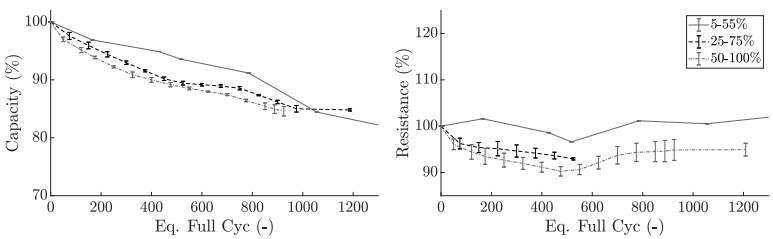

(b) 50% DOD and various average SOC, 1C/1C, 25°C, combined

Figure 3.19: Overview of cycle cell aging results for capacity (left) and resistance (right) for constant DOD at different SOCs.

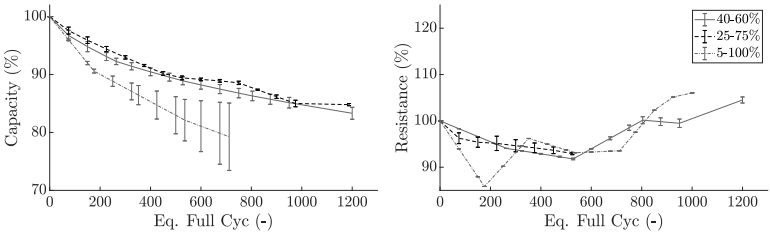

(a) 50% average SOC and various DODs, 1C/1C, 25°C, combined

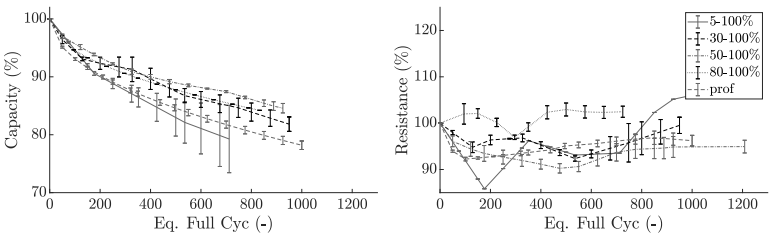

(b) X-100% full charge at different DODs, 1C/1C, 25°C, combined

Figure 3.20: Overview of cycle cell aging results for capacity and resistance for constant average SOC and full charge. The cells labeled by "prof" were tested with a discharge profile (average DCR 0.5 C) instead of a constant DCR but were also cycled between 5-100%.

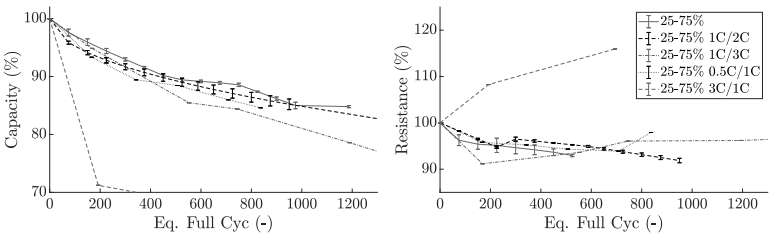

Figure 3.21: Overview of cycle cell aging results for capacity and resistance for different charge and discharge rates (25-75% with various CR/DCR, 25°C).

In general, a typical square root-like capacity loss is observed. Only cells cycled at very low SOC and DOD (for example 10-30% and 5-55%) show a slightly different trend. Cells 17 and 12 show an untypical high capacity loss which could be later recognized as cell failure. The cells showed electrolyte leakage. They are therefore neglected in the further evaluation but included in the calculation of standard deviation. This results in the large error bars for the 5-100% scenario. The other cells showed only small deviations with resistance values differing more than capacity. Fig 3.19 (a) shows the results for 20% DOD. Likewise, 50% DOD is shown in Fig 3.19 (b). The results indicate that a larger

average SOC leads to a larger capacity loss over equivalent full cycles. This corresponds with the observations from calendar aging. A full charge scenario (95% DOD) shows larger capacity loss compared to smaller DOD as seen in Fig. 3.20 (a) and (b). However, this trend does not seem to be linear over DOD. Higher discharge rates have only a small influence on capacity fade. Fig. 3.21 indicates that a high charge rate, on the other hand, leads to a rapid loss in capacity.

Resistance changes show a larger variation. One reason is the low internal resistance of the cells and therefore the lower resolution of the measurement equipment. On the other hand, the connection to and the clamps of the test equipment add up to the total resistance. Slight changes in the physical connection and cables might influence the resistance measurement. However, this issue is also seen in other cell tests published. In general, most cells show an initial resistance drop. Resistance increases only after about 500 equivalent full cycles. Fig 3.19 (a) and (b) indicate that the initial resistance drop decreases the lower the average SOC. Fig 3.21 suggests that a high charge rate enhances resistance increase. However, resistance changes remain rather small compared to capacity variations.

Although cycle aging is presented over equivalent full cycles, aging also propagates over time. Therefore, a distinction between calendar (storage) and "pure" cycle aging effects might provide further insight. This is especially important if mixed storage and cycling scenarios have to be evaluated. One example is a daily routine of an EV or E2W driver, which should be optimized in chapter 4. Assuming that storage effects appear likewise during cycling, a separation of cycle aging results into a calendar aging and pure cycle aging part is possible. Influencing factors of calendar aging are storage SOC or voltage, temperature, and time. It is assumed that the storage SOC can be represented by the average SOC during cycling. Observations described before can be used to set up an empirical calendar aging estimate. The model equations are stated here but not derived. A detailed description of the derivation of such an calendar aging model is provided in the modeling part in section 3.5.2. Assume that Eq. (3.12) can be used to describe the square root-like capacity decrease over time t.

$$C_{cal} = 1 - 1.2448 \cdot 10^5 \, (V - 3.166) \, \exp\left(\frac{44152.3}{R_{gas} \cdot T}\right) t^{0.75} \tag{3.12}$$

The aging equation predicts a linear increase of aging over voltage V and an Arrhenius-like temperature T influence, which has been described before. At the beginning, each cell has 100% of its initial capacity resulting in a value of 1 for C_{cal}. Likewise, 0.8 stands for 80% of the initial capacity. Temperature has to be entered in Kelvin with the gas constant R_{gas} being $8.314 \frac{J}{molK}$. Likewise, resistance can be recalculated based on calendar aging. However, as resistance changes show no clear tendency during cycling, only capacity is further evaluated.

Results of the calculated capacity for a pure cycle aging scenario are displayed in Fig. 3.22. In contrast to the other cell tests, cyclization between 10% to 30% and 5% to 55% shows initially only a small capacity decrease or even a slight increase. However, after about 800 equivalent full cycles, capacity seems to drop in a non-square root like manner. Thus, low SOC scenarios may need special treatment as already seen during the calendar aging tests.
Various average SOC levels are compared in Fig. 3.22 (a) and (b) at a constant DOD of 20% and 50%, respectively. The cells cyclized at 25%-45% and 40%-60% show almost

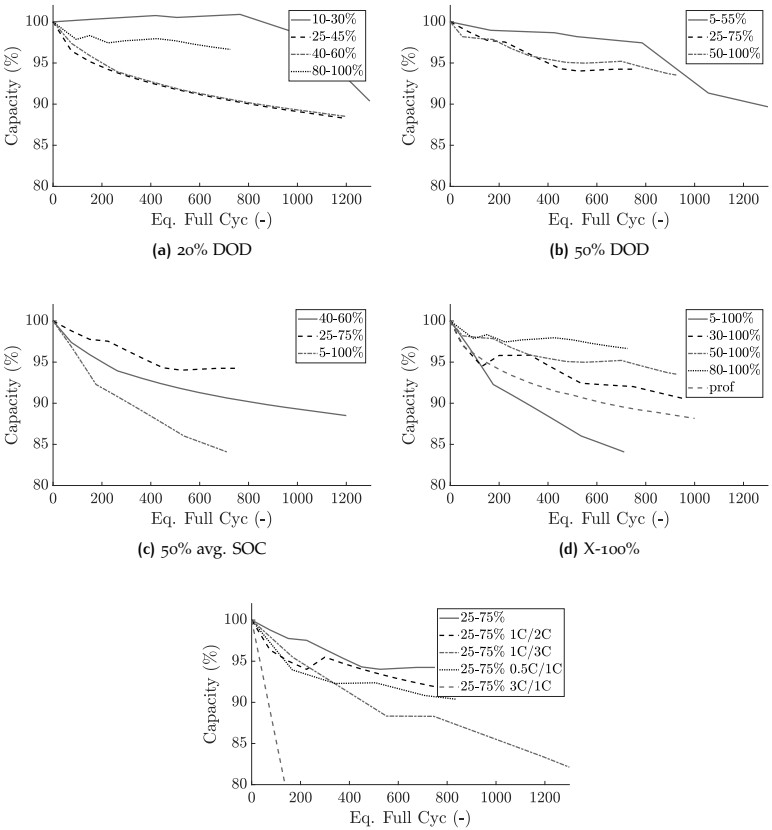

(a) 20% DOD

(b) 50% DOD

(c) 50% avg. SOC

(d) X-100%

(e) 25-75% various CR/DCR

Figure 3.22: Pure cycle aging results for capacity.

the same capacity loss, whereas the cell cyclized between 80% and 100% shows a significantly lower capacity loss. This effect can only be partially observed for the 25-75% and 50-100% cycling scenarios. Fig. 3.22 (c) further shows that capacity loss does not continuously decrease with lower DOD, as expected. The cell cyclized with a DOD of 50% (25%-75%) exhibits only a capacity loss of 5.5% after 800 efc, but the 20% DOD scenario (40%-60%) loses almost twice as much (9.5%). 95% DOD cycling, on the other hand, leads to a capacity loss of approximately 17%. Further, cells cycled around 50% SOC show a similar or even higher capacity decrease than cells with a higher average SOC. This might either show that more complex processes occur during cycling or be a result from the inaccurate calendar aging estimation. However, capacity decreases significantly with lower DOD for a full charge scenario as shown in Fig. 3.22 (d). As a

result, average SOC and DOD might not act independently from each other on capacity loss.
Fig. 3.22 (e) indicates that a higher discharge rate leads to larger capacity loss. Further, exceeding the supplier defined maximum charge rate leads to a significant capacity loss. Lower charge rates than 1 C influence aging less. In this case, even a larger capacity loss was observed for 0.5 C charging than 1 C charging. However, as only one cell was measured for each of these CRs/DCRs and cell-to-cell variations might occur, results are less conclusive. In addition to the otherwise constant current discharge scenarios, also the realistic discharge profile with 5-100% cycling is displayed and denoted by *prof* in Fig. 3.22 (d). In average, the profile showed a DCR of 0.5 C. A lower capacity loss compared to a 5-100% cycling with constant DCR of 1 C is observed.

In short, results for calendar aging show that

- aging increases the higher the SOC and the higher the temperature,
- a temperature increase from 25°C to 45°C has a stronger influence on aging than SOC variation,
- capacity loss follows a square root-like to linear behavior, resistance increases at first linearly and slows down after about 180 days.

Cycle aging increases as a combination of growing average SOC and DOD, as well as with growing CR. Distinct aging influences are harder to identify. A separation of capacity and resistance measurements for cycle aging into a calendar aging and pure cycle aging part can be done for analysis and shows that

- cells cycled at low average SOCs show a slightly different aging propagation over efc (not square root-like but with an initial capacity increase),
- a relatively low average SOC is beneficial for reducing capacity loss but leads to a larger resistance increase,
- capacity loss does not increase linearly with average SOC but shows that both very low and high average SOC lead to a higher cycle life than cycling around 50% SOC,
- a full charge shows the largest capacity loss,
- the lower the DOD of a full charge scenario the lower the capacity loss,
- high CRs (>1) are more critical than high DCRs,
- and a lower CR than 1 is also not beneficial which might be due to enhanced calendar aging effects.

3.3.3 Differential voltage analysis

Capacity and resistance changes provide a first insight into cell degradation. However, results provide only a limited insight into occurring aging mechanisms as they describe the cell as a whole. Cell disassembly and half-cell measurements can be used to get a detailed overview of the cell decomposition. However, they can only be used at the end of lifetime. Furthermore, EIS can be used to correlate resistance increase to specific aging mechanisms. As an AC current or voltage is required, EIS is often only used in laboratory tests. Differential voltage measurements such as DVA and ICA has been

used as a simple yet effective means of identifying aging mechanisms during lifetime and without harming the cell [29, 30, 32, 64, 65, 229, 248].

Detailed results of the initial characterization of the tested LMO cells were already provided in section 3.3.1.3. In addition, this section aims at correlating the ICA lifetime characteristics to cell degradation processes. The influence of different SOC and DOD ranges is evaluated. Calendar aging is not examined. Notes on the effect of calendar aging are, for example, provided in [109, 122, 248]. Analysis results are shown for a 0.1C, 0.2C, and 1C discharge. Likewise, charge characteristics were recorded. As they show similar results as the discharge curves, these are not discussed in this study.

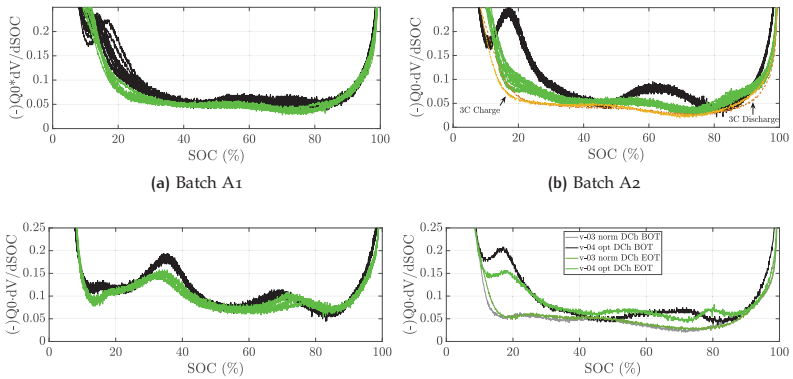

(a) Batch A1 **(b)** Batch A2

(c) Batch B **(d)** Cell v-03 (A1) & v-04 (A2)

Figure 3.23: Comparison of DVA at BOT (black) and EOT (green) for a 0.2 C discharge.

A general overview of the DVA for a 0.2 C discharge at BOT and EOT are presented in Fig. 3.23. The figure displays results separated by cell batch A1 (a), A2 (b), B (c), and cells 3 and 4 of batch B (d), which originally belonged to other batches. In general, all curves are smoothed over time and cycling. Peaks and valleys become less distinct. This effect is especially seen for cells of batch A1 and A2. Batch B shows a lower decrease of the peaks and valleys as the validation tests require less equivalent full cycles and the cells are less stressed. Cell *v*-04 shows similar characteristics to batch A2 and cell *v*-03 is already pre-aged with an initial capacity of about 9.5 Ah (of 12 Ah). Latter shows almost no changes in the DVA indicating that phases become less distinct. An analysis of the validation tests of batch B is provided in section 4.4 as the results can be used to describe the optimization outcome.

ICA can be used to identify the influence of different DOD, SOC, and CR. Four main observations are reported in literature [10, 25, 65, 86, 122, 229]: simultaneous decrease of all peaks, decrease of a specific peak, voltage shift of the peaks, and new peaks arising. These can be correlated to the three main degradation modes: LLI, LAM of the positive electrode, and LAM of the negative electrode. LLI arises due to parasitic reactions such as the formation of an SEI layer or lithium plating. LAM at the positive electrode occurs due to structural changes, cracking and loss of active material such as manganese dissolution (for LMO). Likewise, cracking, stage changes, and contact loss

lead to LAM at the negative electrode (graphite). LAM might cause a decrease of all peaks as the cell structure is damaged and side reactions such as manganese dissolution occur. If a blended positive electrode is used, LAM might occur only for one of the blended materials (e.g. LMO or NMC) and thus lead only to a decrease of a single peak. The decrease of a single peak might also result from changed kinetics or (in the lower voltage area) LLI and a corresponding shift of the negative and positive electrode potential. Resistance changes, or more accurately impedance changes, within the cell lead to a shift of the peaks' positions. The appearance of new peaks can indicate that the positive and negative electrode show different loss rates and thus new interactions between peaks of these electrodes arise. Most effects are correlated to changes in the positive electrode. For example, [219] concluded that only small changes occur in the negative electrode and most changes of the ICA can be accounted to structural changes in the positive electrode. A large influence of the negative electrode potential is mostly reported for LFP positive electrodes, which exhibit a flat voltage characteristic [10, 122].

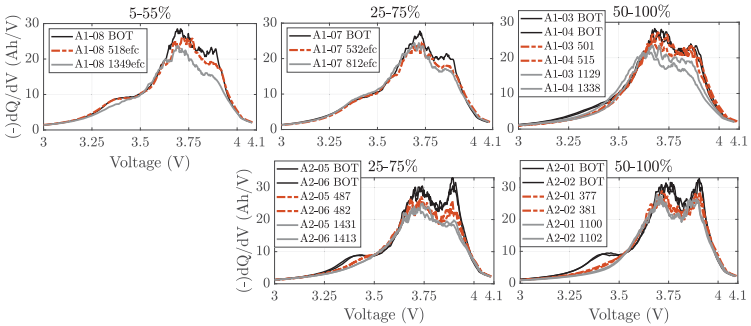

Figure 3.24: ICA with 50% DOD and various SOC for cells of batch A1 (top) and A2 (bottom).

The influence of these effects on the ICA is examined for different cycling scenarios. Characteristics are at first examined for cells cycled at various SOC but with a 50% DOD. Results for a 1 C discharge ICA are presented in Fig. 3.24. Since the ICA of cells cyclized at the same scenario correlate closely, only one cell per scenario is shown. Detailed ICA curves for all cells can be found in Appendix B.2. The evolution of the ICA over cycling is described by efcs. As checkup tests were conducted based on a fixed time and not charge throughput interval, efcs do not exactly match. The same colors are used for measurements with a similar efc. Fig. 3.24 displays results for 5-55% (left), 25-75% (middle) and 50-100% (right). The upper plots show results for batch A1 and the lower plots for A2.

All curves show that peak I lies initially at approximately 3.9 V, peak II at 3.7 V, and peak X at 3.35 V to 3.4 V. Peak X is less distinct for batch A1 as discussed before. Peaks are slightly shifted to the left over efc indicating that the cell impedance increases. Overall, peaks I, II, and X decrease for all scenarios. However, peak I decreases faster than peak II. Only cycling between 50 and 100% for batch A2 shows that peak I and II decrease likewise and slower. This effect is not clearly observable for 50-100% cycling of batch A1 as peak I is already initially less distinct for all cells of batch I. On the other hand, peak X decreases faster for high average SOC than low SOC and is already barely

visible after 500 cycles for 50-100% cycling. Results indicate that peaks in the ICA, which correspond to phase transitions, are longer maintained if they are regularly crossed during cycling. The area under the ICA curves corresponds to the total cell capacity. The total cell capacity can then be divided into the amount of capacity being stored in single peaks. The peaks correspond to specific structures or phases being present in the positive and negative electrode. For example, the area under peak X can be correlated to the amount of Li-ions stored in the NMC part of the positive electrode. If peak X vanishes, either the NMC content of the electrode has significantly decreased (LAM) or less Li-ions are present (LLI) which are already bound by the LMO content (peaks I and II).

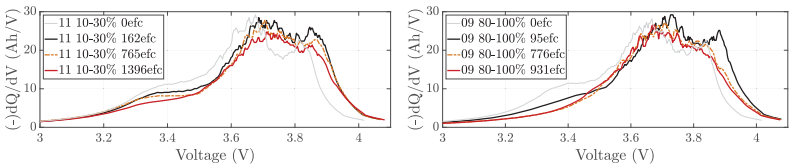

(a) 10-30% **(b)** 80-100%

Figure 3.25: ICA with 20% DOD: low SOC cycling vs high.

The decrease of peak X is further evaluated for 20% DOD at low SOC (10-30%) and high SOC (80-100%). Fig. 3.25 (a) and (b) visualize the ICA obtained by a 1 C discharge. It is clearly visible that cycling from 80-100% leads to a rapid decrease of peak X. Within the first 100 efc, it decreases by half. A similar decrease is only observed after 1300 efc for cycling between 10% and 30%. In contrast to Fig. 3.24, peak I decreases similarly for 10-30% and 80-100%. A shift in peak I to the left can be accounted to an increase in impedance after approximately 780 efc for 80-100% and 1300 efc for 10-30%.

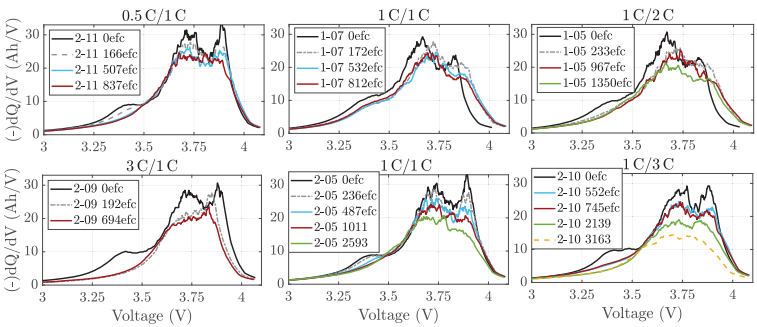

Figure 3.26: ICA with 25-75% and different CR/DCRs.

The influence of charge and discharge rates (CR/DCR) for cycling in between 25% and 75% is examined in Fig. 3.26. A 1 C charge and discharge is used as a reference and displayed in the middle. The left plots show a variation of charge rates and the right ones a variation of discharge rates. Almost no differences are visible between 1 C/1 C

cycling and higher discharge rates (1 C/2 C and 1 C/3 C) after about 800 to 1000 efc (red curves). This indicates that higher discharge rates do lead to altered aging processes. Likewise, a lower charging current of 0.5 C seems to have no impact on the ICA. On the other hand, a higher charging current of 3 C leads to a drastic decrease in and flattening of peak II while peak I decreases slower and remains visible as a distinct peak. In addition, cell impedance increases leading to a significant shift of peak I already after 192 efc. Peak X vanishes at the same time. This indicates that not only LAM occurs but kinetics change and LLI occurs which might not only result in a growth of the SEI layer but also lithium plating.

The above observations can be summarized.

- Peak X at about 3.35 V remains visible for cycling at low SOC (e.g. 10-30% and 5-55%). These scenarios show also a significantly lower capacity loss.
- The larger capacity can be accounted to the larger area under peak X (NMC-related) but also to a larger area correlated to peak I and II (LMO).
- It might therefore be beneficial to cycle at low SOC areas to preserve the advantage of the additional NMC phase.
- Cycling at 25-75% with 1 C/1 C preserves peak X, although to a lesser extent, as well (yellow (a), dark blue (b)).
- Higher discharge rates (2 C dark green (a), 3 C yellow (b)) do not add significant stress to the cell and behave similar to a 1 C discharge.
- A larger charge rate than defined by the cell manufacturer (3 C, dark red (b)) leads to a significant impedance increase. Furthermore, peak II decreases stronger than peak I. Peak X disappears.
- Scenarios with a high average SOC (50-100%, 80-100%, light blue (a), light green (b)) more accurately preserve peak I than other scenarios but lead to a rapid decrease in peak X.
- Peaks I, II and X decrease for a full cycling scenario (without CV charge phase: 5-90%, light blue (b)) but remain all visible indicating that both the negative and the positive electrode age.
- Cycling with a discharge profile shows similar characteristics as cycling with a constant discharge rate.

However, since the differential voltage tests were done at a relatively high discharge rate of 0.2 C, results are less distinct as described in literature such as [29, 30, 32, 64, 65, 229, 248].
The characteristic behavior of capacity and resistance curves obtained by the aging campaign can now be used to identify and adapt a suitable cell aging model. A simplified electrochemical model, the single particle model, is at first introduced in the next section. An electrical equivalent model is motivated thereafter to reduce model complexity.

3.4 EXTENDED AVERAGE SINGLE PARTICLE MODEL (SPM)

Model-based optimization relies on an accurate representation of relevant processes. However, the formulation and solving process of optimization problems becomes more

complex with increasing modeling depth and accuracy. Often, a trade-off between complexity and accuracy must be made. In this context, a simplified electrochemical model, an SPM, is presented at first. This model covers most of the relevant transportation processes, reaction kinetics, and aging mechanisms. An advantage of this model is that most parameters and variables are directly related to physical cell properties. As a drawback, the SPM – although being already a simplified version of common electrochemical models – needs a good knowledge of the cell internal properties and is quite complex to solve due to its coupled PDEs.

Due to the model complexity, only a few optimization methods can be used. Further, with computation times of about 2.5 min for one day of cycling (compared to less than 10 s for an EEM described in section 3.5), it is impractical to run optimizations, which require many iterations of model simulations in each step. The aim of this section is therefore to briefly introduce the model equations of the SPM, to improve the model such that it can be used for different cell chemistries, to use it for simulations so as to compare the accuracy of the EEM presented in section 3.5, and to motivate and improve the empirical aging equations of the EEM. The argumentation follows the description provided in [186] and [182].

As already mentioned, an SPM not only models the changes in current, voltage and temperature, but also describes internal processes leading to concentration shifts, transport processes and chemical reactions. Therefore, it provides a deeper insight into the cell processes and describes aging effects in more detail than an EEM. However, compared to multiphysics models, an SPM already applies simplifications. For example, the SPM is only a one-dimensional model and the electrodes themselves are assumed to consist of one particle, as shown in Fig. 3.27. Still, an SPM is able to sufficiently represent most of the dominant aging effects. The basic equations for the base, thermal and aging model are introduced as described in [182] and [186]. For a more detailed derivation of the equations it is referred to [175, 176, 199].

The diversity of lithium ion chemistry poses a challenge for electrochemical modeling, since every cell chemistry and every cell type requires intensive parametrization. With a basic electrochemical model, such as an average SPM described in the following sections, fewer parameters need to be identified and computation time is reduced. The basic principle of deriving an SPM from the cell design is illustrated in Fig. 3.27. The structure of such an average SPM is shortly described in the next section.

An extended average SPM as developed by [175] and [176] is introduced and improved to investigate aging effects over a long time horizon with acceptable computational effort. The argumentation follows the descriptions published in [182] and [186]. Fig. 3.27 shows that the average model embeds the porous electrode theory in a reduced model. When single particles are used as electrodes, the solid concentration distribution along the electrodes becomes obsolete and is instead resembled by the material diffusion within a solid particle. Additionally, it is assumed that the Li-ion concentrations $c_{s,n}$ and $c_{s,p}$ within the particles are the mean value of the concentration across the electrode radius r and all cyclable lithium is present in the solid particles. The subscript s stands for the solid particle and e for the electrolyte, n, p and sp for the negative electrode, the positive electrode and the separator, respectively. The variable U is the resulting potential of the electrode concentrations, $I(t)$ and $V(t)$ are the discharge current and battery terminal voltage over time. The kinetic overpotential is represented by $\overline{\eta}^k$. As the SPM is a

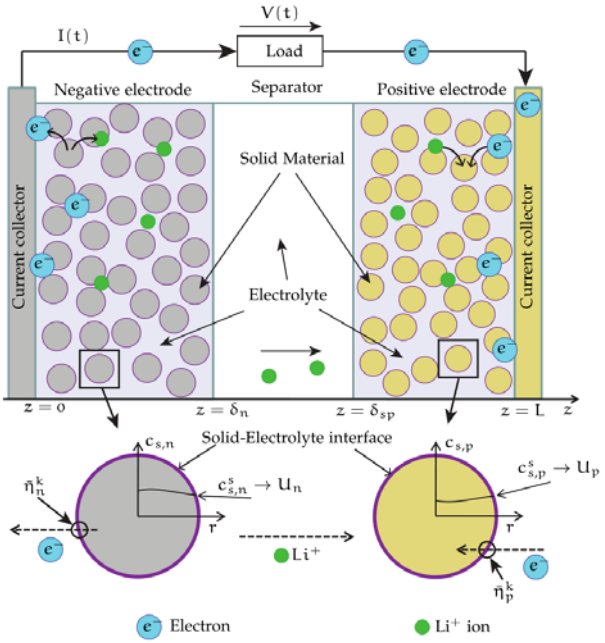

Figure 3.27: Derivation of a single particle model (SPM) [56, 59, 139].

one-dimensional model, the position coordinate is depicted by z, starting from 0 at the negative electrode collector over the negative electrode thickness δ_n and separator δ_{sp} to L. The resulting model has lower accuracy but also lower computation time. The drawback of average assumptions can be partly improved by adding mass conservation in the electrodes and electrolyte, as described in [175, 176]. The resulting model includes the main design parameters of Li-ion models using partial differential equations. The basic model equations are shortly displayed in the following, at first for the base model and then for the aging extension.

3.4.1 Base and thermal model

Basics

In general, processes occurring in a Li-ion cell can be accounted to mass transport processes, kinetics, and thermodynamics. Mass transport processes can be divided into diffusion, migration, and convection. Diffusion is commonly treated as the main effect and the resulting dynamics are therefore often represented by a partial differential equation (PDE). Fick's law of diffusion, which in the one-dimensional case can be written as

$$\frac{\partial}{\partial t} c_j = D_j \frac{\partial^2}{\partial z^2} c_j \,, \tag{3.13}$$

is commonly used as basis. It describes the concentration shift of a substance j over time t and position z using the concentration c and the diffusion coefficient D. In addition, migration effects occur due to electrical interactions between the positive Li-ions and the electrolyte. Thus, a fraction of the total cell current is assumed to be transported by every single Li-ion. This can be described by the transference number t_+. Convection is commonly neglected since its effects are negligible small.

Kinetics and thermodynamics are governed by the chemical reaction processes at the electrodes, within the electrolyte, and at the interphase layer between both. They can be estimated by the Arrhenius law for activation energy (3.14) and the Nernst equation for thermodynamics (3.15).

$$k = \exp\left(-\frac{E_A}{RT}\right) \tag{3.14}$$

$$E_{cell} = E_{cell}^{-} - \frac{RT}{zF}\ln\left(\frac{\alpha_{red}}{\alpha_{ox}}\right) \tag{3.15}$$

The parameter k denotes the reaction rate, E_A the activation energy, R is the gas constant, and F the Faraday constant. These can be converted to the so-called Butler-Volmer equation to combine effects of the current density i_{dB} and kinetic overpotential $\bar{\eta}_j^k$ with j representing the positive (p) or negative (n) electrode.

$$i_{dB} = \alpha_{s,np}\, i_{o,np}\left(\exp\left(\frac{\alpha F}{RT}\bar{\eta}_{np}^{k}\right) - \exp\left(\frac{(1-\alpha)F}{RT}\bar{\eta}_{np}^{k}\right)\right) \tag{3.16}$$

The parameter $\alpha_{s,j}$ is a constant which represents the reaction speed, $i_{o,j}$ presents the initial exchange current density, α the charge transfer coefficient, and T the temperature.

Using the porous electrode theory [61], the model structure is simplified to a coupled one-dimensional problem. In this case, the electrodes are assumed to consist of spherical particles. For the SPM, these spherical particles are further simplified to one representative particle per electrode. Combined with the assumption of homogenous electrochemical reactions within the cell parts, diffusion processes can be separated into diffusion within the electrode particles, which depend on the particle radius r, and diffusion in the electrolyte or more exactly at the interface between electrodes and the electrolyte, where a current density can be defined which resembles the exchange of Li-ions at the interphase.

Model description

In the following, the discharge current I is defined to be positive and the charge current negative. Taking the assumption that all cyclable Li-ions are present in the two particles, the fully charged state results in all Li-ions being present in the negative electrode and vice versa. The radius r dependent *concentration of Li-ions* $c_{s,i}$ *inside these particles* is derived from Fick's law, with $D_{s,i}$ being the diffusion coefficient and subscript i being n or p for negative and positive electrode, respectively.

$$\frac{\partial c_{s,i}}{\partial t} = D_{s,i}\left(\frac{\partial^2 c_{s,i}}{\partial r^2} + \frac{2}{r}\frac{\partial c_{s,i}}{\partial r}\right) \tag{3.17}$$

Subscript s indicates that this process occurs in the solid phase of the electrodes. Likewise, e is used for the electrolyte phase. Further, boundary conditions apply:

$$D_{s,i}\left.\frac{\partial c_{s,i}}{\partial r}\right|_{r=0} = 0, \qquad -D_{s,i}\left.\frac{\partial c_{s,i}}{\partial r}\right|_{r=R_{s,i}} = \nu_i \frac{R_{s,i}}{3\epsilon_{s,i} A \delta_i} I \tag{3.18}$$

The parameter ν_i is 1 for the negative electrode and -1 for the positive electrode. $R_{s,i}$ is the particle radius, A the electrode plate area, $\epsilon_{s,i}$ the active material volume fraction, and δ_i the electrodes' thickness.
By using c_s, the thermodynamic potentials U are derived with the normalized inserted Li-ion concentration θ^s.

$$\theta^s = \frac{c_{s,i}(R_{s,i}, t)}{c_{s,i,max}}. \tag{3.19}$$

The Butler-Volmer equation can be used to determine the kinetic overpotential $\overline{\eta}_i^k$ at each electrode's interface to the electrolyte as a function of the current I.

$$\overline{\eta}_i^k = \frac{R\,T}{\alpha\,F}\,\ln\left(-\frac{\nu_i\,R_{s,i}}{6\epsilon_{s,i}\,t_{0,i}\,A\,\delta_i}\,I + \sqrt{\left(\frac{R_{s,i}}{6\epsilon_{s,i}\,t_{0,i}\,A\,\delta_i}\,I\right)^2 + 1}\right) \tag{3.20}$$

Besides the electrodes' solid phase concentration, also the *Li-ion concentration inside the electrolyte* c_e is defined depending on the diffusion coefficient $D_{e,j}^{eff}$, electrolyte volume fraction $\varepsilon_{e,j}$, location z and current I. The subscript j stands for n, p, and sep for negative and positive electrode and separator, ν_j is 1, 0, and -1 if negative electrode, separator, or positive electrode are evaluated.

$$\frac{\partial \varepsilon_{e,j} c_e}{\partial t} = D_{e,j}^{eff}\frac{\partial^2 c_e}{\partial z^2} + \frac{\nu_j\,(1 + t_+)}{F\,A\,\delta_j}I \tag{3.21}$$

In this case, $\frac{\nu_j}{A\,\delta_j}I$ can be interpreted as the current density, which drives the intercalation process. The concentration is zero at the current collectors as expressed by the boundary conditions (3.22), where L is the total cell length.

$$\left.\frac{\partial c_e}{\partial z}\right|_{z=0} = \left.\frac{\partial c_e}{\partial z}\right|_{z=L} = 0 \tag{3.22}$$

The mass transport overpotential in the electrolyte phase $\phi_e(L) - \phi_e(0)$ can be obtained by the Li-ion concentration at the border of the electrodes $c_e(0)$ and $c_e(L)$. Additionally, when assuming a constant electrolyte concentration along the z axis, the second term represents the ohmic resistance R_{ohm} with area of the electrodes A, thickness of the electrodes and separator δ_n, δ_{sp}, and δ_p, and electrolyte effective conductivity κ_j^{eff}.

$$\phi_e(L) - \phi_e(0) = (1 - t_+)\,\frac{2\,R\,T}{F}\ln\left(\frac{c_e(L)}{c_e(0)}\right) - I\frac{1}{2\,A}\left(\frac{\delta_n}{\kappa_n^{eff}} + 2\,\frac{\delta_{sep}}{\kappa_{sep}^{eff}} + \frac{\delta_p}{\kappa_p^{eff}}\right) \tag{3.23}$$

This distribution is also depicted in Fig. 3.28. Exemplarily, a concentration distribution at the beginning of a discharge process is shown. As a result, the cell ohmic resistance can be derived from (3.23):

$$R_{ohm} = I\frac{1}{2\,A}\left(\frac{\delta_n}{\kappa_n^{eff}} + 2\,\frac{\delta_{sep}}{\kappa_{sep}^{eff}} + \frac{\delta_p}{\kappa_p^{eff}}\right) \tag{3.24}$$

The ionic conductivity κ_j^{eff} is calculated based on the initial ionic conductivity κ_0, the material volume fraction of the filler and solid phase ϵ, and the Bruggman exponent Brugg.

$$\kappa_j^{eff} = \kappa_0\left(1 - \epsilon_{f_j} - \epsilon_{s_j}\right)^{Brugg_j} \tag{3.25}$$

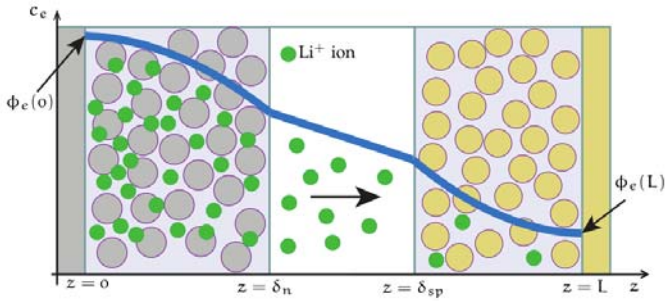

Figure 3.28: Electrolyte concentration distribution within cell at beginning of discharge [56].

In total, the battery terminal voltage consists of the half-cell voltages $U_{p,n}$ of the solid phase diffusion, the kinetic overpotentials $\eta_{p,n}$ and the mass transport overpotential in the electrolyte $\phi_e(L) - \phi_e(0)$ as described in (3.26).

$$V(t) = U_p(\theta_p^s) - U_n(\theta_n^s) + \bar{\eta}_p^k - \bar{\eta}_n^k + \phi_e(L) - \phi_e(0) \tag{3.26}$$

The SOC and capacity C of the cell is evaluated using the normalized bulk Li-ion concentration θ_n^b for the concentrations in a fully charged (100%) and discharged cell (0%).

$$SOC = 100 \left(\frac{\theta_n^b - \theta_{n,0\%}^b}{\theta_{n,100\%}^b - \theta_{n,0\%}^b} \right) \tag{3.27}$$

The capacity of the cell for the electrodes as seen in (3.28) and (3.29) is calculated by the maximum concentration of Li-ions $c_{s,i,max}$ ($i = p, n$), stoichiometric coefficients x and y for negative and positive electrode respectively, as well as active material volume fraction $\epsilon_{s,i}$, electrode plate area A, and Faraday constant F.

$$Q_n = \epsilon_{s,n} F \delta_n A c_{s,n,max} |x_{100\%} - x_{0\%}| \tag{3.28}$$

$$Q_p = \epsilon_{s,p} F \delta_p A c_{s,p,max} |y_{100\%} - y_{0\%}| \tag{3.29}$$

As temperature plays an important role for aging processes, heating and cooling of the cells needs to be evaluated. Using a lumped-parameter thermal model as described in [175], the energy balance

$$\frac{d}{dt} T = \frac{1}{m C_p} (\varphi_{gen} - \varphi_{dis}) \tag{3.30}$$

combines both generated φ_{gen} and dissipated φ_{dis} energy, reversible and irreversible.

$$\varphi_{gen} = -\left((V - (U_p - U_n)) I + T \frac{d(U_p - U_n)}{dT} I \right) \tag{3.31}$$

$$\varphi_{dis} = h_{conv} A_{cell} (T - T_{amb}) \tag{3.32}$$

These basic equations can be used to evaluate both internal T_{int} as well as surface temperature T_{skin}, which depend on the ambient temperature T_{amb} and heat resistances R_{th}.

$$T_{int} = T_{skin} \left(1 + \frac{R_{th,in}}{R_{th,out}} \right) - T_{amb} \frac{R_{th,in}}{R_{th,out}} \tag{3.33}$$

The coupling between electrochemical and thermal model can be expressed by the Arrhenius law as described in (3.34) for all mass transport and kinetic parameters $\psi = (t_i^0, D_{s,i}, D_{e,j}, \kappa, D_{solv})$. For a more detailed description refer to [175].

$$\Psi = \Psi_{ref} \exp\left(\frac{E_a(\Psi)}{R}\left(\frac{1}{T_{ref}} - \frac{1}{T}\right)\right) \tag{3.34}$$

For example, the initial charge transfer exchange density t_i^0 is calculated by:

$$t_i^0 = t_{i,o}^0 \exp\left(\frac{E_{a_{ct,i}}}{R}\left(\frac{1}{T_{ref}} - \frac{1}{T}\right)\right). \tag{3.35}$$

3.4.2 Aging model

As discussed before, the growth of the SEI layer is modeled as dominant aging process. The layer is build up during the initial cycling of the cell and consists of solvent products mixed with Li-ions. During operation, the SEI layer partly blocks the solvents from reaching the negative electrode. As a consequence a reaction with Li-ions from the negative electrode is prevented and less side products form. Latter would add to the layer itself and lead to a resistance increase and capacity fade.

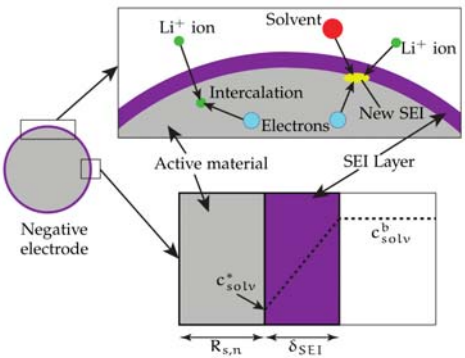

Figure 3.29: Schematic representation of SEI layer and solvent concentration. [56, 173, 176]

3.4.2.1 SEI layer growth

The side reaction can be described by modeling the solvent concentration c_{solv} inside the SEI layer as described in (3.36), which itself depends on the layer thickness δ_{SEI} and the current and temperature dependent diffusion coefficient D_{solv} [199].

$$\frac{\partial c_{solv}}{\partial t} = D_{solv}(I,T)\frac{\partial^2 c_{solv}}{\partial r^2} - \frac{d\delta_{SEI}}{dt}\frac{\partial c_{solv}}{\partial r} \tag{3.36}$$

Boundary conditions specify that the solvent reaches a minimum concentration at the electrode's surface ($r = R_{s,n}$) and remains constant outside the SEI layer.

$$-D_{solv}\frac{\partial c_{solv}}{\partial r}\bigg|_{r=R_{s,n}} + \frac{d\delta_{SEI}}{dt}c^*_{solv} = \frac{i_s}{F}, \qquad c_{solv}|_{r=R_{s,n}+\delta_{SEI}} = \epsilon_{SEI}c^b_{solv} \tag{3.37}$$

This behavior is also illustrated in Fig. 3.29. The solvent concentration at the interface between the electrode and SEI c^*_{solv} plays an important role in cell aging.

This side reaction induces a current i_s (3.38). It is calculated based on a concentration dependent exchange current density i^o_s and an exponential function, which depends on the internal temperature T and potential U. In addition to the Li-ion concentration at the negative particle surface $c^s_{s,n}$, the Faraday constant F and the previous solvent concentration at the surface of the negative electrode c^*_{solv} are introduced. The aging constant k'_f (3.39) accounts for neglected aging effects.

$$i_s = -i^o_s \exp\left(-\frac{E_{a_k}}{R}\left(\frac{1}{T_{int}} - \frac{1}{T_{ref}}\right) - \frac{\beta F}{R\,T_{int}}\left(\phi_{s,n} - \frac{\delta_{SEI}}{\kappa_{SEI}}\frac{I}{S_n} - U_s\right)\right) \tag{3.38}$$

$$i^o_s = 2Fk'_f c^*_{solv}(c^s_{s,n})^2 \tag{3.39}$$

Note that the quadratic choice of $(c^s_{s,n})^2$ depends on observations more than on physical motivation as described in [176]. Other dependencies might occur for a different cell chemistry. For example, LMO cells might show additional aging effects at low SOC due to dissolution of manganese. Therefore, the LMO cell's behavior might be more accurately represented by a function of fourth order as shown in the next section [182].

The SEI layer thickness is evaluated, using its molar mass M_{SEI} and layer density ρ_{SEI}.

$$\frac{d\delta_{SEI}}{dt} = -\frac{M_{SEI}}{2\,F\,\rho_{SEI}} i_s \tag{3.40}$$

The SEI thickness itself influences the ionic conductivity κ^{eff}_n and volume fraction of the electrolyte ϵ_{e_n} in the negative electrode. For example, κ^{eff}_n is extended to:

$$\kappa^{eff}_n = \kappa(\kappa_0, T)\left(1 - \epsilon_{f_n} - \epsilon_{s_n}\left(1 + 3\,\frac{\delta_{SEI}}{R_{s_n}}\right)\right)^{Brugg_n}. \tag{3.41}$$

The remaining capacity C_{rem} (3.42) and resistance increase $R_{s,n} + R_{SEI}$ (3.44) can then be calculated. The variable Q_s describes the capacity loss due to SEI growth, which depends on the negative electrode's thickness δ_n, surface area A, base resistance $R_{s,n}$ and active material volume fraction $\epsilon_{s,n}$. The resistance increase furthermore depends on the SEI ionic conductivity κ_{SEI}. An overview of the solid phase conservation of Li^+ species and model structure is illustrated in Fig. 3.30. The aging equations and their impact on the electrical equations are highlighted in red.

$$\frac{d}{dt}Q_s = \frac{3\,\epsilon_{s,n}\,\delta_n\,A}{R_{s,n}} i_s \tag{3.42}$$

$$C_{rem}(t) = 100\,\frac{Q_n - Q_s(t)}{Q_n} \tag{3.43}$$

$$\frac{dR_{SEI}}{dt} = -\frac{M_{SEI}\,R_{s,n}}{6\,F\,\rho_{SEI}\epsilon_{s,n}\,\delta_n\,A\,\kappa_{SEI}} i_s\,, \tag{3.44}$$

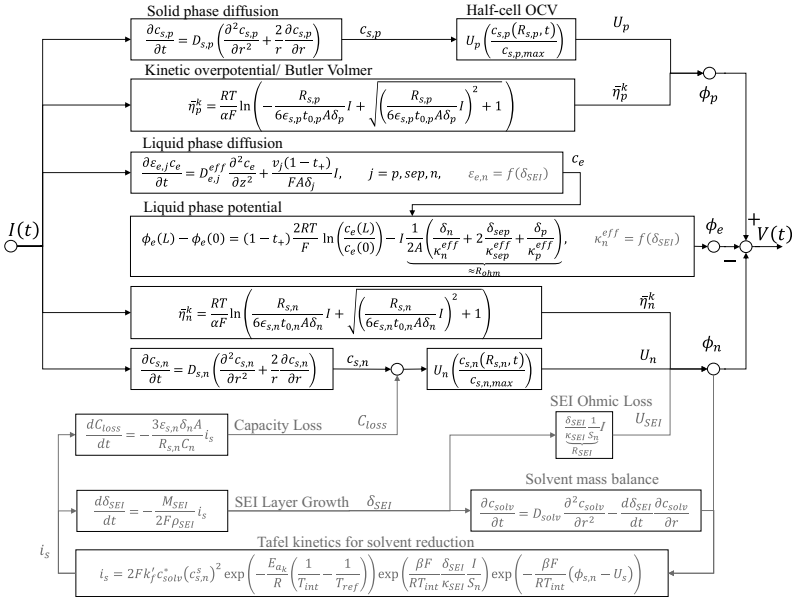

Figure 3.30: Basic electrochemical equations for positive electrode, separator, and negative electrode (top, black) including aging extension for negative electrode (bottom, marked in gray).

3.4.3 Improvements and validation

3.4.3.1 Improvements

The model does not separate between calendar and cycle aging effects. The simplifying assumptions of average electrolyte and solvent concentration infer that different concentration shifts during storage and cycling cannot be represented. Therefore, model adaptions are necessary to improve the model fit for both scenarios. In the case of LMO, Mn^{2+} is dissoluted at low SOC, adding to the formation of side products and SEI growth. This process can either be modeled as another side reaction with Butler-Volmer characteristics based on the electrical charge transfer as described in [130] or by approximation. In this case, Mn^{2+} dissolution related effects are approximated.

The model presented in [176] accounts for a current depending diffusion coefficient increase leading to stronger aging. As described in [91, 200], the diffusion coefficient depends not only on current but also on SOC. In most cases, the influence of SOC is neglected as it only comes into effect at very high or low SOC as depicted in Fig 3.31. Therefore, the SOC dependency is commonly assumed to be constant. Fig 3.31 shows the growth of the diffusion coefficient with increasing current as introduced in [176]. For the given cell chemistry, SEI layer growth is still the dominant aging influence, however, side effects resulting from Mn^{2+} dissolution cannot be ignored. To account for such side

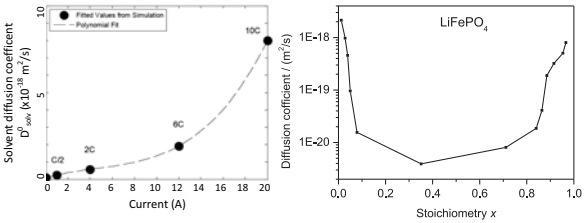

Figure 3.31: Diffusion coefficient depending on current as given in [176] (left), and on stoichiometry (similarly to SOC) as described in [200] and [91] (right).

effects, the model is improved by adding a both current and SOC depending reference diffusion coefficient $D^{o}_{solv}(SOC, I)$.

$$\begin{aligned} D^{o}_{solv}(SOC, I) = D^{o}_{solv,init} &+ p_{12}SOC^2 + p_{11}SOC \\ &+ \left(p_{24}SOC^4 + p_{23}SOC^3 + p_{22}SOC^2 + p_{21}SOC + p_{20}\right)|I| \end{aligned} \tag{3.45}$$

Parameters p_k are empirically determined. Further, temperature effects need to be taken into account. Using an Arrhenius law-like expression as introduced in (3.34) with activation energy of solvent diffusivity $Ea_{D_{solv}}$, the solvent diffusion coefficient becomes

$$D_{solv}(SOC, I, T) = D^{o}_{solv} \exp\left(\frac{Ea_{D_{solv}}}{R}\left(\frac{1}{T_{ref}} - \frac{1}{T_{int}}\right)\right). \tag{3.46}$$

In addition, [176] introduced a quadratic influence of the concentration of lithium at the solid-electrolyte interphase $(c^{s}_{s,n})^2$ on the exchange current density (see (3.39)). As the lithium concentration corresponds to the cell's SOC, this results in a slow aging at low SOC and a quadratic increase with SOC. However, [176] presented only results for different temperatures and charging rates but not different DODs. Although the capacity loss is generally lower the lower the storage SOC, as seen in the calendar aging results, the effect is less dominant for cycle aging. Instead of having the minimum of the quadratic term at 0% SOC, the term is altered to a parabola with the minimum at about 40% SOC. Whereas this is mostly a fit to the given LMO cell, the adaptions are based on modeling the Mn^{2+} dissolution effects. Further, the choice of the influencing factors on the exchange current density i^{o}_{s} is still a research topic and different dependencies have been reported.

For calendar aging, a quadratic influence of $c^{s}_{s,n}$ is observed as described in (3.47) with empirically determined parameters p_k, $k = 0, 1, 2$.

$$i^{o}_{s} = 2\,F\,k_f^{'}\,c^{*}_{solv}\left(p_2\,{c^{s}_{s,n}}^2 + p_1\,c^{s}_{s,n} + p_0\right) \tag{3.47}$$

However, cycle aging effects are more accurately represented by a function of fourth order. One explanation for the different behavior is the dissolution of Mn^{2+} at low SOC and temperatures. An increased aging is observed for cycling as the dissoluted Mn^{2+} increase the side reaction current density. In contrast to calendar aging, where Mn^{2+} might also be dissoluted at low SOC, changes of low and high SOC lead to the faster aging. The resulting current becomes:

$$i^{o}_{s} = 2\,F\,k_f^{'}\,c^{*}_{solv}\left(p_4\,{c^{s}_{s,n}}^4 + p_3\,{c^{s}_{s,n}}^3 + p_2\,{c^{s}_{s,n}}^2 + p_1\,c^{s}_{s,n} + p_0\right). \tag{3.48}$$

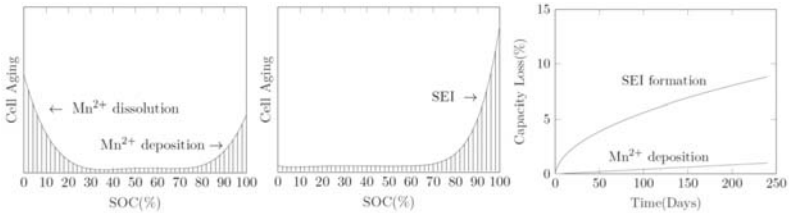

Figure 3.32: Schematic representation of the effective areas of manganese dissolution and deposition (left, middle) as well as the aging effect of SEI formation vs. manganese dissolution (right) as reported by [130].

3.4.3.2 Validation

Although the average SPM together with the lumped parameter thermal and SEI layer growth aging model have been described before, they can be applied to a different cell chemistry without the need of an extensive measurement campaign as well as cell disassembling. An electrochemical model, even if it comes in one of itss simplest forms as an average SPM, requires a lot of parameters to be determined. As many different cell chemistries are available, this would need extensive parametrization of every chemistry itself. Therefore, at first, the LFP model by [175, 176] is used as a basis. Afterwards, a LMO modification is derived from this model. It is evaluated which parameters can be taken directly from the LFP model or literature and how they have to be adapted.

LFP

For system analysis as well as calculation, the partial differential equations describing the concentration in solid phase, electrolyte and SEI layer are most difficult to solve. These result in nonlinear parabolic differential equations with boundary conditions on both sides and variable temperature dependent diffusion coefficients. As the discretized partial differential equations have different time characteristics, they have to be treated as stiff. Furthermore, difficulties arise from changing boundaries due to the SEI layer growth and therefore different layer length δ_{SEI}, leading to a moving boundary. In total, this leads to the need to solve non-linear implicit differential equations with dynamic grid matching. Due to the coupling of i_s and c_{solv} a differential algebraic problem with differentiation index 1 has to be evaluated.

Using the cell parameters given in [175, 176], the model equations are solved. Fig. 3.33 exemplifies the discharge characteristics of the base model for voltage, thermal model for temperature, and aging model for capacity loss. Calendar aging is depicted over time and cycle aging over equivalent full cycles. The average SPM represents the measured behavior well. Larger deviations are observed at low and high SOC together with high current. These result from simplifications used for the SPM. During typical operation the deviation due to such high currents can be neglected. Measured and simulated results for calendar and cycle aging show good accordance.

For evaluation, the root mean square (RMS) error between measurements and model is shortly presented. Table 3.13 lists the results for the presented cases separated by voltage (V), temperature (T) and capacity loss (C) deviations. As the total RMS is only partly comparable, also the RMS error normalized to the measured range nRMS $= \frac{\text{RMS}}{y_{max}-y_{min}}$

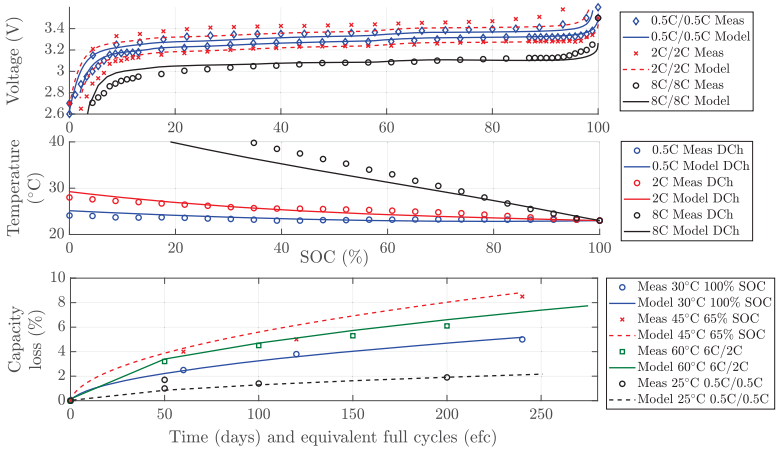

Figure 3.33: Measured (dots) and simulated (line) voltage (top) and temperature (middle) over SOC during discharge and charge. Calendar and cycle aging are shown on the bottom for the LFP cell as given in [175, 176] using the implemented model.

is depicted. Voltage characteristics show a RMS of 0.053 and nRMS of 0.064, temperature 1.295 and 0.263, respectively, as well as the aging deviation using capacity loss as indicator, 0.294 and 0.049. In total, the error for voltage and capacity loss is below 10 %. However, larger deviations occur for temperature (26 %), with charging temperature estimation being the worst (35 %, discharge: 10 %). A more detailed adaption of the simple lumped parameter model, especially the reversible $\frac{dU}{dT}$ characteristic, could improve the error. As such improvements have already been shown in [175, 176], they are not in the focus of this work. By analyzing the sensitivity of the described parameters, the fit can be further improved. However, as not all model parameters and adaptions are described in [175, 176], slightly larger deviations occur, especially when evaluating the temperature curves. Additionally, discharge is more accurately estimated than charge. Model adjustments could improve the fit, but are not shown here.

LMO

One main issue of many electrochemical models is that they are typically designed and adapted to fit one specific cell chemistry and sometimes even only cells from one supplier. However, as shown in the following, an average SPM can be used for a different cell chemistry as well by mainly using easily obtainable current/voltage and temperature measurements. Further, also the aging behavior can be estimated by using a small number of accelerated aging tests. In order to improve the quality of the fit, chemistry specific adaptions can be added. The LMO cell described in 3.2 is used.

The main differences in modeling a LMO and not a LFP cell are due to the different positive electrode materials. To allow a model adaption with only little information, some basic assumptions are made:

Table 3.13: RMSE of average SPM fitted to LFP cell.

	Scenario	RMS_i	$\sum RMS/n$	$nRMS_i$	$\sum nRMS/n$
V	0.5 C Ch	0.052	0.053	0.045	0.064
	2 C Ch	0.068		0.090	
	0.5 C DCh	0.028		0.034	
	2 C DCh	0.050		0.060	
	8 C DCh	0.065		0.092	
T	0.5 C Ch	0.923	1.295	0.515	0.263
	2 C Ch	1.74		0.349	
	0.5 C DCh	0.494		0.214	
	2 C DCh	0.617		0.109	
	8 C DCh	2.700		0.130	
C	30°C 50% cal	0.140	0.294	0.027	0.049
	45°C 65% cal	0.615		0.070	
	25°C 0.5C cyc	0.091		0.048	
	60°C 6C/2C cyc	0.329		0.051	

- The negative electrode of both cell chemistry is graphite and therefore the negative electrode model for LFP and LMO should be very similar. In a first step, the same parameters are used.
- As no information about the used separator and electrolyte is known, these parameters are also assumed to be similar to the LFP cell.
- Although there might be some other aging processes taking place at the negative electrode depending on the electrolyte and positive electrode material, the main aging process is assumed to be the same.

Especially the last assumption is not necessarily true, as LMO cells show additional aging losses due to Mn^{2+} dissolution. These effects are therefore covered by the model improvements discussed in section 3.4.3.

Physical cell parameters for the positive LMO electrode are taken from literature reports for LMO cells [7, 11, 13, 59, 60, 62, 130, 134], where possible, and for separator and negative electrode mainly from the LFP cell [71, 175, 176]. Further, data from other LFP cells [4, 5, 91, 140, 164], NMC-LFP cells [124], and LCO cells [129, 178, 179] is used for comparison. Although various parameter values are available in literature, these vary depending on cell design, exact chemistry, and type, for example high-power or high-energy cells. Tables 3.14, 3.15, and 3.16 provide an overview of some parameters for the base, thermal, and aging model respectively. For a detailed list see Appendix B.3. Parameters are presented for negative electrode, separator, and positive electrode areas. In addition, the data source and how the parameters were determined are marked. For the latter the abbreviations (a)djusted, (e)stimated, (m)easured, parameters obtained by cell (d)esign and no note if data source is unknown are used. If different literature values are available, the used parameter is highlighted.

The tables show that most literature values correlate with each other independent of cell chemistry. Larger deviations occur for cell material and sizing specific parameters such as particle radius and active material volume fraction. These values vary especially for the positive electrode as different materials such as LFP, LMO, and NMC were used.

Table 3.14: Comparison of selected literature values for base and thermal model.

Parameter	Source	Unit	pos. electr.	separator	neg. electr.
			6.2 e^{-5} (e)		
Electrode	[175]		8.0 e^{-5} (m)	**2.5 e^{-5}** (m)	**3.4 e^{-5}** (m)
thickness	[59]	m	3.6 e^{-5}	2.5 e^{-5}	5.0 e^{-5}
δ	[7]		8.0 e^{-5}	2.5 e^{-5}	4.5 e^{-5}
	[11]		3.6 e^{-5} (d)	2.0 e^{-5} (d)	4.3 e^{-5} (d)
	[175]		5.0 e^{-8} (m)		**5.0 e^{-6}** (m)
	[7]		**1.8 e^{-6}**		5.0 e^{-6}
	[124]		3.45 e^{-6} (NMC) (d)		8.5 e^{-7} (d)
Particle	[124]		5.5 e^{-6} (LFP) (d)		8.5 e^{-7} (d)
radius R_s	[129]	m	2.0 e^{-6}		2.0 e^{-6}
	[257]		5.0 e^{-6}		1.0 e^{-7}
	[4, 5]		1.5 e^{-5}		2.64 e^{-4}
	[91]		3.7 e^{-8} (m)		3.58 e^{-6}
			0.538 (e)		**0.624** (e)
	[175]		0.374 (a)	**0.550**	0.580
	[59]		0.500		0.580
Active material	[11]		0.559 (d)		0.566 (d)
volume fraction	[164]	-	0.489 (d)	0.630 (d)	0.645 (d)
ϵ_s	[130, 134]		0.297		0.471
	[4, 5]		0.165		0.797
	[91]		0.330 (m)	0.5 (m)	0.330 (m)
	[178, 179]		0.385		0.485
Solid	[175]		5.9 e^{-17} (a)		**8.0 e^{-12}**
phase Li	[7]	m^2 s^{-1}	2.5 e^{-15}		9.0 e^{-14}
diffusion D_s	[11]		**4.0 e^{-14}** (e)		1.1 e^{-14} (e)
Charge transfer	[175]	J mol^{-1}	**13,000**		**20,000**
activation energy E_{act}	[71]		15,000		15,000
	[91]		41,367 (a)		53,411 (a)

Listed values are (a)djusted, (e)stimated, (m)easured, parameters obtained by cell (d)esign or no note if data source is unknown

Table 3.15: Heat exchange model parameter values.

Parameter	Symbol	Unit	Value
Convective coefficient	h_{conv}	W K^{-1} m^{-2}	10
Heat capacity	C_p	J (kg K)$^{-1}$	1100
Cell lateral surface	A_{cell}	m^2	0.0035
Cell mass	m	kg	0.4

Besides, transport kinetics and reaction rate related parameters such as solid phase Li diffusion, and initial solvent diffusion coefficient show larger variations. Thus, the influence of parameter variations is examined.

Table 3.16: Comparison of relevant aging model literature values.

Parameter	Source	Unit	negative electrode
Initial SEI	[176]	m	**5.0 e^{-9}** (e)
thickness $\delta_{SEI}(0)$	[11]		450 e^{-9}
Solvent bulk	[176]		**4,541**
concentration c^{b}_{solv}	[71]	mol m^{-3}	6,620 (m)
	[130, 199, 257]		4,541
			0.85 e^{-22} calendar aging (a)
Solvent reduction kinetic		m^{7}(s mol)$^{-1}$	**46.75 e^{-22}** cycle aging (a)
constant k'_f	[176]		1.18 e^{-22} calendar aging (a)
	[176]		141.6 e^{-22} cycle aging (a)
SEI layer density ρ_{SEI}	[176]	kg m^{-3}	**1,690**
SEI ionic conductivity	[176]	S m^{-1}	**17.5 e^{-5}** (a)
κ_{SEI}	[11]		2.4 e^{-4}
SEI porosity		%	**1.5** from calendar aging (a)
ϵ_{SEI}	[176]		1.0 from calendar aging (a)
			8.58 e^{-19} from calendar aging (a)
	[176]		8.84 e^{-20} from calendar aging (a)
Solvent diffusion	[11]	m^2 s^{-1}	2.85 e^{-16}
coefficient $D^{o}_{solv,init}$	[71]		2.20 e^{-19} (a)
	[257]		2.00 e^{-18} (a)
	[130]		5.00 e^{-11} (a)
Activation energy of	[176]	J mol^{-1}	**5.55 e^{4}** (e)
solvent diffusivity $E_{a_{Dsolv}}$	[71]		7.59 e^{4} (a)
Activation energy of			**4.5 e^{4}**
side reaction $E_{a_{kf}}$	[176]	J mol^{-1}	6.0 e^{4} (e)
	[75]		4.47 e^{4}

3.4.3.3 Influence of parameter variations

An SPM comprises typically around 100 model parameters. Although some are already pre-defined by cell shape and material as shown in the previous section, still a large number of parameters needs to be adapted and a lot of degrees of freedom exist. An analysis of the model equations aids in this adaption process to reduce complexity. A model is typically more sensitive towards some parameters and others influence the outcome less. It is, therefore, useful to analyze parameter variations. Such a parameter variation analysis can either be done based by analyzing the system itself or be conducted by varying parameters in a specific range such as described in [71].

The evaluation criteria are defined at first. In this case a good aging representation of the model is desired. Parameter variations over voltage, current, and temperature have already been shown in [71]. In this study, capacity loss is used as evaluation criteria since an accurate aging prediction is desired. Parameters are slightly varied around their initial value to record their influence on capacity loss. Therefore, simulations were performed with the initial parameter set marked in bold in Appendix B.3. In the following simulations, individual parameters were varied by $\pm 10\%$ around their initial value.

The original capacity loss without any parameter variation was then compared to the capacity loss of each single parameter variation. The mean of the positive and negative 10% variations was used to assess the influence of a variation of this parameter.

Further, the parameter variation analysis is separated into a calendar and cycle scenario. This is useful as different processes might be dominant during storage and cycling. Therefore, all parameters were varied by $\pm 10\,\%$ and changes on calendar aging over 180 days of storage at 50 % SOC and cycle aging for 10 full cycles with a 1 C charge and 2 C discharge were recorded.

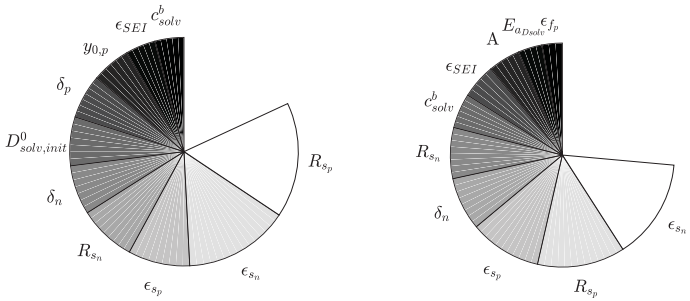

(a) 180 days of storage **(b)** 10 full cycles

Figure 3.34: 10 most dominant parameters on (a) calendar and (b) cycle aging.

The results are displayed in Fig. 3.34 (a) for calendar and (b) for cycle aging. The particle radius of the positive R_{s_p} and the negative R_{s_n} electrode, the active material volume fraction ϵ_{s_p} and ϵ_{s_p}, and the electrode thickness δ_n are the most dominant parameters for both calendar and cycle aging. This contrasts with the expectation that aging parameters would influence the aging behavior most. This is reasonable as the particle radius and the active material volume fraction are central cell properties and responsible for the kinetic overpotential. Further, a larger particle radius leads to a larger reaction surface. Likewise, a change in the active material volume fraction directly influences the cell's capacity. The thickness of the negative electrode correlates also to the capacity loss as seen in (3.42). Calendar aging is further strongly affected by the initial solvent diffusion coefficient $D^o_{solv,init}$. Besides, capacity is sensitive towards stoichiometry $y_{0,p}$, electrode thickness δ_p of the positive electrode, the SEI porosity ϵ_{SEI}, and the solvent bulk concentration c^b_{solv}. In contrast to calendar aging, variations in $D^o_{solv,init}$ are relative unimportant for cycling. During cycling, D_{solv} depends only initially on $D^o_{solv,init}$ as seen in (3.46). Afterwards, current, SOC, and temperature change this parameter. As a result, the model is less sensitive towards $D^o_{solv,init}$ for capacity loss during cycling. At the same time, the activation energy of this solvent diffusion coefficient $E_{a_{Dsolv}}$ becomes more important. The activation energy describes the influence of temperature on the solvent diffusion and indicates that temperature plays an important part during cycling.

Since it is assumed that mainly cell structure and positive electrode parameters change, particle radius, active material volume fraction, and electrode thickness are assumed to

be the most critical factors when adjusting the model to another cell chemistry. Further, initial solvent diffusion, stoichiometry and solvent bulk concentration should be adjusted well for calendar aging. Solvent bulk concentration, SEI porosity and activation energy for solvent diffusion need to be estimated or fitted well for cycle aging.

The physical cell properties were adapted at first based on the sensitivity results. Cell equations (3.28) and (3.29) as well as literature data were used to adapt the cell model to 12 Ah. This results in estimates for the electrode thickness δ_p and electrode plate area A. Similarly, the internal resistance of 3 mΩ can be included. On the basis of resistance information, the exchange current density $i_{o,n}$ and $i_{o,p}$ and the active material volume fraction ϵ_n and ϵ_p could be determined. Further parameters were adapted based on the previous results. If the variation of a parameter had only a small influence on the capacity loss, the literature values of the LFP cell were used. If a strong influence was observed, for example for the radius and active volume fraction of the positive electrode, realistic values for a LMO cell were selected from literature. In the end, the parameters marked in bold in Table 3.14 to 3.16 and Appendix B.3 were obtained.

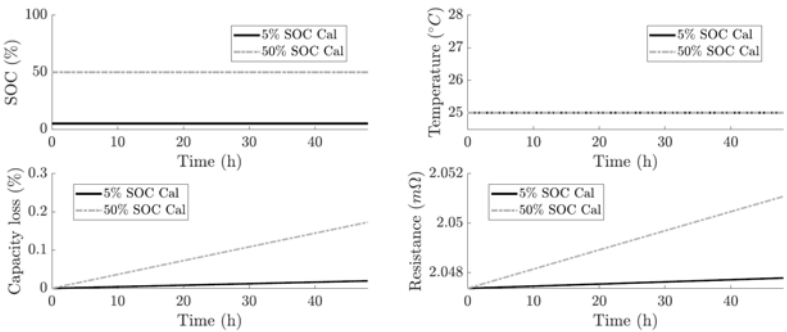

(a) Overview

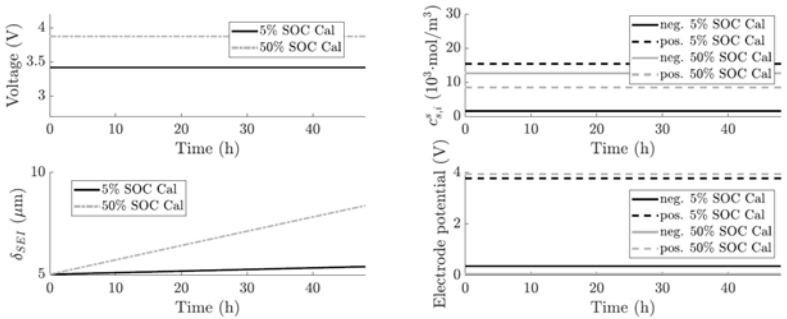

(b) Cell internal parameters

Figure 3.35: SPM results for a calendar aging scenario. (a) overview, (b) cell internal parameters.

Fig. 3.35 (a) compares the simulation results of two calendar aging scenarios. Since no current is applied and the cells' temperature is initialized at the ambient temperature of

25°C, both the SOC and the temperature show almost no variations. The cells exhibit a capacity loss of approximately 0.02% and 0.17% for storage at 5% SOC and 50% SOC, respectively. The capacity loss increases rather linearly than square root-like during these initial 2 days. A similar linear increase in resistance is also predicted. In Fig. 3.35 (b), the cell voltage, the solid phase Li-ion concentration at the particle surface $c^s_{s,i}$ of the negative and positive electrode, the thickness of the SEI layer δ_{SEI}, and the electrodes' potential are displayed. A constant cell voltage is maintained, which corresponds to the SOC. Likewise, no changes in the Li-ion concentration and electrode potentials occur and they remain at their initial value. In contrast to storage at 50% SOC, the Li-ion concentration of the positive electrode is higher than that of the negative electrode for storage at 5% SOC. This reflects the reality since almost no Li-ions are stored in the negative electrode if the cell is discharged and they have migrated to the positive electrode.

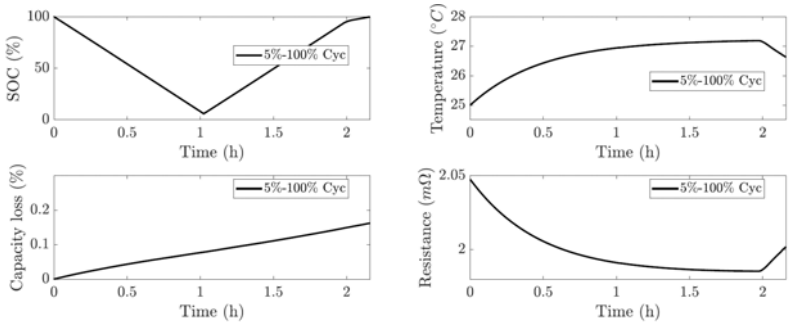

(a) Overview

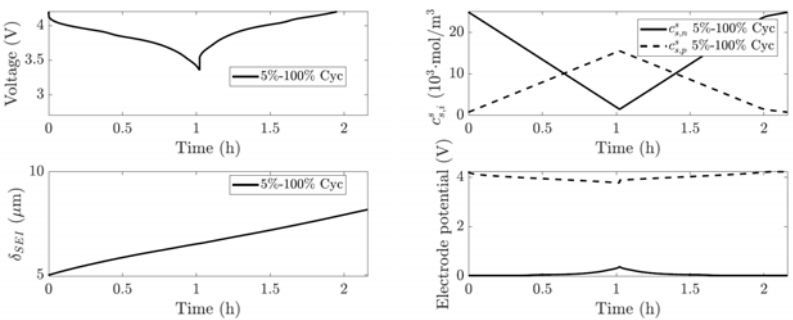

(b) Cell internal parameters

Figure 3.36: SPM results for cycling from 5-100%. (a) overview, (b) cell internal parameters.

If the cells are cycled, as for example shown in Fig. 3.36, further effects can be recognized. The shape of the SOC curve in Fig. 3.36 (a) reflects the cycling between 5% and 100% SOC. The results are presented for one discharge and charge cycle. As a charge and discharge rate of 1 C is used, the cycle takes approximately 2 h to finish. Since a switch from CC to CV charging is required for a full charge, the SOC curve flattens in

the end. During discharging and charging, the cell temperature rises by approximately 2 K. If the current becomes lower, in this case once the CV phase is entered, the temperature decreases again due to cooling effects. The ambient temperature is set to 25°C. Capacity loss increases almost linearly, but in contrast to the storage scenario, aging is amplified during charging. Resistance variations reflect the strong influence of the resistance value on the cell temperature. Thus, resistance drops at first and increases once the temperature decreases. During cycling, the voltage drops from 4.2 V to 3.3 V as displayed in Fig. 3.36 (b) and the characteristic shape can be seen. As already seen before in the calendar aging case, the Li-ion concentrations of the positive electrode increases at first due to the discharge. Afterwards, it increases again to its initial value. The shape of the concentration shifts corresponds to the SOC curve. The thickness of the SEI layer can be matched to the capacity loss since the SPM models this process as main aging cause. The subtraction of the negative electrode potential from the positive potential matches the cell voltage in steady state. During constant charging or discharging, also the mass transport overpotential, electrode overpotential, and ohmic losses need to be taken into account. In summary, the SPM is able to model cell internal effects. A closer comparison to the cell measurements including additional voltage, temperature, and aging characteristics is presented later on in section 3.6, where a comparison of the SPM and EEM model is provided.

3.4.4 From SPM to EEM

Within the class of electrochemical models, SPMs use already some simplifications to reduce model complexity and computation time while maintaining the electrochemical model structure. Various approaches have been presented to further simplify SPMs by converting the PDEs to ODEs. They are based on Pade approximation [141], orthogonal decomposition [40], and many other simplification methods [27, 129]. However, they tend to lose the physical properties of the model parameters. The aim is, therefore, not to simplify the SPM by model approximation methods but to incorporate the model knowledge of the SPM aging relations into the aging model of an EEM. The aging equations of the EEM are developed based on knowledge of electrochemical models but mostly based on aging observations. To fill in the gap between electrochemical motivation and empirical equations, a simplified aging expression is derived based on the presented SPM as published in [186].

Taking a look at the SPM model presented before, the equations can be combined and rearranged to derive a simplified relation. By inserting (3.38) in (3.42) and combining constant terms, the following representation is obtained:

$$\frac{\mathrm{d}}{\mathrm{d}t}C = \frac{1}{Q_n}\frac{\mathrm{d}}{\mathrm{d}t}Q_s = \frac{1}{Q_n}\underbrace{\frac{3\,\epsilon_{s,n}\,\delta_n\,A}{R_{s,n}}}_{=S_n} i_s \tag{3.49}$$

$$\begin{aligned}\frac{\mathrm{d}}{\mathrm{d}t}C = -\frac{S_n}{Q_n}\underbrace{i_s^0 \exp\left(\frac{E_{a_k}}{R}\frac{1}{T_{ref}}\right)}_{=\zeta_2}\cdot\exp\left(-\underbrace{\frac{E_{a_k}}{R}}_{=\zeta_1}\frac{1}{T_{int}}\right)\\ \cdot\exp\left(-\underbrace{\frac{\beta F}{R}}_{=\zeta_3}\frac{1}{T_{int}}\left(\phi_{s,n}-U_s\right)\right)\cdot\exp\left(\frac{\beta F}{R\,T_{int}}\frac{\delta_{SEI}}{\kappa_{SEI}}\frac{I}{S_n}\right)\end{aligned} \tag{3.50}$$

$$\frac{d}{dt}C = -\underbrace{\frac{S_n\,\zeta_2}{Q_n}\,2Fk_f'\left(c^s_{s,n,max}\right)^2}_{=\zeta_4} c^*_{solv}\,(\theta^s_n)^2 \cdot \exp\left(-\frac{\zeta_1}{T_{int}}\right) \cdot \exp\left(-\frac{\zeta_3}{T_{int}}\left(\phi_{s,n}-U_s\right)\right)\cdot\exp\left(\frac{\zeta_3}{T_{int}}\frac{\delta_{SEI}}{\kappa_{SEI}}\frac{I}{S_n}\right) \tag{3.51}$$

$$\frac{d}{dt}C = -\zeta_4\, c^*_{solv}\,(\theta^s_n)^2 \cdot \exp\left(-\frac{1}{T_{int}}\left(\zeta_1+\zeta_3\left(\left(\phi_{s,n}-U_s\right)-\frac{\delta_{SEI}}{\kappa_{SEI}}\frac{I}{S_n}\right)\right)\right). \tag{3.52}$$

In (3.51), the normalized inserted Li ion concentration at the surface $\theta^s_n = c^s_{s,n}/c^s_{s,n,max}$ is introduced. Terms, which are material specific and therefore do not change, are simplified by introducing the constants ζ_j with $j = 1$ to 7.

3.4.4.1 Calendar aging

Assuming pure calendar aging, the equations can be further simplified as $I = 0$, and the concentrations will be in a steady state leading to $c^s_{s,n} = \text{constant}$. Furthermore, temperature changes are neglected, as the internal cell temperature will only change if the ambient temperature is changing (which is not the case in the aging tests conducted for empirical aging evaluation).

$$\frac{d}{dt}C_{cal} = -\zeta_4\, c^*_{solv}\,(\theta^s_n)^2 \exp\left(-\frac{\zeta_1}{T_{int}}\right)\exp\left(-\frac{\zeta_3}{T_{int}}\left(\phi_{s,n}-U_s\right)\right) \tag{3.53}$$

Assuming that only the solvent concentration at the interface between SEI and negative electrode c^*_{solv} is changing during calendar aging, which is true if a constant voltage and temperature is maintained or the changes are negligible small, the total capacity loss due to calendar aging can be reformulated as

$$C_{cal}(t) = C_0 - \zeta_4\left(\theta^s_n\right)^2 \cdot \exp\left(\frac{-\zeta_3}{T_{int}}\left(\phi_{s,n}-U_s\right)\right) \cdot \exp\left(\frac{-\zeta_1}{T_{int}}\right)\cdot\int_{\tau=0}^{t} c^*_{solv}(\tau)\,d\tau \tag{3.54}$$

Determining the solvent concentration at the surface c^*_{solv} remains a main challenge. Furthermore, the partial differential equation (3.36) is hard to solve analytically. Therefore, SPM results are analyzed in order to establish the following relationships. As for example described in [166, 174] and [173], the solvent concentration leads to a square root-like SEI layer growth over time. Although they use some simplifications – [174] assumes a solvent diffusion equation neglecting the direct influence of the SEI layer growth (see (3.36)) – the fundamental assumption of a square root-like layer increase holds. This results from the solvent concentration at the interface between SEI and negative electrode c^*_{solv}. In Fig. 3.37 (a), c^*_{solv} is compared to SEI layer thickness δ_{SEI} and remaining capacity Q_s.

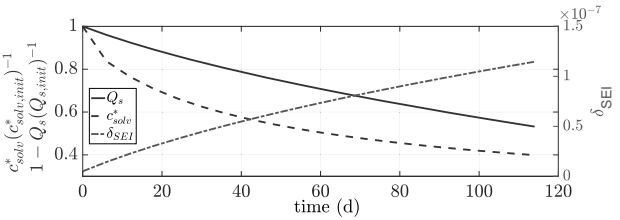

(a)

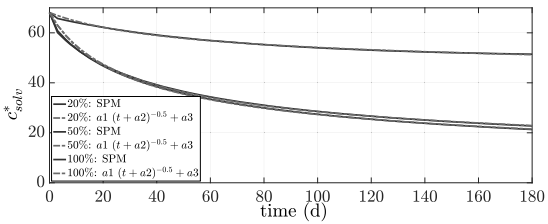

(b)

Figure 3.37: (a) Square root like progress of solvent concentration at the interface between SEI and negative electrode c^*_{solv} normalized to initial concentration at start of calendar aging, SEI layer thickness δ_{SEI} and remaining capacity Q_s normalized to initial capacity taken from the SPM fitted to the LMO cell. Part (b) shows fits of an inverse square root curve for c^*_{solv}.

Changes of δ_{SEI} and Q_s depend on the current of the side reaction i_s as seen in (3.40) and (3.42), and, therefore, on c^*_{solv}. As displayed in Fig. 3.37 (b), c^*_{solv} itself shows an inverse square-root-like behavior, which can be simplified as

$$c^*_{solv}(t) = \zeta_{c_{solv,1}} \frac{1}{\sqrt{t + \zeta_{c_{solv,2}}}} + \zeta_{c_{solv,3}} \tag{3.55}$$

and the integral becomes

$$\int_{\tau=0}^{t} c^*_{solv}(\tau)\, d\tau = 2\, \zeta_{c_{solv,1}} \sqrt{t + \zeta_{c_{solv,2}}} + \zeta_{c_{solv,3}}\, t \tag{3.56}$$

Assuming capacity loss instead of remaining capacity for simplicity ($C_0 = 0$), (3.54) becomes

$$\begin{aligned} C_{loss,cal} = \zeta_4 \exp\left(-\frac{\zeta_1}{T_{int}}\right) (\theta^s_n)^2 \exp\left(-\frac{\zeta_3}{T_{int}} (\phi_{s,n} - U_s)\right) \\ \cdot \left(2\, \zeta_{c_{solv,1}} \sqrt{t + \zeta_{c_{solv,2}}} + \zeta_{c_{solv,3}}\, t\right) . \end{aligned} \tag{3.57}$$

By substituting the constant terms with $\zeta_{c1} = \zeta_4\, 2\, \zeta_{c_{solv,1}}$ and $\zeta_{c2} = \frac{\zeta_{c_{solv,3}}}{2\,\zeta_{c_{solv,1}}}$ and using the series expansion of the exponential function, the capacity loss over time is approximately

$$\begin{aligned} C_{loss,cal} = &-\zeta_{c1}\,(\theta_n^s)^2 \cdot \exp\left(-\frac{\zeta_1}{T_{int}}\right)\ \left(\sqrt{t+\zeta_{c_{solv,2}}} + \zeta_{c2}\, t\right) \\ &\cdot \left(1 + \left(-\frac{\zeta_3}{T_{int}}(\phi_{s,n} - U_s)\right) + \frac{1}{2}\left(-\frac{\zeta_3}{T_{int}}(\phi_{s,n} - U_s)\right)^2 + \cdots\right). \end{aligned} \tag{3.58}$$

The dependency of the normalized Li concentration at the surface of the electrode on the SOC can be shown by including the boundary conditions:

$$\begin{aligned} \theta_n^s &= \frac{c_{s,n}^s}{c_{s,n,max}^s} = \frac{1}{c_{s,n,max}^s}\int \frac{1}{r^2}\frac{\partial}{\partial r}\left(r^2\, D_{s,n}\frac{\partial}{\partial r} c_s\right)\Bigg|_{r=R_{s,n}} dt \\ &= \frac{1}{c_{s,n,max}^s}\int \frac{1}{R_{s,n}^2}\, 2\, R_{s,n}\left(\frac{-I}{F\, A_n}\right) dt \\ &= \frac{-2}{R_{s,n}\, F\, A_n\, c_{s,n,max}^s}\int I\, dt = \frac{-2}{R_{s,n}\, F\, A_n\, c_{s,n,max}^s} Q_c\,. \end{aligned} \tag{3.59}$$

In (3.59), the charge throughput Q_c resembles the SOC of the cell. Furthermore, $\phi_{s,n}$ represents the open circuit voltage of the negative electrode in steady state. Both θ_n^s and $\phi_{s,n}$ attain values between 0 and 1 depending on the SOC and equivalently voltage V. Thus, (3.58) can be rewritten to resemble an empirical relation for an EEM, where only current, voltage, SOC, and temperature measures are available:

$$\begin{aligned} C_{loss,cal,SPM} = &-\zeta_{c1}\,(\theta_n^s)^2 \cdot f(T, (\phi_{s,n} - U_s)) \\ &\cdot \exp\left(-\frac{\zeta_1}{T_{int}}\right) \cdot \left(\sqrt{t+\zeta_{c_{solv,2}}} + \zeta_{c2}\, t\right)\,. \end{aligned} \tag{3.60}$$

If it is assumed that SOC$\hat{=}\theta_n^s$, V$\hat{=}\phi_{s,n}$, and temperature influences on the voltage term are negligibly small, the following simplified SPM–EEM equation holds:

$$C_{loss,cal,SPM-EEM} = -\zeta_{c1}\, f(SOC^2, V)\, \exp\left(-\frac{\zeta_1}{T_{int}}\right) \cdot \left(\sqrt{t} + \zeta_{c2}\, t\right) \tag{3.61}$$

Similarities can be observed by comparing the SPM–EEM equation (3.61) to the EEM calendar aging represented in [28, 205], which is repeated for clarity:

$$C_{loss,cal,EEM} = a_1\,(V + a_2)\exp\left(-\frac{a_3}{T_{int}}\right)\sqrt{t}\,. \tag{3.62}$$

In (3.61) and (3.62) the Arrhenius law is used for temperature modeling. The SPM–EEM shows a more complex dependency on voltage than the linear term for the EEM. However, for small voltage changes, the exponential term can be approximated by its series expansion and a linear expression showing a $(V - U_s)$-dependency is obtained. The derived simplified SPM–EEM equation (3.61) shows not only a square root-like development over time but additionally linear influences. This corresponds well with the SPM predicted aging and the measured capacity loss of the LMO cell (markers) depicted in Fig. 3.38. The original SPM results for 25 °C and 20%, 50%, and 100% SOC are marked as solid lines and the fit based on the derived simplified equation (3.60) as dashed lines. In literature, time dependency is often noted by a term t^{z_t} with $z_t = 0.5$. However, some authors such as [205] reported that $z_t = 0.75$ shows a closer correlation to the measurements. Linear and square root-like time dependency can be approximated by a term with z_t being approx. 0.75, leading to the observed behavior.

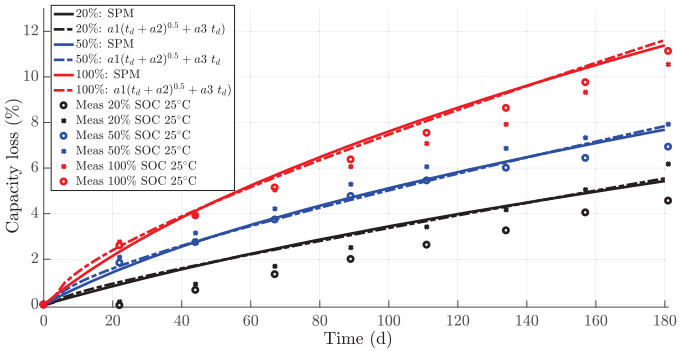

Figure 3.38: Measured capacity loss (markers) versus capacity loss estimated by SPM (line) as well as time-dependent functions fitted to SPM data (dashed) for $T = 25°C$ and $SOC = 20\%$ (black), 50% (blue), and 100% (red).

3.4.4.2 Cycle aging

In case of cycling, I is not 0 and can, therefore, not be neglected. Eq. (3.52) results in

$$\begin{aligned}\frac{d}{dt}C = &-\zeta_4\, c^*_{solv,init}\ (\theta^s_n)^2\, f(T, \phi_{s,n} - U_s) \exp\left(-\frac{\zeta_1}{T_{int}}\right) \\ &\cdot \exp\left(\frac{\zeta_3}{T_{int,avg}} \frac{\delta_{SEI}}{\kappa_{SEI}} \frac{I}{S_n}\right) \left(1 - \frac{\zeta_{csolv}}{c^*_{solv,init}\sqrt{t}}\right)\end{aligned} \tag{3.63}$$

and

$$\begin{aligned}C_{loss,cyc} = \zeta_4\, c^*_{solv,init} &\int (\theta^s_n)^2\, f(T, \phi_{s,n} - U_s) \exp\left(-\frac{\zeta_1}{T_{int}}\right) \\ &\cdot \exp\left(\frac{\zeta_3}{T_{int,avg}} \frac{\delta_{SEI}}{\kappa_{SEI}} \frac{I}{S_n}\right) \left(1 - \frac{\zeta_{csolv}}{c^*_{solv,init}\sqrt{t}}\right) dt\,.\end{aligned} \tag{3.64}$$

Although voltage and temperature varies during cycling, some simplifications can be used if cycling with a constant DOD and average SOC is assumed. In this case, voltage and temperature dependencies are represented by their average ($\theta^s_n(t) = \varnothing\theta^s_n$, $\phi_{s,n}(t) = \varnothing\phi_{s,n}$, $T_{int}(t) = \varnothing T_{int}$), which is reasonable if the same cycle is repeated as in the aging tests. Further, the normalized inserted Li-ion concentration at the surface depends linearly on the charge throughput as derived in (3.59). Therefore, its average can be described by $\varnothing\theta^s_n = 0.5\,(\theta^s_{n,max} - \theta^s_{n,min}) = \zeta_{\theta,n,1}\ DOD + \zeta_{\theta,n,2}$, with DOD being the depth of discharge. Eq. (3.63) can be rewritten as:

$$\begin{aligned}C_{loss,cyc} = &\zeta_4\, c^*_{solv,init} \cdot (\zeta_{\theta,n,1}\ DOD + \zeta_{\theta,n,2})^2 \\ &\cdot f(\varnothing T_{int}, \varnothing\phi_{s,n} - U_s) \cdot \exp\left(-\frac{\zeta_1}{\varnothing T_{int}}\right) \\ &\cdot \int \exp\left(\frac{\zeta_3}{\varnothing T_{int}} \frac{\delta_{SEI}}{\kappa_{SEI}} \frac{I(t)}{S_n}\right) \left(1 - \frac{\zeta_{csolv}}{c^*_{solv,init}\sqrt{t}}\right) dt\end{aligned} \tag{3.65}$$

During constant current discharging and charging with amplitude I_o, the current $I(t)$ switches between I_o and $-I_o$. As the exponential term is strictly monotonically increasing, an upper bound for capacity loss is provided when using $I(t) = I_o$. In this case the capacity loss is

$$\begin{aligned} C_{loss,cyc} \leqslant \zeta_{c1}\, \zeta_{\varnothing\theta,n}^2 \cdot DOD^2 \cdot f(\varnothing T_{int}, \varnothing\phi_{s,n} - U_s) \\ \cdot \exp\left(-\frac{\zeta_1}{\varnothing T_{int}}\right) \cdot \exp\left(\frac{\zeta_3}{\varnothing T_{int}} \frac{\delta_{SEI}}{\kappa_{SEI}} \frac{I_o}{S_n}\right) \\ \cdot \left(t - \zeta_{c2}\sqrt{t}\right) \end{aligned} \tag{3.66}$$

This term can be separated in a quasi-calendar aging and cycle aging part by using the series expansion of the exponential function:

$$\begin{aligned} C_{loss,cyc} \leqslant \zeta_{c1}\, (\zeta_{\theta,n,1}\, DOD + \zeta_{\theta,n,2})^2 \cdot f(\varnothing T_{int}, \varnothing\phi_{s,n} - U_s) \\ \cdot \exp\left(-\frac{\zeta_1}{\varnothing T_{int}}\right) \cdot \left(t - \zeta_{c2}\sqrt{t}\right) \\ + \zeta_{c1}\, \zeta_{\theta,n}^2 \cdot DOD^2 \cdot f(\varnothing T_{int}, \varnothing\phi_{s,n} - U_s) \\ \cdot \exp\left(-\frac{\zeta_1}{\varnothing T_{int}}\right) \cdot \left(t - \zeta_{c2}\sqrt{t}\right) \\ \left(\left(\frac{\zeta_3}{\varnothing T_{int}} \frac{\delta_{SEI}}{\kappa_{SEI}} \frac{I_o}{S_n}\right) + \frac{1}{2}\left(\frac{\zeta_3}{\varnothing T_{int}} \frac{\delta_{SEI}}{\kappa_{SEI}} \frac{I_o}{S_n}\right)^2 + \cdots\right) \end{aligned} \tag{3.67}$$

When neglecting higher order terms of the series expansion, inferences from SPM aging about empirical aging can be drawn.

$$\begin{aligned} C_{loss,cyc} \leqslant \zeta_{c1}\, (\zeta_{\theta,n,1}\, DOD + \zeta_{\theta,n,2})^2 \cdot f(\varnothing T_{int}, \varnothing\phi_{s,n} - U_s) \\ \cdot \exp\left(-\frac{\zeta_1}{\varnothing T_{int}}\right) \cdot \left(t - \zeta_{c2}\sqrt{t}\right) \\ + \zeta_{c1} \cdot (\zeta_{\theta,n,1}\, DOD + \zeta_{\theta,n,2})^2 \cdot f(\varnothing T_{int}, \varnothing\phi_{s,n} - U_s) \\ \cdot \exp\left(-\frac{\zeta_1}{\varnothing T_{int}}\right) \cdot \left(\frac{\zeta_3}{\varnothing T_{int}} \frac{\delta_{SEI}}{\kappa_{SEI}} \frac{1}{S_n}\right) \\ \cdot \underbrace{I_o\, t}_{Q_{Ah}} \left(1 - \zeta_{c2} \frac{1}{\sqrt{t}}\right) \end{aligned} \tag{3.68}$$

After some rearrangement, this leads to

$$\begin{aligned} C_{loss,cyc,SPM} \leqslant \zeta_{c1}\, f\,(DOD + \zeta_{\theta,n,2})^2 \cdot f(\varnothing V - U_s) \\ \cdot \exp\left(-\frac{\zeta_1}{\varnothing T_{int}}\right) \cdot \left(t - \zeta_{c2}\sqrt{t}\right) \\ + \zeta_{c10}\, f\,(DOD + \zeta_{\theta,n,2})^2 \cdot f(\varnothing V - U_s) \\ \cdot \exp\left(-\frac{\zeta_1}{\varnothing T_{int}}\right) \cdot Q_{Ah} \left(1 - \zeta_{c2} \frac{1}{\sqrt{t}}\right), \end{aligned} \tag{3.69}$$

The SPM aging equation (3.69) can be transformed into a simpler SPM–EEM aging equation (3.70) by neglecting the DOD influence on the quasi-calendar aging part and temperature influence on cycle aging.

$$\begin{aligned} C_{loss,cyc,SPM-EEM} = a_1 \left(t + a_2\sqrt{t}\right) \cdot (V + a_3) \\ \cdot \left(\exp\left(\frac{a_4}{T}\right) + I_o \cdot a_5\, (DOD + a_6)^2\right) \end{aligned} \tag{3.70}$$

In (3.70), a_j with $j = 1, 2, .., 6$ are constants, which have to be estimated or fitted according to measurements. Still, the simplifications used to derive this empirical relation are only true for constant cycling situations as conducted during accelerated aging tests. As empirical aging models are also commonly fitted using such accelerated aging tests, (3.70) might be able to represent the aging behavior well.

In the empirical model presented by [205] and adapted to the LMO cell in [184], aging is divided into a calendar and cycle aging part. During storage, aging shows a square root-like time t dependency, which is influenced by the voltage level and temperature during storage. Cycle aging depends on the charge throughput Q, average voltage $\varnothing V$ and depth of discharge DOD. Both, capacity loss C_{loss} and resistance increase R_{inc} are described in [205].

$$C_{loss} = \overbrace{\alpha_c(V,T)\, t^{0.75}}^{\text{calendar}} - \overbrace{\beta_c(\varnothing V, DOD)\, \sqrt{Q}}^{\text{cycle}} \tag{3.71}$$

$$\alpha_c(V,T) = a_1 (V + a_2) \exp\left(\frac{a_3}{T}\right) \tag{3.72}$$

$$\beta_c(\varnothing V, DOD) = b_1 (\varnothing V + b_2)^2 + b_3\, DOD + b_4\,. \tag{3.73}$$

The parameters a_i and b_i with $i = 1, 2, 3, 4$ have to be identified using aging measurements and have no direct physical meaning.

Comparing this to the derived aging relation (3.70) similarities and differences can be observed. In the calendar aging case, I_0 becomes 0 and

$$C_{loss,SPM-EEM} = a_1 \left(V + a_3\right) \cdot \exp\left(\frac{a_4}{T}\right) \left(t + a_2 \sqrt{t}\right) \tag{3.74}$$

Hence, calendar aging depends on the same influencing factors as in (3.72). The only difference is the time dependency. However, as shown before, $t^{0.75}$ and $t + a_2 \sqrt{t}$ lead to a similar relation. When neglecting the calendar aging part to see cycling specific effects, on the other hand, (3.70) becomes

$$C_{loss,SPM-EEM} = a_1 \left(V + a_3\right) \cdot a_5 \left(DOD + a_6\right)^2 \cdot I_0 \cdot \left(t + a_2 \sqrt{t}\right) \tag{3.75}$$

Compared to (3.73), voltage dependency is not quadratic but DOD. And instead of a sum, both factors multiply in the SPM–EEM equation. The term $I_0 \left(t + a_2 \sqrt{t}\right)$ corresponds to the charge throughput Q_{Ah} and shows also both linear and square root dependencies on that factor. In total, the SPM–EEM equations correspond to already derived EEM empirical aging relations, which were mostly proven by fitting the parameters to measurements. This indicates, that such empirical relations do indeed represent the chemical processes occurring, although in a simplified manner. The applicability of the described empirical aging equations to an electrical equivalent model is described in the next section.

3.5 ELECTRICAL EQUIVALENT MODEL (EEM)

A proper battery and aging model builds the central part of the battery cell model. On the one hand, the aging model should be as accurate as possible to represent all relevant degradation processes. On the other hand, with increasing accuracy, overall validity, and

comprehensiveness, the model becomes more complex and the amount of background information and cell data increases. In this context, the previously presented SPM provides a relatively complex yet still calculable lifetime representation of a cell. However, the solving of the partial differential equations together with the algebraic equations requires a suitable solver and computation power and time. In the given case, the simulation model takes approximately 10 min to solve 180 days of pure calendar aging on a standard laptop and even 7h if the cell is cycled. In comparison, an EEM is less complex as cell internal effects are neglected, rebuilt based on observations and basic physical properties, or estimated. If no cell internal properties such as concentration distributions and kinetics are required, it can still be used as a black or, more specifically, grey box model to estimate cell voltage, current, and state of health. The previous section motivated the validity of empirical aging equations as used for EEMs. A description of the model itself is provided in the next sections.
An EEM typically consists of three parts: an electrical equivalent circuit representing current-voltage characteristics, a lumped parameter thermal model, and an empirical aging model. Many different approaches are presented in literature, covering only an electrical and thermal model in most automotive applications or including an aging extension as described in [52, 170, 205, 245]. One possible implementation is described in the following sections.

3.5.1 Base and thermal model

The base electrical equivalent circuit of an EEM typically consists of a voltage source, which represents the OCV of the cell, and at least one series resistance, which resembles the ohmic resistance of the electrodes and electrolyte. The representation of a cell or battery by a single series resistance is often used in overall system descriptions of automotive applications and illustrated in Fig. 3.39 (a). A first extension to model also dynamic voltage losses is to add a parallel connection of a resistor and a capacitor, often labeled as RC element. Such a model consisting of one series resistance and a RC element is often also labeled as a first order Randles circuit [181]. In this case, the RC element represents the double layer capacity of the electrode surface together with the resistance of the electrode reaction. More effects can be represented by adding additional RC elements. For example, Fig. 3.39 (b) displays a second order Randles circuit with two RC elements, which is found accurate enough to represent the studied LMO cell.

Fig. 3.39 (c) extends the electrical circuit by a third RC element to account for the three dominant cell processes as introduced in section 3.3: surface film (SEI) formation, charge transfer & double layer capacitance, and Li-ion diffusion, with time constants increasing from the first to the last process. Furthermore, an inductance is added in series to account for cable and electrode inductances. An even more realistic representation follows the observations obtained by EIS. RC elements lead to a half circle in the imaginary and real impedance plane. However, the half circle is not always ideal with its center at zero in the imaginary axis and might be stretched. Such effects cannot be represented by conventional electrical components such as resistors, capacitors, and inductances. The capacitance of a RC element is, therefore, replaced by a CPE, which is, in combination with a parallel resistance, also labeled as a ZARC element. The third process of Li-ion diffusion and Li accumulation is often also modeled as a single CPE or more accurately a Warburg element, which shows a constant phase of 45°. Refer to section 3.1.2.4 for

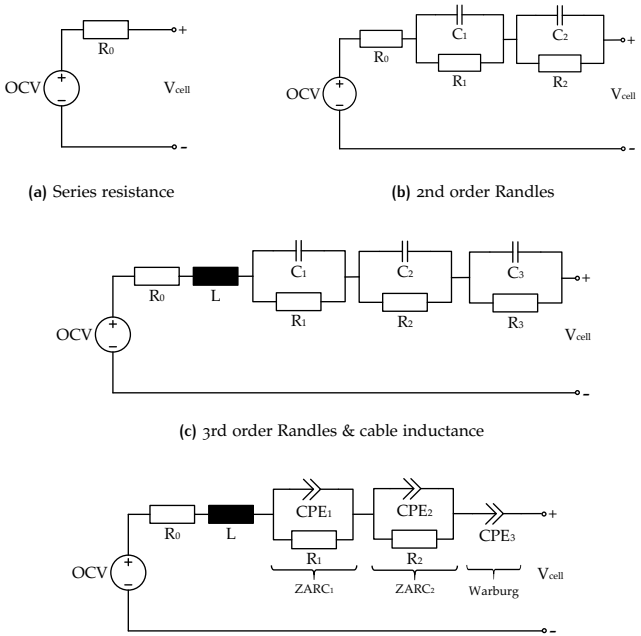

(a) Series resistance

(b) 2nd order Randles

(c) 3rd order Randles & cable inductance

(d) 2nd order ZARC & Warburg

Figure 3.39: Different electrical equivalent circuits used to represent a battery or cell.

a motivation of these elements. Fig. 3.39 (d) displays such an electrical equivalent circuit. In addition, a separation between the electrical circuit of the negative and positive electrode is possible to cover electrode specific effects as described in [219]. On the one hand, each of these expansions of the electric equivalent circuit improve the accuracy of the voltage predictions. On the other hand, they add to the complexity of the model. Whereas the first circuit consisting of a voltage source and series resistance resolves in a purely algebraic equation which is straight forward to solve, adding RC elements leads to ordinary differential equations. As a result, a tradeoff between accuracy and complexity is necessary if algorithms should be implemented online or included into an optimization.

For further analysis, a 2nd order Randles circuit as visualized in Fig. 3.39 (b) is used leading to a resulting cell voltage $V(t)$ of

$$V(t) = V_{OCV} + R_o\, I(t) + V_{RC1}(t) + V_{RC2}(t) \tag{3.76}$$

and

$$\frac{dV_{RCi}(t)}{dt} = -\frac{1}{R_i\, C_i}\, V_{RCi}(t) + \frac{1}{C_i}\, I(t)\,. \tag{3.77}$$

In (3.76) and (3.77), V_{OCV} represents the OCV of the cell, R_0 is the series resistance, R_i, C_i with $i = 1, 2$ resemble the resistance and capacity of the two RC-elements, I is the current applied to the cell, and V_{RCi} is the voltage loss over the RC-elements. SOC is determined using ampere counting starting from an initial SOC_0.

$$SOC(t) = SOC_0 + \int_{t_0}^{t} I(\tau)d\tau \tag{3.78}$$

The lumped parameter thermal approach models resistive losses as cause of heat generation and convection results in heat exchange and cooling. Temperature T changes are induced based on cell mass m, heat capacity c, convective constant h_{conv}, cell area A, and ambient temperature T_{amb}.

$$\frac{d}{dt}T = \frac{1}{mc}\left(|V_{OCV} - V|\, I - h_{conv}\, A\, (T - T_{amb})\right) \tag{3.79}$$

If a uniform heat distribution is assumed, the lumped parameter thermal model can directly be used to describe the cell temperature.
In addition, a skin and internal cell temperature can be defined as shown for the SPM. Reversible effects can also be included. In this case, a single temperature value for the whole cell is used to describe the temperature of the EEM to reduce complexity. The aging model itself as introduced in the next paragraph cannot distinguish between cell internal and skin temperature.

3.5.2 Aging model

Different empirical or physically motivated aging relations have already been described in section 3.1.5. In accordance with aging observations, time t and charge throughput Q are used as main aging factors for calendar and cycle aging respectively. Besides, influences of voltage, SOC, temperature, DOD, and charge rate occur. A model should be developed which is able to represent these influencing factors for the tested LMO cell but can be adapted to other cell chemistries as well. Different empirical model relations are examined at first for pure calendar aging scenarios and then extended to cover also cycling effects. During model development, the model fit is evaluated not only for the tested LMO cell but also for other cell types as reported in literature. As a result, a generalized aging model should be developed and verified.

3.5.2.1 Calendar Aging - Model development & fit

Empirical aging relations can be developed based on measurable properties and model parameters of the base and aging model. In the described case, this limits the aging model to five model outputs: voltage, SOC, current, temperature, and time. Relevant for calendar aging are only voltage and the corresponding SOC, temperature and time as the current remains 0 under open circuit conditions. Therefore, a relation between these measures should be found which describes the capacity loss and resistance increase of Li-ion cells at various conditions with proper accuracy and a relatively low amount of parameters.

Model development for LMO cell
At first, the general tendency of capacity over time is analyzed. Three promising relationships are examined:

$$C_1 = \alpha_t \, t^{0.75}, \tag{3.80}$$

$$C_2 = \alpha_t \, t^{\alpha_z}, \tag{3.81}$$

$$C_3 = \alpha_1 \left(t + \alpha_2 \sqrt{t} \right). \tag{3.82}$$

The first approach assumes the capacity to decrease over time with an exponent of 0.75 and a variable pre-factor α_t as proposed by [205]. In the second case, a similar function is assumed but a second DOF is added by introducing a variable exponent α_z. The third case is motivated by the simplification of the SPM aging description provided in section 3.4.4. Capacity is assumed to decrease partly linear and partly square root-like.

These relationships can then be fitted in a least-squares sense to each of the calendar aging scenarios. The resulting values of the free parameters α are used for further analysis. Results for the first fit function are visualized in Fig. 3.40 (a). The plots draw the capacity of each scenario over time. Markers represent the measured cell capacity. If more than one cell is measured at one scenario, results are averaged into one value. The lines show the estimated capacity loss using the fit function. In general, the model is able to represent most scenarios with only little deviation. Larger deviations occur after about 200 days for a fully charged cell (100% SOC) and for very low SOC of 5% and 20%. Cells stored at very high SOC show a capacity drop after about 200 days which can be accounted to a rapid growth in SEI and additional lithium plating. This transition marks the EOL of the cell. This shows one limitation of empirical relations. They are only valid for a limited area, in this case only for the first stage in aging before the rapid capacity loss occurs. As a result, only the first 200 days of storage were used for determining the parameters of the empirical models. The square root-like capacity decrease seems to be less dominant for very low SOC. As a constant exponent of 0.75 is used, this effect cannot be handled by the model.

Therefore, the exponent is selected as additional DOF in the second fit function. Results are presented in Fig. 3.40 (b). An improvement is clearly visible for low SOCs. The initial slow decrease in capacity can be predicted more accurately by selecting a negative value of the exponent. However, the rapid capacity loss of the cell stored at 100% after 200 days is still not predictable.
Likewise, results of the third fit function, which comprises a linear and square root term with an additional DOF for the pre-factor of the square root term, are shown in Fig. 3.40 (c). Results are almost identical to the previous function. The model performs slightly better at 5% SOC as the initial capacity increase can be represented by a combination of a linear and square root term. In general, all three functions are valid candidates for representing the capacity drop over time with the first requiring only one fit parameter and the remaining two offering two DOFs but also two fit parameters.

So far, the pre-factors α have been determined separately for each individual scenario. In a next step, the behavior of these factors over SOC and temperature is identified to formulate a general relationship. Fig. 3.41 draws the parameter α of the first fit function over voltage (top), SOC (middle) and temperature (bottom). Markers represent the values of α obtained by individual fits for a temperature of 25°C (circle) and 45°C (x). SOC and voltage are no independent variables as SOC is a function of the open circuit

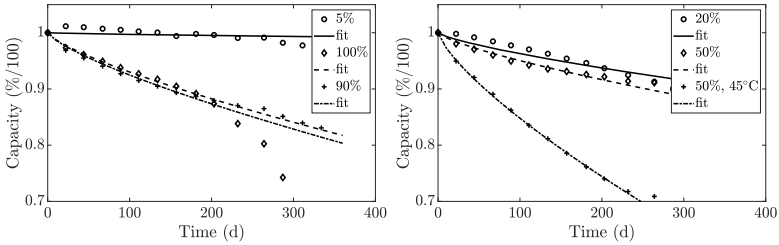

(a) LMO: $\alpha_t\, t^{0.75}$

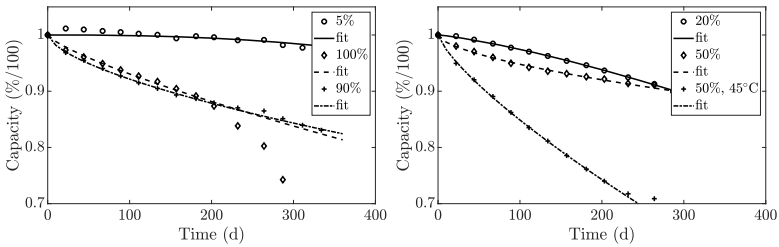

(b) LMO: $\alpha_t\, t^{\alpha_z}$

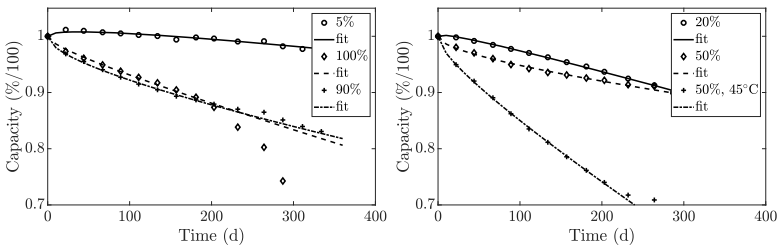

(c) LMO: $\alpha_1\ \left(t + \alpha_2\ \sqrt{t}\right)$

Figure 3.40: Comparison of capacity characteristics for calendar aging using (a) $\alpha_t\, t^{0.75}$, (b) $\alpha_t\, t^{\alpha_z}$, and (c) $\alpha_1\ \left(t + \alpha_2\ \sqrt{t}\right)$ as fit function. Parameters α_t and α_z are adjusted separately for each curve in a least-squares sense.

voltage. Therefore, the same parameter α_V is used to describe them. In addition, α_T is used to highlight a separate dependency of the parameter α on temperature. Aim is to identify relationships of the parameter α on voltage V (or SOC) and temperature T such that the remaining cell capacity (normed to 1) can be written as

$$C(t, V, T) = 1 - \underbrace{\alpha_V(V) \cdot \alpha_T(T)}_{=\alpha} \cdot t^{0.75}\,. \tag{3.83}$$

For the given LMO cell, a linear relationship between capacity loss and voltage seems to be reasonable. Likewise, voltage might be replaced by SOC. An estimate of the linear term is shown in Fig. 3.41 as dashed line. As only two different temperatures were

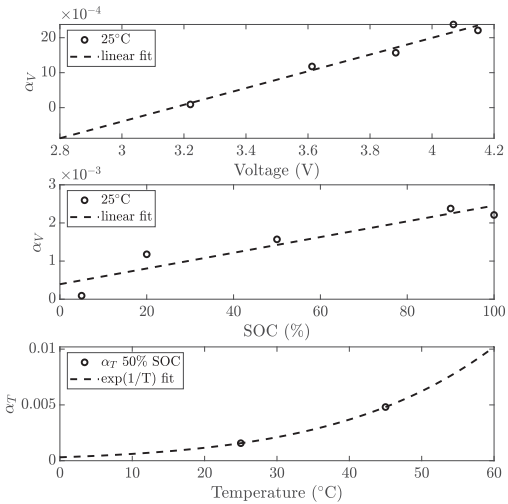

(a) $\alpha(V, T)\, t^{0.75}$

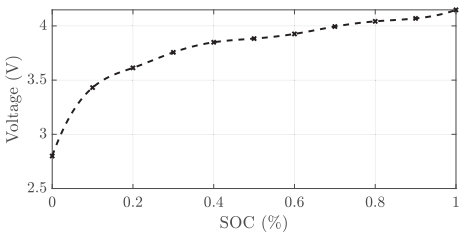

(b) V over SOC

Figure 3.41: (a) Voltage, SOC, and temperature dependencies for α using the fit function $\alpha\, t^{0.75}$. Results for $1 - \alpha_V\, t^{0.75}$ (at same temperature) and $1 - \alpha_T\, t^{0.75}$ (at same SOC) are shown for the LMO cell. (b) shows the relationship between voltage and SOC.

recorded during the test campaign, too little information is available to identify a relationship. However, other researches in literature [52, 68, 205] suggest, that temperature follows an Arrhenius-like tendency which leads to an exponential term, with inverse temperature characteristic. As a result, an exponential fit is added as a dashed line in the bottom plot of Fig. 3.41. In total, the fit function might be written as

$$C(t, V, T) = 1 - (a_{V,1}\,(V + a_{V,2})) \cdot a_{T,1} \cdot \exp\left(\frac{a_{T,2}}{T}\right) \cdot t^{0.75}\,. \tag{3.84}$$

Likewise, the remaining two time-dependencies can be analyzed. As two DOF and, therefore, two pre-factors are available, both need to be analyzed separately. Fig. 3.42 (a)

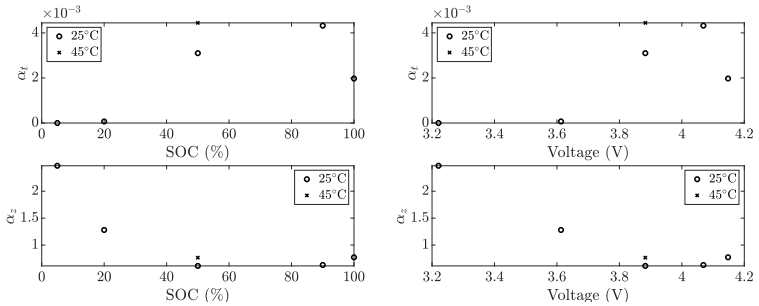

(a) LMO: $\alpha_t\, t^{\alpha_z}$

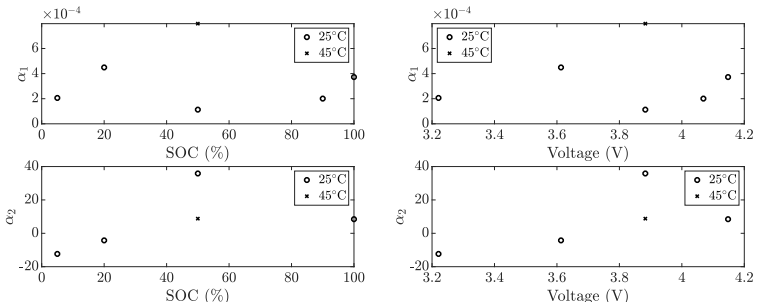

(b) LMO: $\alpha_1\, \left(t + \alpha_2\, \sqrt{t}\right)$

Figure 3.42: Voltage (and SOC) development of the two fit variables using (a) $\alpha_t\, t^{\alpha_z}$ and (b) $\alpha_1\, \left(t + \alpha_2\, \sqrt{t}\right)$ as fit function.

displays the values that α_t and α_z take, once over SOC (left) and voltage (right). Furthermore, results for α_1 and α_2 are depicted in Fig. 3.42 (b). In both cases results are less distinct. Temperature is not separately analyzed as only two different temperatures were analyzed and the exponential Arrhenius-like relationship is well researched. However, the Arrhenius-law only applies for temperatures larger than approximately 5°C and below the critical maximum temperature defined by the manufacturer. At lower temperatures, cell degradation increases due to Li-plating and other side effects. Furthermore, cell materials decompose also at higher temperatures. As the Arrhenius law merely describes the influence of the reaction rate, the rule only applies in the area where the reaction rate is the dominant influence on aging.

In the first case of a $\alpha_t\, t^{\alpha_z}$-relationship, parameter α_z is larger than 1 for low SOC. This implicates that the function increases slowly when the SOC is low, but then increases stronger over time. This is in contrast to the general assumption of a square root-like decrease over time but correlates closer to the recorded cell degradation of the LMO cell. Between 50% and 100% SOC, the exponent results in relatively constant values between 0.5 and 0.8 leading to the classical linear to square root-like behavior. On the other hand, α_t is almost 0 for low SOC and becomes larger with increasing SOC. Merely the value at 100% SOC is lower than for 90%, which can be accounted to the larger value of α_z. However, too little measurements and scenarios are available to draw a distinct conclu-

sion.
For the second case of summing a linear and square root time influence up, no simple relationships between the value of α_1 or α_2 and voltage or SOC can be identified. Too few SOC scenarios could be evaluated to state a well-founded relationship. As the amount of test scenarios is limited, further cell tests reported in literature are used to get a more comprehensive data set and to be able to generalize the empirical relationships to other cells and cell chemistry.

Generalization to different Li-ion cell types
Although more accurate empirical relations can be designed to reduce deviations and increase the overall model fit, this would result in overfitting. However, the aim is to identify a model which is not only valid for this specific LMO cell but also for other Li-ion cell chemistries, power levels, and design and can be easily adapted to these. Thus, a relatively simple model is desired. To show the applicability of the described approaches to other cell chemistries, a comparison with other available cell studies is presented. Data of a NMC cell presented by Ecker et al. [69] and LFP high power cell by Naumann et al. [150, 203] are selected. Both studies show a thorough calendar aging analysis of their cells.

First, fit results are presented using the $\alpha_t\, t^{0.75}$ fit function. Fig. 3.43 (a) and (b) display the measured (markers) and estimated (lines) capacity of the LFP and NMC cell, respectively. In general, the assumed $t^{0.75}$-dependency can also be recognized for a LFP and NMC cell. Whereas the NMC is represented well, the LFP cell shows a more square root-like ($t^{0.5}$) than $t^{0.75}$ capacity decrease for larger SOCs. Still, the overall trend is resembled. In a next step, the development of the fit parameter α is analyzed. In Fig. 3.43 (c), the fit coefficient α is drawn over SOC and voltage (top) as well as temperature (bottom). If the voltage dependency is examined, temperature is kept constant at 25°C (LMO), 50°C (NMC), and 40°C (LFP). Likewise, temperature changes are evaluated at a constant SOC of 50%. Once again, voltage and SOC represent the same DOF and can be converted into each other. Since different cell chemistries with different voltage levels are evaluated, the results are more comparable by examining the SOC dependency. In general, the LFP cell seems to age least for both SOC and temperature due to very low values of α. The NMC cell shows the largest spread of α over SOC indicating that the cell is more sensitive to its SOC level than the LMO and LFP cell. However, as the LMO cell is only recorded at 25°C and the NMC cell at 50°C, the effect might be enhanced by the significantly higher temperature. On the other hand, the LFP cell is measured at a lower temperature than NMC. This indicates that the LFP cell is less influenced by SOC variations. The linear increase of the NMC cell with SOC (marked as dashed line) is valid for lower SOCs than 70%. Larger deviations occur for high SOC. Still, a linear increase in the parameter α over SOC seems to be reasonable for all three cell chemistries. An inverse exponential increase of α over temperature seems also a suitable approximation. In this case, a different sensitivity of the cell chemistries to temperature is clearly visible. Whereas α increases only slightly for the LFP cell, the NMC cell shows a more distinct exponential increase. The LMO cell shows the largest sensitivity to temperature and also the largest overall aging. This correlates well with the general description of cell advantages and disadvantages provided in section 3.1.3.

Two further studies of NMC and LFP cells are used to support the assumptions on differences between cell chemistries. In addition to the evaluated 12 Ah prismatic LMO cell, the 18650 high energy 2.05 Ah NMC cell by Ecker et al. [69], and the 2.85 Ah LFP

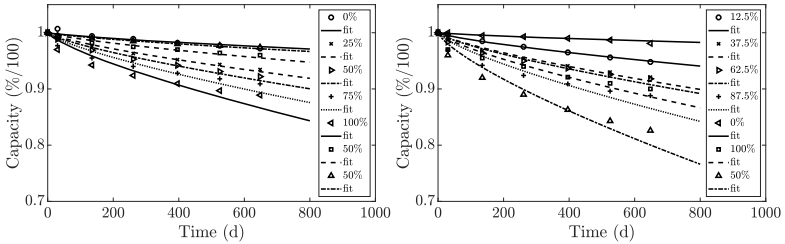

(a) LFP capacity fit

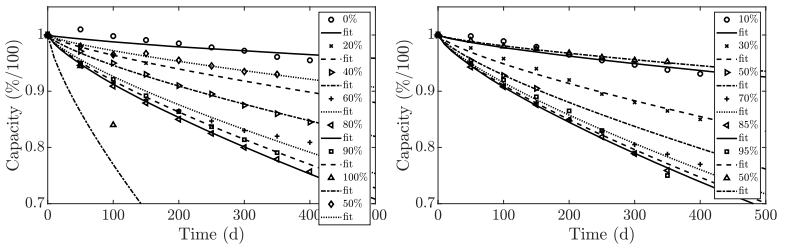

(b) NMC capacity fit

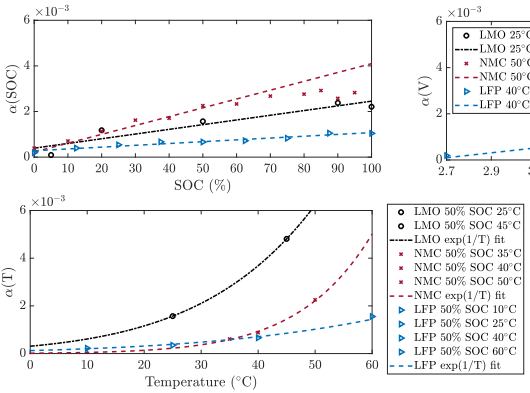

(c) Fit parameters over SOC (left) and voltage (right)

Figure 3.43: Comparison of voltage characteristics for calendar aging using a $\alpha_t\, t^{0.75}$ fit function. Measured capacity is compared to the model fit and results for α_t are shown over SOC, voltage, and temperature. Part (a) shows the fit for LFP cell [150], and (b) for NMC cell [69]. (c) compares the fit coefficients for the LMO, LFP, and NMC cell.

cell by Naumann et al. [150], a 8 Ah cylindrical cell by Lewerenz et al [121] and a 18650 high energy 2.15 Ah NMC cell by Schmitt et al. [207] are fitted using the presented $\alpha\, t^{0.75}$ function. The cells are in short marked as LMO, NMC1, LFP1, LFP2, and NMC2,

respectively. Fig. 3.44 displays the resulting linear SOC (top) and exponential temperature (bottom) dependencies of these cells. The results support the assumption that aging can be described by a $\alpha\, t^{0.75}$ fit function with linear SOC and exponential temperature dependency of the pre-factor α. In general, LFP cells seem to be less susceptible to high temperatures than LMO and NMC cells. However, the cell NMC2 is predicted to age less than cell LFP2 at 60°C. As no measurement of NMC2 at temperatures higher than 45°C is available, this cannot be verified. A comparison of voltage ranges and, therefore, sensitivity of the different cells to voltage or SOC is only possible to a limited extent as the SOC variations were done at different temperatures, e.g. 25°C for LMO and 50°C for NMC1.

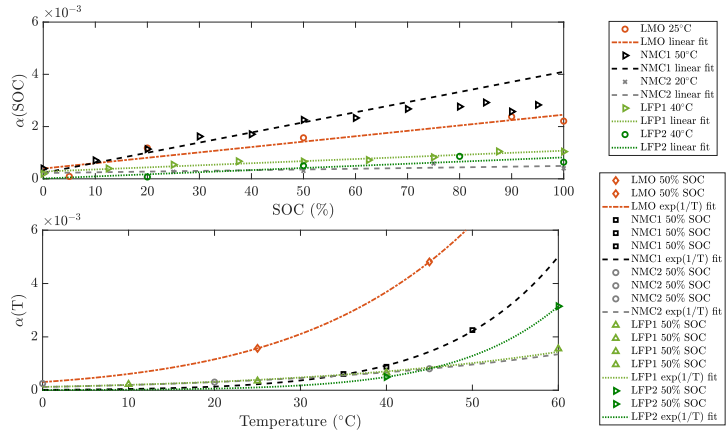

Figure 3.44: Overview of SOC and temperature dependencies of the parameter α for LMO, NMC, and LFP cells for calendar aging using $\alpha\, t^{0.75}$ as fit function.

The dependencies of parameter α on voltage, SOC, and temperature were determined separately based on the following equations.

$$\alpha(V) = a_{V,1} \cdot (V + a_{V,2}) \tag{3.85}$$

$$\alpha(SOC) = a_{SOC,1} \cdot (SOC + a_{SOC,2}) \tag{3.86}$$

$$\alpha(T) = a_{T,1} \cdot \exp\left(\frac{a_{T,2}}{T}\right) \tag{3.87}$$

The parameters a in these formulas are fitted in a least-squares sense. Table 3.17 provides an overview of the fit results. When looking at the SOC dependency, $a_{SOC,1}$ represents the slope of the function $\alpha(SOC)$. The larger the slope the larger the influence of the cell's SOC on aging. However, as the cells are not tested at the same temperature, a larger temperature typically leads also to a larger slope. Parameter $a_{T,2}$ can be interpreted as the negative activation energy of the reaction E_a divided by the gas constant R with $R \approx 8.314$. Temperature is inserted in Kelvin.

As remarked before, voltage and SOC are not independent parameters and can be calculated from each other. Fig. 3.45 provides an overview of the different OCV to SOC

Table 3.17: Resulting fit coefficients and measures to analyze the sensitivity of voltage and temperature on cell chemistry.

Type	$a_{V,1}$	$a_{V,2}$	$a_{SOC,1}$	$a_{SOC,2}$	$a_{T,1}$	$a_{T,2}$
LMO	$2.39\,10^{-3}$	-3.17	$2.06\,10^{-5}$	19.08	$8.53\,10^{4}$	-5310.3
NMC1	$5.01\,10^{-3}$	-3.32	$3.87\,10^{-5}$	5.79	$1.47\,10^{9}$	-8796.1
NMC2	$3.26\,10^{-4}$	-2.65	$2.71\,10^{-6}$	81.82	$7.37\,10^{1}$	-3634.1
LFP1	$1.07\,10^{-3}$	-2.61	$7.97\,10^{-6}$	34.93	$5.30\,10^{2}$	-4248.5
LFP2	$8.43\,10^{-4}$	-2.76	$8.08\,10^{-6}$	1.38	$1.09\,10^{10}$	-9620.3

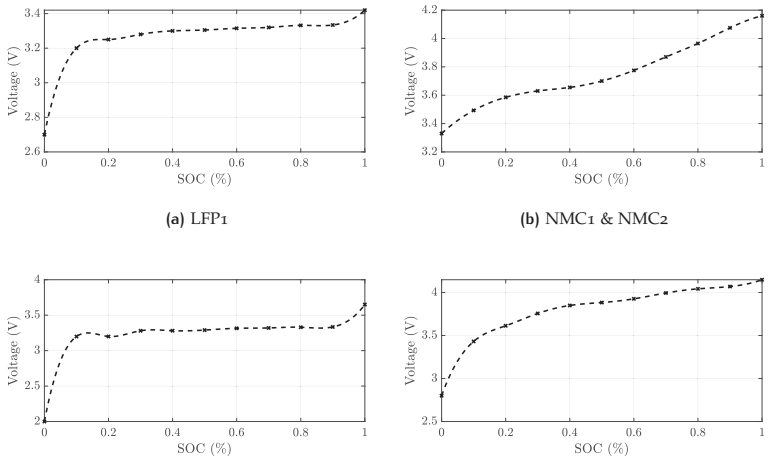

(a) LFP1 **(b)** NMC1 & NMC2

(c) LFP2 **(d)** LMO

Figure 3.45: OCV vs SOC characteristics. Markers represent measured values and the dashed line shows the polynomial fit to estimate the voltage for different SOCs.

characteristics. Recorded voltage vs SOC values are marked by x and a polynomial approximation is provided as a dashed line. The voltage characteristic of the NMC1 and NMC2 cell are identical as no information about the OCV vs SOC curve was provided for NMC2. A large voltage drop is observed for LFP and LMO cells at low SOC which leads to the distorted linear fit of the linear voltage estimation.

In general, results show that the relatively simple empirical aging equation is able to represent both calendar and cycle aging results over a wide variety of Li-ion cell chemistries. Likewise, the additional two time dependencies can be analyzed for different cell chemistries. A detailed comparison is provided in Appendix A.3.1.

Overall calendar aging fit for LMO

Previous results described the fit function if voltage, SOC and temperature are fit independently from each other. However, both voltage and temperature fit depend on each other and have to lead to the same characteristic. Therefore, either both dependencies

can be fit independently at first and then be adapted to each other based on the common data basis. For example, different voltage levels were examined at 25°C and temperature variations at 50% SOC. As a result, both fits have to result in the same value at 25°C and 50% SOC or be normalized accordingly. On the other hand, an overall fit function as presented in (3.88) can be used to fit all parameters at the same time by minimizing the root mean square error (RMSE) or similar characteristics. In this case, the latter approach is used.
Primarily, a $t^{0.75}$ fit function is used as the voltage/SOC relationship is more distinct and a higher generalization to other cell chemistries is possible as described before. In addition, voltage is used instead of SOC as voltage is easier to measure in real applications and does not lead to additional errors due to SOC offset. Further, the linear relationship over voltage offered a lower root-mean-square error. The overall calendar aging expression is displayed in (3.88).

$$C = a_1 (V - a_2) \cdot \exp\left(\frac{-a_3}{T}\right) t^{0.75} \tag{3.88}$$

with

$$a_1 = 3.5758 \cdot 10^4,\ a_2 = 3.2748,\ a_3 = 4886.9\,. \tag{3.89}$$

Although the determination of a general voltage relationship is hard, the SPM-EEM aging approximation using a $t + \sqrt{t}$-relationship is also used and fitted. Eq. (3.90) presents the resulting calendar aging equation and fit values.

$$C = a_1 (V - a_2) \cdot \exp\left(\frac{-a_3}{T}\right) (t + a_4 \sqrt{t}) \tag{3.90}$$

with

$$a_1 = 34.34 \cdot 10^{-7},\ a_2 = 3.23,\ a_3 = 5010,\ a_4 = 35\,. \tag{3.91}$$

A comparison of the quality of these two calendar aging models is presented in section 3.6, where both SPM and EEM results are presented.

3.5.2.2 Cycle Aging - Model development & fit

In a next step, cycle aging effects are examined. Cycle aging might either be treated independently from calendar aging as described in [52, 170, 245] or in addition to calendar aging [83, 97, 205]. In this study, the second approach is used. It is assumed that calendar aging effects also occur during cycling. As a result, the recorded capacity loss during cycling has to be separated into a capacity loss due to calendar aging and loss due to pure cycle aging. The influence of this separation on cycle aging results has already been described in 3.3.2. The evaluation of influencing factors for cycling is challenging as more complex effects occur within the cell during cycling. Furthermore, the test procedure has more DOF for cycle than for calendar aging. For example, in addition to temperature, voltage, and storage procedure (open circuit or charge sustaining), charge and discharge rate, DOD, maximum SOC, and the rest period in between charges can be chosen. Only few test campaigns for cycle aging are available in literature and they differ in the number of tested cells and test scenarios. In most cases only full charge scenarios are evaluated [52, 245]. Results are therefore less distinct and a comparison between different test campaigns becomes harder. Further, if no calendar aging tests are available or no time information is provided for cycle aging tests, an exact recalculation of the capacity loss due to calendar aging is impossible. Therefore, the

cells NMC1, NMC2, LFP1, and LFP2, which were used for generalization of the calendar aging results, are also used for cycle aging. Unfortunately, a cycle aging test campaign is not available for the LFP1 cell. Calendar and cycle aging tests of the NMC1 cell by [69] are extended by a cycle aging study described in [205] covering different DODs and mean SOCs. A cycle aging test campaign is described in [138], which corresponds to the NMC2 cell introduced in [207]. Temperature, CR, DOD, and mean SOC variations are examined. In addition to calendar aging tests, [121] also describes cycle aging tests for different CRs and DODs for the LFP2 cell.

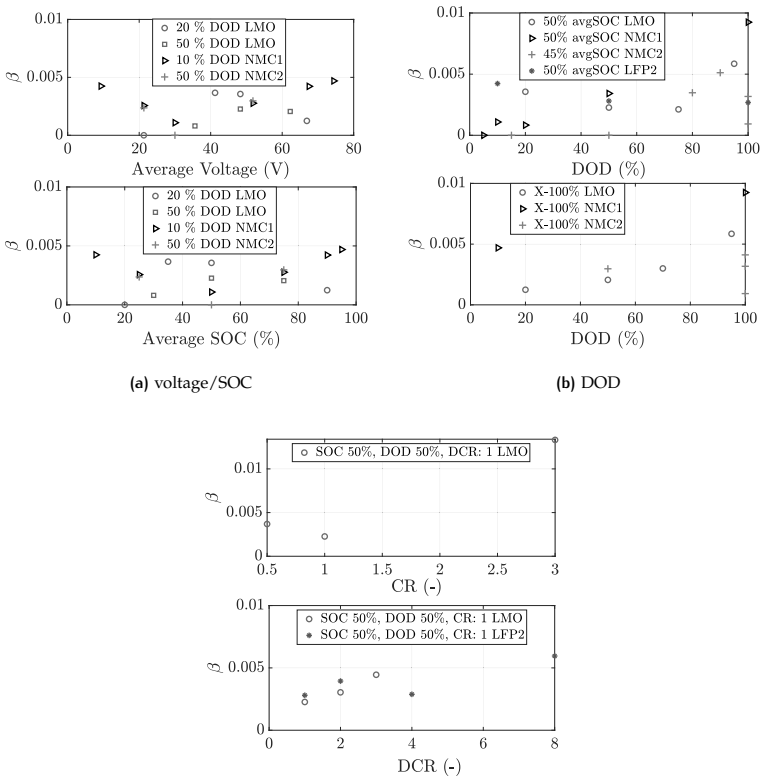

(a) voltage/SOC

(b) DOD

(c) CR/DCR

Figure 3.46: Comparison of voltage characteristics for cycle aging using a $\beta\sqrt{Q}$ fit function. Measured capacity is compared to the model fit and results for β are shown over SOC, voltage (a), DOD (b), and CR (c).

In a first step, it is assumed that cycle aging can be represented by the total charge throughput $Q = \int |I|\,t\,dt$ which the cell has experienced over its whole lifetime. The charge throughput can be converted into the equivalent number of full cycles (efc) by

dividing Q by the (either the nominal or actual) cell capacity. In the case of LMO, cells cycled at a low average SOC and DOD such as 10-30% and 5-55% show a significantly lower aging during the initial 800 efc. Afterwards, the capacity loss increases disproportionately, which can be accounted to side effects due to manganese dissolution as discussed in section 3.1.1. This rapid loss cannot be represented by a square root-like dependency of loss over charge throughput. The battery in E2Ws in China is generally replaced after 2 years and the battery is discharged by approximately 25% DOD every day as analyzed in section 2.1. Thus, the battery experiences an approximate number of 183.5 efc over 2 years or 365 efc over 4 years of operation. Even if the battery is fully discharged every day, the battery is unlikely to experience more than 800 efc over its lifetime under the given circumstances.

As a result, only the first 800 efc are used to parametrize the cycle aging model such that a square root-like empirical relation of

$$C_{cyc} = \beta \sqrt{Q} \tag{3.92}$$

can be applied. The parameter β is fitted to the data. Fig. 3.46 displays the results for β for the LMO, LFP2, NMC1, and NMC2 cell. Variations are presented over average voltage and SOC (a), DOD (b), and CR and DCR (c). LMO cells were cycled at various average SOCs with a DOD of 20% and 50%. Resulting β are displayed in Fig. 3.46 (a) as circle and rectangle markers, respectively. These indicate that aging is lower at very high and low SOC levels than at medium SOCs. The behavior might be approximated by a quadratic function with a maximum at about 50% average SOC. Likewise, results for cell NMC1 and NMC2 are shown. These show a different behavior than the LMO cells with both high and low average SOC accelerating and not decelerating capacity loss. Still, the behavior might be described by a quadratic relationship.
Fig. 3.46 (b) examines the influence of DOD on aging. Results for the LMO, NMC1, NMC2 and LFP2 cell are presented in the top plot if the average SOC is kept constant at about 50% and only DOD is varied. Results vary between different cell chemistries. Whereas the NMC1 cell shows a linear increase of β over DOD, the parameter remains almost constant or slightly quadratic for the LMO and LFP2 cell, and shows no clear trend for the LFP2 cell. In Fig. 3.46 (c), the influence of charge and discharge rate is evaluated. Charge rate CR is evaluated for the LMO cell only as the other studies show no variation in CR. It can be recognized that CRs of 1 and 0.5 show approximately the same value for β. However, for larger CRs, in this case 3, β triples in comparison to a CR of 1. In literature, an exponential increase of aging with CR is observed [176]. The discharge rate DCR seems to have a lower influence on aging than the charge rate. Results indicate that aging increases slightly with DCR. For the LMO cell, a linear increase from a CR of 1 to CR of 3 can be assumed. The LFP2 cell shows a similar trend, indicating a linear or no significant increase of aging with DCR.
One reason for the various aging behaviors might be that the time axis had to be added manually for most cells and might thus differ resulting in a false calendar aging estimate of the cycle aging part. In addition, the test protocols of the evaluated cell chemistries vary and might lead to lower battery stress and aging if the cells are rested in between cycles.

Although cycle aging results are less distinct, an approximation might be given by means of linear, quadratic and exponential empirical relations as summarized from [52, 69, 86, 97, 105, 170, 205, 224, 245]:

$$\beta(V/SOC) = b_1 (V - b_2)^n,\ n = 1,2 \tag{3.93}$$

$$\beta(DOD) = b_1 (DOD + b_2)^n,\ n = 1,2 \tag{3.94}$$

$$\beta(CR) = b_1 \exp(CR) \tag{3.95}$$

$$\beta(DCR) = b_1 (DCR + b_2) \tag{3.96}$$

In total, two expressions can be derived. The first is based on the results presented by [205], who propose a combined quadratic voltage (SOC) and linear DOD dependency.

$$C_{cyc,1} = \left(b_1 (\varnothing V_{cell} + b_2)^2 + b_3\, DOD + b_4\right)\ \sqrt{Q} \tag{3.97}$$

In addition, results of the SPM derived EEM aging equation in (3.75) are used.

$$C_{cyc,2} = b_1 (V - b_2) (DOD + b_3)^2 (Q + b_4\, I\, \sqrt{t}) \tag{3.98}$$

A detailed comparison of both cycle aging empirical equations is provided in the next section.

3.6 COMPARISON OF SPM AND EEM

Results of the SPM and EEM are compared for electrical, thermal, and aging behavior. Additionally, two different empirical aging equations are analyzed, which base on the same electrical and thermal EEM. The argumentation follows the description provided in [186].

Base & thermal model
The electric parameters of the EEM can be identified using one charge and discharge cycle or impulses. Similarly thermal model parameters can be fit. For a second order Randles circuit with one series resistance and two RC-elements, this results in resistances $R_0 = 7\,m\Omega$, $R_1 = 0.6\,m\Omega$, and $R_2 = 6\,m\Omega$, as well as capacities of $C_1 = 4600\,F$, and $C_2 = 9100\,F$. The heat model parameters are the effective surface area $A = 0.035\,m^2$ and heat capacity $c = 900\,J\,(kg\,K)^{-1}$, heat transfer coefficient $h_{conv} = 10\,W m^{-2} K^{-1}$ and cell mass $m = 0.4\,kg$. These static measurements can be extended to characteristic maps covering temperature, SOC and resistance depending effects. Likewise, parameters of the SPM base and thermal model can be taken from Table 3.14, 3.15, and 3.16.

Fig. 3.47 visualizes the model fit for a charge and discharge cycle (top) and temperature profile (bottom) for the EEM (a) and SPM (b). In general, recorded cell voltage and temperature values (dashed lines) can be tracked well by both EEM and SPM. The SPM approach, which assumes an averaged Li-ion concentration in the electrolyte instead of a dynamic transport process, is less accurate at higher currents than 1 C. Therefore, results are presented at 0.2 C and 0.5 C. The electrical circuit representation of the EEM can also predict voltage drops due to larger currents than 1 C well but covers less effects. Temperature predictions are provided for a 1 C charge and 3 C discharge (blue) and 0.5 C discharge (green). Both models are able to estimate the trend and extent of temperature

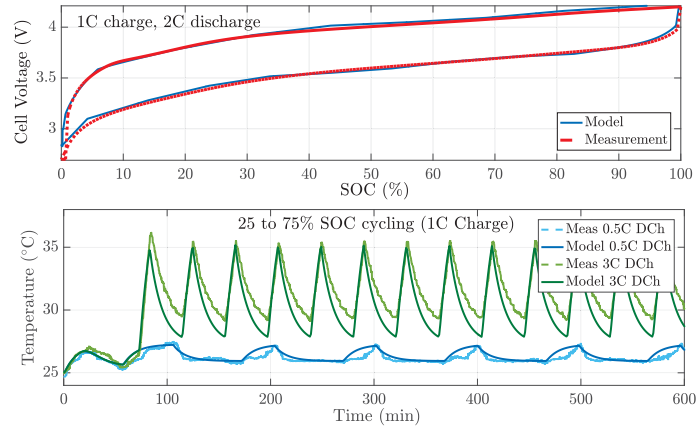

(a) EEM

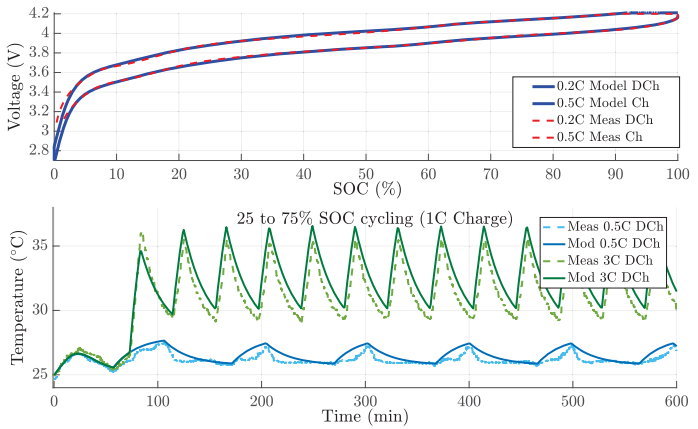

(b) SPM

Figure 3.47: EEM (a) and SPM (b) base and thermal model fit.

changes well, although with some slight deviations. These occur as the exact cooling power of the fan inside the temperature chamber is unknown and needs to be estimated.

Aging model

The SPM and EEM base and thermal model are expanded by aging relations. In case of the SPM, the growth model of the SEI layer is modeled. Two different empirical aging relations are used for the EEM base and thermal model. Once an EEM with an empirical aging model presented in (3.99). Furthermore, the same basic EEM with an

aging model derived from the simplification of the SPM in (3.100), which is in short noted as SPM-EEM.

For the EEM aging model, parameters of the empirical relation for calendar aging $a_{1,2,3}$ and cycle aging $b_{1,2,3,4}$ need to be calculated. The values are fit to the accelerated aging measurements. This can either be done simultaneously for all cell parameters and measurements, or at first for calendar and then cycle aging, as described in [205].

$$\begin{aligned} C_{loss} &= a_1 \left(V_{cell} + a_2\right) \exp\left(\frac{-a_3}{T}\right) t^{0.75} \\ &\quad + \left(b_1 \left(\varnothing V_{cell} + b_2\right)^2 + b_3\, DOD + b_4\right) \sqrt{Q} \\ &= 3.58 \cdot 10^4 \left(V_{cell} - 3.27\right) \exp\left(\frac{-4886.9}{T}\right) t^{0.75} \\ &\quad + \left(9.052 \cdot 10^{-3} \left(\varnothing V_{cell} + 3.88\right)^2 + 1.09 \cdot 10^{-3}\, DOD + 0\right) \sqrt{Q} \end{aligned} \tag{3.99}$$

Likewise, for identification of the SPM motivated EEM model parameters in (3.100), the model is adapted to the calendar aging curves at first. This results in parameter estimates on the influence of the average voltage a_3 and activation energy a_4 for the Arrhenius term. Then, these values can be used to fit the model to the cycle aging scenarios and to identify a_1, a_2, a_5 and a_6. All estimations are done in a least-squares sense.

$$\begin{aligned} C_{loss} &= a_1 \left(t + a_2 \sqrt{t}\right) \cdot \left(V - a_3\right) \cdot \left(\exp\left(\frac{-a_4}{T}\right) + I_o \cdot a_5 (DOD + a_6)^2\right) \\ &= 4.34 \cdot 10^{-7} \left(t + 35 \sqrt{t}\right) \cdot \left(V - 3.23\right) \\ &\quad \cdot \left(\exp\left(\frac{-5010}{T}\right) + I_o \cdot 0.64 (DOD + 63.7)^2\right) \end{aligned} \tag{3.100}$$

As described before, parametrization of an EEM is easier than for an SPM. An EEM usually consists of less than 10 parameters for the base and thermal model, depending on the used electrical equivalent representation. Although no uniform empirical aging model is available at the moment, both the initial EEM and the described SPM–EEM aging model show good accordance with some cells presented in literature such as [69, 121, 150, 207] as introduced in section 3.5.2 and common aging models [52, 205, 245]. An SPM requires intensive parametrization as many internal cell parameters and transportation processes need to be evaluated. Although most values are determined by physical and chemical relations, they are either hard to measure or cannot be measured at all. Every cell chemistry, type of electrolyte and separator influences the internal processes and thus need known or identified. In total, this leads to more than 60 parameters for the base and thermal model. Additionally, more than 15 parameters are required for the SEI aging extension, some of which are dependent on current and SOC.

The resulting aging behavior in comparison to the measurements obtained by an accelerated aging test campaign is shown in Fig 3.48. At the top, pure calendar aging for a SOC of 20%, 50% and 100% is displayed. The SPM–EEM aging model (dotted line) and initial EEM model (solid line) show good accordance with the measured capacity loss (markers). The first is able to more accurately represent higher temperatures and the second has a closer fit at 100% SOC and 25°C. In average, the sum of the squared deviations for both empirical aging models and all measured SOCs and temperatures

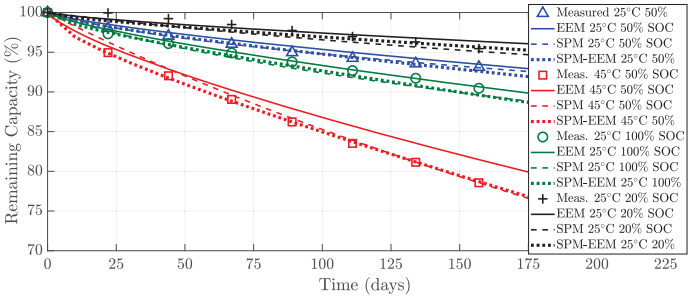

(a) Calendar

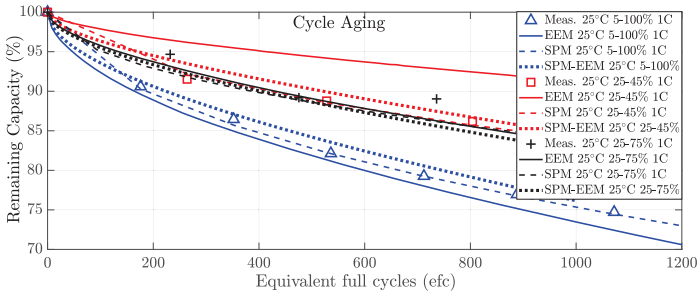

(b) Cycle

Figure 3.48: EEM, SPM, and SPM–EEM aging model results in comparison to measurements: (a) calendar aging and (b) cycle aging.

shows only small differences. Results obtained by the SPM are displayed as dashed lines. The SPM has a lower squared deviation than the SPM–EEM and EEM. However, at the same time the computation time and effort for the SPM is much higher. In total, all methods provide good results for calendar aging and vary only at computation time and parametrization effort.

Fig 3.48 (b) provides results for cycling between 25% and 45% SOC, 5 to 100%, and 25 to 75%. The advantage of the SPM can be observed in this figure. As more complex processes occur during cycling, empirical capacity estimates cannot represent all of these. Whereas EEM and SPM–EEM are able to predict the full cycling (5–100%) with an acceptable error, the EEM aging relation (solid line) has difficulties predicting the 25%-45% cycling, as a linear influence on DOD is assumed. Therefore, the cell cycled between 25% and 45% cannot be properly modeled. This cell shows similar aging as the cell cycled between 25% and 75%, but the equations would indicate that the aging has to be lower due to the smaller DOD and lower average SOC. The SPM–EEM (dotted line) is able to more accurately predict this scenario but is bound by the assumptions stated in the empirical equations. Therefore, larger deviations occur at other cycle depths.

In general, EEM, SPM–EEM, and SPM are able to represent the voltage and thermal behavior of the cell. The root mean square error RMSE and normalized RMSE are used

Table 3.18: Model error.

Model	EEM	SPM	SPM–EEM
RMSE cal	0.77	0.54	0.38
RMSE cyc	3.66	1.20	1.44
RMSE overall	1.93	0.67	0.77
RMSE norm	0.021	0.007	0.008

to quantify the aging model fit. Therefore, the deviation of measurement y_n of every aging scenario n is compared to the model prediction $\hat{y}_n$ over all time instances T (for calendar aging) and equivalent full cycles (for cycling).

$$\mathrm{RMSE} = \sqrt{\frac{\sum_{t=1}^{T}\left(\hat{y}_n(t) - y_n(t)\right)^2}{T}} \tag{3.101}$$

The average measurement value $\bar{y}$ is used for presenting a normalized RMSE.

$$\mathrm{RMSE}_{norm} = \frac{\mathrm{RMSE}}{\bar{y}} \tag{3.102}$$

Table 3.18 presents the RMSE results for calendar and cycle aging and the overall model fit. For calendar aging all models and the measurements show good accordance with the SPM and the SPM–EEM being slightly more accurate. The advantage of the SPM can be observed during cycle aging. Whereas the EEM and SPM–EEM are restricted to the modeled linear, exponential and quadratic aging dependencies, the SPM is also able to resemble more complex behaviors. Still, with an RMSE of 1.44, the SPM–EEM has a higher accuracy than the EEM (3.66).

Besides the amount of variables, parametrization effort, and accuracy, the calculation time plays an important role when choosing a model. In the presented case, a comparison between the models, which were implemented in Matlab [143], was done using a standard working laptop. For a simulation time of 180 days, pure calendar and continuous fixed discharge cycle aging calculations were executed. For pure calendar aging, the SPM–EEM and EEM finish in less than 1 min and the SPM in approximately 10 min. For continuous cycling the SPM–EEM and EEM simulation requires at most 25 min (using derivatives of the aging relation to be able to adapt for changing temperature and cycle depth), whereas the SPM runs for at least 7 h covering the same scenario. Although the SPM takes about 15 times longer than the EEM, this is, for simulation purposes, acceptable. On the other hand, in combination with a vehicle model and an optimization strategy this might be costly. Further, an SPM requires PDEs to be solved whereas the SPM–EEM and EEM use algebraic equations and ODEs. This provides challenges for SPM implementation on control devices.

In total, the SPM provides an insight into cell concentrations and degradation behavior. In comparison to other electrochemical models, the complexity of SPMs is acceptable. Still, the SPM–EEM and initial EEM show already a good electrical, thermal, and aging estimate, which is sufficient for most automotive applications. By deriving the empirical aging equations from the SPM, a novel SPM–EEM aging model is described. It

provides comparable results as the EEM aging relations described in literature. Additionally, the empirical relations might be further improved by incorporating more parameters and more complex dependencies. This would lead to more fit parameters and a slightly higher parametrization effort. As the empirical relations are algebraic expressions, adding more parameters will increase the computational load only slightly. Still, the EEM aging equations rely on basic electrical and thermal parameters. Therefore, this approach is limited since the electrical and thermal model cannot provide cell internal information such as concentrations and layer growth which the SPM uses.

3.7 OVERALL SIMULATION MODEL

Based on the results of the motor and power electronics modeling and the previously introduced Li-ion base, thermal, and aging model, an overall simulation environment can be built up. Different levels of detail can be represented and interactions between models observed. For example, driver behavior can either be input directly by the throttle demand or a recorded speed profile can be loaded. The motor model takes this torque or speed demand together with the available battery voltage as input signal and outputs a corresponding required current. Due to motor efficiency of approximately 93% and additional losses in the powertrain, the current is higher than the pure electric motor current. The battery electric and thermal model reacts to the desired motor current typically by a drop in voltage and temperature increase. The resulting electric and thermal properties are fed into the battery aging model. The aging model computes the resulting capacity loss and resistance increase and outputs it to the battery electric model. Resistance changes influence the resistance values in the electric equivalent model. Likewise, a variation in cell capacity influences the capacitance. After a driving cycle is completed or the battery is fully discharged, a charging controller needs to be implemented to simulate battery charging. This module takes the current battery SOC and voltage, and resistance as input and calculates a corresponding charging current. Furthermore, the PMSM model is deactivated to speed the simulation up. This process is depicted in Fig 3.49 as a schematic of the different simulation component models and their interaction.

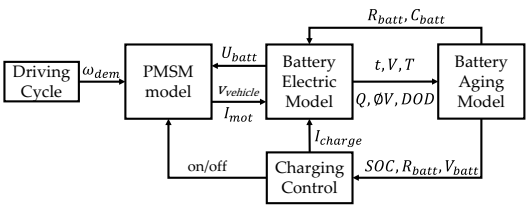

Figure 3.49: Overall simulation model.

In addition, influences of the vehicle speed on cooling are included. In this case, an empirical relation is used which correlates variations in the air speed v_{air} to a change in

Table 3.19: Levels of modeling depth.

Model	Motor model	Battery electric model	Battery aging model
Static-EEM	static	EEM	empirical
Static-SPM	static	SPM	SEI growth
PMSM-EEM	dq, no inverter	EEM	empirical
PMSM-SPM	dq, inverter	SPM	SEI growth
PMSM-Inverter-EEM	dq, inverter	EEM	empirical

the convective heat coefficient h_{conv}. This air speed dependent convective hear transfer coefficient due to wind chill, $h_{conv,wc}$, can be approximated by

$$h_{conv,wc} = 10.45 + 10\, v_{air}^{\frac{1}{2}} - v_{air}\,, \tag{3.103}$$

for wind speeds of 2 m/s to 20 m/s as shown in [162]. Since it is assumed that the battery is only cooled from two sides, h_{conv} is chosen to be $\frac{1}{2}\, h_{conv,wc}$. For speeds lower than 2 m/s (7.2 km/h), a convective heat coefficient of $10\,W/(m^2K)$ is used.

Table 3.19 provides an overview of possible combinations of the derived models to achieve various levels of detail. The motor can either be neglected (static conversion), modeled as a PMSM in dq-coordinates (PMSM) without or including inverter switching (PMSM-Inverter). The choice of the battery model is between EEM and SPM. For example, if motor dynamics are neglected and the EEM is used in combination with the presented empirical aging relation, the simulation yields a basic but computationally fast approximation of cell aging, referred to as Static-EEM. Likewise, the substitution of the EEM by the SPM (Static-SPM) leads to a more detailed insight into cell aging, but comes at a higher computation time. By combining different models, model complexity can be estimated by the computation time on a simulation computer, as summarized in Table 3.20. Simulations were performed over 7000 s repeatedly with the combined SE2WC for discharge and a 1 C charge thereafter. Matlab/Simulink® [144] is used as simulation platform. An overview of the applied speed and resulting SOC profile is displayed in Fig. 3.50 for the first cycle. The Static-EEM takes in average 12 s to finish the simulation. If the SPM is used instead of the EEM, the simulation time increases to about 91 s. Once the PMSM model is included, the simulation becomes more complex and simulation time increases to 586 s. Adding inverter and switching dynamics with a frequency of 1 kHz increases simulation time even more as the step size needs to be decreased.

Fig. 3.50 indicates that a combination of different motor and battery models is possible and leads to similar results. The top plots show results for the three described motor models using the EEM and the lower plots for the SPM. In both cases, the combined SE2WC was input as speed profile for the motor model. The resulting speed profile is displayed in the left plots of Fig. 3.50. Battery SOC is shown on the right. Overall, the models match closely and small variances are due to differences in the modeled effects.

The behavior of the different models is illustrated in detail in Fig. 3.51 for a time range of 1200 s to 1500 s. Vehicle and motor characteristics such as vehicle speed v, motor current I_{mot}, and motor angular speed ω_{mech} are presented in the left plots. Battery

Table 3.20: Characteristics of models for a simulation of 7000s (75% initial SOC, 2x combined SE2WC driving cycle, 1 C charge).

Model	Sim. time (HH:MM:SS)	Application
Static-EEM	00:00:12	fast aging approximation
Static-SPM	00:01:31	pure aging approximation
PMSM-EEM	00:09:46	basic motor & battery aging simulation
PMSM-SPM	00:10:15	basic motor & complex aging simulation
PMSM-Inverter-EEM	03:50:51	motor & power electronics effects; simulation including all components

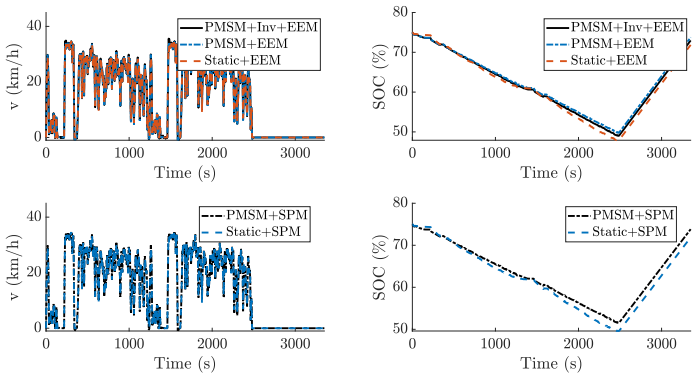

Figure 3.50: Overview of simulation results.

properties such as voltage V, SOC, and cell temperature are shown on the right. Fig. 3.51 (a) compares different levels of motor modeling in combination with the EEM. The speed output of the Static-EEM is the same as the input as no motor model is employed. In the simulation, the motor is operated in PI speed control and not torque control mode as used in most E2W. Therefore, small deviations in speed are observed for the PMSM-EEM and PMSM-Inv-EEM in comparison to the Static-EEM. This can especially be seen around 1450 s, where the maximum motor power is exceeded and the speed lags a little behind and shortly overshoots. This effect can also be recognized in the voltage and current signal. Positive currents correspond to regenerative braking. Both the basic PMSM without inverter and with inverter show almost the same angular speeds. The battery SOC shows also a similar characteristic for the PMSM-EEM and PMSM-Inv-EEM with the only difference being a small offset of 0.2 V. The Static-EEM shows larger fluctuations in the current since a static force conversion is used. Thus, also the SOC deviates slightly from the models including motor characteristics. Differences occur mostly during a full stop of the vehicle. In this case, the Static-EEM models only the power loss due to electric consumers such as lights and electronics. The motor models

need to maintain a small current for motor operation. Likewise, cell temperature is approximately 0.1°C higher for the Static-EEM as larger current fluctuations occur.
A comparison of the different battery models is given in Fig. 3.51 (b). The models match closely in terms of speed since the same motor model is employed. The models also match each other closely for current and voltage. The EEM shows a slightly lower voltage drop which might result from a lower internal resistance. EEM and SPM show an offset of approximately 1% in the SOC after 1400 s. Still, the reaction of the SOC to current changes follows the same pattern. A small offset of approximately 0.1°C can also be observed for cell temperature. The EEM approximates the cell by a lumped parameter thermal model. Thus only one temperature value is shown. The SPM calculates both an internal and surface cell temperature. The internal cell temperature exceeds the surface cell temperature if large currents are applied. Then the heat transport from the cell interior to the surface is lower than the heat convection between cell surface and surrounding air.

Overall, differences in the electrical and thermal parameters between the different modeling depths are relatively small. Thus the presented different modeling depths can be used to simulate the behavior of an E2W and to validate the results of the optimization. However, results also show that motor dynamics are negligible if only battery behavior and aging are to be observed. It is sufficient for the optimization to use the battery model with a current profile as input. Furthermore, the EEM and SPM show only small differences in accuracy but the SPM is more complex in terms of model structure (coupled PDEs with a DAE) than the EEM (ODEs). This leads both to a longer simulation time and a more difficult selection of a suitable optimization formulation and solver. As a result, the EEM is used for optimizations in the next chapter and the SPM for validation of the optimization results.

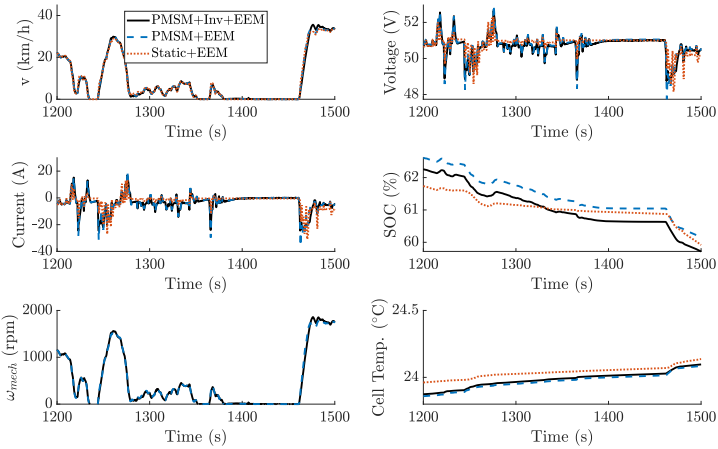

(a) Results when comparing motor models

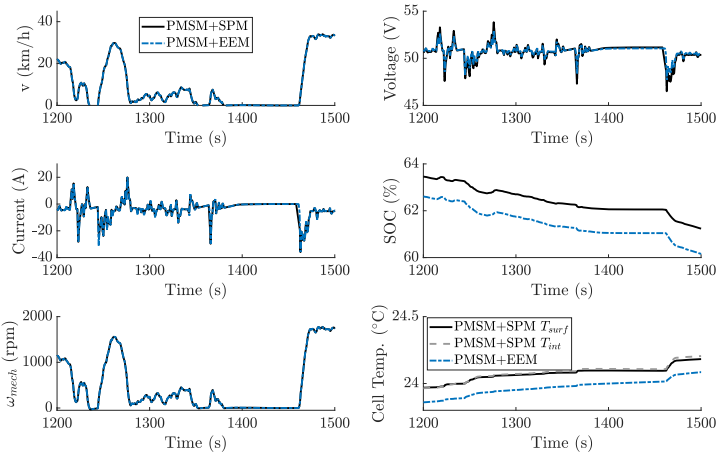

(b) Results when comparing battery models

Figure 3.51: Detail view of simulation results.

4

MODEL-BASED OPTIMIZATION

The previous chapters showed how a typical E2W operation can be identified, how such a driving cycle can be converted into a power profile for the battery, what battery stress it causes, and how an accurate, yet efficient battery aging model can be derived. Based on this, a model-based optimization strategy is described and implemented in this chapter. To simplify the optimization process two different aging models were used to validate each other. It was shown that the model simplifications of the EEM were appropriate. Additionally, extensive aging tests with one cell type showed that the models represent the real aging behavior. A model-based approach is thus expected to provide good performance and a realistic view on the topic of battery lifetime optimization for the given scenario.

Based on the results of the previous chapters, this chapter answers the overarching question of how a lifetime-optimal operation strategy looks like. First, some general aspects of the optimization such as the identification of suitable DOFs, the choice of an optimization aim, and optimization scope have to be evaluated. It is possible to formulate key questions which lead to the derivation and validation of an optimal strategy:

- Which DOFs exist for optimizing the battery lifetime? Where is an improvement possible? And which of these measures are feasible and might be accepted by E2W drivers?
- Focusing on charging optimization: which DOFs exist for this case? (charging time, current/profile, maximum SOC)
- How can the previous models be adapted and integrated into an optimization formulation?
- Which outcomes can be identified? How does the optimized strategy look like? Which factors influence it?
- Are the optimization results valid? Does the optimal strategy show an improved performance?
- Can the results be implemented online and run on a control device where computation time and power play an important role?

4.1 OPTIMIZATION PROBLEM FORMULATION

4.1.1 Operational strategy

The optimal operation of an EV or E2W comprises all phases of usage. For example, the driving phase itself can be influenced but also the charging and the storage phases.
Within the driving phase, optimization can be achieved by improving the environmental conditions or the driver input itself. Beneficial environmental conditions can be created by searching for a more suitable route with less traffic, lower slope, or favorable outside temperature. Furthermore, the trip start and end time might be adjusted. Driving optimization is closely linked to the driver's behavior and preferences. The driver or – in the case of autonomous vehicles – the planning algorithm can decide when to start and end, which route to travel, and set the desired speed and acceleration. In this context, intelligent operation strategies, which look ahead of the route to identify slopes or traffic have been developed to optimize battery usage in HEVs. For example, the electric motor can be used to provide additional torque at low speeds or slopes and recuperation phases can be identified.

Besides optimizing driving, the charging strategy plays an important role for pure EVs and E2Ws. In contrast to vehicles with a combustion engine, "refueling" of EVs and E2Ws takes much longer. Batteries can only be charged with a relatively low current. Although battery technology is being continuously improved to allow for higher charging currents and the number of charging stations is being increased, a full charge takes at least 30 min with a 2 C charge rate. Lower charging currents are often desired to reduce battery stress and prolong battery lifetime. Charging optimization can tackle different issues such as adapting the charging time and current to either reduce the overall time spent at a charging station or to reduce battery degradation. Various charging approaches such as multistage CC, pulse, and sinusoidal or ripple charging have been presented in addition to the commonly used CC/CV charging [110, 127]. In combination with information about the route and distance also the maximum battery SOC can be used as DOF for charging optimization. For example, if only 50% of the battery charge are required to drive to the desired point, the battery is not required to be fully charged at the beginning of the trip.
In addition, vehicles remain unused for most of the day. This storage phase offers a large potential for (battery) optimization. Temperature, SOC, and in some cases time can be varied and used as DOF for optimization.

During the aforementioned operational phases, different optimization goals can be formulated for EVs and E2Ws, such as maximizing driving range, minimizing travel time, or improving battery lifetime. This study focuses mainly on battery lifetime. As a result, strategies for reducing battery stress and for efficient operation are evaluated. Such a driving strategy, which minimizes battery degradation, could also improve the range. This results from minimizing the total charge throughput to increase range, which is also one of the aging factors as described in the previous chapter. For an overall lifetime-optimal operation strategy, each of the three operation phases – driving, charging, and storage – have to be considered and DOF need to be defined.
Optimization of the driving phase typically focuses on improving the interaction between vehicle components or the modification of the route. First, gear shift or switching between different power sources can be improved. For E2Ws, where the powertrain

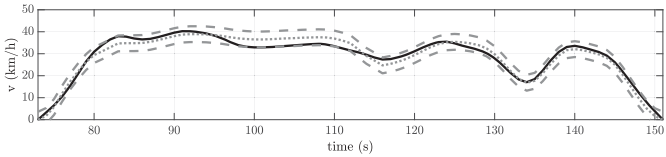

Figure 4.1: Optimized speed profile (black) by allowing speed deviations (gray dashed) around the desired speed (gray dotted).

setup is very basic and only one motor, no gearbox, and no dual power sources are available, an improvement of vehicle components is only possible during the design phase.
Second, the desired route can be adjusted. If a navigation system is utilized, the route can be designed to minimize battery consumption and maximize battery lifetime. For example, traffic can be avoided to minimize driving time and to reduce high acceleration phases which lead to additional battery stress. Furthermore, the maximum acceleration and speed can be limited or a deviation from the desired acceleration and speed can be allowed.

Fig. 4.1 displays the results of such an optimization of the speed profile. A part of the WMTC driving cycle is used for reference. The aim is to drive the same distance in the same time as the original WMTC (gray dotted). The speed is allowed to deviate from the desired speed by $\pm 1\,\mathrm{m/s}$ ($3.6\,\mathrm{km/h}$) representing the DOF for the optimizer. Overall, the optimized driving profile (black) shows a higher speed than the input speed at the start but reduces the speed afterwards to have a smoother transition at about $110\,\mathrm{s}$ to $120\,\mathrm{s}$ thus accelerating less. However, the estimated battery lifetime improvement was only very small and would only come into effect if long distances are traveled. Combined with the low operation range of an E2W ($4.5\,\mathrm{km}$ for BSES and $10.2\,\mathrm{km}$ for SSES), the approach did not yield any significant results. Furthermore, the speed profile of an E2W is not known beforehand and the driver indicates the speed only by the throttle signal which correlates to a motor torque. As typically no navigation device is available for an E2W, it is hard to optimize the route itself. The maximum power and, therefore, acceleration and speed of the E2W can be limited. However, the driver would perceive a lower acceleration and – with the already low power of the E2Ws in Shanghai – feel a negative impact of the optimization. The acceptance of the optimization is expected to be low. As a result, an optimization of the driving phase shows only little potential for lifetime improvement.

On the other hand, charging has a large influence on battery aging. A variation of the charge current influences aging more than a variation of the discharge current. Charging optimization – in combination with optimization of storage phases – is a promising approach for extending battery lifetime without interfering with user preferences. For example, if the E2W is charged overnight for use on the next day, not only the charging profile can be influenced but also the start and end time of the charging phase. In this case, it is irrelevant to the user when his E2W is charged overnight as long as it is available and recharged the next morning. The charging time, e.g. immediately after the user's return in the evening or shortly before his departure in the morning, can be

specified as an additional DOF. The next section examines such a combined charging and storage optimization in detail.

4.1.2 Charging strategy

Charging optimization has received increased attention in recent years and many studies are presented which either optimize charge station distribution, aim on minimizing charging time, or modify the driving profile [2, 3, 19, 72, 96, 123, 208, 226, 241, 265]. However, most optimizations are limited to the charging profile without taking different driving profiles and, therefore, storage periods into account. Furthermore, the maximum charging SOC is not optimized and in most cases aging is not explicitly addressed. Thus, an optimized charging strategy regarding battery aging and a daily driving scenario is described in the following. The algorithm is developed for E2Ws, however, the approach can be extended and applied to any EV. Main goal of the charging optimization is to improve battery lifetime based on a daily driving characteristic without affecting the driver's daily routine. Therefore, the driving profile is not optimized to extend the E2W range or lifetime, as this would imply performance limitations for the driver. The optimization scenario described focuses on optimizing the charging procedure. Charging time, current, and maximum SOC can be altered to minimize battery aging. General correlations, such as a higher SOC and stronger current lead to a faster degradation, have already been described in literature [28, 52, 78, 205, 245]. However, the influence of interconnections based on a realistic everyday driving routine has not yet been sufficiently analyzed.

A daily driving routine is identified to optimize the battery lifetime by adapting the charging scenario based on the driving profile, user behavior, and battery model. The argumentation follows the description provided in [187] and is based on the results of the previous chapters. The main reason for driving an E2W in Shanghai is to commute to work. Such a daily commuting routine can be separated into 4 parts: driving to work in the morning, work time where the E2W is not used, driving back home in the evening, and overnight charging of the E2W .
Some further assumptions are made: The user drives the same route every day, both in the morning and in the evening. The test subject has the same working hours every day, which are known beforehand. No charging is done during the E2W rest time at work. As soon as the user returns home, he connects the charging device to the E2W to charge. In cases where no full battery charge is required to accomplish the daily driving cycle, the targeted final SOC of the charging profile represents an additional degree of freedom. It is assumed that the battery behavior can be represented by the battery aging model introduced before, which means, for example, that no mechanical stress or other unforeseen events occur.

If this simplified and fixed scenario is assumed and weekends are excluded, the optimization problem might be reduced to a daily scenario. A charging strategy which is optimal for one day is very likely to provide improvements for the whole battery lifetime. An overview of the daily driving cycle is depicted in Fig. 4.2. The daily driving is separated into the 4 steps as described before. An exemplary speed profile is shown as black line with two times the same driving profile in the morning and evening. The remaining SOC is depicted as red line starting from an initial SOC_0. While driving, the battery is discharged to a certain extent depending on the driving cycle applied. In

total, two times the DOD induced by one driving cycle is discharged from the battery. Overnight, the battery is recharged to its initial SOC_o. For optimization purposes, the cycle is divided into a known discharge part that starts from $t_{DC,o}$ with the drive to work in the morning and ends at $t_{DC,f}$ when the driver returns home in the evening, and a charging optimization overnight from t_o to t_f. The optimization setup is described in the next section.

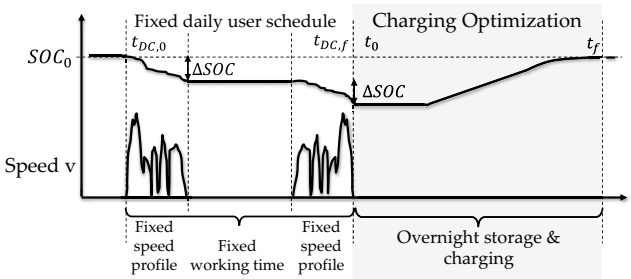

Figure 4.2: Daily driving routine used for optimization.

SOC and charging optimization

Two degrees of freedom can be identified for the optimization. Firstly, the charging profile can be freely selected to charge the battery overnight. Charging time and current can be set within the charging profile. Secondly, if the battery capacity exceeds the power consumed during the daily driving, a full charge is not required. Therefore, the initial SOC_o might be adapted to increase battery lifetime.

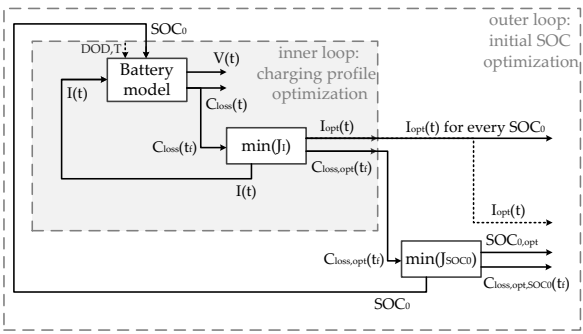

Figure 4.3: Sequence of optimization iterations.

The optimization is divided into two steps: an optimal control problem for charging profile optimization and a parameter optimization for the initial SOC. Fig. 4.3 illustrates the interconnection between these optimization loops. The battery model calculates the cell or battery voltage $V(t)$ change due to an applied current profile $I(t)$. In addition, an estimate of the capacity loss $C_{loss}(t)$ is provided based on the previously derived

empirical relations. The capacity loss at the end of the charging phase is used as cost functional J for the optimal control problem. By adapting the input $I(t)$, the minimum capacity loss is identified for one set of parameters such as one fixed initial SOC (SOC_0), DOD, and temperature T.
In the superimposed loop, the initial SOC is the DOF for the parameter optimization. Once again, the capacity loss is used as cost function, but this time the capacity loss for the optimal current $I_{opt}(t)$ for each iteration of SOC_0. The initial SOC, which results in the minimum capacity loss, is determined by iterating over the allowed SOC range. The minimization provides the optimal initial SOC ($SOC_{0,opt}$), the capacity loss for this SOC ($C_{loss,opt}$), and can be related to the optimal current profile for this choice of initial SOC. As depicted in pseudocode in algorithm 1, the initial SOC_0 can be increased iteratively from the minimum possible SOC_0. The minimum SOC_0 results from the charge throughput due to the DOD of the driving profile, which is driven twice a day. An iterative approach is useful to obtain a lookup table for the optimal charge profile I_{opt,SOC_0} for different initial SOCs in addition to the results at the optimal initial SOC.

Algorithm 1 Optimization framework

```
for SOC_0 ← 2 · DOD to 1 do
    optimize charging
end for
```

For charging profile optimization, the daily driving scenario can be separated into a static discharge and rest part during daytime and a charging time overnight, which should be optimized. The battery aging during the discharge can be calculated by using the aging model presented in section 3.5, by using the known power profiles for the WMTC or the SE2WC as introduced in section 2.3, and by assuming a rest time of 8.5 h at work. The state of charge SOC, charge throughput Q, voltage V, and temperature T are calculated based on the current I. Based on these values, the aging of the cell can be calculated. The EOL criteria for capacity (20% loss) is commonly reached before the EOL for resistance (reached if the resistance is twice as high as the original resistance). Consequently, capacity is used to describe aging. The aim of the optimization is to minimize the cost functional, which equals the capacity loss C_{loss}, by selecting an appropriate input or control $I(t)$ at each time t as shown in (4.8). The characteristics after the discharge phase ($t_{DC,f}$), e.g. the current I_{prof}, are obtained from the driving cycle and rest time and are calculated before the optimization starts. The states of the system $x(t)$ represent SOC, Q, V, T, and the calendar aging C_{cal}. Calendar aging has to be regarded as a separate state as it depends on voltage and temperature, which might change within every iteration. Therefore, the calendar aging part of the empirical aging equations needs to be derived.

Two aging equations are analyzed as introduced before:

1. Conventional equation based on [205]:

$$C_{loss,1} = \overbrace{\alpha_{c,1}(V,T)\, t^{0.75}}^{\text{calendar}} - \overbrace{\beta_{c,1}(\varnothing V, DOD)\, \sqrt{Q}}^{\text{cycle}} \tag{4.1}$$

$$\alpha_{c,1} = a_1\, (V + a_2)\, \exp\left(\frac{a_3}{T}\right) \tag{4.2}$$

$$\beta_{c,1} = b_1\, (\varnothing V + b_2)^2 + b_3\, DOD + b_4 \tag{4.3}$$

2. SPM equivalent EEM equation as derived in (3.70):

$$C_{loss,2} = \overbrace{\alpha_{c,2}\left(t + e_1\sqrt{t}\right)}^{\text{calendar}} + \overbrace{\beta_{c,2}\underbrace{I\left(t + e_1\sqrt{t}\right)}_{Q + e_1\sqrt{Q}\sqrt{I}}}^{\text{cycle}} \tag{4.4}$$

$$\alpha_{c,2} = a_1\,(V + a_2)\,\exp\left(\frac{a_4}{T}\right) \tag{4.5}$$

$$\beta_{c,2} = b_1\,(\varnothing V + b_2)\,b_3\left(DOD + b_4\right)^2 \tag{4.6}$$

It is assumed that $b_1 = a_1$ and $b_2 = a_2$ due to the model structure in (3.70).

The solution is then subject to the dynamic constraints of the state equation (4.10), the boundary conditions (4.11)-(4.13), and the path constraints (4.14). Further variables are the final time t_f and the state variables x_{SOC}, x_Q, $x_{C_{cal}}$, x_{iV}, and x_T representing SOC, charge throughput, calendar aging, the integral over the voltage, and temperature. Voltage is approximated by a lookup table for the OCV (V_{OCV}) and the serial resistance R_0 as

$$V = V(x_{SOC}, I) = V_{OCV}(x_{SOC}) - R_0\,I\,. \tag{4.7}$$

The charging optimization for the two aging equations can then be formulated.

1. First, the resulting optimal control problem and state representation for the conventional equation (4.1) is described:

$$\min_{x(t),I(t)} \; C_{loss}\left(x\left(t_f\right), t_f\right) \tag{4.8}$$

with

$$\begin{aligned} C_{loss} &= C_{cal} + C_{cyc} \\ &= x_{C_{cal}} + \left(b_1\left(\frac{x_{iV}}{t_f - t_0} + b_2\right)^2 + b_3\,DOD + b_4\right)\sqrt{x_Q} \end{aligned} \tag{4.9}$$

subject to

$$\dot{x} = \begin{bmatrix} \dot{x}_{SOC} \\ \dot{x}_Q \\ \dot{x}_{C_{cal}} \\ \dot{x}_{iV} \\ \dot{x}_T \end{bmatrix} = \begin{bmatrix} \frac{I}{C_n} \\ |I| \\ \frac{3}{4}a_1(V - a_2)\exp\left(\frac{-a_3 + 300\,\frac{|I|}{C_n}}{x_T}\right)(t + t_{dc})^{-0.25} \\ V \\ \frac{1}{m_c\,c_{p,c}}\left((V - V_{OCV})\,I - \frac{x_T - T_{amb}}{R_{cell2air}}\right) \end{bmatrix} \tag{4.10}$$

$$x(t_0) = x_{DC}(t_{DC,f})\,, \qquad I(t_0) = 0 \tag{4.11}$$

$$x_{SOC}(t_f) - x_{SOC,DC}(t_{DC,o}) = 0\,, \qquad I(t_f) = 0 \tag{4.12}$$

$$x_T(t_f) \leqslant T_{amb} + \varepsilon \tag{4.13}$$

$$0 \leqslant x_{SOC}(t) \leqslant 1 \qquad 0 \leqslant I(t) \leqslant I_{max} \tag{4.14}$$

2. Likewise, the SPM equivalent EEM equation (4.4) can be used, resulting in the following optimization setup, with modifications in particular for $\dot{x}_{C_{cal}}$ and C_{cyc}:

$$\min_{x(t),I(t)} \; C_{loss}\left(x\left(t_f\right), t_f\right) \tag{4.15}$$

with

$$\begin{aligned} C_{loss} &= C_{cal} + C_{cyc} \\ &= x_{C_{cal}} + b_1 \left(\frac{x_{iV}}{t_f - t_o} + b_2 \right) \; b_3 \; (DOD + b_4)^2 \left(x_Q + b_5 \; \sqrt{x_Q} \, \sqrt{I} \right) \end{aligned} \tag{4.16}$$

subject to

$$\dot{x} = \begin{bmatrix} \dot{x}_{SOC} \\ \dot{x}_Q \\ \dot{x}_{C_{cal}} \\ \dot{x}_{iV} \\ \dot{x}_T \end{bmatrix} = \begin{bmatrix} \frac{I}{C_n} \\ |I| \\ a_1 \; (V + a_2) \; \exp\left(\frac{a_4}{x_T}\right) \left(1 + 0.5 \, b_5 \, t^{-0.5}\right) \\ V \\ \frac{1}{m_c \, c_{p,c}} \left((V - V_{OCV}) \, I - \frac{x_T - T_{amb}}{R_{cell2air}} \right) \end{bmatrix} \tag{4.17}$$

$$x(t_o) = x_{DC}(t_{DC,f}), \qquad I(t_o) = 0 \tag{4.18}$$

$$x_{SOC}(t_f) - x_{SOC,DC}(t_{DC,o}) = 0, \qquad I(t_f) = 0 \tag{4.19}$$

$$x_T(t_f) \leqslant T_{amb} + \varepsilon \tag{4.20}$$

$$0 \leqslant x_{SOC}(t) \leqslant 1 \qquad 0 \leqslant I(t) \leqslant I_{max} \tag{4.21}$$

C_n is the nominal cell capacity, m_c the thermal mass, $c_{p,c}$ the cell specific heat capacity, V_{OCV}, the open circuit voltage, T_{amb} the ambient temperature, and $R_{cell2air}$ the thermal resistance between cell surface and the ambient air. The constraints (4.11) and (4.18) specify that the states at the end of the discharge phase are equal to the states at the beginning of the charge phase. At the end of the optimization, the initial SOC SOC_o has to be recovered (4.12). Additionally, the temperature at the end of charge should be within a small tolerance band ε between the ambient temperature T_{amb} and $T_{amb} + \varepsilon$ as described by (4.13) and (4.20). Since the maximum battery charge current is restricted by the manufacturer, this limit is included in (4.14) and (4.21).

Moreover, temperature and driving profile changes are analyzed. Although no temperature changes have been implemented within one daily profile, the influence of outside temperature changes on the results can be investigated by iterating over different ambient temperatures. In addition, the length of the driving cycle can be easily modified by combining n_{cyc} of driving cycles, resulting in different DODs (DOD between 0 and 1). Altogether, the optimization framework presented in algorithm 1 can be extended to algorithm 2 by superimposing two additional iterations for DOD and temperature.

Algorithm 2 Extended optimization framework

```
for T ← T_min to T_max do
    for n_cyc ← 1 to 1/(2·DOD) do
        for SOC_o ← 2 · DOD to 1 do
            min_{x(t),I(t)}  C_loss(x(t_f), t_f)
        end for
    end for
end for
```

The two outer loops can be seen as a grid covering different environmental conditions, in particular temperature variations and variations in the route. If a specific route and temperature is known beforehand, the framework simplifies to algorithm 1 as illustrated in Fig. 4.3. If more general statements about the influence of different driving cycles and temperatures should be drawn, the optimization framework presented in algorithm 2 can be used to obtain characteristic maps as described in the following sections.

4.2 OPTIMAL OPERATION/CHARGING

The optimal operation with respect to charging and storage of an E2W (or EV) can be separated into the optimization of the charging profile, and the maximum (or initial) SOC. Results are first presented for the conventional aging equation (4.1). Differences to the derived SPM-EEM are introduced in section 4.3.3.

4.2.1 Charging profile optimization

At first, results of the optimal charging profile are evaluated. The optimization problem is solved using a direct method. In this case, an implementation of the SQP algorithm in ACADO [98] and Matlab is used. Therefore, an initial solution is calculated for the input by simulating the model with a constant charge current of 1 A starting from $t_o = 0\,s$ until the cell is fully charged. The time horizon of the optimization is fixed for a given driving cycle and DOD. However, since the driving cycles differ in their duration, the optimization horizon varies. For example, if the WMTC is driven once, the end time of the discharge phase $t_{DC,f}$ as illustrated before in Fig. 4.2 is at

$$t_{DC,f,1WMTC} = 1 \cdot \underbrace{\frac{600}{60}\,\text{min}}_{t_{WMTC}} + 8.5 \cdot 60\,\text{min} + 1 \cdot \frac{600}{60}\,\text{min} = 530\,\text{min} = 8.83\,\text{h}\,. \tag{4.22}$$

If the WMTC is driven four times instead, then $t_{DC,f,4WMTC} = 9.83\,h$. Since the optimization is based on a daily driving schedule, the time horizon $t_f = 24\,h - t_{DC,f}$ for the two optimization scenarios is then $t_{f,1WMTC} = 15.17\,h = 910\,min$ and $t_{f,4WMTC} = 14.17\,h = 850\,min$, respectively. Due to the increasing solution effort with an increase in the time horizon of an optimal control and is this case SQP problem, the input is discretized such that the control can only be changed every 2 min resulting in average 450 control intervals.
The optimization of the charging profile for one scenario with a given initial SOC converges in average in 10 SQP iterations with approximately 6000 QP iterations. These evaluations are calculated on a conventional laptop in approximately 50 min. If the number of control intervals is reduced to 180 (5 min intervals), the optimization time reduces to approximately 3 min. Likewise, if the control iterations are increased to 900 (1 min intervals), the optimization converges after approximately 8 h.

Fig. 4.4 (a) presents the resulting current profile for the optimal strategy with a given initial SOC of 75%. Control intervals of 2 min are defined. In comparison, a conventional strategy is shown in Fig. 4.4 (b) with a 6 A (0.5 C) CC charge starting from $t_o = 0\,min$. Two main observations can be made. First, aging can be reduced by charging as late as possible. Thus the optimal profile starts its main charge only about 1.5 h prior to the

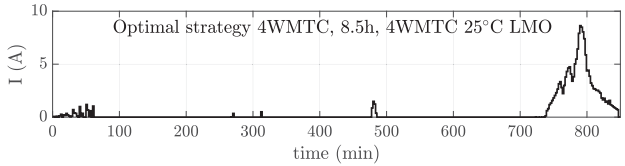

(a) Optimal

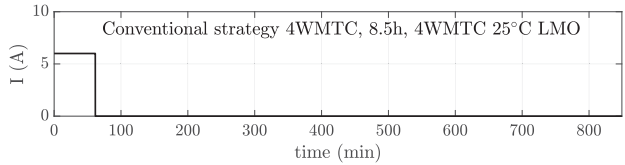

(b) Conventional

Figure 4.4: Current profile of an (a) optimal charging profile in comparison to (b) a conventional charging strategy with a constant current of 6 A.

defined end time. Second, the optimized profile does not result in a constant charging current. The current increases at first to approximately 9 A and decreases afterwards. In addition, the optimal charge current shows smaller charging phases at the beginning and in the middle. Since the position and amplitude of these phases varied for different initial conditions, these are likely to result from the discretization of the control interval in combination with the compliance with the boundary constraints.

The conventional strategy in comparison to the optimization outcome is furthermore illustrated in Fig. 4.5 for the entire daily scenario. The current profile $I(t)$, as well as the resulting temperature T, SOC, calendar and cycle aging losses C_{loss} are presented. Results are presented over a time period of 24 h, which equals one daily cycle. The first driving phase to work starts at $t = 0$ h and lasts for 40 min. Since recuperation is allowed, both positive (recuperation) and negative (discharge) currents occur. For a detail view of the current profile during driving see Fig. 2.15 (b). After a rest period of 8.5 h, which represents the working time, the battery is discharged again to drive home. The charging profile introduced in Fig. 4.4 starts after the second driving phase at about 9.5 h. Since both the conventional (solid line) and the optimal charging strategy (dashed line) are based on the same driving scenario, the results differ only for $t > 9.5$ h.
A temperature increase of approximately 0.8 K from the ambient temperature of 25 °C is observed during the driving phase. The cell cools down to the ambient temperature if no current is applied. The conventional strategy results in an additional temperature increase of 0.25 K due to the 6 A charge shortly after the second driving phase is finished. The optimal charging strategy results in no temperature increase at the beginning since only a small charging current is applied. On the other hand, a temperature increase of 0.65 K is observed during the charge phase at the end. The ambient temperature is not completely restored at the end of the cycle because the optimization allowed a small variation ε of the cell temperature. Due to the later start of the charge phase of the optimal strategy, the SOC remains longer at a low level of approximately 26%. A lower

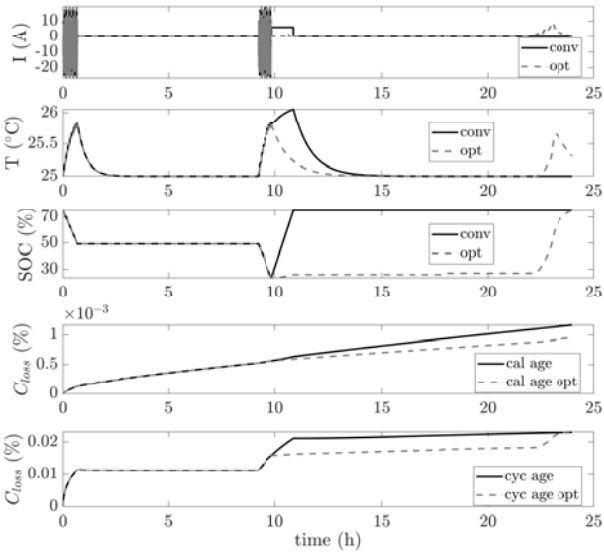

Figure 4.5: Comparison of simulation results of the whole daily cycle using a conventional CC charge (solid line) and the optimal charge profile (dashed line) for an initial SOC of 75%.

SOC leads to a lower voltage level, which in turn leads to a lower capacity loss due to calendar aging. At the end of the day, the optimal strategy results in 18% less capacity loss due to calendar aging than the conventional scenario. The delayed charge is also reflected in the capacity loss due to cycle aging. Since cycle aging is based on the charge throughput, the capacity loss of the optimal charging scenario increases similarly to the increase in SOC. The capacity loss due to cycle aging effects of both the conventional and optimal strategy differs by less than 0.4%. The average voltage enters the cycle aging equation squarely with its minimum at 3.88 V as seen in Eq. (3.99). Thus, lower average voltage levels, as they occur for the optimal strategy, do not significantly improve aging. The total capacity loss due to cycle aging is approximately 18 times higher than the calendar aging loss.

A similar optimal charging behavior can be observed for different scenarios as illustrated in Fig. 4.6. Fig. 4.6 (a) investigates the results of the optimal charging profile for different initial SOCs if the WMTC is driven four times in the morning and in the evening with 8.5 h rest (or working) time in between. In addition, Fig. 4.6 (b) presents the charging profile if the WMTC is driven only twice in the morning and evening. This resembles the average distance driven by an E2W driver in Shanghai as described in section 2.1.1.4 and corresponds to driving the SE2WC once. As already mentioned, the battery is charged as late as possible. This is reasonable since aging increases with a higher SOC. Due to the temperature boundary constraint, which forces the cell temperature to be within 0.1 K of

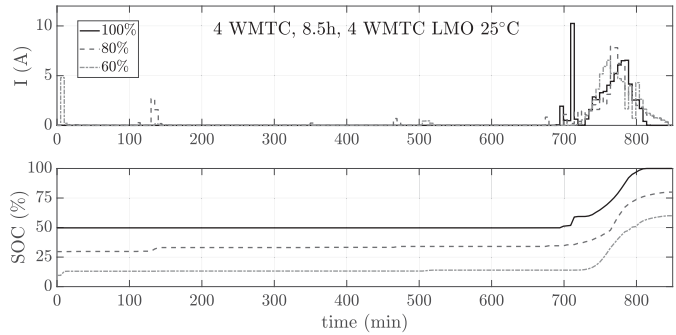

(a) 2xWMTC

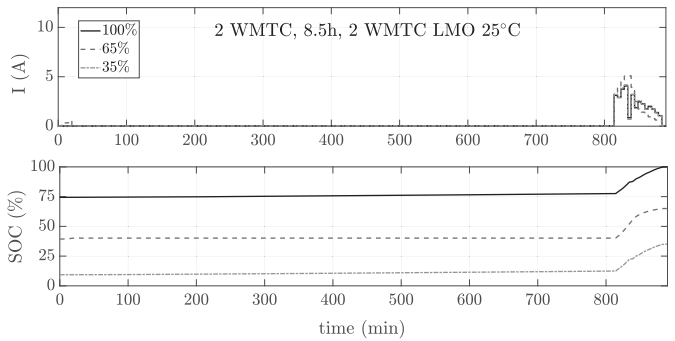

(b) 4xWMTC

Figure 4.6: Optimal charging profiles for (a) 4xWMTC as driving cycle, and (b) 2xWMTC. Depicted are the results of different initial SOCs over time for current and SOC.

the ambient temperature, charging starts about 2 h prior to the scheduled driving time in the morning for a DOD of 51% (4WMTC) and 1 h prior for 25% DOD (2WMTC). This together with the increased aging at higher currents leads to currents below 12 A (1 C). A similar charging behavior can be observed for all initial SOCs.

Longer distances, where the battery is almost depleted show that it might be beneficial to separate the charge phase into a smaller charge at the beginning and a longer charge phase at the end. This can be seen in Fig. 4.6 (a) in case of driving the WMTC 4 times. For example, for an initial SOC of 60%, the cell is slightly charged right at the start. Although typically calendar aging is lower for a low SOC, the optimal SOC obtained by combining calendar and cycle aging is higher. In addition, the effect might be amplified by the limited number of control intervals and the negative influence of high currents. The control interval was set to 5 min in Fig. 4.6. If the control interval is reduced to 2 min as shown in Fig. 4.4 (a), this effect is less dominant. The initial charge only seems

to come into effect at larger DODs. In Fig. 4.6 (b), this charge is not observed at all. This initial charge phase seems to wander to the right for higher initial SOCs. Whereas the first charge peak occurs at approximately 5 min for an initial SOC of 60%, it appears only after 125 min for 80% SOC and around 700 min for 100% SOC.

4.2.2 Initial SOC optimization

With the knowledge of the optimal charging profile for one initial SOC, the parameter optimization of the initial SOC can be investigated. The aim of this second optimization, as illustrated in Fig. 4.3, is to identify the initial SOC, which results in the minimum capacity loss. Therefore, the charging optimization is iterated over a discretized SOC grid. The optimization time increases then linearly with the step size of the initial SOC. For example, the optimization starts at 100% initial SOC and decreases the initial SOC in 1% SOC steps to the minimum possible SOC, which equals the DOD of the cycle. Instead of iterating over all possible initial SOCs, a parameter optimization can be set up to identify the optimal initial SOC. The advantage of a full enumeration is that the resulting capacity loss over the choice of the initial SOC ($SOC_{start} = SOC_0$), as presented in Fig. 4.7, can be used to generate a heuristic rule for implementation of the optimal operation strategy in a vehicle. In addition, the resulting lookup table can be used to identify the estimated increase in aging if the optimal SOC cannot be used, for example, because the user manually selects a higher initial SOC.

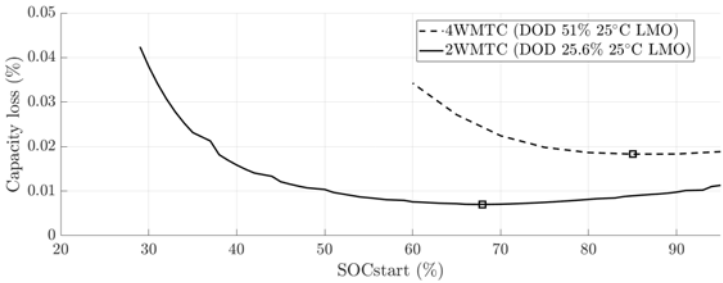

Figure 4.7: Capacity loss over initial SOC for driving the WMTC twice (solid line) and four times (dashed line).

Fig. 4.7 depicts the evolution of the capacity loss over the initial SOC for driving the WMTC twice (solid line) and four times (dashed line). The SOC value, which results in the minimum capacity loss, is marked by a rectangle. In both cases, the capacity loss decreases from its maximum at the lowest possible initial SOC to its minimum before rising slightly again towards 100% initial SOC. For driving the WMTC twice, which results in a DOD of 25.6%, the optimal initial SOC is 68%, whereas a higher initial SOC of 85% is beneficial for a larger DOD of 51%.

An increase in aging at very low SOC can be explained by the larger effect of cycle aging on the total capacity loss. Calendar aging decreases linearly over voltage thus indicating that the voltage should be as low as possible. However, the average voltage is quadratically included in the empirical cycle aging equation with its minimum at approximately 3.88 V. Since the cell voltage varies between 2.7 V (0% SOC) and 4.2 V

(100% SOC), the optimal choice of the initial SOC lies in between the optima of the calendar and cycle aging equation. In the following, these findings can be used to analyze various scenarios.

4.3 INFLUENCES ON OPTIMAL OPERATION/CHARGING

The optimization framework can be used to evaluate the influence of different driving and environmental influences on the charging strategy. Characteristic curves and maps are derived by iterating over additional influencing factors such as the length of the driving phase and therefore DOD, the temperature while driving, the type of the driving cycle, the cell chemistry and the selected empirical aging model.

4.3.1 Influence of DOD (length of the driving phase)

First, influences of the length of the driving phase are examined in detail. As already mentioned, the choice of the charging strategy and initial SOC varies according to the length of the driving phase, which in this case is represented by the concatenation of a given driving cycle. If the driver drives a longer distance than usual, the DOD of the daily driving scenario increases. This is illustrated in and Fig. 4.8 (a), where the capacity loss is presented as a function of DOD. Results are presented for four different initial SOCs. If the cell is charged to an initial SOC of 95% (solid line), the capacity loss increases from 0.005% at 3% DOD to approximately 0.047% at 84% DOD. This is a nine-fold increase in the loss of capacity. The increase itself might be approximated by a quadratic or exponential term with its minimum at 0% DOD.
A similar trend is observed for initial SOCs of 75% (dashed), 50% (dash-dotted), and 25% (dotted). Only DODs lower than the initial SOC can be selected and thus the DOD range shrinks for lower SOCs. The influence of the initial SOC can be recognized especially at lower DODs. At approximately 10% DOD, the lowest capacity loss is observed for an initial SOC of 50% and the highest for 25% SOC. If only the four displayed SOCs can be used – for example due to the limited memory space in an E2W – the intersections of the curves indicate when another initial SOC should be used. For example, a SOC of 50% provides the greatest lifetime saving potential for DODs from 0 to 15%, a SOC of 75% is best for DODs between 15% and 48%, and a SOC of 100% should be used for larger DODs.
Fig. 4.8 (b) shows the capacity loss for various DOD between 6% (half a WMTC) and 71% (6 times the WMTC). As discussed before, minimum aging is achieved not at the minimally possible initial SOC and not at full charge for low DOD. For 20% DOD this optimal value is achieved at approximately 65% initial SOC. As expected, aging increases with higher DOD. Furthermore, the optimal initial SOC value shifts closer to 100% for larger DODs. The lower the initial SOC compared to the optimal initial SOC, the more serious the capacity loss becomes. At very low initial SOCs, the algorithm fails because the power to follow the driving cycle can no longer be provided.

Fig. 4.9 summarizes the results in a surface plot of the capacity loss for different initial SOCs and DODs at 25 °C. The capacity loss is drawn over initial SOC (SOC_{start}) and DOD for the WMTC. The initial SOCs, which result in the minimal capacity loss for different DODs, are highlighted using markers. For DODs up to 65%, the optimal

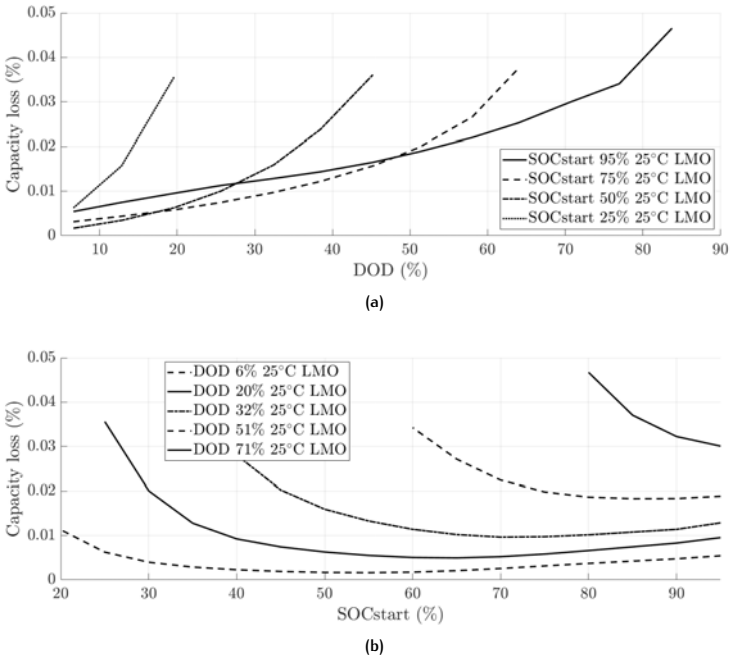

Figure 4.8: Capacity loss for (a) different initial SOCs over DOD and (b) different DODs over the initial SOC using the WMTC.

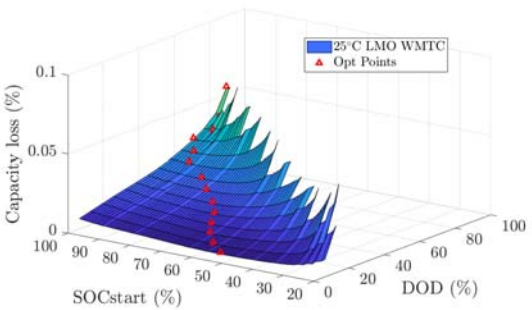

Figure 4.9: Capacity loss depicted over initial SOC and DOD at 25°C using the WMTC. Additionally, the minimum loss point for every DOD is indicated as a red marker.

choice of initial SOC is neither the minimum possible SOC nor a full charge, but lies somewhere in between. Fig. 4.10 highlights the optimal initial SOCs to be picked for a particular DOD. For each DOD evaluated, the markers indicate the initial SOC with

minimal capacity loss. The optimal initial SOC increases almost linearly with an increase in DOD. In case of driving the WMTC, the optimal choice of initial SOC starts from 55% SOC at 7% DOD up to 95% SOC at 65% DOD. For higher DOD, an initial SOC of almost 100% remains the optimal solution.

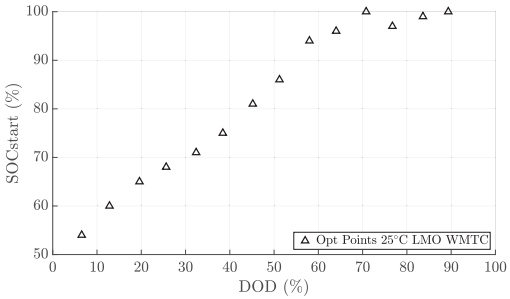

Figure 4.10: Optimal points over DOD and initial SOC for WMTC operation at 25°C.

4.3.2 Influence of driving cycle and temperature

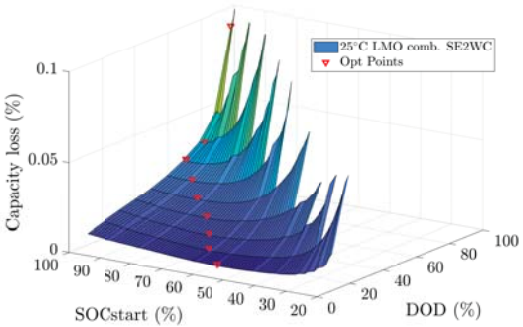

Figure 4.11: Capacity loss depicted over initial SOC and DOD at 25°C using the combined SE2WC (b). Additionally, the minimum loss point for every DOD is indicated as a red marker.

Previous descriptions focused on the evaluation of the WMTC as driving cycle. Still, a variation of the driven route or driving behavior might influence aging and the charging strategy. Fig. 4.9 provided a 3D visualization of the capacity loss using the WMTC. In addition, Fig. 4.11 shows the development of the capacity loss over SOC and DOD for the combined SE2WC. In general, a similar trend can be observed for both scenarios. The combined SE2WC shows a slightly larger capacity loss at low SOC and high DOD. However, the optimal choice of initial SOC seems to be similar. Less optimal points occur because the combined SE2WC is approximately twice as long as the WMTC, thus resulting in a larger DOD per iteration. Fig. 4.12 compares the optimal choice of initial

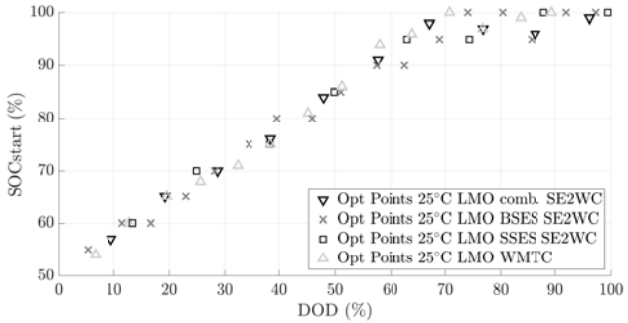

Figure 4.12: Capacity loss depicted over initial SOC and DOD at 25°C using different driving cycles.

SOC over DOD for all four evaluated driving cycles – WMTC, combined SE2WC, BSES SE2WC, and SSES SE2WC. The points lie close together with in average less than 5% deviation. This indicates that, if distance and DOD are known for the daily driving cycle, the same initial SOC can be used for all driving cycles.

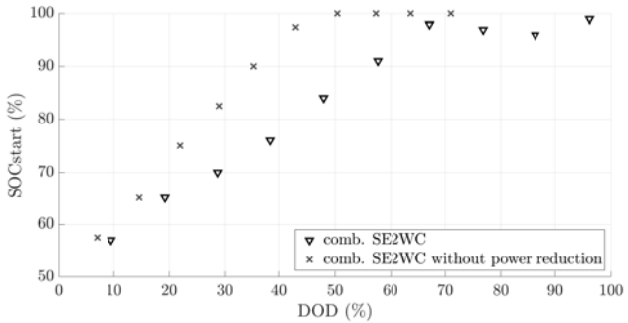

Figure 4.13: Optimal results if motor limitations are neglected and larger current/power spikes occur.

However, further analysis showed that the results differ more when the driving cycle contains higher accelerations. At higher accelerations, a peak power of up to 2 kW can be observed when converting the speed into a power profile. Since a rated motor power of 500 W with a peak power of 1 kW were allowed for the conversion to a power profile, the speed profile was filtered to reduce excessive accelerations. Although the test drivers used an E2W with a rated power of 500 W or lower, larger accelerations and therefore power demands could occur since the E2W motors might still offer a higher peak power. If the power is not limited, the optimal maximum SOC shifts. Fig. 4.13 depicts the results for the combined SE2WC once with respect to SSES power limitations and once without. The optimal maximum SOC is generally higher if the power is not limited. Fig. 4.13 indicates that a higher initial SOC is beneficial if larger peak powers are requested. This

is reasonable because the voltage drops more if high currents are applied. Since the model predicts that very low voltages increase the degradation of the cell, the optimal initial SOC is shifted upwards to avoid too low voltages. In addition, a lower limit for voltage and SOC is set to ensure that safe operation conditions are not violated. If the voltage is already low and large currents are applied, this limit is exceeded and the optimization result is invalid. This study utilizes an averaged driving cycle so that a distinction between driver-specific behavior is not possible. Still, the unlimited case might correspond to the characteristics of a very aggressive driver. Then, results indicate that the selection of the maximum SOC depends on the driver's behavior. If the driver accelerates more abruptly and faster, the maximum SOC must be shifted accordingly to avoid undercharging. Otherwise, the driver might feel a negative impact if his power is suddenly limited at low SOCs.

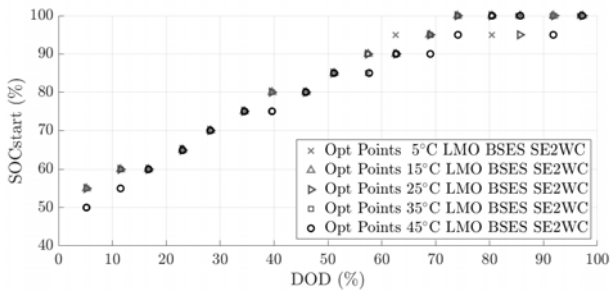

(a)

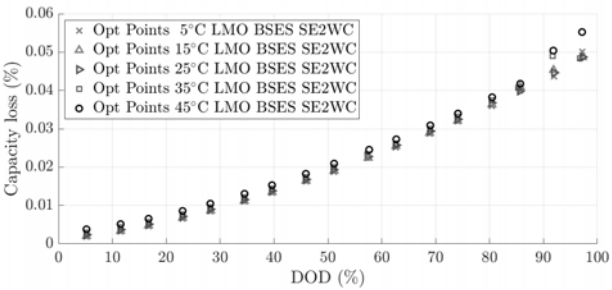

(b)

Figure 4.14: Influence of temperature on optimization results.

Since temperature is reported to accelerate aging, Fig. 4.14 illustrates the influence of temperature changes on the choice of optimal initial SOC. Fig. 4.14 (a) presents the correlation of the optimal initial SOC over DOD for different temperatures from 5°C to 45°C. The positions of the optimal points vary only slightly and without a temperature-induced trend. Fig. 4.14 (b) depicts the capacity loss over DOD. Whereas capacity loss

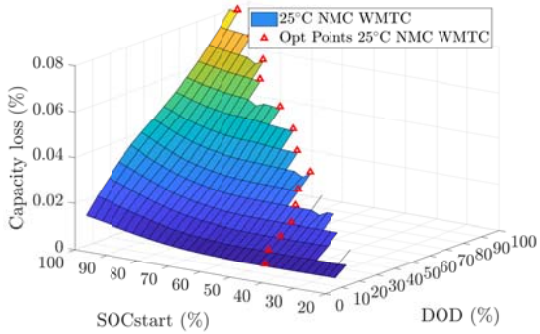

(a) NMC with WMTC

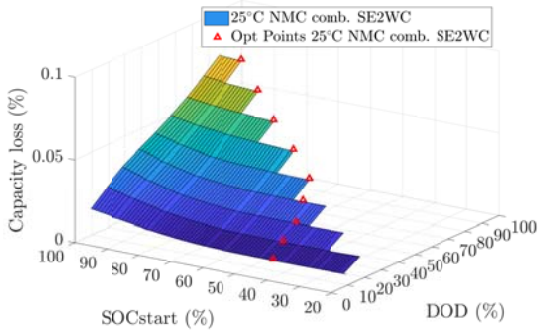

(b) NMC with combined SE2WC

Figure 4.15: Optimal initial SOC vs DOD for a NMC cell as presented in [205].

is almost the same for 5°C and 15°C, an increase is observed for larger temperatures. Observations correlate with the exponential trend of the Arrhenius law which has been used to describe thermal effects. This approximation applies to typical operation temperatures, but no negative effects of very low temperatures can be modeled. Overall, temperature variations do not seem to influence the choice of the optimal initial SOC for positive temperatures.

4.3.3 Influence of cell chemistry and aging model

Model-based optimization relies on the underlying model for solving the given problem and can only converge to the optimal solution on the basis of this model. The results of the test campaign showed that – although a similar general aging trend can be observed – the aging characteristics are not necessarily uniform and differ between different cell types. However, a diligent comparison with other cell chemistries is only possible to a limited extent as the model development and adaption requires a thorough test cam-

paign with both calendar and cycle aging scenarios over various influencing factors. In this case, only the NMC cell described in [68, 205] provides sufficient information for accurate model fitting. The EEM base and thermal model as well as the empirical aging relationships are built up for this chemistry and optimized accordingly.

Fig. 4.15 depicts the resulting capacity loss of a daily cycle over DOD and initial SOC. Markers highlight the optimal initial SOC for each DOD. In comparison to the optimization results of the LMO cell in Fig 4.9 (b), the increased capacity loss at lower initial SOCs is less dominant. As a result, the optimal SOC is the lowest possible SOC for DODs larger than 40%. At lower DODs, the lowest aging is achieved at about 42% to 50%. Still, the optimal values can be approximated by linear functions with a lower slope for DODs below 40% than in between 40% and 90%. Thus, the optimal solution is limited by the electrical properties of the cell. Lower initial SOCs would result in a violation of the lower voltage limit of the cell during discharge.

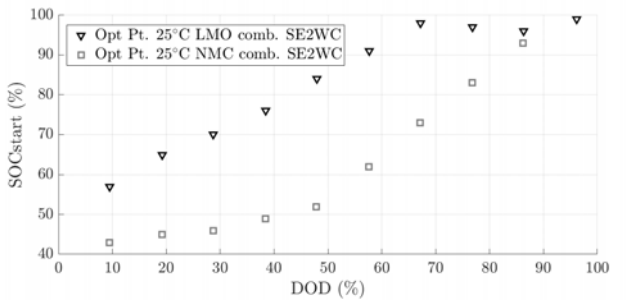

(a)

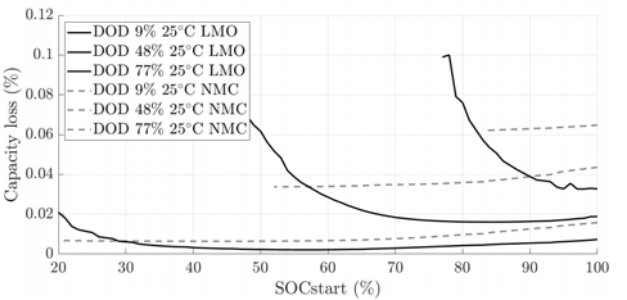

(b)

Figure 4.16: Comparison of optimization results of the LMO to a NMC cell.

Fig. 4.16 describes the differences between LMO and NMC in more detail. In Fig. 4.16 (a) the optimal initial SOC to DOD characteristic is presented. In the case of LMO, the optimal choice of initial SOC starts at 57% for a DOD of 9.7% and increases linearly to

98% at 68%. The optimal choice for NMC starts already lower at 42% SOC and increases to approximately 52% SOC for a DOD of 48%. From 48% to 86% DOD, the minimum initial SOC with which the driving cycle can still be completed shows the least capacity loss. Fig. 4.16 (b) displays the contour lines of the initial SOC for three DOD. Capacity loss of the LMO cell increases slightly for low initial SOCs and a shallow cycle of 9% DOD. Larger DODs such as 48% and 77% indicate that aging increases drastically at low voltages and, therefore, initial SOCs. This effect cannot be recognized in case of the NMC cell. Here, capacity loss decreases steadily over SOC. This shows that the NMC cell can be operated in a lower voltage range than the LMO cell. LMO suffers from manganese dissolution and the formation of Mn-ions at low voltages, which lead to an increase in the formation of side products during cycling. NMC is less susceptible to manganese dissolution due to the lower manganese content and improved material stability. This allows NMC to operate at lower voltages without increased aging.

Aging varies with the choice of different cell chemistries as some reactions are accelerated, decelerated, or do not occur at all. Electrode, separator, and electrolyte material influence aging. If an empirical aging model is used, it can be adapted to the peculiarities of each cell and cell chemistry. Therefore, the influence of the cell model and model variations on the optimization results are examined. Both empirical relations, which were introduced in section 4.1.2, are compared.

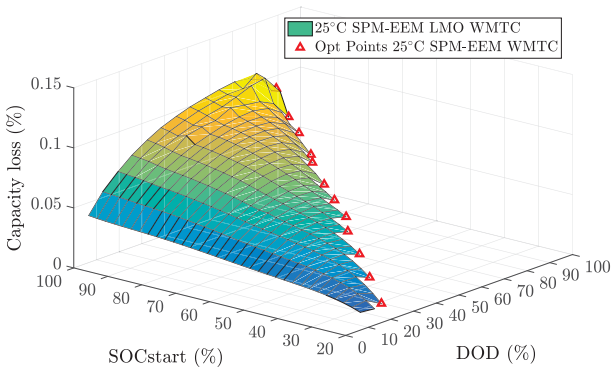

Figure 4.17: Optimal initial SOC vs DOD for the LMO cell using the SPM-EEM model.

The SPM-EEM aging relation leads to slightly different characteristics than the previously presented model. Fig. 4.17 indicates that the lowest possible SOC leads in this case to the least capacity loss. In contrast to the previous results using the conventional model, no quadratic behavior is observed. Fig. 4.18 (a) draws the choice of the optimal initial SOC over DOD. At a DOD of 20%, the optimization results using the SPM-EEM aging model indicate that an initial SOC of 25% leads to the least battery aging while still being able to reach the destination. Likewise, the optimal SOC lies 5% above the DOD for each of the scenarios. This corresponds to the SOC grid width. Contour lines for the development of capacity loss over initial SOC at four DOD levels are presented in Fig. 4.18 (b). Results show an almost linear decrease of capacity loss over initial SOC. In contrast to the conventional aging model, the SPM-EEM leads to a linear influence of

average voltage on aging and not a quadratic one. This might explain the linear decrease in the optimization.

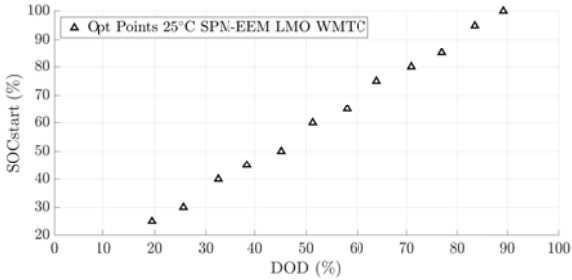

(a)

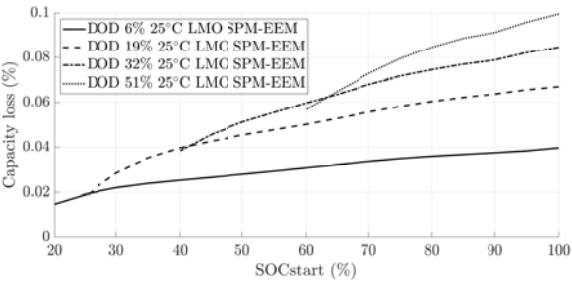

(b)

Figure 4.18: Resulting optimal initial SOC over DOD (a) and capacity loss over DOD at exemplary initial SOC (b) for the LMO cell using the SPM-EEM model.

As optimization results seem to be susceptible to model changes, additional simulations using a more accurate model and validation cell tests should be conducted. In addition, it has to be proven that this one-day optimization represents the capacity loss and aging over the whole lifetime. Validation tests and simulations are, therefore, described in the next section.

4.4 VALIDATION

4.4.1 Cell test setup

The obtained optimal initial SOC and charging profile were used to validate the optimization results and the basic assumption that such a one-day optimization is able to represent the whole lifetime. Therefore, nine LMO cells were cycled using the described one-day profile.

- Three cells were charged using the optimal initial SOC and charging profile. These are labeled as OPT cells in the following.
- Two cells were charged in a conventional way (CONV), meaning full CC/CV charging using a constant current of 6 A (0.5 C).
- Additional two cells are cycled by using the optimal maximum SOC obtained from the optimization but a conventional 0.5 C charge directly after the charger is plugged in in the evening. These are referred to as CONV-SOC cells.
- The remaining two cells, which were taken from batch A1 and A2 (see section 3.2.2) are used to identify differences between the cell batches.

The derived combined SE2WC is used instead of WMTC as test profile because it is able to more accurately predict the Shanghai driving style and battery stress. In addition, at the start of the validation tests only optimization results for the combined SE2WC were available. The cycle was repeated twice instead of once to accelerate the aging process due to a larger DOD (29%). In this case, an optimal initial SOC of 82.5% was calculated for the unlimited combined SE2WC as introduced in Fig. 4.13.

The current profiles applied to the cells are shown in Fig. 4.19 and some areas are enlarged in Fig. 4.20. The cells are fully charged at the beginning. The cells, which are cycled using optimized SOC and both optimal and conventional charging, are discharged to reach an initial SOC of 82.5% based on ampere counting (Fig. 4.19 middle and bottom, Fig. 4.20 3)). Then, 2 times the current calculated from the SE2WC is applied. After a rest period of 8.5 h resembling the working time, the same driving profile is repeated again. In case of the conventional strategy, the cells are then fully charged using CC/CV charging. For the OPT profile, the optimal charging profile is used to charge to the optimal initial SOC again. Similar to the optimized charging profile using 4xWMTC, the profile charges the cell a little bit at the beginning and then almost at the end of the charging period. The CONV-SOC strategy charges the cells directly in the evening. However, a lower and constant CR of 0.5 C is used to resemble similar charging currents as for the OPT strategy. After 3 weeks of cycling, the capacity of the cells is measured and the cells are fully charged and discharged. Afterwards, the same process is repeated.

4.4.2 Validation results

Results of the validations tests are presented for capacity loss at first. DVA is then used to briefly discuss the source of different aging characteristics.

Capacity
Fig. 4.21 (a) displays the resulting remaining capacity of the CONV (crosses), OPT (tri-

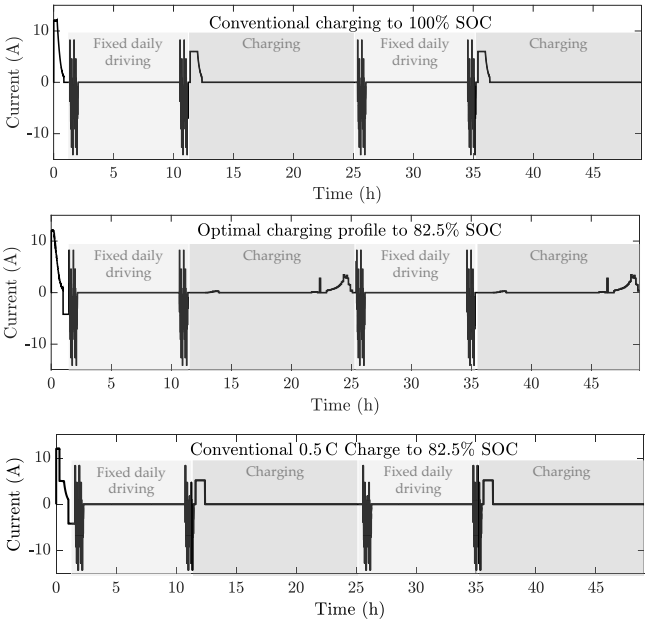

Figure 4.19: Current profiles used for validation for conventional CC/CV charging after driving SE2WC twice in the morning and twice in the evening (CONV, top) and optimized initial SOC of 82.5% together with optimal charging profile (CONV-SOC, middle) and conventional 0.5 C CC charging at optimal initial SOC (OPT, bottom).

angles), and CONV-SOC (circles) cells. Both equivalent full cycles and passed time in days are presented as x-axis. During the cycling period of half a year, the cells cycled using the OPT strategy showed a higher remaining capacity. The capacity even slightly increased initially for one cell. During the test, the capacity of the OPT cells showed almost no capacity loss within the first 40 days. Subsequently, a slightly faster capacity decrease is observed for the OPT cells than for the CONV cells. The CONV-SOC strategy shows a similar characteristic to the OPT one. The cells age only slight faster than with the optimal strategy. Only after 180 days, the cells showed a small increase in capacity. An explanation might be that the cells were not cycled for several days in between these measurements as the tests had to be shortly stopped. It seems that the cells cycled at OPT conditions recovered some capacity during this phase. Results indicate that most of the capacity saving potential can be already achieved by using a lower initial SOC for cycling. After 11 efcs or 45 days, the CONV cells show a capacity loss of already 3.5% whereas the CONV-SOC leads only to a loss of 0.7% and the OPT strategy does not show any decrease in capacity at all. At this stage, 80% less aging can be achieved by solely adapting the initial SOC. After approximately 39 efc and 150 days, capacity loss is in average at 7%, 5.5%, and 5% for the CONV, CONV-SOC and OPT strategy,

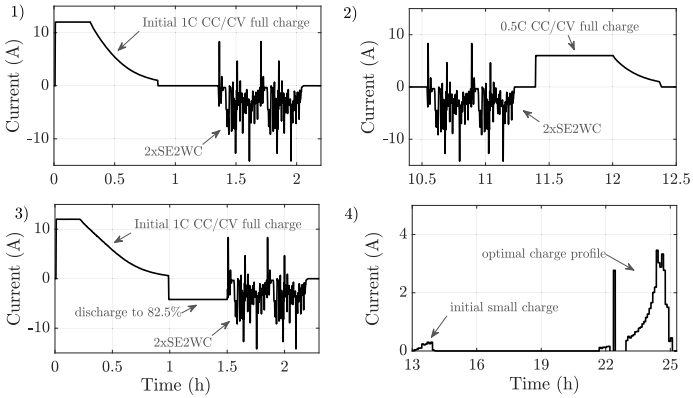

Figure 4.20: Detail view of current profiles used for validation. 1) Initial full charge and first discharge/driving phase and 2) second discharge phase and CC/CV charge for conventional strategy. 3) Initial full charge and discharge to 82.5% SOC followed by first discharge phase and 4) charging phase for the optimal strategy.

respectively. This corresponds to 21% less aging by decreasing the initial SOC and an additional 8% by adapting the charging time and profile.

An SPM as introduced in section 3.4 and [182, 186] is used to estimate the expected total lifetime of the cells. SPM offer a higher accuracy and provide a deeper insight into cell processes compared to the EEM used for optimization. They can therefore be used to justify the results. Besides, results of the calendar aging campaign can be used to compare the estimated lifetime. Approximately 85% of the optimized day profile are storage phases. The E2W is only operated or charged for a duration of 3.6 h each day. This leads to a high proportion of calendar aging compared to cycle aging effects. A detailed description of SPM equations is provided in section 3.4. In addition to the SEI aging description, a lithium plating model is supplemented to predict the sudden capacity drop at the EOL. The side current induced by lithium plating $i_{s,lipl}$ can be described by the exchange current density induced by lithium $i_{o,lipl}$, charge transfer coefficient $\alpha_{a/c,lipl}$, and the overpotential of the lithium plating side reaction η_{lipl} as described in [136, 257].

$$i_{s,lipl} = i_{o,lipl} \left(\exp\left(\frac{\alpha_{a,lipl} F}{R T_{int}} \eta_{lipl} \right) - \exp\left(\frac{-\alpha_{c,lipl} F}{R T_{int}} \eta_{lipl} \right) \right) \tag{4.23}$$

Lithium plating occurs only at negative potentials η_{lipl}. Lithium stripping is neglected. The exchange current density $i_{o,lipl}$ results from the electrolyte lithium content. It can be adjusted by a reaction rate for plating k_{lipl}: $i_{o,lipl} = F k_{lipl} c_e^{\alpha_{a,lipl}}$. This side current induces a growth of plated lithium. The layer thickness δ_{lipl} can be described by

$$\frac{\partial \delta_{lipl}}{\partial t} = \frac{i_{s,lipl} M_{lipl}}{F \rho_{lipl}}. \tag{4.24}$$

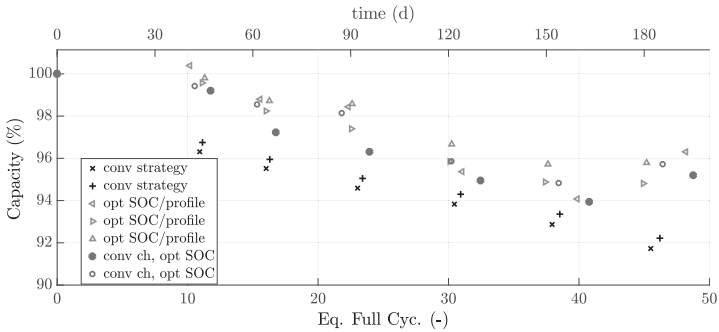

(a) Test results

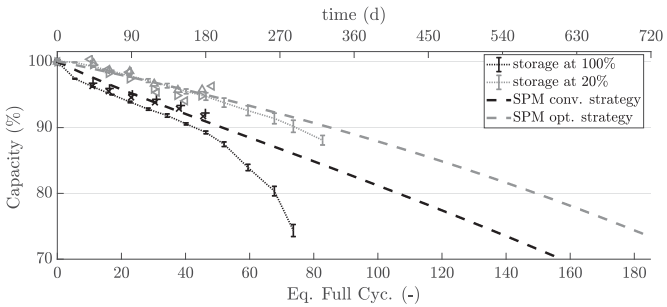

(b) Prediction

Figure 4.21: Remaining capacity of the cells cycled under the optimized (OPT), conventional (CONV), and conventional charging with optimal SOC strategy (CONV-SOC). (a) Detail of validation tests. (b) Lifetime prediction using storage results and SPM.

A resulting lifetime approximation and improvement might be given as shown in Fig. 4.21 (b). Results of the SPM aging model are shown as dashed lines for the conventional and optimal strategy. Further, results of the test campaign for storage at 20% and 100% are displayed as solid line. The CONV strategy leads to a slightly lower aging than storing the cells at 100% SOC. If the EOL of the cell is defined at 80% remaining capacity (EOL80), the stored cells reach it after approximately 270 days (0.75 years). The SPM model predicts the EOL80 of the CONV cells after 400 days (1.1 years). In case of the OPT charging strategy, the SPM predicts that the cells reach their EOL80 criteria after 580 days (1.6 years). Storage results at 20% SOC indicate a similar trend. Overall, storage and SPM results show that the OPT strategy might be able to improve the lifetime by half a year. In total, the optimization of initial SOC together with the charging profile shows promising results. Validation tests indicate that the optimal solution for a one-day scenario is also optimal for repetitions of the same cycle and the simplified EEM with empirical aging equations predicts the overall aging well.

Differential curve

An analysis of the ICA might provide a deeper insight into the reason of the lower capacity loss of the optimal strategy. Fig 4.22 presents the resulting incremental capacity over voltage for a (a) 1 C and (b) 0.1 C discharge at the end of the tests. The total capacity corresponds to the area under these curves. As described in section 3.3.3, three distinct peaks can be identified which become more dominant the lower the discharge rate. Results for the first two cells correspond to the CONV strategy (red line). Cells 7 and 8 represent the CONV-SOC strategy with a charge to the optimal SOC (yellow dashed). The OPT strategy was used to cycle cells 9 and 10 (green). All cells showed an almost identical DVA curve at the beginning of the tests.

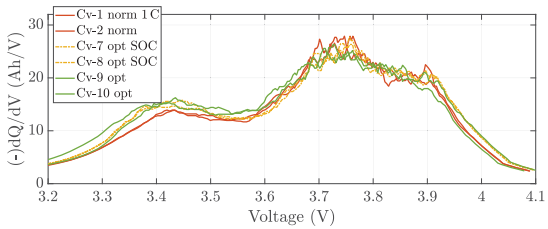

(a) 1 C

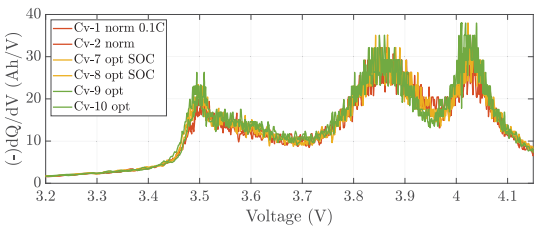

(b) 0.1 C

Figure 4.22: Comparison of ICA at EOT for validation tests at 1 C (a) and 0.1 C (b) for the three test cases (approx. 46 efc).

For a 1 C discharge, the NMC induced peak at about 3.4 V reduced visibly for the conventional strategy. However, differences are quite small due to the low number of efcs. For lower discharge rates, the difference becomes less distinct. Still, a slight shift of the NMC peak to the right can be observed. This corresponds well to the observations of the aging test campaign where this NMC peak X remained visible for cycling at low SOCs of 10-30% and 5-55%. Peak II at about 3.75 V for 1 C and 3.85 V for 0.1 C seems to be mostly unaffected by the selected strategy. For low discharge rates, peak I at approximately 4.02 V also shows a larger decrease for the conventional strategy. The combined strategy also shows a visible decrease in peak I, although it preserves the peak more accurately than the conventional strategy. It can be concluded that a change of initial SOC mostly influences peak X, which corresponds to the NMC content in the positive electrode. In addition, peak I seems to be influenced also by the charging strategy and

current. However, no reliable conclusions can be drawn as the curves vary only slightly due to the low capacity loss.

Influence of cell progress
Whereas cell batches A1 and A2 are specified as pure LMO cells, cells of batch B are labeled as LMO-NMC cells. The higher NMC content has already been observed in the initial DVA analysis in section 3.3.1.3. Since variations in the aging behavior between batch A2 and B might occur, a reference validation test using the optimal strategy was conducted to identify these.

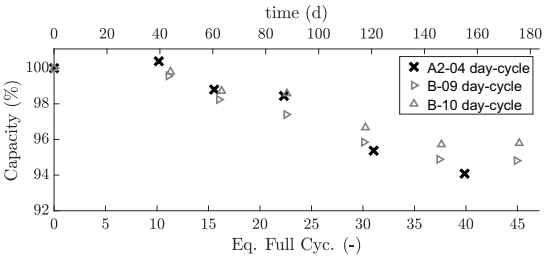

Figure 4.23: Aging comparison of batch A2 and B.

A comparison of the capacity loss of the cell batches A2 and B is provided in Fig. 4.23. Approximately 45 efc were recorded over 180 days of cycling. The cells show a similar aging behavior at first. Since the cells are rested during approximately 90% of the day, a capacity loss of only about 5% is observed after half a year. This equals the capacity loss of a calendar aging scenario with 50% SOC. Only after 30 efc, the capacity of batch A2 decreases slightly more than the capacity of batch B. This might result from the influence of the increased NMC content of cell batch B, which improves the cycle life stability of the cells. However, the differences are relatively small and might also result from cell-to-cell variations.

Results can be further analyzed using the ICA curves as shown in Fig. 4.24. The initial ICA at 0 efc is compared to the ICA at 45 efc. The increased NMC content of batch B is clearly visible by the larger peak X at 3.45 V and the less distinct LMO-specific peaks I and II, which are superimposed by NMC-specific characteristics. After approximately 45 efc and 180 days, peak X has in both cases barely changed but peak I and II are less distinct. The cell resistance of batch A2 decreased, thus a lower capacity drop is observed. Peak I is shifted by 0.05 V to about 3.9 V. Peak II becomes less distinct but is also shifted by 0.5 V. Peak X, on the other hand, remains at approximately 3.4 V or is even shifted to lower voltages. The cells of batch B show no significant change in resistance, which might result from improved cell composition and formation. Peaks I and II are less dominant for batch B and they are superimposed by other side peaks due to the increased influence of NMC. In both cases, the main loss in capacity is observed in the voltage range above 3.6 V, mainly due to LMO. Thus, it can be assumed that the aging properties, using a realistic operating scenario, show no significant changes after 180 days and between an NMC content of about 5% (A2) and 30% (B).

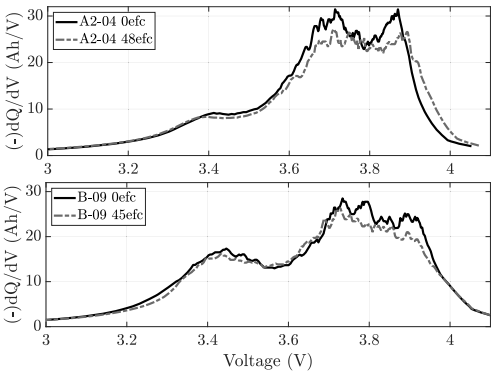

Figure 4.24: ICA of batch A2 (top) and B (bottom).

4.5 HEURISTICS

Although simplified models are already derived and used for optimization, the solution of such a problem requires suitable solvers and computational power. Only very basic control devices are available in most E2W with limited memory and computation units. Therefore, characteristic maps or other heuristic rules are commonly used. In this case, heuristics for the optimal charging strategy can be derived. The optimal maximum SOC can directly be taken from Fig. 4.12 or similar initial SOC vs DOD characteristic maps. A linear relationship of the maximum SOC over cycle DOD can be seen which varies slightly depending on the used driving profile, cell chemistry and aging model.
The optimized charging profile itself varies more. However, if the optimized charging profiles are evaluated more closely and the initial small charge is neglected, a common trend for larger DODs can be observed in Fig. 4.25. Optimal charging profiles and corresponding temperature increases for various maximum SOCs are depicted for driving 2, 3 and 4 times the SE2WC.

In average, the optimal profiles all show an exponential decrease in current shortly before the end of the charging period. An explanation of the exponential decrease is given by the temperature characteristics. The charging profile needs to satisfy the temperature constraints. The cooling characteristic leads to an exponential decrease in temperature. The current rises approximately linearly before the exponential decrease. In total, a heuristic approximation might be given by

$$I_{ch,lin}(t) = m\,t + I_0\,, \qquad I_{ch,exp}(t) = I_0\,\exp(-a\,t)\,. \tag{4.25}$$

The charging profile needs to charge the cell by the lost charge throughput Q given in Ah. As a result, $\int I_{ch}(t)\,dt = Q$, or more explicitly:

$$\int_{\tau=-t_{lin,h}}^{0} (m\,\tau + I_0)\,d\tau_h + \int_{\tau=0}^{t_{exp,h}} I_0\,\exp(-a\,\tau_h)\,d\tau_h \overset{!}{=} Q \tag{4.26}$$

Without loss of generality, let the time t range be $-t_{lin}$ to 0 for the linear and 0 to t_{exp} for the exponential charge phase. Assuming $a = 1.8$ and the charging times to be

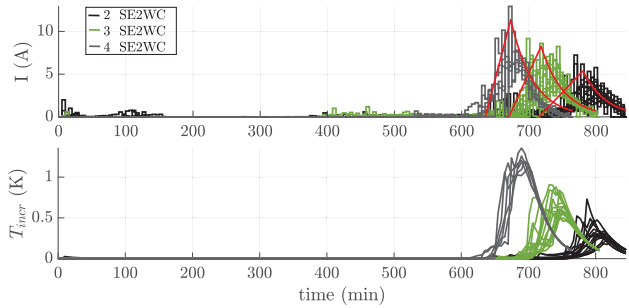

Figure 4.25: Overview of optimal charging profile and corresponding temperature increase for driving the SE2WC 2, 3 and 4 times. The derived heuristic charging strategy is shown in red.

fixed, this equation can be solved for the maximum charging current I_o at given DODs represented by Q according to

$$I_o = \frac{a\,Q}{0.5\,a\,t_{lin} - (\exp(-a\,t_{exp}) - 1)}. \tag{4.27}$$

The total charging time remains at about 130 min for all scenarios. However, the linear charging time becomes smaller the larger the DOD (Q), and the exponential time increases likewise. This leads to the empirical relation that

$$t_{lin} = \frac{Q_{total}}{Q}\,0.5\,h \text{ and } t_{exp} = 2.17\,h - t_{lin}. \tag{4.28}$$

In (4.27) time is of unit h as charge throughput is typically provided in Ah. Q_{total} represents the maximum cell charge throughput. This results in values I_o of 5.4 A, 8.3 A, and 11.4 A for the given three scenarios with Q being 5.0 Ah, 7.2 Ah, and 9.5 Ah, respectively. Fig. 4.25 shows the resulting estimated charging currents in red. They match the optimal profiles well. This empirical relation can, therefore, be used to minimize cell aging. Parameter a is set empirically but corresponds closely to the cooling characteristic of the cell. A low DOD results in a smaller amount of charge and thus to a lower temperature increase. Consequently, the described empirical relation correlates closer to the optimal charging strategy for large DODs. Results for lower DODs as shown in Fig. 4.6 deviate slightly from the derived heuristic.

5

CONCLUSION

The transition from lead-acid to Li-ion batteries has significantly enhanced e-mobility in recent years. The range could be extended, but battery aging and the resulting replacement costs are still high. Especially for E2Ws, which are popular in Chinese metropolises such as Shanghai, the battery is the most expensive part. Battery lifetime and its extension is therefore a key challenge.

Before battery lifetime can be improved, a typical operation and use case of the system under consideration must be identified and described. This study focuses on E2W operation in Shanghai. Most standardized driving cycles are developed for emission testing of conventional vehicles and use American or European driving conditions. Due to the specific power limitations of E2Ws in Shanghai and different street and traffic conditions, E2W driving behavior differs from the common standardized driving cycles. Driving conditions are recorded using survey and speed data from test participants. The quality of speed tracking by conventional smartphone apps is evaluated. Two different E2W types, BSES and SSES, are identified and a novel Shanghai E2W driving cycle (SE2WC) is derived which resembles local peculiarities. In combination with vehicle and motor dynamics, the recorded typical speed can be converted into load profiles and localized battery stress information.

The analysis and modeling of battery lifetime is an important aspect of this study. Starting from the introduction of basic cell aging processes, differences between different Li-ion cell chemistries and modeling approaches are highlighted. The LMO cell is investigated in more detail because it is a promising candidate for use in E2Ws in China due to its relatively high energy content and low price. Accelerated aging tests conducted over a period of three years provide a profound background for analyses. Capacity loss, resistance increase, and DVA are presented and aging behavior is examined. Results are then used to establish a SPM. Model simplifications are derived and a novel SPM motivated EEM aging relation presented. Results of LMO aging are compared with other cell chemistries such as NMC and LFP to investigate chemistry-specific effects. Subsequently, both the conventional EEM and the SPM-EEM are adapted to the LMO cell. The results of these simplified models are compared and validated against the SPM model and additional cell measurements. These show that the simplifications used for the EEM and empirical aging are valid and accurate, while the complexity of the model and computation time are reduced.

With a model of all powertrain components such as vehicle dynamics, motor characteristics, and battery aging, a simulation environment covering various depths of detail can be built. A detailed microscopic model, which covers motor dynamics and electrochemical cell processes, can be used for simulation and validation purposes. A derived

simplified macroscopic model reduces the complexity and time of the calculation with an acceptable loss of accuracy and generality. The latter consists of a static speed-to-power conversion and an electrical equivalent representation of the cell and is better suited for complex optimization tasks. Both modeling depths are compared and validated against each other.
Finally, a model-based optimization framework for battery lifetime improvement by SOC and charging optimization for E2W, which is based on an empirical battery aging model, can be set up. The results indicate that the battery should be charged as late as possible using the daily commuting scenario. Derived heuristics show that the optimal charging time is about 2 h prior to usage. The battery current used for charging is limited due to the temperature boundary condition as well as higher aging at larger currents. It can be approximated by a linear and exponential function. The maximum charging current depends on the DOD. Under consideration of the driving cycle and corresponding DOD, an optimum targeted SOC level of the optimized charging profile has been identified. Since E2W power is not limited and no changes have been made to the driving profile, the driver should not experience any negative effects of the optimization. A simplified charging heuristic is introduced, showing a linear increase of the maximum SOC over the DOD. The charging profile indicates that an exponential decrease in charging current at the end of the predefined charging interval may be optimal.

In summary, following key aspects are the main contributions of this study:

- Model-based optimization of the battery charging strategy using a daily driving profile.
- Shanghai E2W driving cycle and daily driving behavior.
- Accelerated aging tests and aging analysis of a LMO cell.
- Li-ion modeling in different levels of detail (EEM and SPM) and cross-connections between these models.
- Heuristics for lifetime improvement by an optimized charging profile and SOC.
- Validation using the optimized charging strategy and a realistic use case for E2W in Shanghai.

Many questions regarding the influence of driving cycles and battery aging on the optimal operation and charging of an electric vehicle could be answered, but further research may improve the predictions. A first localized Shanghai E2W driving cycle has been introduced. An extended test campaign covering different districts in Shanghai and other cities can provide more insights into driving cycle variations and may help to generalize this SE2WC.
The modeling of lithium ion batteries and aging processes remains a challenging topic. In addition to the system-level modeling carried out in this study, more advanced electrochemical models together with half-cell tests and cell disassembly can provide a better understanding of the causes of aging.
Considering the optimization structure itself, a static setup is presented in this study. However, temperature fluctuations also occur over a day or a year, so that the strategy may vary. For example, it may make sense to pre-heat the battery in winter by allowing a higher temperature at the end of the charging process.
The use case can be adapted to different daily driving habits. If, for example, only a short

distance is driven each day, it may not be necessary to charge after each day, but perhaps once after two days. In addition, varying daily driving schedules such as working days and weekend schedules may lead to more realistic strategies. In this context, the scheme can be extended to use real-time driving data and route information provided by a smartphone instead of averaged driving patterns. In this case, the user-specific driving style and aggressiveness can be included and used to improve predictions and thus the charging strategy.

A

METHOD DETAILS AND DESCRIPTIONS

A.1 DRIVING DATA COLLECTION CAMPAIGN

A.1.1 Vehicle and simulation parameters

Table A.1: Test E2W overview.

Component	Parameter	Details
Battery	Voltage	60 V
	Current Range	-30 to 40 A
	Nominal capacity	unknown
	Type	lead-acid
	Cells	5 x 12 V
Motor	Nominal Power	500 W
	Type	in-wheel
	Transmission	1:1
General	Range (approx.)	40 km
	Max. Speed	45 km/h
Data logger	Type	Vector GL 1000
	Analog resolution	10 bit
	Analog sampling rate	up to 1 kHz
	Analog voltage range	0-16 V
IMU & GPS	Type	IMAR iμVRU-01
Power measurement	Type	self-built
	Voltage range	0-60 V
	Current range	variable (0-20,40,80 A)
	Current measurement	non-invasive (hall sensor)

Table A.2: Vehicle parameters used for static power conversion.

Parameter	Variable	Initial Estimate	Unit
Vehicle mass	m	150	kg
Rolling resistance	c_r	0.017	-
Gravitational acceleration	g	9.81	$m\,s^{-2}$
Air drag coefficient	c_w	0.6	-
Air density	ρ_{air}	1.293	$kg\,m^{-3}$
front area	A_{front}	0.33	m^2
Slope force	F_{slope}	0	N
Motor efficiency coefficient	η	1	-
Nominal motor power	P	500	W
Consumer power consumption	P_{con}	20	W
(Nominal) battery voltage	U_{batt}	60	V
Cells in serial	N_s	16	-
Cells in parallel	N_p	2	-

Table A.3: PMSM parameters used for whole powertrain simulation. PMSM parameters as, for example, derived in [112].

Parameter	Variable	Value	Unit
stator flux inductance	L_d	$6.6\,10^{-3}$	H
stator flux inductance	L_q	$7.0\,10^{-3}$	H
pole pairs	p	3	-
motor inertia	J	$1.76\,10^{-3}$	$kg\,m^2$
permanent magnet flux	ψ_{PM}	0.053	$V\,s$
coil resistance	R_s	0.8	Ω
viscous friction gain	B	$3.88\,10^{-4}$	$N\,m\,s$
stator diameter	d_{st}	0.15	m
rotor diameter	d_{rot}	0.24	m
motor length	l_{mot}	0.05	m
Air gap	l_{gap}	0.001	m
motor mass	m_{PMSM}	0.5	kg
thermal conductivity stator/rotor	k_{sr}	50	$W\,(m\,K)^{-1}$
thermal conductivity to air	k_{gap}	0.2	$W\,(m\,K)^{-1}$
specific heat capacity	c_{pc}	800	$J\,(kg\,K)^{-1}$
copper factor	a_{Cu}	$3.9{\cdot}10^{-3}$	

Table A.4: Vehicle parameters used for whole powertrain simulation.

Parameter	Variable	Value	Unit
E2W wheel radius	r_{wheel}	0.1524	m
E2W & driver mass	m	150	kg
Rolling resistance	c_r	0.017	-
Gravitational acceleration	g	9.81	$m\,s^{-2}$
Air drag coefficient	c_w	0.6	-
Air density	ρ_{air}	1.293	$kg\,m^{-3}$
front area	A_{front}	0.33	m^2
Slope force	F_{slope}	0	N
Transmission factor	n	2	
Motor & transmission efficiency	η_{prop}	0.9	-
Reg. braking efficiency	η_{reg}	0.7	-
(Nominal) battery voltage	U_{batt}	60	V
Cells in serial	N_s	16	-
Cells in parallel	N_p	2	-
Air temperature	T_{air}	30	°C
Wind speed	v_{air}	1.4	$km\,h^{-1}$

A.1.2 Analysis of speed tracking equipment

Time-series data can be collected using smartphone sensors or professional test equipment on a test E2W. In this case, only a relatively low recording frequency of 1 Hz is possible using the selected smartphone applications. Data on the test E2W can be gathered at up to 100 Hz. The results are also published in [185]. The recording frequency has to be chosen in accordance with occurring dynamics. In this case, vehicle dynamics should be captured. Vehicle dynamics of EVs are reported to lie at about 3 Hz [54, 135]. However, as E2Ws are of a relatively low power (below 500 W), dynamics lower than 3 Hz might be possible. Additionally, [135] reported that recording frequencies below 10 Hz show a large energy variance. Recording frequencies above 15 Hz are recommended. However, too high recording frequencies amplify measurement noise and do not add information. [54] showed that too low recording frequencies as obtained in fleet management and recording over internet lead to an altered estimation error mean and variance.
Smartphone tracking and data collection have already been used for various studies. For example, [14] presented a research on smartphone-based travel behavior tracking. Methods for smartphone data based transportation mode or trip end time recognition were introduced in [222, 242] and [270]. [220] described a data collection campaign for cyclist speeds using a smartphone app by implementing a high and low speed filter. However, no analysis of the smartphone signal or comparison to more accurate speed estimations were done. Likewise, [51] analyzed the cycling speed using smartphone GPS data with similar filtering techniques but without an in-depth analysis. Thus, it has to be analyzed if the smartphone data are still able to estimate the driving profile and energy consumption.

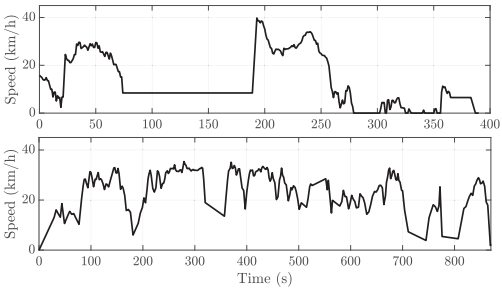

Figure A.1: Possible data inconsistencies occurring during smartphone test: no data being recorded due to missing signal (top) and low accuracy at slow speeds as some apps record depending on velocity changes (bottom).

As a reference, data recorded by the data logger on the test E2W is used. Recording frequencies of up to 100 Hz can be selected. A frequency of 5 Hz and 10 Hz is selected as the error means and variance is still acceptable, most vehicle dynamics can be covered, and higher frequencies might be seen. According to [135], standard deviation at 10 Hz compared to 100 Hz recording frequency is about 10^{-3} kWh/km in contrast to 10^{-1} kWh/km at 1 Hz. Typically, frequencies of 10 Hz or higher [22, 135] should be used for driving cycle synthesis. However, other studies select a lower recording frequency of 5 Hz [210] or even 1 Hz [34, 76, 119, 213, 265, 267] and still provide solid results. However, this might lead to erroneous energy predictions.
During the tests the E2W is equipped with professional measurement equipment including an IMAR IμVRU IMU and GPS based speed estimation, CAN based data logger as well as voltage, current and throttle measurement as described before. The test E2W reaches a top speed of 40 km/h during the drives.

Before being able to evaluate the smartphone data, it has to be analyzed and data inconsistencies as well as possible sensor failures have to be taken into account. As displayed in the exemplary data set in Fig. A.1, the accuracy of some smartphone data is low at slow speeds and data loss might occur. For example, a large time step between two consecutive measurement points was observed. Data inconsistencies can be identified based on the number of satellites in view, dilution of precision, or by analyzing the data. As the test area is located in the suburban area of Shanghai, buildings and other obstacles might block the view to the satellites. In average, the measurement equipment on the E2W used 7 satellites with a position dilution of precision (PDOP) below 5. A PDOP below 5 is rated as good and can be used for routing. On the other hand, no precision information could be automatically recorded for the smartphone tests. Based on observations during the test drives, the number of satellites used by the SME varied between 3 and 8. Data showing data inconsistencies as shown in Fig. A.1 were therefore neglected. This shows one drawback of using smartphones instead of professional test equipment, as the exact configuration and test setup cannot be checked. Instructions were handed to the participants on how to use the apps, however, misconfiguration as well as signal loss can still occur.

Fig. A.2a displays the speed profiles of 4 of the recorded trips. Data collected via smartphone measurement equipment (SME, red) are compared to the data recorded by E2W measurement equipment (E2WME, blue). Speed profiles recorded by SME and E2WME show similar results. The difference between data collected by SME and E2WME is rather small. Between 400 and 500 s of driving, data access is limited as the street is located under a bridge of the local highway. Here, the smartphone data show some inaccuracies, as the sensor is not able to estimate the location properly. Due to a more accurate measurement equipment, the test E2W is still able to provide accurate results. As the trips have a different length, the error ε is presented normalized by dividing the integral over the differences of each time step by the end time t_{end}.

$$\varepsilon = \frac{1}{t_{end}} \int_{t=0}^{t_{end}} |v_{SME}(\tau) - v_{E2WME}(\tau)| d\tau \tag{A.1}$$

Variable v_{SME} is the speed collected by SME and v_{E2WME} the speed collected by E2WME. The mean error between smartphone and test equipment is 0.87 m/s with a standard deviation of 0.28 m/s. Compared to the maximum speed of 40 km/h, the error is less than 10 % and, at a first glance, in an acceptable range. However, as described before, the influence of the different recording frequency might lead to a loss of information in context of vehicle dynamics and energy consumption. Therefore, the data are further analyzed.

Fig. A.2b presents the speed and acceleration of one test drive without SM inaccuracies due to signal loss. Data obtained by smartphone are displayed as red line, by E2WME as blue line and IMU acceleration is shown as dashed green line. The time from 1015 s to 1075 s is enlarged and displayed on the right side of this figure. When looking at the speed profile, both E2WME and SME, show a good match as already observed in Fig. A.2a. E2WME shows more fluctuations than SME. This can also be seen when looking at the acceleration. For both sensors, the acceleration is derived based on the speed profile. As a reference for the vehicle dynamics, the acceleration directly measured by the IMU is added. The E2WME shows larger fluctuations in the signal leading to unlikely acceleration values of $\pm 6\,m/s^2$. With a 500 W motor with peak power of 1.5 kW, a reasonable maximum acceleration at 10 km/h and 150 kg E2W mass would be

$$a_{max} = \frac{P_{peak}}{m\,v} = \frac{1000\,W}{150\,kg\,\frac{10}{3.6}\,\frac{m}{s}} = 2.4\frac{m}{s^2}\,. \tag{A.2}$$

This is a common issue of the raw data, as a maximum accuracy of ± 5m can be achieved without using aiding data. Therefore, often a Savitzky-Golay filter (sgf) is used to eliminate outliers and to smoothen the data. During standstill, the IMU sensor might show a small offset as the E2W cannot be held steadily and is turned to one side.

For a clearer comparison, the filtered E2WME signal is also shown in Fig. A.2b (dashed cyan). It can be seen that the filtered E2WME signal (light blue) correlates closer to the reference of the IMU signal and is able to smoothen outliers. However, low-pass filtering as done by a Savitzky-Golay filter, which uses polynomial regression and works similarly to a phase-offset free moving average filter, can be seen as an intelligent way of reducing the sampling frequency. Frequency peaks at multiples of 0.5 Hz are due to spectral leakage. This can be seen in the frequency analysis using fast Fourier transformation (FFT). Fig. A.3 shows the resulting frequency domain amplitude for all 8 driving profiles. The IMU frequency response shows no dominant vehicle dynamics

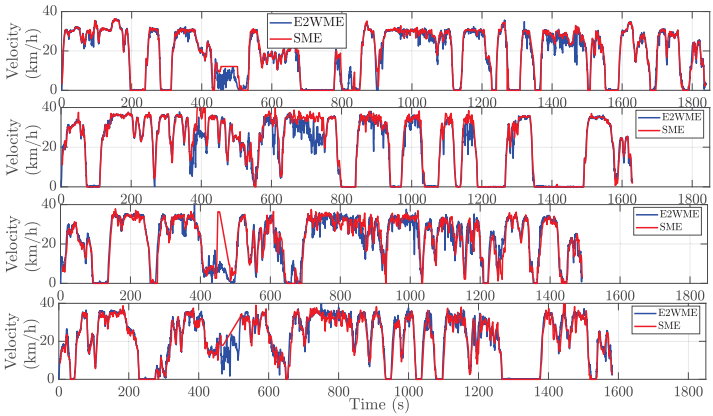

(a)

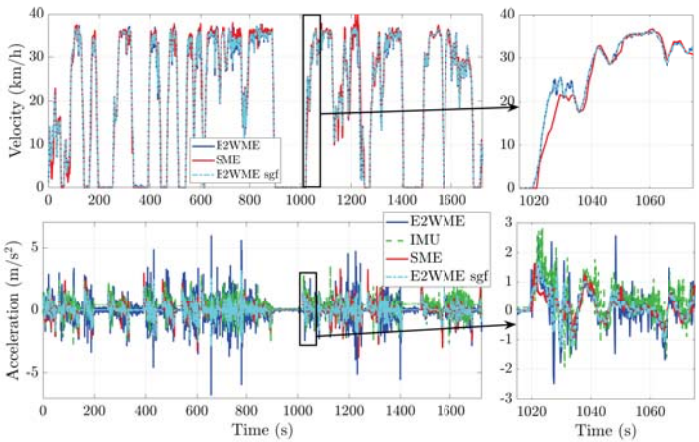

(b)

Figure A.2: a) Comparison of speed profiles recorded on the representative route showing the characteristic loss of the SME. The data collected by E2WME (blue) and SME (red) is displayed for four test drives on the test E2W. b) Detail comparison of driving profile using E2WME, SME, and E2WME adding a Savitzky-Golay filter. Vehicle speed is shown at the top and acceleration at the bottom.

above 0.5 Hz. Higher dynamics at about 3 Hz as suggested by [54, 135] might occur but no dominant frequency can be seen. As explained before, the E2W has a relatively low power which might lead to less influence of dynamic effects. In comparison to the unfiltered E2WME signal (second from top), the filtered E2WME signal (third from top) shows similar characteristics up to 0.5 Hz and suppresses higher frequencies as expected.

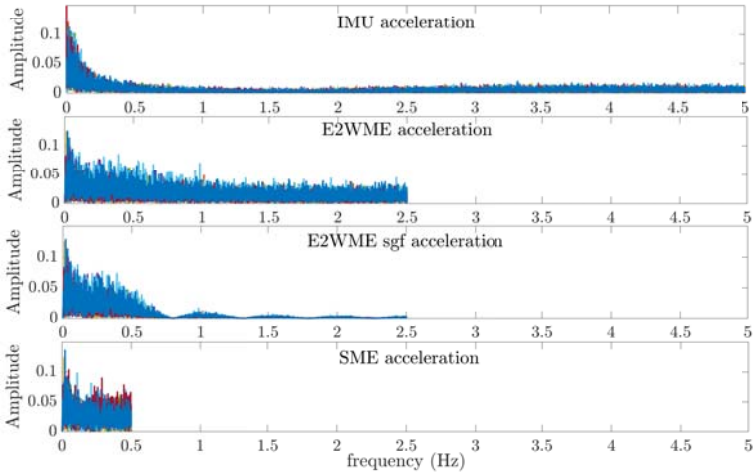

Figure A.3: Overview of FFT frequency analysis for the acceleration signals measured by E2W IMU (top), E2WME (second), E2WME filtered (third), and SME (bottom).

By doing so, a similar frequency domain behavior as the SME is obtained. The degree of filtering can, of course, be adapted by choosing different window sizes of the filter. In this case, the window size was increased until a good fit with the IMU acceleration was achieved leading to a window size of 11. As already seen in Fig. A.2b, the filtered E2WME and SME speed show similarities. For a more accurate evaluation, also the energetic consumption of the driving cycle is compared.

Therefore, a simple vehicle model is used. Total motor force F is calculated based on the acceleration F_a, air drag F_{drag}, rolling friction F_{roll}, and slope force F_{slope}.

$$\begin{aligned} F &= F_a + F_{drag} + F_{roll} + F_{slope} \\ &= m\,a + \frac{1}{2} c_w\,\rho_{air}\,A\,v^2 + m\,c_r\,g + 0 \end{aligned} \tag{A.3}$$

In this case, the slope force is assumed to be zero, as the test area in Shanghai is quite flat and no slope profile has been recorded. An overview of the parameters is displayed in Table A.2. The power P can then be calculated based on the forces F and speed v using the powertrain efficiency η. Additionally, a constant power P_{cons} of 25 W is added to account for additional consumers such as electric components, lighting, etc. A more detailed motivation and description of a powertrain model to convert the speed to a battery stress is provided in section 2.3. Summing up all power P from the trip start time t_0 to trip end time t_f, the energy E is estimated.

$$P(t) = \frac{1}{\eta} F(t)\,v(t) + P_{cons}, \quad E(t) = \int_{t_0}^{t_f} P(t)\,dt \tag{A.4}$$

The energy consumption using the E2WME, filtered E2WME, and SME is compared to the actual energy consumption based on battery current and voltage (Batt). The real

consumed power P_{batt} can be calculated based on battery current I and voltage V by $P_{batt} = V \cdot I$. In average, an actual energy consumption of 26 Wh/km is obtained as shown in Table A.5. As a comparison, Saxena et al. [202] reported that the average electrical consumption of 1.5 kW E2W with a top speed of 50 km/h in India is about 33 Wh/km. A lower power consumption might result from the lower power and top speed of 40 km/h of the Shanghai E2W.

Table A.5: Energetic analysis.

Measurement method	Mean energy (Wh/km)	Std. dev. (Wh/km)	Deviation to real (%)
Battery	26.07	1.38	0
E2WME	28.59	1.16	9.68
E2WME sgf	25.30	1.31	-2.95
SME	21.29	2.03	-18.32

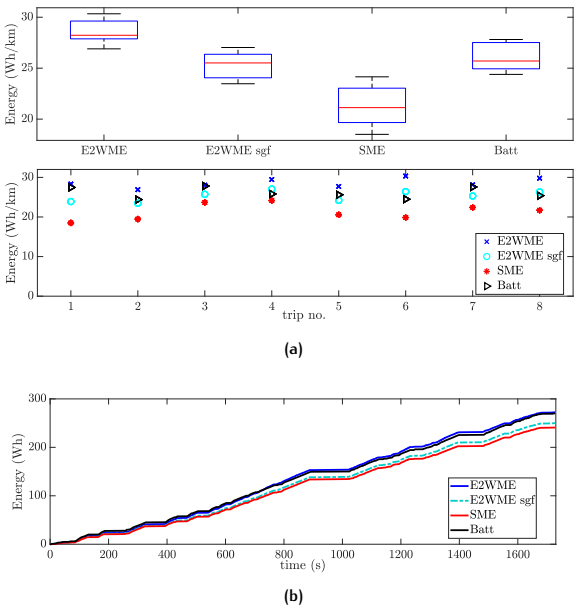

Figure A.4: a) Overview of median energy predictions, 25% and 75% percentiles, and minimum/maximum value obtained by E2WME, E2WMEsgf, SME, and based on battery measurements (top). Total energy for each trip using the four methods is shown at the bottom. b) Exemplary energy calculation for the trip shown in Fig A.2b.

Table A.5 provides an overview of the average energy calculated by using the E2WME, E2WMEsgf, and SME in comparison to the real energy consumption recorded. Additionally, standard deviations over the 8 recorded trips are shown. In this case, the raw E2WME data overestimates the energy consumption by about 10%. A Savitzky-Golay

Table A.6: Key characteristics of representative route.

Criteria	Unit	SME	E2WME	E2WME sgf	IMU / Battery
Distance	km	10.40	9.53	9.53	
Time	s	1727	1727	1727	
Avg. Speed	km/h	20.1	20.0	20.0	
Max. Speed	km/h	40.3	41.3	38.9	
Idling	%	19.2	14.0	18.4	
Cruising	%	19.9	10.0	17.4	
Accelerating	%	31.3	38.0	32.0	
Decelerating	%	29.6	38.0	32.2	
(Avg.) Accel.	m/s^2	0.55	0.73	0.57	0.54
(Avg.) Decel.	m/s^2	-0.58	-0.74	-0.57	-0.51
Energy	Wh/km	21.29	28.59	25.30	26.07

filter, which averages the data, reduces the energy and only slightly underestimates the real energy consumption by 3%. The SME leads to a lower energy approximation of 21.3 Wh/km, which is about 18% less than the real power consumption. Fig. A.4 underlines the lower energy estimation of the filtered and SME signal. The top plot shows the median (red line) and 25th and 75th percentiles (box) of the energy consumption using the four data sources. The lower plot displays the energy consumption separately for each trip. Similar results are also shown in [54]. However, energy calculation using (A.3) and (A.4) is very sensitive towards the vehicle parameters such as vehicle mass and motor efficiency as shown in [202]. Therefore, the total values and deviations from the real energy have to be taken with care. Still, the effect of lower accelerations leading to a lower energy consumption estimation can be seen. A detailed comparison of all key characteristics of the different data collection methods is provided in Table A.6.

Characteristic values representing a driving cycle are average velocity, trip time, distance, acceleration, and energy consumption as mentioned before. [128, 230, 231] evaluated that average trip length and distance, average speed, acceleration and deceleration, and proportion of drive to stop times can be used as representative parameters. Further evaluation criteria include maximum speed, average speed excluding standstill, average length of a single driving period from start till the next stop (for example due to traffic lights), proportion of driving patterns such as idling, cruising or acceleration and deceleration phases, and deviation from the speed or acceleration distribution. Phases are defined as follows: an acceleration phase corresponds to times when the acceleration is larger than $0.1\,m/s^2$, a deceleration phase likewise has an acceleration lower than $-0.1\,m/s^2$. Idling is present for $v < 0.5\,m/s$ & $|a| \leqslant 0.1\,m/s^2$, and cruising phases occur when $v \geqslant 0.5\,m/s$ & $|a| \leqslant 0.1\,m/s^2$. For average acceleration and deceleration calculation, only values greater than $0.1\ m/s^2$ are taken into account to adapt for measurement noise. The results can be summarized in short:

- Data need to be preprocessed to identify outliers, data failure, and other inaccuracies.
- This is commonly done by using accuracy measures such as dilution of precision and satellite number. Similarly, outliers and fluctuations can be smoothed by using a Savitzky-Golay filter which has a similar effect to an averaging filter.

- Energy differences mostly result from lower accelerations as a result of the recording frequency (smoothing). The same effect can also be seen for the Savitzky-Golay filter, which suppresses higher frequencies.
- Energy underestimation on a specific test route seems to be static. Therefore, a lower frequency data might also be used. In this case, more accurate energy estimations can be achieved by increasing the smartphone energy prediction by 10% to 20%.
- A lower recording frequency does not necessarily lead to erroneous acceleration and deceleration estimations.
- Raw E2WME data shows higher acceleration estimations due to the limited resolution of the signal (random jumps of about ± 5 m).
- The same effect results in longer acceleration and deceleration phases being identified in the raw E2WME data than in the SME and filtered E2WME data (see Table A.6).

In total, energy predictions might vary depending on the recording frequency and device but do not necessarily lead to false dynamics estimations. Results from smartphone tracking with 1 Hz resemble, in this case, most of the dynamics. This can be seen by comparing the accelerations to the IMU as shown in Fig. A.2b. Other vehicle types might, of course, show other dynamics. Therefore, no generalized statement about recording frequency and accuracy of driving cycles is possible. The influence depends on the test vehicle (different vehicle dynamics), test equipment (accuracy and frequency of the sensor), sensor data fusion (pre-filtering, etc.), and other environmental influences. If a proper smartphone app and test route is selected, the accuracy of data collection using smartphones with only 1 Hz recording frequency might still be sufficient for a driving cycle estimation.

In case a more accurate acceleration and energy consumption estimation is required, the data have to be improved. On the one hand, this can be done by increasing the recording frequency and accuracy of the data logging devices. On the other hand, if this is not possible, a driving cycle can be generated based on the lower frequency data. As introduced in Appendix A.1.3, this driving cycle might be enhanced by artificially increasing the sampling frequency. Therefore, information from a reference database is required. Differences between a more accurate and a lower frequency recording equipment can be derived based on reference drives as presented in this chapter.

A.1.3 Sensor fusion with sampling rate adjustment

The introduced driving cycle construction methods such as cut and clip and Markov chains typically rely on speed data obtained by one data collection method. Data from different sensors might also be used but is not combined. The cut and clip approach uses the recording frequency of the used microtrips. A sampling rate has to be pre-defined for the Markov chain approach and should represent the sampling rate of the data. In general, these approaches cannot combine different sensors and data sources. The used data collection method, smartphone speed tracking, provides only speed profiles with a sampling rate of 1 Hz. However, additional measurement equipment on the test E2W might be used to record data using 5 Hz or 10 Hz. This leads to the question whether and how data from different sensors and sampling rates can be fused to increase the sampling rate of a derived typical driving cycle and improve its dynamics?

Generally, different sensor fusion methods exist to combine signals of different sampling frequencies. For example, a Kalman or particle filter can be implemented to fuse data from different sensors [38, 84, 85] and multi-rate signals [55]. This results in an improved estimation result as every sensor has different advantages and disadvantages such as recording frequency and accuracy. Kalman filters can be implemented online or offline. However, a Kalman filter assumes that all sensors are available at (almost) every time instance and record the same route. In this study, only one sensor is available during the smartphone test campaign. Reference data using three sensors is available for a limited number of drives. These drives were conducted on a test route which resembles the average data collection results best. As the aim is to improve a typical and not an actual driving cycle for Shanghai E2Ws, the reference data might be used to estimate typical higher frequency dynamics.

In case a specific frequency is dominant or a frequency spectrum is known using other sensors, these frequencies might be added to a signal. Based on the discrete Fourier transformation (DFT), a signal can be transformed from the time to a frequency domain. A continuous time signal $x(t)$ is therefore resembled by a sampled signal $x(n)$ consisting of superposed cosine signals as shown in (A.5).

$$x(n) = \sum_{k=0}^{N-1} X_F(k) \left[\cos\left(\omega_o \, k \, n + \varphi(k)\right)\right] \tag{A.5}$$

Only real-valued signals are assumed to occur in a speed profile. Parameter N stands for the total number of frequency coefficients, k is the current index. Further, the phase offset $\varphi(k)$ and angular frequency $\omega_o = \frac{2\pi}{N}$ are introduced. By knowing the magnitude $X_F(k)$, frequency $\omega_o \, k$, and phase offset $\varphi(k)$ of a signal in the frequency domain, the time domain signal can be reconstructed. For a signal recorded at 1 Hz, only frequencies up to 0.5 Hz can be used (Nyquist Shannon sampling theorem). When re-sampling a 1 Hz signal to 10 Hz by inserting zero valued samples in the time signal no additional frequency information is added. However, after up-sampling by 1-to-M (with M being a multiple of the initial sampling rate), a filter has to be added to reject spectral replicas as described in [90]. In case zero-order hold or linear interpolation is used for re-sampling, the frequency spectrum is slightly distorted but less dominant changes in the up-sampled time signal occur. As the signal should be compared in the time domain later on, linear interpolation is used for simplicity.

If higher frequency (f_{hf}) information from another sensor is available, the higher frequencies of this signal might be used to describe the dynamics. This is exemplarily shown in (A.6), where a lower frequency signal (lf) is aided by the higher frequency (hf) components of a second sensor.

$$\begin{aligned} x(n) &= x_{lf}(n) + x_{hf}(n) \\ &= \sum_{k=0}^{N_{lf}-1} X_{F,lf}(k) \, \cos\left(\omega_{o,lf} \, k \, n + \varphi_{lf}(k)\right) \\ &+ \sum_{k=N_{lf2hf}}^{N_{hf}-1} X_{F,hf}(k) \, \cos\left(\omega_{o,hf} \, k \, n + \varphi_{hf}(k)\right) \end{aligned} \tag{A.6}$$

Once the maximum frequency of the lower frequency signal is reached, higher frequencies are added based on the frequency spectrum of the second sensor. The crossover

point is denoted here by the index N_{lf2hf}, which corresponds to 0.5 Hz in the given example. The idea behind the sensor fusion of differently sampled signals can be considered as similar to the signal decomposition in a wavelet transformation.

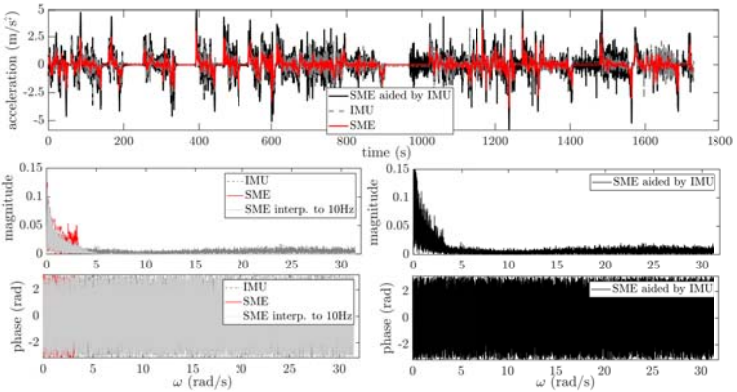

(a) acceleration

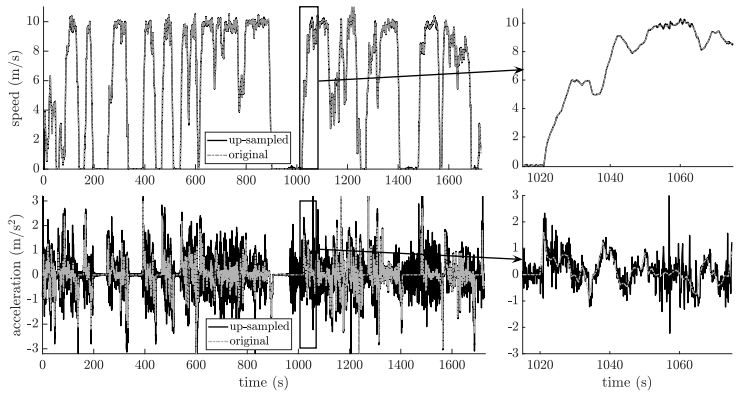

(b) speed

Figure A.5: Time and frequency analysis of up-sampling process for acceleration (a) and resulting speed profile and derived acceleration in comparison to original 1 Hz signal (b).

First, the lower frequency signal has to be re-sampled to the higher frequency using, for example, zero-order hold or linear interpolation. Then, (A.6) can be used to add higher frequencies (obtained by E2WME and IMU) to a lower frequency signal (SME). As a rectangular window is used, some side effects due to spectral leakage occur. Fig. A.5 a) illustrates the time and frequency spectrum of the sensors. The top plot shows the acceleration obtained by IMU (green dashed), SME (red), and the up-sampled SME signal using IMU information and (A.6). Likewise, the lower plots display the magnitude X_F and phase φ of the signals. Additionally, results for the re-sampled SME signal using

linear interpolation are shown. It can be seen that linear interpolation slightly distorts the signal at higher frequencies but adds no dynamics. The lower right plots show the frequency spectrum of the up-sampled SME signal by adding the higher frequencies of the IMU in (A.6). As every sensor has a slightly different sensitivity to measurement noise, the magnitude of the IMU signal is increased to fit the SME magnitude around 0.5 Hz. The IMU is able to measure acceleration directly, whereas the speed profile of the SME has to be derived at first. Therefore, a larger influence of measurement noise on the SME is expected. Fig. A.5 a) illustrates that the acceleration profile obtained by up-sampling the SME signal is valid. In comparison to the E2WME as displayed in Fig A.3, which was sampled at a higher frequency, a similar behavior of the acceleration and frequency profile is obtained.

However, the speed and not the acceleration profile should be improved for driving cycle construction. Still, it is more suitable to use a frequency analysis of the acceleration signals as it is offset-free and the aiding sensor (IMU) directly measures accelerations. As a result, the frequency spectrum of the acceleration signal has to be integrated once. Integration can be done by convoluting the resulting signal with the Heaviside step function. In this case, the up-sampled speed signal in the time domain $x_v(t)$ consists of the measured speed signal of the SME $x_{v,lf}(t)$ and the integrated acceleration profile of the IMU $x_{a,hf}(t)$.

$$x_v(t) = x_{v,lf}(t) + \int_{t=o}^{t_{end}} x_{a,hf}(t)dt \tag{A.7}$$

The integral over a sum is the same as the sum of the integrals of the terms. Further, it holds that $\int \cos(c\,t)dt = \frac{1}{c}\cos(c\,t - \frac{\pi}{2})$ with c being a constant. Therefore, (A.7) can be written as:

$$x_v(t) = x_{v,lf}(t) + \sum_{k=N_{lf2hf}}^{N_{hf}-1} \frac{X_{F,hf}(k)}{\omega_{o,hf}\,k} \cos\left(\omega_{o,hf}\,k\,n + \varphi_{hf}(k) - \frac{\pi}{2}\right) \tag{A.8}$$

The integration has, therefore, a similar effect to a low-pass filter as the intensity decreases with increasing frequency $\omega_{o,hf}\,k$.

Fig. A.5 b) illustrates the results. The up-sampled speed using (A.8) and derived acceleration are compared to the original speed and acceleration. As expected, speed and acceleration match each other besides the higher frequency parts. As a result, the up-sampling process of a low-frequency signal using a higher frequency signal can be broken down into the following steps:

1. Calculate magnitude, phase, and frequency of all signals using the DFT or FFT.
2. Re-sample the lower frequency signal to the higher sampling rate using linear interpolation.
3. Use (A.6) to add the higher dynamics to the lower frequency signal.
4. In case the integral of the signal should be aided by the higher frequency data, use (A.8) instead of (A.6).

A.1.4 Up-sampling

The synthesized driving cycles are built up using a sampling rate of 1 Hz. However, vehicle dynamics might lie at about 3 Hz. For SSES, no dominant dynamics higher than

0.5 Hz are observed as discussed before. Still, the driving cycle might be up-sampled and higher frequency components of a second sensor might be used to add more dynamics. The up-sampling process described in section A.1.3 can be applied to the derived SSES SE2WC as shown in Fig. A.6. The up-sampled speed profile resembles the speed

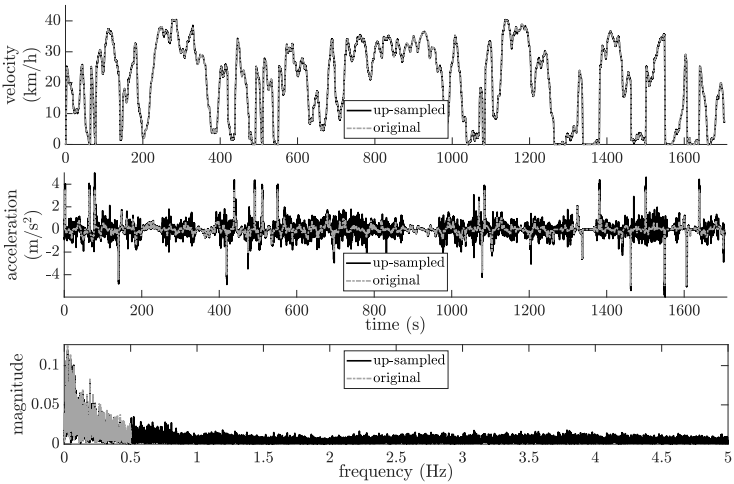

Figure A.6: Comparison of original SSES SE2WC and up-sampled SE2WC.

profile of the derived SE2WC well. The effect of higher frequencies can clearly be seen in the acceleration profile. When looking at the frequency spectrum in the lower plot of Fig. A.6, the amplitude of the original and up-sampled signal correspond well for 0 Hz to 5 Hz. However, dominant frequencies above 0.5 Hz cannot be seen. In this case, the higher frequency part (> 0.5 Hz) of IMU signal behaves like white noise. Therefore, the used method can also be described as a method for adding white, or, more accurately, colored noise to a signal. In case an equal intensity is present at the considered frequency area, the added signal resembles white noise. If the intensity contains some peaks, the colored noise simulates, besides the white noise effects, also vehicle dynamics. Therefore, this method can still be used to improve the quality of a synthesized driving cycle if relevant frequencies and dynamics are missing.

Table A.7 provides an overview of the key characteristics. The averages of all SSES drives are compared to the original SE2WC and the up-sampled speed profile. Besides distance, time, average and maximum speed, and driving phases, energy is displayed. The average data obtained by data collection is resembled quite well. Deviations lie within 15 % for the designed average parameters. The SE2WC using Markov chains shows slightly longer cruising and shorter acceleration times than the average data.

Distance, time and speed are not affected by the up-sampling process. Larger fluctuations in the acceleration values lead to less phases being identified as idling or cruising phases. This is mostly due to the defined limits of $|a| \leqslant \pm 0.1\,\mathrm{m/s^2}$ for identifying these phases. Larger average accelerations and decelerations result from the same effect. This

Table A.7: Key characteristics of SSES data collection and SE2WC.

Criteria	Unit	SSES Data	SE2WC Markov	SE2WC up-sampled
Distance	km	10.23	9.43	9.43
Time	s	1549	1704	1704
Avg. Speed	km/h	20.8	19.9	19.9
Max. Speed	km/h	39.9	40.4	40.4
Idling	%	10.7	10.5	9.5
Cruising	%	26.3	33.0	20.2
Accelerating	%	34.7	27.3	34.6
Decelerating	%	28.3	29.6	35.7
Avg. Accel.	m/s^2	0.50	0.50	0.55
Avg. Decel.	m/s^2	-0.49	-0.45	-0.53
Energy	Wh/km	23.4	21.6	24.5

can be accounted to the colored noise characteristic of the higher frequency dynamics, which were added to the original 1 Hz driving cycle.

A realistic energy consumption is measured based on battery voltage and current for a representative route. In comparison to the realistic energy consumption of about 26 Wh/km, the smartphone data collection leads to a 10% lower consumption estimate of about 23.4 Wh/km. This corresponds well with the observation that smartphone tracking leads to lower energy consumption estimates. One reason is the lower recording frequency and, therefore, less fluctuations in the acceleration. The constructed SE2WC based on Markov chains consumes even less with about 21.6 Wh/km. This is mainly due to the stochastic construction process. If the energy consumption per km is added to the weighting criteria in (2.1), energy deviations might also be penalized stronger. However, as deviations lie within 10%, the SE2WC fulfills the driving cycle synthesis requirements. Further, energy consumption increases by up-sampling the designed SE2WC to about 24.5 Wh/km. With about 6% less energy consumption than the realistic measurement, it is able to predict the energy characteristics better. As discussed before, a higher sampling rate leads to more changes in and higher average accelerations as the added signal shows a colored noise characteristic for higher frequencies.

A.2 PMSM MOTOR MODEL

A.2.1 Derivation of model equations & dq-transformation

The PMSM description and model derivation follows the descriptions provided in [114, 116, 172].

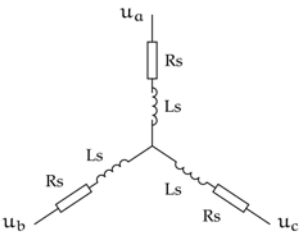

Figure A.7: Three phase electrical equivalent circuit of PMSM.

Three-phase system

The three phases of a PMSM are usually connected in a star connection so that the sum of the currents at the star point is zero. The PMSM is at first assumed to consist only of the three-phase elements presented in the equivalent circuit diagram in Fig. A.7. The electrical behavior of the motor is modeled as a serial connection of a resistor R_s, which corresponds to the ohmic losses in the stator windings, and an inductance L_s. Using Ohm's ($U_R = R \cdot I$) and Faraday's law ($U_{ind} = -\frac{d}{dt}\psi(t) = -\frac{d}{dt}[L(t)\,i(t)]$) the voltage $u(t)$ over each of the three phases can be calculated.

$$u_a(t) = R_s\, i_a(t) + \frac{d}{dt}\psi_a \tag{A.9}$$

$$u_b(t) = R_s\, i_b(t) + \frac{d}{dt}\psi_b \tag{A.10}$$

$$u_c(t) = R_s\, i_c(t) + \frac{d}{dt}\psi_c\,. \tag{A.11}$$

Parameters a, b and c are the indices for the three phases, $i(t)$ is the current and $\psi(t)$ the magnetic flux.

These equations can also be described in a orthogonal 2D coordinate system containing the same information, by using the notation of (α, β, Clarke transformation). This results in the components of the stator voltages $\underline{u}^{\alpha,\beta}$ being offset by 120° ($=\frac{2\pi}{3}$) each.

$$\underline{u}^{\alpha,\beta} = \frac{2}{3}\left(u_a + \exp\left(j\,\frac{2\pi}{3}\right)u_b + \exp\left(-j\,\frac{2\pi}{3}\right)u_c\right) \tag{A.12}$$

However, this illustration is still unattractive as sinusoidal voltages are present due to the rotation of the motor. The aim of the following transformation is to convert this stator-fixed system into a rotating (rotor-fixed) coordinate system. Thus the voltages and currents appear constant in the rotation coordinate system.

dq-transformation (Park's transformation)

As the model is intended for the use with battery aging calculations, the commonly used dq-approach [172], which simplifies the PMSM equations, will be used. The dq-transformation, often also referred to as Park's transformation, converts the stator-fixed coordinate system into a rotor-fixed one. The total transformation comprises the conversion from the 3D stator-fixed abc-system into the 2D stator-fixed $\alpha\beta\gamma$-system (γ is the null system and is not important in symmetric three-phase systems as used here) shown in (A.13) and into the 2D rotor-fixed dq-system afterwards shown in (A.14).

$$u_{\alpha,\beta,\gamma} = \begin{bmatrix} u_\alpha \\ u_\beta \\ u_\gamma \end{bmatrix} = \frac{2}{3} \begin{bmatrix} 1 & -\frac{1}{2} & -\frac{1}{2} \\ 0 & \frac{\sqrt{3}}{2} & -\frac{\sqrt{3}}{2} \\ \frac{1}{2} & \frac{1}{2} & \frac{1}{2} \end{bmatrix} \cdot \begin{bmatrix} u_a \\ u_b \\ u_c \end{bmatrix} \tag{A.13}$$

$$u_{dq} = \begin{bmatrix} u_d \\ u_q \end{bmatrix} = \frac{2}{3} \begin{bmatrix} \cos(\Theta) & \sin(\Theta) \\ -\sin(\Theta) & \cos(\Theta) \end{bmatrix} \cdot \begin{bmatrix} u_\alpha \\ u_\beta \end{bmatrix} \tag{A.14}$$

The resulting combined rotation matrix results in:

$$u_{dq0} = \begin{bmatrix} u_d \\ u_q \\ u_o \end{bmatrix} = \frac{2}{3} \begin{bmatrix} \cos(\Theta) & \cos(\Theta - \frac{2\pi}{3}) & \cos(\Theta + \frac{2\pi}{3}) \\ -\sin(\Theta) & -\sin(\Theta - \frac{2\pi}{3}) & -\sin(\Theta - \frac{2\pi}{3}) \\ \frac{1}{2} & \frac{1}{2} & \frac{1}{2} \end{bmatrix} \cdot \begin{bmatrix} u_a \\ u_b \\ u_c \end{bmatrix} \tag{A.15}$$

This transformation is amplitude invariant using a factor of $\frac{2}{3}$, as introduced in (A.15), and power invariant if the factor is set to $\sqrt{\frac{2}{3}}$. The same transformation can be used to transform the corresponding currents into the dq-coordinates.

As a result, transforming the three phase voltages to a rotating 2D reference frame using the dq-transformation leads to the general PMSM voltage equations

$$\begin{aligned} u_d &= R_s\, i_d + \frac{d}{dt}\psi_d - \omega_{el}\,\psi_q \\ u_q &= R_s\, i_q + \frac{d}{dt}\psi_q + \omega_{el}\,\psi_d \end{aligned} \tag{A.16}$$

with

$$\omega_{el} = \frac{d}{dt}\Theta_{el} = \frac{d}{dt}\Theta_{mech}\, p \tag{A.17}$$

and p being the number of pole pairs.

Torque & load

In addition to the electrical behavior, the mechanical load attached to the motor needs to be considered. Assuming no losses, the torque generated by the motor T_{mot} has to be equal to the motor's rotational inertia T_{rot} and the torque of the load attached to the motor T_{load}.

$$T_{mot} = T_{el} = T_{rot} + T_{load} \tag{A.18}$$

The motor inertia T_{rot} can be calculated from the rotational energy P_{rot} if the inertia J is assumed constant. Eq. (A.19) describes the correlation of motor inertia, power and angular speed.

$$T_{rot} = \frac{P}{\omega} = J\,\frac{d}{dt}\omega \tag{A.19}$$

The rotational energy is calculated from the work W_{rot} as presented in (A.20).

$$\begin{aligned} P_{rot} &= \frac{d}{dt} W_{rot} = \frac{1}{2} J \left(2\omega \dot{\omega}\right) = J\,\omega \frac{d}{dt}\omega \\ \text{with} \qquad W_{rot} &= \frac{1}{2} J\,\omega^2 \end{aligned} \tag{A.20}$$

The electrical torque, which is in this context equivalent to the motor torque T_{mot}, can be derived from the motor fluxes as described in [114]. It results in

$$T_{mot} = \frac{3}{2} p \left(\psi_d\, i_q - \psi_q\, i_d\right), \tag{A.21}$$

and in total

$$T_{mot} = J \frac{d}{dt}\omega_m + T_{load} = \frac{3}{2} p \left(\psi_d\, i_q - \psi_q\, i_d\right) \tag{A.22}$$

with $\omega_m = \frac{1}{p}\omega_{el}$. J is the rotational inertia, ω_m the mechanical rotational speed, ω_{el} the equivalent electrical speed, p the number of pole pairs.

The load torque T_{load} can be calculated taking the forces resulting from rolling friction F_r, drag resistance F_d, slope F_s and acceleration F_a into account. These can be calculated as shown in (A.23) with rolling resistance c_r, vehicle mass m, gravitational constant g and slope angle α.

$$\begin{aligned} F_r &= c_r\, m\, g\, \cos(\alpha), \qquad & F_w &= \frac{1}{2} c_w\, A_{front}\, \rho_{air}\, v^2 \\ F_s &= m\, g\, \sin(\alpha), \qquad & F_a &= (m + m_{add})\, a \end{aligned} \tag{A.23}$$

Further parameters are the drag coefficient c_w, effective front area of the vehicle A_{front}, air density ρ_{air}, velocity v, additional mass m_{add} and acceleration a. Using the wheel radius r_{wheel}, the load torque can then be calculated by

$$T_{load} = (F_r + F_w + F_s + F_a)\, r_{wheel}. \tag{A.24}$$

In total, the speed equation becomes

$$\frac{d}{dt}\omega_{el} = \frac{p^2}{J} \frac{3}{2} \left(\psi_d\, i_q - \psi_q\, i_d\right) - \frac{p}{J} T_{load}. \tag{A.25}$$

A.2.2 Basic PMSM model

If nonlinear effects such as hysteresis and saturation are negligible or when the accuracy demands are not so high, the general equations in (A.16) can be simplified. The fluxes are assumed to be independent of each other and using the inductance law and derivatives

$$\begin{aligned} \psi_d &= L_d\, i_d + \psi_{PM}, \qquad & \frac{d}{dt}\psi_d &= L_d \frac{d}{dt} i_d \\ \psi_q &= L_q\, i_q, & \frac{d}{dt}\psi_q &= L_q \frac{d}{dt} i_q \end{aligned} \tag{A.26}$$

the system equations become more simple. L_d and L_q stand for the equivalent inductances in dq coordinates and ψ_{PM} is the flux induced by the permanent magnet. Applying these relations to (A.16), leads to the simplified voltage characteristics in (A.27).

$$\begin{aligned} u_d &= R_s\, i_d + L_d \frac{d}{dt} i_d - \omega_{el}\, L_q\, i_q \\ u_q &= R_s\, i_q + L_q \frac{d}{dt} i_q + \omega_{el} \left(\psi_{PM} + L_d\, i_d\right) \end{aligned} \tag{A.27}$$

As a result, the simplified PMSM equations in state space representation become

$$\begin{aligned}
\frac{d}{dt} i_d &= \frac{1}{L_d} \left(u_d - R_s \, i_d + \omega_{el} \, L_q \, i_q \right) \\
\frac{d}{dt} i_q &= \frac{1}{L_q} \left(u_q - R_s \, i_q - \omega_{el} \, L_d \, i_d - \omega_{el} \, \psi_{PM} \right) \\
\frac{d}{dt} \omega_{el} &= \frac{p^2}{J} \frac{3}{2} \left[\psi_{PM} \, i_q + (L_d - L_q) i_d \, i_q \right] - \frac{p}{J} T_{load} \, .
\end{aligned} \tag{A.28}$$

Although the basic model equations are easy to implement and, for example, sufficiently accurate for a basic simulation, they cannot represent all effects, especially at the boundaries. For example, saturation effects and cross-coupling occur, which lead to varying inductances. Accordingly, the derivatives that occur are no longer trivial. As the main focus of this study is on battery-related effects and only little motor data for parametrization is available, a highly accurate motor model is not required.

A.3 ADDITIONAL BATTERY MODEL DESCRIPTIONS

A.3.1 Generalization of EEM aging equations to different Li-ion cell types

Besides a $t^{0.75}$-time dependency, the additional two aging equations can be analyzed. At first, $\alpha_t\, t^{\alpha_z}$ is examined for the LMO, LFP1, and NMC1 cell. Fig. A.8 (a) and (b) display the measured and estimated normed cell capacity for the LFP1 and NMC1 cell. In general, a closer fit is obtained than for the $\alpha\, t^{0.75}$ relationship as an additional DOF is available. Fig. A.8 (c) displays the value of both parameters over SOC (left) and voltage (right). As observed before for the LMO cell, the exponent α_z in the term $\alpha_t\, t^{\alpha_z}$ starts at values larger than 1 for low SOC and voltages and converges to an almost constant value for larger SOCs and voltages. The final value seems to depend on the cell and cell chemistry. α_z converges to approximately 0.5 for the LFP cell, 0.7 for the LMO cell and 0.75 for the NMC cell. The large value of approximately 1.9 for 100% SOC of the NMC cell can be accounted to the rapid capacity decrease of the NMC cell at this SOC. As only two values were available before the cell reached its EOL, the fit function is not able to represent this characteristic. When examining the SOC dependency, the exponent might be approximated by an exponential decrease with a limited growth of $(\alpha_{z,min} - (\alpha_{z,min} - b_0)\, e^{-\lambda x})$. Parameter b_0 represents the initial value, $\alpha_{z,min}$ the lower limit, and λ the decay constant. At the same time, parameter α_t is almost zero if α_z is larger than 1 and becomes almost linear for larger SOCs. The linear behavior appears to be very sensitive to small variations of α_z at higher SOC. For example, the NMC1 cell shows an almost constant value for SOCs larger than 60% instead of the linear increase if the parameter α_z is set to 0.75.

Second, Fig. A.9 displays results using a fit function of $\alpha_1\,(t + \alpha_2\,\sqrt{t})$. Part (a) and (b) visualize the quality of approximating the capacity of the LFP1 and NMC1 cell, respectively. Values of both parameters α_1 and α_2 are drawn over SOC and voltage in Fig. A.9 (c). The decrease in capacity is approximated well, however, no clear trend in the parameters α can be recognized in the data. Whereas α_1 slightly decreases for the LFP1 cell, it increases for NMC1 and shows no distinct behavior in the case of the LMO cell. Likewise, results for α_2 indicate a linear increase for LFP1 but values for NMC1 and LMO remain almost constant.

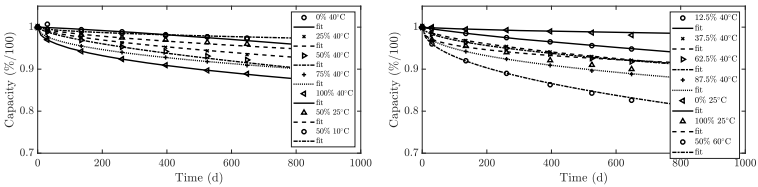

(a) LFP capacity fit

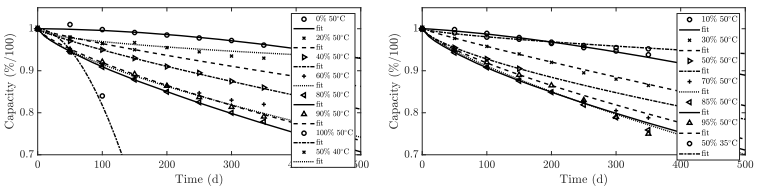

(b) NMC capacity fit

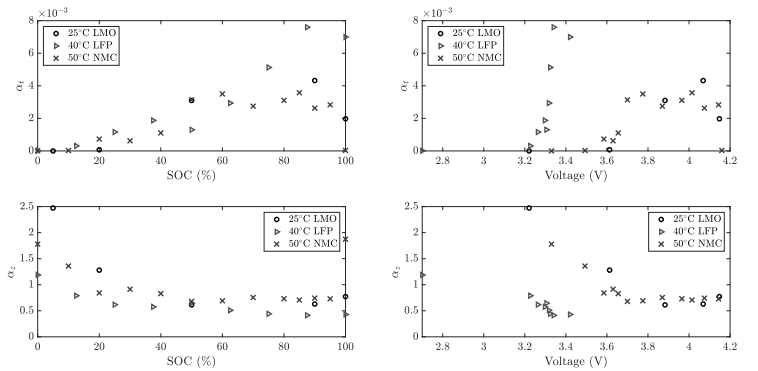

(c) Fit parameters over SOC (left) and voltage (right)

Figure A.8: Comparison of voltage characteristics for calendar aging using a $\alpha_t \, t^{\alpha_z}$ fit function. Measured capacity is compared to the model fit and results for α_t and α_z are shown over SOC and voltage. Part (a) shows the fit for LFP cell [150], and (b) for NMC cell [69]. (c) compares the fit coefficients for the LMO, LFP, and NMC cell.

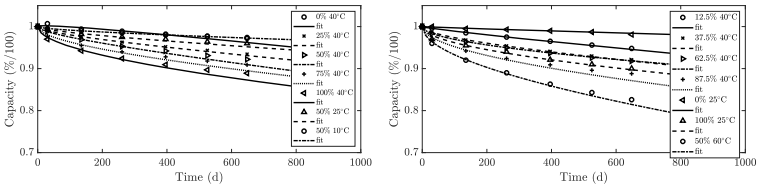

(a) LFP capacity fit

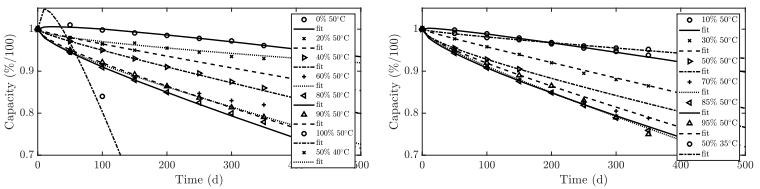

(b) NMC capacity fit

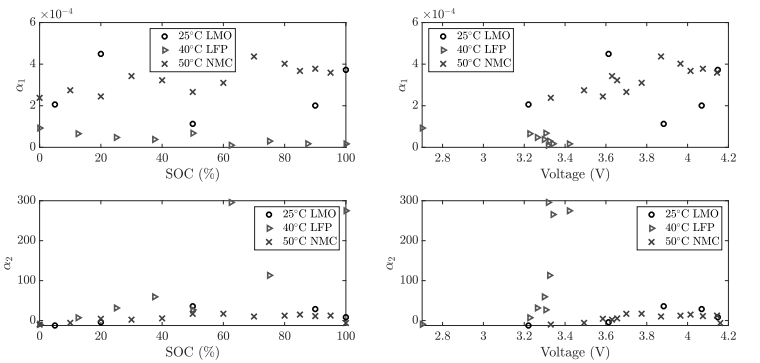

(c) Fit parameters over SOC (left) and voltage (right)

Figure A.9: Comparison of voltage characteristics for calendar aging using a $\alpha_1 (t + \alpha_2 \sqrt{t})$ fit function. Measured capacity is compared to the model fit and results for α_t and α_z are shown over SOC and voltage. Part (a) shows the fit for LFP cell [150], and (b) for NMC cell [69]. (c) compares the fit coefficients for the LMO, LFP, and NMC cell.

B

ADDITIONAL DATA SETS

B.1 AGING MEASUREMENTS & MODEL PARAMETERS

B.1.1 Calendar and cycle aging results

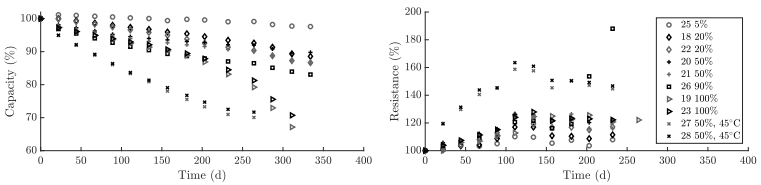

Figure B.1: Overview of calendar cell aging results for capacity (left) and resistance (right).

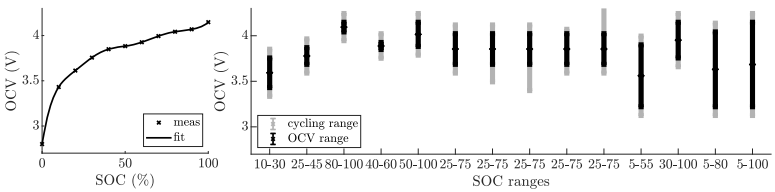

Figure B.2: Overview of voltage ranges corresponding to a specific cycling scenario. General OCV vs. SOC characteristic of LMO cell (left). Voltage range for each cycling scenario (right). The voltage ranges due to the OCV at the minimum and maximum SOC are shown as black bars. The gray bars indicate the actual voltage range, which is larger since the applied current leads to an additional ohmic voltage loss $U_{ohm} = I R_{cell}$.

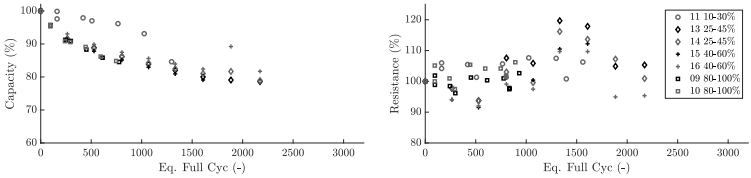

(a) 20% DOD and various average SOC, 1C/1C, 25°C, single cells

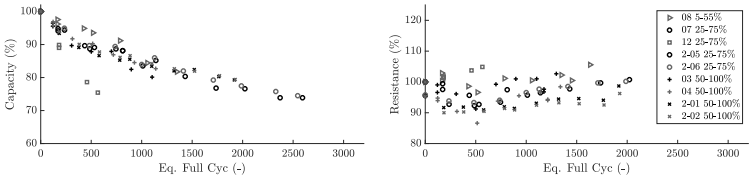

(b) 50% DOD and various average SOC, 1C/1C, 25°C, single cells

Figure B.3: Overview of cycle cell aging results for capacity (left) and resistance (right) for constant DOD at different SOCs.

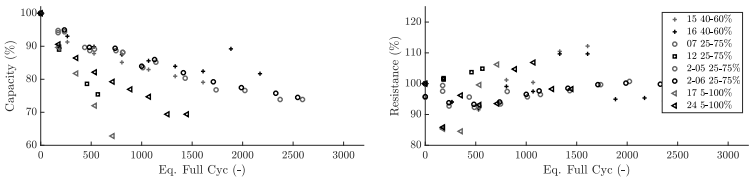

(a) 50% average SOC and various DODs, 1C/1C, 25°C, single cells

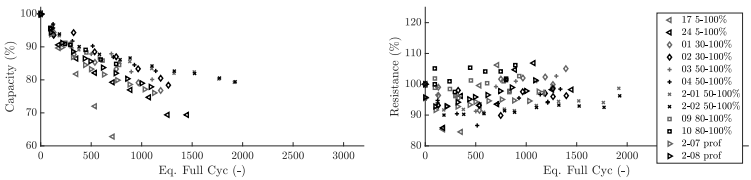

(b) X-100% full charge at different DODs, 1C/1C, 25°C, single cells

Figure B.4: Overview of cycle cell aging results for capacity and resistance for constant average SOC and full charge. The cells labeled by "prof" were tested with a discharge profile (average DCR 0.5 C) instead of a constant DCR but were also cycled between 5-100%.

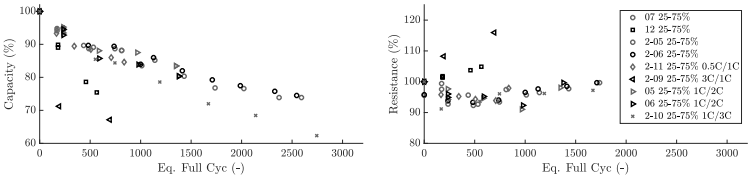

Figure B.5: Overview of cycle cell aging results for capacity and resistance for different charge and discharge rates.

B.1.2 Model fits

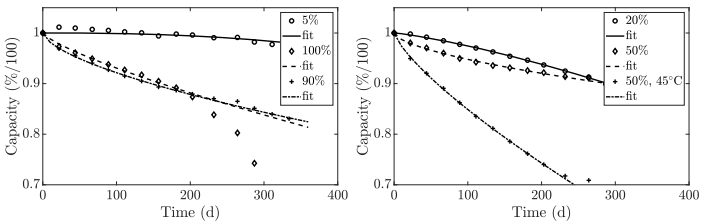

(a) LMO capacity fit

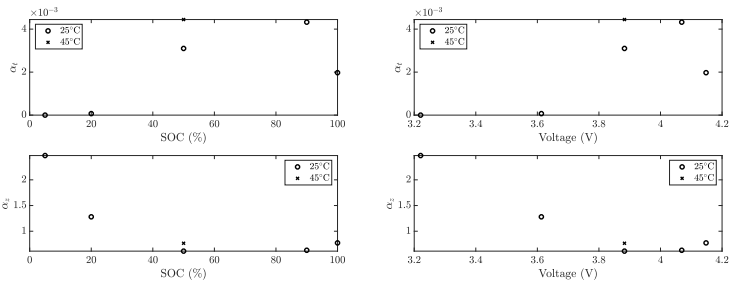

(b) LMO fit parameters over SOC (left) and voltage (right)

Figure B.6: Comparison of voltage characteristics for calendar aging using a $\alpha_t\, t^{\alpha_z}$ fit function. Measured capacity is compared to the model fit and results for α_t and α_z are shown over SOC and voltage for LMO cell

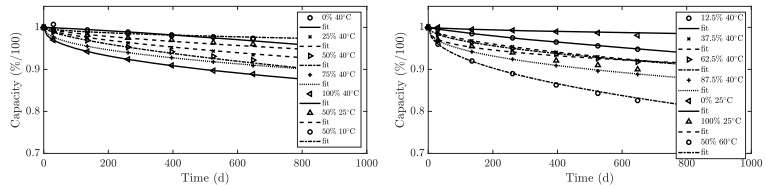

(a) LFP capacity fit

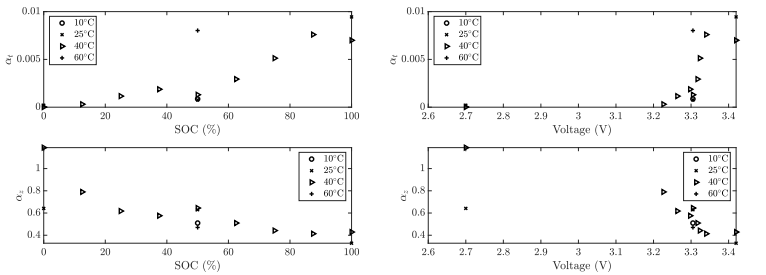

(b) LFP fit parameters over SOC (left) and voltage (right)

Figure B.7: Comparison of voltage characteristics for calendar aging using a $\alpha_t\, t^{\alpha_z}$ fit function. Measured capacity is compared to the model fit and results for α_t and α_z are shown over SOC and voltage for LFP cell [150].

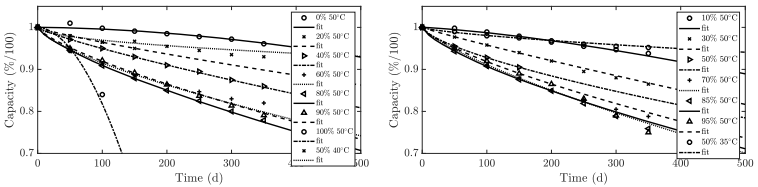

(a) NMC capacity fit

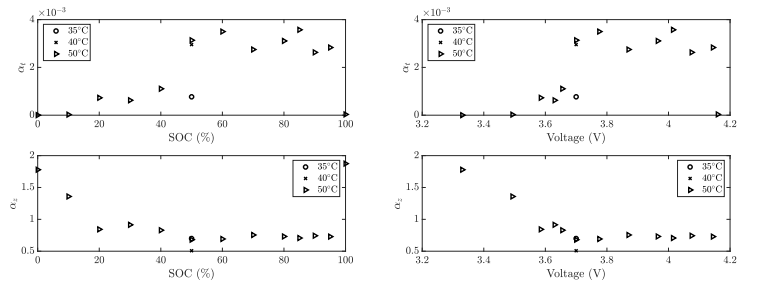

(b) NMC fit parameters over SOC (left) and voltage (right)

Figure B.8: Comparison of voltage characteristics for calendar aging using a $\alpha_t\, t^{\alpha_z}$ fit function. Measured capacity is compared to the model fit and results for α_t and α_z are shown over SOC and voltage for NMC cell [69].

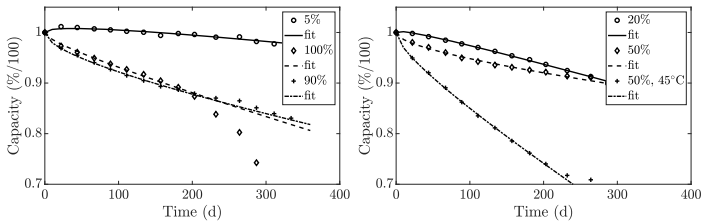

(a) LMO capacity fit

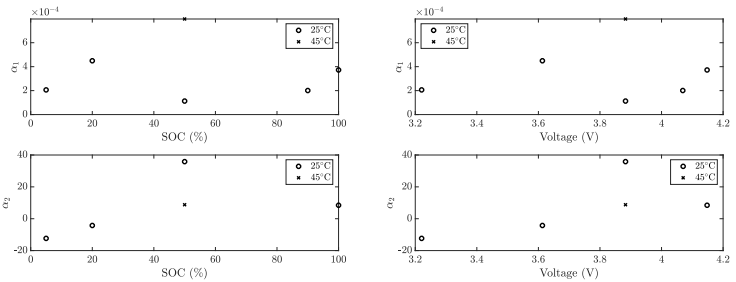

(b) LMO

Figure B.9: Comparison of voltage and temperature characteristics for calendar aging using a $\alpha_1 (t + \alpha_2 \sqrt{t})$ fit function. Measured capacity is compared to the model fit (left) and results for α_1 and α_2 are shown on the top and bottom right respectively for LMO cell.

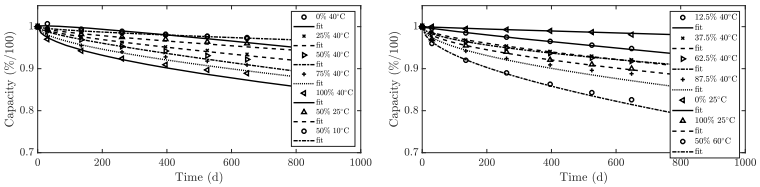

(a) LFP capacity fit

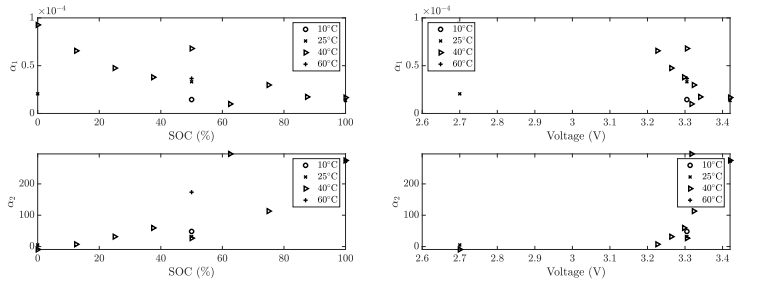

(b) LFP

Figure B.10: Comparison of voltage and temperature characteristics for calendar aging using a $\alpha_1\,(t + \alpha_2\,\sqrt{t})$ fit function. Measured capacity is compared to the model fit (left) and results for α_1 and α_2 are shown on the top and bottom right respectively for LFP cell [150].

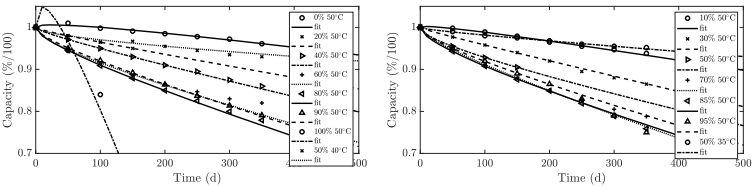

(a) NMC capacity fit

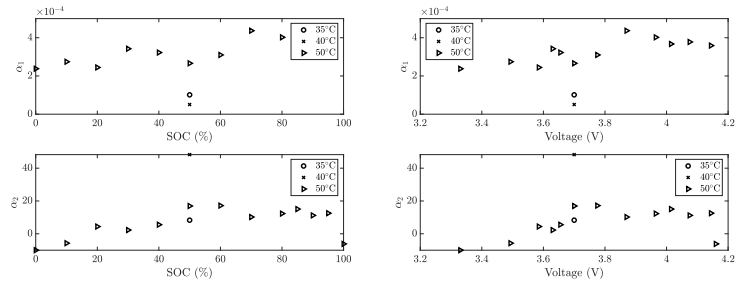

(b) NMC

Figure B.11: Comparison of voltage and temperature characteristics for calendar aging using a $\alpha_1 (t + \alpha_2 \sqrt{t})$ fit function. Measured capacity is compared to the model fit (left) and results for α_1 and α_2 are shown for NMC cell on the top and bottom right [69].

B.2 DIFFERENTIAL VOLTAGE ANALYSIS

B.2.1 Comparison

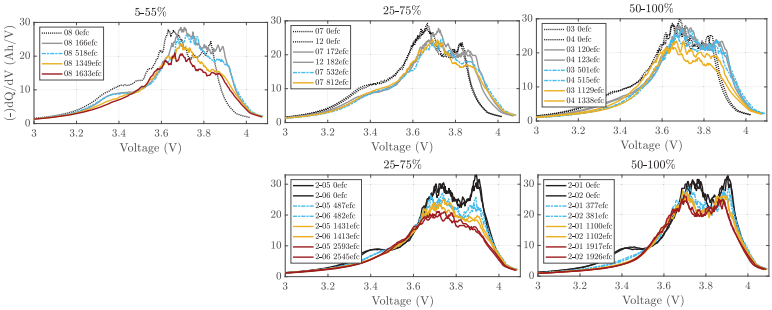

Figure B.12: ICA with 50% DOD and various SOC for cells of batch A1 (top) and A2 (bottom).

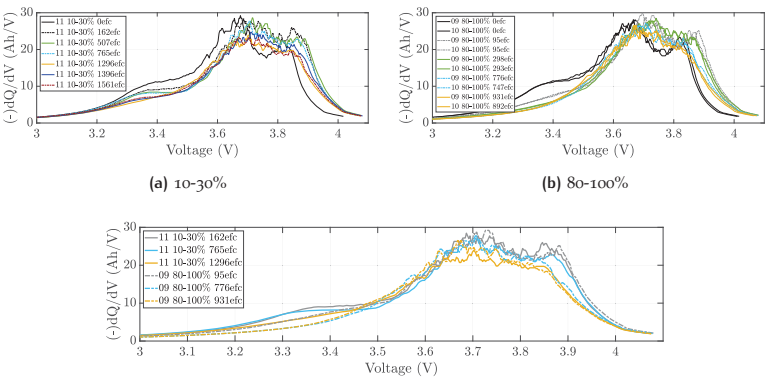

(a) 10-30%

(b) 80-100%

(c) 10-30% vs 80-100% direct comparison

Figure B.13: ICA with 20% DOD: low SOC cycling vs high.

For a clearer comparison, ICA characteristics are presented after approximately 800 efc for batch A1 (a) and after 1000 efc for batch A2 (b) in Fig. B.14. They are colored according to their behavior.

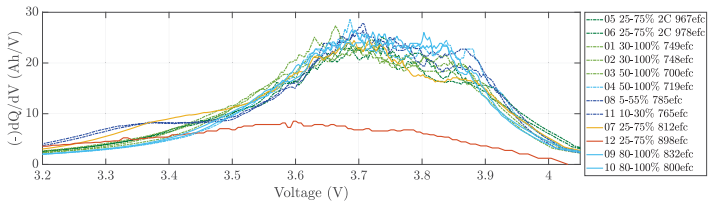

(a) A1 after approx. 800 efc

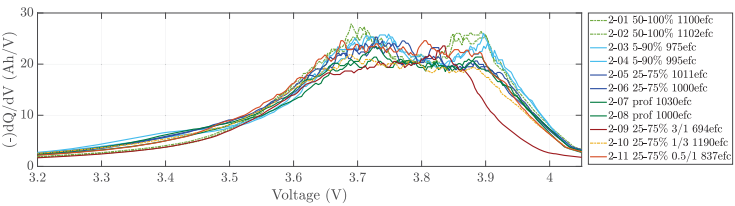

(b) A2 after approx. 1000 efc

Figure B.14: ICA comparison after approx. 800 efc for A1 (a) and 1000 efc for A2 (b).

B.2.2 Single cell data

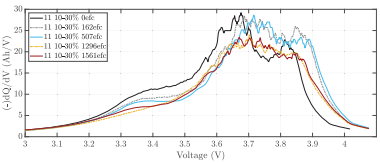

(a) 10-30%

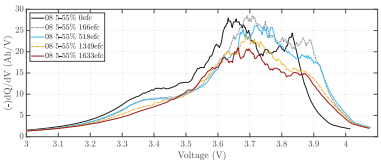

(b) 5-55%

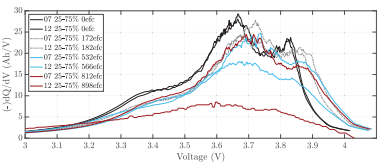

(c) 25-75% 1C/1C

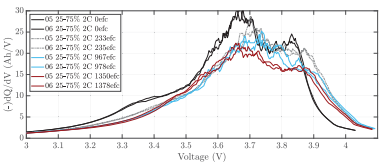

(d) 25-75% 1C/2C

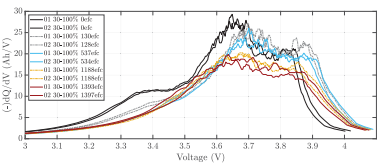

(e) 30-100%

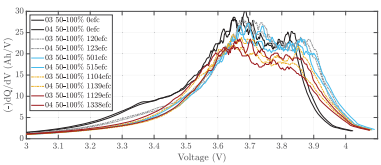

(f) 50-100%

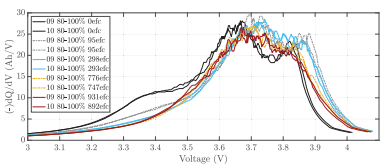

(g) 80-100%

Figure B.15: DVA at various efc of A1.

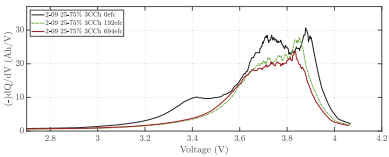

(a) 25-75% 3C/1C

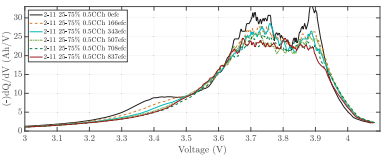

(b) 25-75% 0.5C/1C

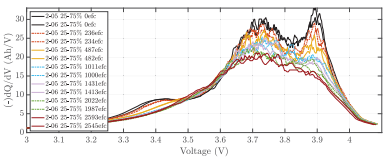

(c) 25-75% 1C/1C

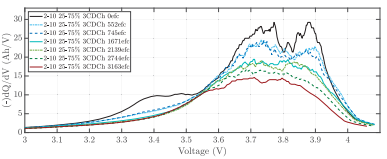

(d) 25-75% 1C/3C

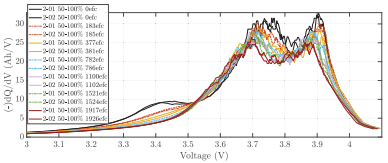

(e) 50-100%

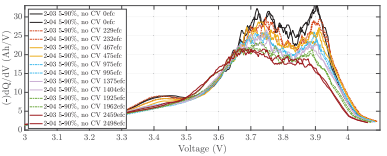

(f) 5-90%

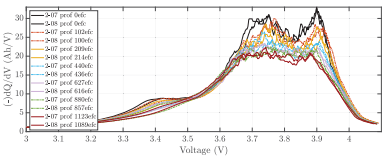

(g) 5-100% discharge profile

Figure B.16: DVA at various efc of A2.

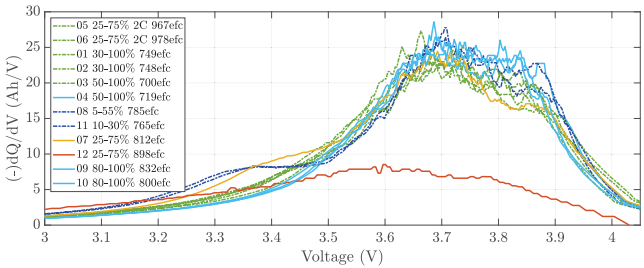

(a) A1 800 efc

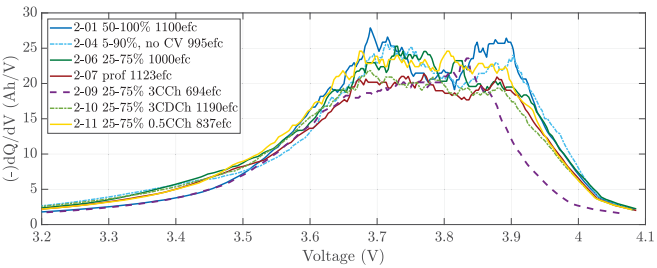

(b) A2 1000 efc

Figure B.17: Comparison of aging after 800 efc for A1 (a) and after 1000 efc for A2 (b).

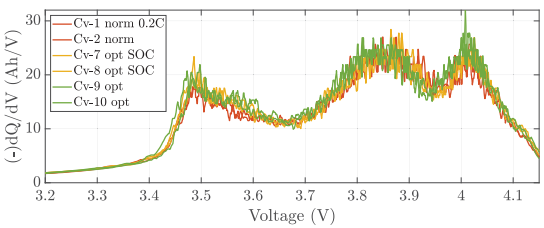

Figure B.18: ICA at EOT for validation tests at 0.2 C for the three test cases (approx. 46 efc).

B.3 SPM PARAMETERS

Table B.1: Comparison of base model literature values.

Parameter	Source	Unit	positive electrode	separator	negative electrode
			6.2 e^{-5} (e)		
	[175]		8.0 e^{-5} (m)	**2.5 e^{-5}** (m)	**3.4 e^{-5}** (m)
	[59]	m	3.6 e^{-5}	2.5 e^{-5}	5.0 e^{-5}
	[7]		8.0 e^{-5}	2.5 e^{-5}	4.5 e^{-5}
Electrode	[11]		3.6 e^{-5} (d)	2.0 e^{-5} (d)	4.3 e^{-5} (d)
thickness δ	[124]		1.35 e^{-4} (d)	2.5 e^{-5} (d)	1.0 e^{-4} (d)
	[257]		4.075 e^{-5}	2.5 e^{-5}	4.87 e^{-5}
	[62]		1.74 e^{-4}	5.2 e^{-5}	1.00 e^{-4}
	[27]		7.0 e^{-5}	2.5 e^{-5}	7.35 e^{-5}
	[130]		1.1 e^{-4}	3.0 e^{-5}	1.5 e^{-4}
	[178, 179]		2.0 e^{-6}		2.0 e^{-6}
	[175]		5.0 e^{-8} (m)		**5.0 e^{-6}** (m)
	[7]		**1.8 e^{-6}**		5.0 e^{-6}
	[124]	m	3.45 e^{-6} (NMC) (d)		8.5 e^{-7} (d)
	[124]		5.5 e^{-6} (LFP) (d)		8.5 e^{-7} (d)
Particle	[129]		2.0 e^{-6}		2.0 e^{-6}
radius R_s	[257]		5.0 e^{-6}		1.0 e^{-7}
	[164]		5.0 e^{-7} (d)		6.0 e^{-6} (d)
	[134]		8.0 e^{-6}		1.25 e^{-5}
	[27]		8.5 e^{-6}		1.25 e^{-5}
	[4, 5]		1.5 e^{-5}		2.64 e^{-4}
	[130]		8.5 e^{-6}		1.25 e^{-5}
	[91]		3.7 e^{-8} (m)		3.58 e^{-6}
			0.538 (e)		**0.624** (e)
	[175]	-	0.374 (a)	**0.550**	0.580
	[59]		0.500		0.580
Active material	[11]		0.559 (d)		0.566 (d)
volume fraction	[164]		0.489 (d)	0.630 (d)	0.645 (d)
ϵ_s	[130, 134]		0.297		0.471
	[27]		0.300		0.4382
	[4, 5]		0.165		0.797
	[140]		0.350		0.350
	[91]		0.330 (m)	0.5 (m)	0.330 (m)
	[178, 179]		0.385		0.485

Listed values are (a)djusted, (e)stimated, (m)easured, parameters obtained by cell (d)esign or no note if data source is unknown

Table B.2: Comparison of base model literature values (continued I).

Parameter	Source	Unit	positive electrode	separator	negative electrode
	[176]		**0.426** (e)	**0.450**	**0.360**
	[59]		0.330	0.500	0.332
	[7]		0.300		0.330
	[11]		0.330 (d)	0.410 (d)	0.380 (d)
Electrolyte volume	[124]		0.280 (d)	0.500 (d)	0.320 (d)
fraction/ porosity	[129]	-	0.385	0.724	0.485
ϵ_e	[257]		0.33	0.4	0.32
	[164]		0.407 (d)		0.301 (d)
	[62, 130, 134]		0.444	1	0.357
	[27]		0.45	0.45	0.45
	[140]		0.52	0.52	0.52
	[175]		**0.200** (e)		**0.060** (e)
	[7]		0.217		0.250
Filler volume	[129]	-	0.025		0.033
fraction ϵ_f	[62]		0.073		0.026
	[27]		0.15		0.0566
	[130]		0.259		0.172
Electrode plate			**0.94** (e)		**0.94** (e)
area A	[71]	m^2	0.18 (m)		0.18 (m)
	[124]		2.2290 (d)		2.3675 (d)
	[175]		**22,806**		**30,555**
	[11]		23,230		27,362
	[13]		22,860		30,540
Max. solid	[124]		15,000 (NMC) (e)		12,000
phase concentration	[124]	$mol\ m^{-3}$	7,000 (LFP) (e)		12,000
$c_{s,max}$	[164]		22,836 (d)		30,537 (d)
	[134]		22,860		26,390
	[27, 178, 179]		51,555		30,555
	[4, 5]		47,820 (a)		81,470 (a)
	[130]		22,860		26,390
			0.712 (e)		**0.0127** (e)
Stoichiometry at	[175]	-	0.740 (m)		0.0132 (m)
0% SOC y_0, x_0	[124]		0.943 (NMC) (m)		0.01 (m)
	[124]		0.928 (LFP) (m)		0.01 (m)
					0.8125 (e)
Stoichiometry at	[175]	-	**0.035** (m)		0.8110 (m)
100% SOC y_{100}, x_{100}	[124]		0.436 (NMC) (m)		0.87 (m)
	[124]		0.0012 (LFP) (m)		0.87 (m)

Table B.3: Comparison of base model literature values (continued II).

Parameter	Source	Unit	positive electrode	separator	negative electrode
	[175]		**0.360**	**0.360**	**0.360**
Ionic transference	[59]	-	0.363	0.363	0.363
number t_+	[11]		0.370	0.370	0.370
	[129]		0.363		0.637
	[130, 178, 179]		0.363	0.363	0.363
	[175]			**1200** (a)	
	[11]			1150 (d)	
	[13]			1000	
Average electrolyte	[124]			1230 (m)	
concentration at rest	[129]	$mol\ m^{-3}$		1000	
c_e	[257]			1000	
	[164]			1150 (d)	
	[134]			2000	
	[4, 5]			85100	
	[130]			1000	
	[175]	-	**1.5**	**1.5**	**1.3**
Bruggman exponent	[11]			1.5	7.5 (e)
$Brugg$	[129]		0.5		0.5
	[140]		2.8		2.8
	[130]		1.5	1.5	1.5
			1.6 (e)		**1.6** (e)
Exchange current	[176]	$A\ m^{-2}$	0.05 (e)		7.5 (e)
density i_o	[13]		0.416		0.688
	[62]		0.8		1.1
Charge transfer	[175]		**0.5**		**0.5**
coefficients	[59]	-	0.5		0.5
α_{ox}, α_{red}	[11]		0.5		0.5
	[175]		$5.9e^{-17}$ (a)		**$8.0e^{-12}$**
	[7]		$2.5e^{-15}$		$9.0e^{-14}$
	[11]		**$4.0e^{-14}$** (e)		$1.1e^{-14}$ (e)
	[71]		$5.9e^{-18}$		$3.0e^{-14}$ (e)
	[124]		$2.22e^{-13}$ (NMC) (e)		$3.2e^{-14}$
Solid phase Li	[124]	$m^2\ s^{-1}$	$1.3e^{-13}$ (LFP) (m)		$3.2e^{-14}$
diffusion D_s	[129]		$3.9e^{-14}$		$1.0e^{-14}$
	[164]		$6.5e^{-13}$		$5.8e^{-14}$
	[62, 130, 134]		$1.0e^{-13}$		$3.9e^{-14}$
	[27]		$1.0e^{-11}$		$5.5e^{-14}$
	[4, 5]		$7.43e^{-13}$		$1.14e^{-13}$
	[178]		$1.0e^{-14}$		$3.9e^{-14}$

Table B.4: Comparison of base model literature values (continued III).

Parameter	Source	Unit	positive electrode	separator	negative electrode
	[175]		**$2.0\,e^{-10}$**	**$2.0\,e^{-10}$**	**$2.0\,e^{-10}$**
Electrolyte	[59]		$2.6\,e^{-10}$	$2.6\,e^{-10}$	$2.6\,e^{-10}$
phase Li^+	[13]	$m^2\,s^{-1}$	$3.35\,e^{-6}$	$3.35\,e^{-6}$	$3.35\,e^{-6}$
diffusion D_e	[71]		$1.20\,e^{-10}$	$1.20\,e^{-10}$	$1.20\,e^{-10}$
	[124]		$2.60\,e^{-10}$	$2.60\,e^{-10}$	$2.60\,e^{-10}$
	[130]		$7.5\,e^{-11}$	$7.5\,e^{-11}$	$7.5\,e^{-11}$

Table B.5: Comparison of thermal model literature values.

Parameter	Source	Unit	positive electrode	separator	negative electrode
Charge transfer	[175]	$J\,mol^{-1}$	**13,000**		**20,000**
activation energy $E_{a_{ct}}$	[71]		15,000		15,000
	[91]		41,367 (a)		53,411 (a)
Solid phase diffusion	[175]	$J\,mol^{-1}$	**39,000**		**35,000**
activation energy $E_{a_{diff,s}}$	[71]		30,600 (a)		30,000
Electrolyte phase Li^+ diffusion	[175]	$J\,mol^{-1}$	**26,600**	**26,600**	**26,600**
activation energy $E_{a_{diff,e}}$	[71]		25,039 (a)		25,039 (a)
Electrolyte phase conductivity	[175]	$J\,mol^{-1}$	**11,000**	**11,000**	**11,000**
activation energy $E_{a_{cond,e}}$	[71]		10,578 (a)		10,578 (a)

Table B.6: Cell specific thermal properties.

Parameter	Symbol	Source	Unit	Value
Convective coefficient	h_{conv}		$W\,K^{-1}\,m^{-2}$	**10** (m)
		[175]		5-10 for free convection air cooling
		[175]		10-70 for forced air convection
		[175]		>100 for liquid cooling
		[27]		30
Heat capacity	C_p		$J\,(kg\,K)^{-1}$	**1100** (a)
		[175]		1100 (m)
		[164]		881 (e)
		[27]		750
Cell lateral surface	A_{cell}		m^2	0.0035 (m)
Cell mass	m		kg	0.4 (m)

Table B.7: Comparison of aging model literature values.

Parameter	Source	Unit	negative electrode
Initial SEI	[176]	m	**5.0 e^{-9}** (e)
thickness $\delta_{SEI}(0)$	[11]		450 e^{-9}
			0.85 e^{-22} calendar aging (a)
			46.75 e^{-22} cycle aging (a)
	[176]		1.18 e^{-22} calendar aging (a)
Solvent reduction kinetic	[176]	m^7(s mol)$^{-1}$	141.6 e^{-22} cycle aging (a)
constant k_f'	[71]		6.85 e^{-11} (a)
	[129]		5.03 e^{-11}
	[257]		1.0 e^{-12} (a)
	[130]		6.0 e^{-10} (a)
SEI layer molar	[176]		**0.162**
mass M_{SEI}	[130, 199, 257]	kg mol^{-1}	0.162
	[164]		0.0881 (d)
	[176]		**1,690**
SEI layer density ρ_{SEI}	[130, 199, 257]	kg m^{-3}	1,690
	[164]		1,321
	[176]		**17.5 e^{-5}** (a)
SEI ionic conductivity	[11]	S m^{-1}	2.4 e^{-4}
κ_{SEI}	[71]		17 e^{-5} (a)
	[199, 257]		5 e^{-6}
SEI porosity		%	**1.5** from calendar aging (a)
ϵ_{SEI}	[176]		1.0 from calendar aging (a)
Solvent reduction equilibrium potential U_s	[176]	V vs Li	**0.5** (e)
Charge transfer coefficient		-	**0.2** (a)
for the side reaction β	[176]		0.5 (a)
			8.58 e^{-19} from calendar aging (a)
	[176]		8.84 e^{-20} from calendar aging (a)
Solvent diffusion	[11]	m^2 s^{-1}	2.85 e^{-16}
coefficient $D^0_{solv,init}$	[71]		2.20 e^{-19} (a)
	[257]		2.00 e^{-18} (a)
	[130]		5.00 e^{-11} (a)
Solvent bulk	[176]		**4,541**
concentration c^b_{solv}	[71]	mol m^{-3}	6,620 (m)
	[130, 199, 257]		4,541
Activation energy of	[176]	J mol^{-1}	**5.55 e^4** (e)
solvent diffusivity $E_{a_{Dsolv}}$	[71]		7.59 e^4 (a)
			4.5 e^4
Activation energy of	[176]	J mol^{-1}	6.0 e^4 (e)
side reaction $E_{a_{kf}}$	[71]		11.4 e^4 (a)
	[75]		4.47 e^4

LIST OF SYMBOLS

Symbol	Description
a	acceleration (or fitting parameter)
a_{Cu}	copper factor
$a_{1,2,3,...}$	empirical calendar aging fitting parameters
$b_{1,2,3,...}$	empirical cycle aging fitting parameters
c	heat capacity
c_r	rolling resistance
c_e	liquid phase (electrolyte) concentration
$c_{s,i}$	solid phase Li-ion concentration
$c_{s,i,max}$	maximum solid phase Li-ion concentration
$c^s_{s,i}$	solid phase Li-ion concentration at particle surface
c_{solv}	solvent concentration
c^*_{solv}	solvent boundary concentration
c_w	air drag coefficient
e^-	electron
g	gravitational constant
h_{conv}	convective constant
k	reaction rate
k'_f	solvent reduction kinetic aging constant
k_{lipl}	reaction rate constant
$i_{o,lipl}$	exchange current density by lithium plating
$i_{a,b,c}$	current in a, b, and c phase of motor
i_{dq}	current in dq system
i_{dB}	simplified current density in Butler equation
i_s	exchange current density of the side reaction
i^o_s	exchange current density for solid phase
i_o	general description of exchange current density
$i_{s,lipl}$	side current induced by lithium plating
j	complex indicator
m	mass
p	number of pole pairs

p_k	fit parameters for SPM diffusion coefficient and current calculation
r	electrode radial variable
t	time
t_+	Li-ion transference number
t_i^0	initial charge transfer exchange density
$t_{0,i}$	initial exchange density constant
$t_{0/f}$	optimization start/final time
$t_{DC,0/f}$	discharge phase start/final time
v	velocity
x	optimization state vector
$x_{0/100}$	stoichiometric coefficient at 0% or 100% SOC
$x_{C_{cal}}$	state representing calendar aging
x_{iV}	state representing the integral over voltage
x_Q	charge throughput state
x_{SOC}	state representing SOC
x_T	temperature state
$y_{0/100}$	stoichiometric coefficient at 0% or 100% SOC
y_n	measured capacity loss for RMSE evaluation of n-th aging scenario
$\hat{y}$	predicted capacity loss
$\bar{y}$	mean value
z	spatial variable in SPM or power factor in empirical equations
z_t	exponent for EEM estimation of time influence
A	electrode plate area
A_{front}	E2W front area
B	viscous friction gain
$Brugg$	Bruggman exponent
$C_{cal/cyc}$	capacity loss due to calendar/cycle aging
C_{loss}	capacity loss
C_n	nominal (initial) capacity
$C_{n,e}$	negative electrode capacity
C_p	cell heat capacity
$C_{p,e}$	positive electrode capacity
C_{rem}	remaining relative capacity
$C_{1,2}$	capacity of EEM capacitors

CR	charge rate
$D_{s/e}$	solid or electrolyte phase diffusion coefficient
D_{solv}	solvent diffusion coefficient
DOD	depth of discharge
E_a	activation energy
$E_{a_{cond}}$	conductivity activation energy
$E_{a_{ct}}$	charge transfer activation energy
$E_{a_{diff}}$	diffusion activation energy
$E_{a_{D_{solv}}}$	activation energy of solvent diffusivity
E_{a_k}	process specific activation energy
$E_{a_{kf}}$	activation energy of side reaction
E^-_{cell}	cell energy potential
F	Faraday constant
F_a	acceleration force
$F_{drag/slope}$	air drag/ slope force
F_{pen}	penalty term (driving cycle synthesis)
F_{roll}	rolling friction
F_{total}	total applied forces
I	current
$I_{cell,batt}$	cell/battery current
J	(motor) inertia
L	distance between negative and positive current collector
$L_{d,q}$	inductance in d, q coordinates
L^x	self and mutual inductance
L_s	serial inductance
M_{lipl}	molar mass of lithium in lithium plating
M_{SEI}	SEI molar mass
$N_{p/s}$	number of cells in parallel/serial
P	power
P_{con}	electrical consumer power
$P_{el/mech}$	electrical/mechanical power
Q	charge throughput for empirical aging
$Q_{d,g}$	dissipated and generated energy
Q_i	cell electrode's capacity

Q_s	capacity loss due to SEI layer growth
Q_c	charge throughput for SPM based on current I (similar to SOC)
R	ideal gas constant
$R_{cell2air}$	thermal resistance
$R_{s,i}$	particle radius
R_s	serial resistance
R_{ohm}	ohmic resistance
R_{SEI}	SEI layer total resistance
$R_{0,1,2}$	resistance of EEM resistors
R_i	resistance
$Ratio$	ratio between charge sustaining and charge depletion in HEVs
S_n	electroactive surface of the negative electrode
SOC_0	initial state of charge
T	temperature in Kelvin
$T_{el,mot,rot,load}$	torque (electrical, motor, rotational, load, ...)
T_{int}	internal cell temperature
T_{ref}	reference cell temperature
T_{amb}	ambient temperature
U	potential
U_i	electrode's half-cell OCV
$V_{(cell,batt)}$	(cell/battery) voltage
V_{OCV}	open circuit voltage
$V_{RC,i}$	voltage loss over the RC-elements
α	charge transfer coefficient or fitting parameter in empirical equation
$\alpha_{a/c,lipl}$	li plating anodic/cathodic charge-transfer coeff.
$\alpha_{c,r}$	calendar fitting parameter for capacity and resistance empirical aging equation
$\alpha_{red/ox}$	charge transfer coefficient for reduction or oxidation
β	charge transfer coefficient of side reaction
$\beta_{c,r}$	cycle fitting parameter for cap. and res. empirical aging eq.
δ_i	electrode's and separator's thickness
δ_{lipl}	lithium plating thickness
δ_{SEI}	SEI layer thickness

Δa_{avg}	trip average acceleration
Δs_{end}	trip distance
$\Delta v_{avg/max}$	trip average/maximum velocity
$\Delta t_{end/stop}$	trip end/stop time
$\epsilon_{s/e/f}$	active material volume fraction of separator/ electrolyte/filler
ϵ_{SEI}	SEI porosity
ε	end temperature variation restriction
$\varepsilon_{e,i}$	volume fraction of electrolyte
η	efficiency
η_{lipl}	potential for lithium plating reaction
$\bar{\eta}_i^k$	kinetic overpotential
κ_i^{eff}	effective ionic conductivity
κ_{SEI}	SEI ionic conductivity
ω	angular velocity
ϕ_e	liquid phase (electrolyte) potential
ϕ_i	negative/positive electrode potential
$\phi_{s,i}$	electrode potential between solid phase of negative/positive electrode
$\phi_{s,i,avg}$	average of $\phi_{s,i}$ during fixed cycle depth
ψ	magnetic flux
ψ_{PM}	magnetic flux of permanent magnet
$\varphi_{gen,dis}$	generated and dissipated energy
ρ_{air}	air density
ρ_{lipl}	lithium plating layer density
ρ_{SEI}	SEI layer density
θ_i^b	normalized bulk Li-ion concentration
θ_i^s	normalized inserted Li-ion concentration at the particle surface
$\theta_{i,avg}^s$	average normalized inserted Li-ion concentration at the particle surface during fixed cycle depth
Θ	rotor angle
$\zeta_{1,2,...}$	constant parameters for simplification of SPM
$\varnothing V$	average voltage

LIST OF FIGURES

LIST OF TABLES

BIBLIOGRAPHY

[1] Mohamed Abdel-Monem, Khiem Trad, Noshin Omar, Omar Hegazy, Peter Van den Bossche, and Joeri Van Mierlo. "Influence analysis of static and dynamic fast-charging current profiles on ageing performance of commercial lithium-ion batteries". In: *Energy* 120 (2017), pp. 179–191. DOI: https://doi.org/10.1016/j.energy.2016.12.110.

[2] A. Abdollahi, X. Han, G.V. Avvari, N. Raghunathan, B. Balasingam, K.R. Pattipati, and Y. Bar-Shalom. "Optimal battery charging, Part I: Minimizing time-to-charge, energy loss, and temperature rise for OCV-resistance battery model". In: *Journal of Power Sources* 303 (2016), pp. 388–398. DOI: https://doi.org/10.1016/j.jpowsour.2015.02.075.

[3] A. Abdollahi, X. Han, N. Raghunathan, B. Pattipati, B. Balasingam, K.R. Pattipati, Y. Bar-Shalom, and B. Card. "Optimal charging for general equivalent electrical battery model, and battery life management". In: *Journal of Energy Storage* 9 (2017), pp. 47–58. DOI: https://doi.org/10.1016/j.est.2016.11.002.

[4] R. Ahmed, M. E. Sayed, I. Arasaratnam, J. Tjong, and S. Habibi. "Reduced-Order Electrochemical Model Parameters Identification and State of Charge Estimation for Healthy and Aged Li-Ion Batteries Part II: Aged Battery Model and State of Charge Estimation". In: *IEEE Journal of Emerging and Selected Topics in Power Electronics* 2.3 (Sept. 2014), pp. 678–690. DOI: 10.1109/JESTPE.2014.2331062.

[5] R. Ahmed, M. E. Sayed, I. Arasaratnam, J. Tjong, and S. Habibi. "Reduced-Order Electrochemical Model Parameters Identification and SOC Estimation for Healthy and Aged Li-Ion Batteries Part I: Parameterization Model Development for Healthy Batteries". In: *IEEE Journal of Emerging and Selected Topics in Power Electronics* 2.3 (Sept. 2014), pp. 659–677. DOI: 10.1109/JESTPE.2014.2331059.

[6] K. Ahn, A. E. Bayrak, and P. Y. Papalambros. "Electric Vehicle Design Optimization: Integration of a High-Fidelity Interior-Permanent-Magnet Motor Model". In: *IEEE Transactions on Vehicular Technology* 64.9 (Sept. 2015), pp. 3870–3877. DOI: 10.1109/TVT.2014.2363144.

[7] Paul Albertus, Jeremy Couts, Venkat Srinivasan, and John Newman. "II. A combined model for determining capacity usage and battery size for hybrid and plug-in hybrid electric vehicles". In: *Journal of Power Sources* 183.2 (2008), pp. 771–782. DOI: https://doi.org/10.1016/j.jpowsour.2008.05.012.

[8] D. Andre, M. Meiler, K. Steiner, Ch. Wimmer, T. Soczka-Guth, and D.U. Sauer. "Characterization of high-power lithium-ion batteries by electrochemical impedance spectroscopy. I. Experimental investigation". In: *Journal of Power Sources* 196.12 (2011). Selected papers presented at the 12th Ulm ElectroChemical Talks (UECT): 2015 Technologies on Batteries and Fuel Cells, pp. 5334–5341. DOI: https://doi.org/10.1016/j.jpowsour.2010.12.102.

[9] D. Andre, M. Meiler, K. Steiner, H. Walz, T. Soczka-Guth, and D.U. Sauer. "Characterization of high-power lithium-ion batteries by electrochemical impedance spectroscopy. II: Modelling". In: *Journal of Power Sources* 196.12 (2011). Selected papers presented at the 12th Ulm ElectroChemical Talks (UECT): 2015 Technologies on Batteries and Fuel Cells, pp. 5349–5356. DOI: https://doi.org/10.1016/j.jpowsour.2010.07.071.

[10] D. Ansean, V. M. Garcia, M. Gonzalez, C. Blanco-Viejo, J. C. Viera, Y. F. Pulido, and L. Sanchez. "Lithium-Ion Battery Degradation Indicators Via Incremental Capacity Analysis". In: *IEEE Transactions on Industry Applications* 55.3 (May 2019), pp. 2992–3002. DOI: 10.1109/TIA.2019.2891213.

[11] Williams Agyei Appiah, Joonam Park, Seoungwoo Byun, Myung-Hyun Ryou, and Yong Min Lee. "A Mathematical Model for Cyclic Aging of Spinel LiMn2O4/Graphite Lithium-Ion Cells". In: *Journal of The Electrochemical Society* 163.13 (2016), A2757–A2767. DOI: 10.1149/2.1061613jes.

[12] Pankaj Arora, Ralph E. White, and Marc Doyle. "Capacity Fade Mechanisms and Side Reactions in Lithium-Ion Batteries". In: *Journal of The Electrochemical Society* 145.10 (1998), pp. 3647–3667. DOI: 10.1149/1.1838857.

[13] Pankaj Arora, Marc Doyle, Antoni S. Gozdz, Ralph E. White, and John Newman. "Comparison between computer simulations and experimental data for high-rate discharges of plastic lithium-ion batteries". In: *Journal of Power Sources* 88.2 (2000), pp. 219–231. DOI: https://doi.org/10.1016/S0378-7753(99)00527-3.

[14] Yasuo Asakura and Eiji Hato. "Tracking survey for individual travel behaviour using mobile communication instruments". In: *Transportation Research Part C: Emerging Technologies* 12.3 (2004). Intelligent Transport Systems: Emerging Technologies and Methods in Transportation and Traffic, pp. 273–291. DOI: https://doi.org/10.1016/j.trc.2004.07.010.

[15] T.R. Ashwin, A. Barai, K. Uddin, L. Somerville, A. McGordon, and J. Marco. "Prediction of battery storage ageing and solid electrolyte interphase property estimation using an electrochemical model". In: *Journal of Power Sources* 385 (2018), pp. 141–147. DOI: https://doi.org/10.1016/j.jpowsour.2018.03.010.

[16] Asian Development Bank. *Urban Transport Strategy to Combat Climate Change in the People's Republic of China (English)*. 978-92-9092-573-6. Asian Development Bank, 2012.

[17] Doron Aurbach. "Review of Selected Electrode-solution Interactions Which Determine the Performance of Li and Li Ion Batteries". In: *Journal of Power Sources* 89.2 (2000), pp. 206–218. DOI: https://doi.org/10.1016/S0378-7753(00)00431-6.

[18] T. J. Barlow, S. Latham, I. S. McCrae, and P. G. Boulter. *A reference book of driving cycles for use in the measurement of road vehicle emissions*. Published Project Report PPR354. TRL Limited, 2009.

[19] Saeid Bashash, Scott J. Moura, Joel C. Forman, and Hosam K. Fathy. "Plug-in hybrid electric vehicle charge pattern optimization for energy cost and battery longevity". In: *Journal of Power Sources* 196.1 (2011), pp. 541–549. DOI: https://doi.org/10.1016/j.jpowsour.2010.07.001.

[20] Richard Bellman. "Dynamic programming and the numerical solution of variational problems". In: *Operations Research* (1957), pp. 277–288.

[21] Maya Ben Dror, Lanzhi Qin, and Feng An. "The gap between certified and real-world passenger vehicle fuel consumption in China measured using a mobile phone application data". In: *Energy Policy* 128 (2019), pp. 8–16. DOI: https://doi.org/10.1016/j.enpol.2018.12.039.

[22] Frank A. Bender, Martin Kaszynski, and Oliver Sawodny. "Drive cycle prediction and energy management optimization for hybrid hydraulic vehicles". In: *IEEE Transaction on Vehicular Technology* 62.8 (Oct. 2013), pp. 3581–3592.

[23] Bernd A Berg. *Markov Chain Monte Carlo Simulations and Their Statistical Analysis*. WORLD SCIENTIFIC, 2004. DOI: 10.1142/5602.

[24] Lorenzo Berzi, Massimo Delogu, and Marco Pierini. "Development of driving cycles for electric vehicles in the context of the city of Florence". In: *Transportation Research Part D: Transport and Environment* 47 (2016), pp. 299–322. DOI: https://doi.org/10.1016/j.trd.2016.05.010.

[25] Christoph R. Birkl, Matthew R. Roberts, Euan McTurk, Peter G. Bruce, and David A. Howey. "Degradation diagnostics for lithium ion cells". In: *Journal of Power Sources* 341 (2017), pp. 373–386. DOI: https://doi.org/10.1016/j.jpowsour.2016.12.011.

[26] Justin D.K. Bishop, Reed T. Doucette, Daniel Robinson, Barnaby Mills, and Malcolm D. McCulloch. "Investigating the technical, economic and environmental performance of electric vehicles in the real-world: A case study using electric scooters". In: *Journal of Power Sources* 196.23 (2011), pp. 10094–10104. DOI: https://doi.org/10.1016/j.jpowsour.2011.08.021.

[27] A.M. Bizeray, S. Zhao, S.R. Duncan, and D.A. Howey. "Lithium-ion battery thermal-electrochemical model-based state estimation using orthogonal collocation and a modified extended Kalman filter". In: *Journal of Power Sources* 296 (2015), pp. 400–412. DOI: https://doi.org/10.1016/j.jpowsour.2015.07.019.

[28] I Bloom, B.W Cole, J.J Sohn, S.A Jones, E.G Polzin, V.S Battaglia, G.L Henriksen, C Motloch, R Richardson, T Unkelhaeuser, D Ingersoll, and H.L Case. "An accelerated calendar and cycle life study of Li-ion cells". In: *Journal of Power Sources* 101.2 (2001), pp. 238–247. DOI: https://doi.org/10.1016/S0378-7753(01)00783-2.

[29] Ira Bloom, Andrew N. Jansen, Daniel P. Abraham, Jamie Knuth, Scott A. Jones, Vincent S. Battaglia, and Gary L. Henriksen. "Differential voltage analyses of high-power, lithium-ion cells: 1. Technique and application". In: *Journal of Power Sources* 139.1 (2005), pp. 295–303. DOI: https://doi.org/10.1016/j.jpowsour.2004.07.021.

[30] Ira Bloom, Jon Christophersen, and Kevin Gering. "Differential voltage analyses of high-power lithium-ion cells: 2. Applications". In: *Journal of Power Sources* 139.1 (2005), pp. 304–313. DOI: https://doi.org/10.1016/j.jpowsour.2004.07.022.

[31] Ira Bloom, Jon P. Christophersen, Daniel P. Abraham, and Kevin L. Gering. "Differential voltage analyses of high-power lithium-ion cells: 3. Another anode phenomenon". In: *Journal of Power Sources* 157.1 (2006), pp. 537–542. DOI: https://doi.org/10.1016/j.jpowsour.2005.07.054.

[32] Ira Bloom, Lee K. Walker, John K. Basco, Daniel P. Abraham, Jon P. Christophersen, and Chinh D. Ho. "Differential voltage analyses of high-power lithium-ion cells. 4. Cells containing NMC". In: *Journal of Power Sources* 195.3 (2010), pp. 877–882. DOI: https://doi.org/10.1016/j.jpowsour.2009.08.019.

[33] Paul T. Boggs and Jon W. Tolle. "Sequential Quadratic Programming". In: *Acta Numerica* 4 (1995), pp. 1–51. DOI: 10.1017/S0962492900002518.

[34] John Brady and Margaret O'Mahony. "Development of a driving cycle to evaluate the energy economy of electric vehicles in urban areas". In: *Applied Energy* 177 (2016), pp. 165–178.

[35] M. J. Brand, M. H. Hofmann, S. S. Schuster, P. Keil, and A. Jossen. "The Influence of Current Ripples on the Lifetime of Lithium-Ion Batteries". In: *IEEE Transactions on Vehicular Technology* 67.11 (Nov. 2018), pp. 10438–10445. DOI: 10.1109/TVT.2018.2869982.

[36] M Broussely, S Herreyre, P Biensan, P Kasztejna, K Nechev, and R.J Staniewicz. "Aging mechanism in Li ion cells and calendar life predictions". In: *Journal of Power Sources* 97-98 (2001). Proceedings of the 10th International Meeting on Lithium Batteries, pp. 13–21. DOI: https://doi.org/10.1016/S0378-7753(01)00722-4.

[37] M. Broussely, Ph. Biensan, F. Bonhomme, Ph. Blanchard, S. Herreyre, K. Nechev, and R.J. Staniewicz. "Main aging mechanisms in Li ion batteries". In: *Journal of Power Sources* 146.1 (2005). Selected papers presented at the 12th International Meeting on Lithium Batteries, pp. 90–96. DOI: https://doi.org/10.1016/j.jpowsour.2005.03.172.

[38] T. H. Bryne, J. M. Hansen, R. H. Rogne, N. Sokolova, T. I. Fossen, and T. A. Johansen. "Nonlinear Observers for Integrated INSGNSS Navigation: Implementation Aspects". In: *IEEE Control Systems Magazine* 37.3 (June 2017), pp. 59–86. DOI: 10.1109/MCS.2017.2674458.

[39] Stephan Buller, Marc Thele, Rik W. A. A. De Doncker, and Eckhard Karden. "Impedance-Based Simulation Models of Supercapacitors and Li-Ion Batteries for Power Electronic Applications". In: *IEEE Transactions on Industry Applications* 41.3 (May 2005), pp. 742–747.

[40] Long Cai and Ralph E. White. "An Efficient Electrochemical-Thermal Model for a Lithium-Ion Cell by Using the Proper Orthogonal Decomposition Method". In: *Journal of The Electrochemical Society* 157.11 (2010), A1188–A1195. DOI: 10.1149/1.3486082.

[41] Christian Campestrini, Peter Keil, Simon F. Schuster, and Andreas Jossen. "Ageing of lithium-ion battery modules with dissipative balancing compared with single-cell ageing". In: *Journal of Energy Storage* 6 (2016), pp. 142–152. DOI: https://doi.org/10.1016/j.est.2016.03.004.

[42] R. Carter, A. Cruden, and P. J. Hall. "Optimizing for Efficiency or Battery Life in a Battery/Supercapacitor Electric Vehicle". In: *IEEE Transactions on Vehicular Technology* 61.4 (May 2012), pp. 1526–1533. DOI: 10.1109/TVT.2012.2188551.

[43] M. Ceraolo, G. Lutzemberger, and D. Poli. "Aging evaluation of high power lithium cells subjected to micro-cycles". In: *Journal of Energy Storage* 6 (2016), pp. 116–124. DOI: https://doi.org/10.1016/j.est.2016.03.006.

[44] Chin-Yao Chang, Punit Tulpule, Giorgio Rizzoni, Wei Zhang, and Xinyu Du. "A probabilistic approach for prognosis of battery pack aging". In: *Journal of Power Sources* 347 (2017), pp. 57–68. DOI: https://doi.org/10.1016/j.jpowsour.2017.01.130.

[45] Christopher Cherry, Jonathan Weinert, Xinmiao Yang, and Eric. Van Gelder. *Electric Bikes in the People's Republic of China (PRC)-Impact on the Environment and Prospects for Future Growth*. RPT090040. Asian Development Bank, 2009.

[46] Christopher R. Cherry, Hongtai Yang, Luke R. Jones, and Min He. "Dynamics of electric bike ownership and use in Kunming, China". In: *Transport Policy* 45 (2016), pp. 127–135. DOI: https://doi.org/10.1016/j.tranpol.2015.09.007.

[47] Hung-Lung Chiang, Pei-Hsiu Huang, Yen-Ming Lai, and Ting-Yi Lee. "Comparison of the regulated air pollutant emission characteristics of real-world driving cycle and ECE cycle for motorcycles". In: *Atmospheric Environment* 87 (2014), pp. 1–9. DOI: https://doi.org/10.1016/j.atmosenv.2013.12.031.

[48] John Christensen and John Newman. "A Mathematical Model for the Lithium-Ion Negative Electrode Solid Electrolyte Interphase". In: *Journal of The Electrochemical Society* 151.11 (2004), A1977–A1988. DOI: 10.1149/1.1804812.

[49] Jon P. Christophersen. *Battery Test Manual For Plug-In Hybrid Electric Vehicles - Revision 3*. Manual. INL/EXT-14-32849. Idaho National Laboratory, U.S. Department of Energy, Sept. 2014.

[50] Jon P. Christophersen. *Battery Test Manual For Electric Vehicles - Revision 3*. Manual. INL/EXT-15-34184. Idaho National Laboratory, U.S. Department of Energy, June 2015.

[51] Andrew Clarry, Ahmadreza Faghih Imani, and Eric J. Miller. "Where we ride faster? Examining cycling speed using smartphone GPS data". In: *Sustainable Cities and Society* 49 (2019), p. 101594. DOI: https://doi.org/10.1016/j.scs.2019.101594.

[52] Andrea Cordoba-Arenas, Simona Onori, Yann Guezennec, and Giorgio Rizzoni. "Capacity and power fade cycle-life model for plug-in hybrid electric vehicle lithium-ion battery cells containing blended spinel and layered-oxide positive electrodes". In: *Journal of Power Sources* 278 (2015), pp. 473–483. DOI: https://doi.org/10.1016/j.jpowsour.2014.12.047.

[53] Andrea Cordoba-Arenas, Simona Onori, and Giorgio Rizzoni. "A control-oriented lithium-ion battery pack model for plug-in hybrid electric vehicle cycle-life studies and system design with consideration of health management". In: *Journal of Power Sources* 279 (2015), pp. 791–808.

[54] A. Corti, V. Manzoni, and S. M. Savaresi. "Vehicle's energy estimation using low frequency speed signal". In: *2012 15th International IEEE Conference on Intelligent Transportation Systems*. Sept. 2012, pp. 626–631. DOI: 10.1109/ITSC.2012.6338758.

[55] Roberto Cristi and Murali Tummala. "Multirate, multiresolution, recursive Kalman filter". In: *Signal Processing* 80.9 (2000), pp. 1945–1958. DOI: https://doi.org/10.1016/S0165-1684(00)00104-3.

[56] Benjamin Czech. "Electrochemical Modeling of the Aging Behavior of Li-Ion Battery Cells". Student thesis. University of Stuttgart, 2017.

[57] J. R. Dahn. "Phase diagram of Li_xC_6". In: *Phys. Rev. B* 44 (17 Nov. 1991), pp. 9170–9177. DOI: 10.1103/PhysRevB.44.9170.

[58] A. De Keyser, M. Vandeputte, and G. Crevecoeur. "Convex Mapping Formulations Enabling Optimal Power Split and Design of the Electric Drivetrain in All-Electric Vehicles". In: *IEEE Transactions on Vehicular Technology* 66.11 (Nov. 2017), pp. 9702–9711. DOI: 10.1109/TVT.2017.2745101.

[59] Domenico Di Domenico, Anna Stefanopoulou, and Giovanni Fiengo. "Lithium-Ion Battery State of Charge and Critical Surface Charge Estimation Using an Electrochemical Model-Based Extended Kalman Filter". In: *Journal of Dynamic Systems, Measurement, and Control* 132.6 (Oct. 2010), pp. 061302–061302-11. DOI: 10.1115/1.4002475.

[60] Christopher Marc Doyle. "Design and simulation of lithium rechargeable batteries". PhD thesis. University of California, 1995.

[61] Marc Doyle, Thomas F. Fuller, and John Newman. "Modeling of Galvanostatic Charge and Discharge of the Lithium/Polymer/Insertion Cell". In: *Journal of The Electrochemical Society* 140.6 (1993), pp. 1526–1533. DOI: 10.1149/1.2221597.

[62] Marc Doyle, John Newman, Antoni S. Gozdz, Caroline N. Schmutz, and Jean-Marie Tarascon. "Comparison of Modeling Predictions with Experimental Data from Plastic Lithium Ion Cells". In: *Journal of The Electrochemical Society* 143.6 (1996), pp. 1890–1903. DOI: 10.1149/1.1836921.

[63] Stuart E Dreyfus. *A comparison of linear programming and dynamic programming*. Tech. rep. RAND CORP SANTA MONICA CA, 1956.

[64] Matthieu Dubarry, Cyril Truchot, Mikael Cugnet, Bor Yann Liaw, Kevin Gering, Sergiy Sazhin, David Jamison, and Christopher Michelbacher. "Evaluation of commercial lithium-ion cells based on composite positive electrode for plug-in hybrid electric vehicle applications. Part I: Initial characterizations". In: *Journal of Power Sources* 196.23 (2011), pp. 10328–10335. DOI: https://doi.org/10.1016/j.jpowsour.2011.08.077.

[65] Matthieu Dubarry, Cyril Truchot, Bor Yann Liaw, Kevin Gering, Sergiy Sazhin, David Jamison, and Christopher Michelbacher. "Evaluation of commercial lithium-ion cells based on composite positive electrode for plug-in hybrid electric vehicle applications. Part II. Degradation mechanism under 2C cycle aging". In: *Journal of Power Sources* 196.23 (2011), pp. 10336–10343. DOI: https://doi.org/10.1016/j.jpowsour.2011.08.078.

[66] Matthieu Dubarry, Carlos Pastor-Fernandez, George Baure, Tung Fai Yu, W. Dhammika Widanage, and James Marco. "Battery energy storage system modeling: Investigation of intrinsic cell-to-cell variations". In: *Journal of Energy Storage* 23 (2019), pp. 19–28. DOI: https://doi.org/10.1016/j.est.2019.02.016.

[67] Matthieu Dubarry, George Baure, Carlos Pastor-Fernandez, Tung Fai Yu, W. Dhammika Widanage, and James Marco. "Battery energy storage system modeling: A combined comprehensive approach". In: *Journal of Energy Storage* 21 (2019), pp. 172–185. DOI: https://doi.org/10.1016/j.est.2018.11.012.

[68] Madeleine Ecker, Jochen B. Gerschler, Jan Vogel, Stefan Kaebitz, Friedrich Hust, Philipp Dechent, and Dirk Uwe Sauer. "Development of a lifetime prediction model for lithium-ion batteries based on extended accelerated aging test data". In: *Journal of Power Sources* 215 (2012), pp. 248–257. DOI: https://doi.org/10.1016/j.jpowsour.2012.05.012.

[69] Madeleine Ecker, Nerea Nieto, Stefan Kaebitz, Johannes Schmalstieg, Holger Blanke, Alexander Warnecke, and Dirk Uwe Sauer. "Calendar and cycle life study of Li(NiMnCo)O2-based 18650 lithium-ion batteries". In: *Journal of Power Sources* 248 (2014), pp. 839–851. DOI: https://doi.org/10.1016/j.jpowsour.2013.09.143.

[70] Akram Eddahech, Olivier Briat, and Jean-Michel Vinassa. "Performance comparison of four lithium-ion battery technologies under calendar aging". In: *Energy* 84 (2015), pp. 542–550. DOI: https://doi.org/10.1016/j.energy.2015.03.019.

[71] C. Edouard, M. Petit, C. Forgez, J. Bernard, and R. Revel. "Parameter sensitivity analysis of a simplified electrochemical and thermal model for Li-ion batteries aging". In: *Journal of Power Sources* 325 (2016), pp. 482–494. DOI: https://doi.org/10.1016/j.jpowsour.2016.06.030.

[72] H. Fang, Y. Wang, and J. Chen. "Health-Aware and User-Involved Battery Charging Management for Electric Vehicles: Linear Quadratic Strategies". In: *IEEE Transactions on Control Systems Technology* 25.3 (May 2017), pp. 911–923. DOI: 10.1109/TCST.2016.2574761.

[73] Alexander Farmann and Dirk Uwe Sauer. "Comparative study of reduced order equivalent circuit models for on-board state-of-available-power prediction of lithium-ion batteries in electric vehicles". In: *Applied Energy* 225 (2018), pp. 1102–1122. DOI: https://doi.org/10.1016/j.apenergy.2018.05.066.

[74] Xuning Feng, Chengshan Xu, Xiangming He, Li Wang, Gan Zhang, and Minggao Ouyang. "Mechanisms for the evolution of cell variations within a LiNixCoyMnzO2/graphite lithium-ion battery pack caused by temperature non-uniformity". In: *Journal of Cleaner Production* 205 (2018), pp. 447–462. DOI: https://doi.org/10.1016/j.jclepro.2018.09.003.

[75] Sebastian Frey. *Modellierung des Alterungsverhaltens von Li-Ionen-Batterien*. Tech. rep. Institute for System Dynamics, University of Stuttgart, 2016.

[76] M. Fries, A. Baum, M. Wittmann, and M. Lienkamp. "Derivation of a real-life driving cycle from fleet testing data with the Markov-Chain-Monte-Carlo Method". In: *2018 21st International Conference on Intelligent Transportation Systems (ITSC)*. Nov. 2018, pp. 2550–2555. DOI: 10.1109/ITSC.2018.8569547.

[77] H. Fujimoto and S. Harada. "Model-Based Range Extension Control System for Electric Vehicles With Front and Rear Driving-Braking Force Distributions". In: *IEEE Transactions on Industrial Electronics* 62.5 (May 2015), pp. 3245–3254. DOI: 10.1109/TIE.2015.2402634.

[78] Yang Gao, Jiuchun Jiang, Caiping Zhang, Weige Zhang, Zeyu Ma, and Yan Jiang. "Lithium-ion battery aging mechanisms and life model under different charging stresses". In: *Journal of Power Sources* 356 (2017), pp. 103–114. DOI: https://doi.org/10.1016/j.jpowsour.2017.04.084.

[79] Yang Gao, Jiuchun Jiang, Caiping Zhang, Weige Zhang, and Yan Jiang. "Aging mechanisms under different state-of-charge ranges and the multi-indicators system of state-of-health for lithium-ion battery with Li(NiMnCo)O2 cathode". In: *Journal of Power Sources* 400 (2018), pp. 641–651. DOI: https://doi.org/10.1016/j.jpowsour.2018.07.018.

[80] Yuan Gao, Jeffrey R. Kenworthy, Peter Newman, and Weixing Gao. "2.2 - Transport and Mobility Trends in Beijing and Shanghai: Implications for Urban Passenger Transport Energy Transitions Worldwide". In: *Urban Energy Transition (Second Edition)*. Ed. by Peter Droege. Second Edition. Elsevier, 2018, pp. 205–223. DOI: https://doi.org/10.1016/B978-0-08-102074-6.00025-5.

[81] R. Genieser, S. Ferrari, M. Loveridge, S.D. Beattie, R. Beanland, H. Amari, G. West, and R. Bhagat. "Lithium ion batteries (NMC/graphite) cycling at 80°C: Different electrolytes and related degradation mechanism". In: *Journal of Power Sources* 373 (2018), pp. 172–183. DOI: https://doi.org/10.1016/j.jpowsour.2017.11.014.

[82] Huiming Gong, Yuan Zou, Qingkai Yang, Jie Fan, Fengchun Sun, and Dietmar Goehlich. "Generation of a driving cycle for battery electric vehicles - A case study of Beijing". In: *Energy* 150 (2018), pp. 901–912. DOI: https://doi.org/10.1016/j.energy.2018.02.092.

[83] Clemens Guenther, Benjamin Schott, Wilfried Hennings, Paul Waldowski, and Michael A. Danzer. "Model-based investigation of electric vehicle battery aging by means of vehicle-to-grid scenario simulations". In: *Journal of Power Sources* 239 (2013), pp. 604–610. DOI: https://doi.org/10.1016/j.jpowsour.2013.02.041.

[84] F. Gustafsson. "Particle filter theory and practice with positioning applications". In: *IEEE Aerospace and Electronic Systems Magazine* 25.7 (July 2010), pp. 53–82. DOI: 10.1109/MAES.2010.5546308.

[85] D. L. Hall and J. Llinas. "An introduction to multisensor data fusion". In: *Proceedings of the IEEE* 85.1 (Jan. 1997), pp. 6–23. DOI: 10.1109/5.554205.

[86] Xuebing Han, Minggao Ouyang, Languang Lu, and Jianqiu Li. "A comparative study of commercial lithium ion battery cycle life in electric vehicle: Capacity loss estimation". In: *Journal of Power Sources* 268 (2014), pp. 658–669. DOI: https://doi.org/10.1016/j.jpowsour.2014.06.111.

[87] Xuebing Han, Minggao Ouyang, Languang Lu, Jianqiu Li, Yuejiu Zheng, and Zhe Li. "A comparative study of commercial lithium ion battery cycle life in electrical vehicle: Aging mechanism identification". In: *Journal of Power Sources* 251 (2014), pp. 38–54. DOI: https://doi.org/10.1016/j.jpowsour.2013.11.029.

[88] C. Hardt and K. Bogenberger. "Usability of eScooters in Urban Environments - A Pilot Study". In: *2017 IEEE IV Symposium*. June 2017, pp. 1650–1657.

[89] Cornelius Hardt and Klaus Bogenberger. "Usage of e-Scooters in Urban Environments". In: *Transportation Research Procedia* 37 (2019). 21st EURO Working Group on Transportation Meeting, EWGT 2018, 17th - 19th September 2018, Braunschweig, Germany, pp. 155–162. DOI: https://doi.org/10.1016/j.trpro.2018.12.178.

[90] Fred Harris, Elettra Venosa, and Xiaofei Chen. "Chapter 7 - Multirate Signal Processing for Software Radio Architectures". In: *Academic Press Library in Signal Processing: Volume 1*. Ed. by Paulo S.R. Diniz, Johan A.K. Suykens, Rama Chellappa, and Sergios Theodoridis. Vol. 1. Academic Press Library in Signal Processing. Elsevier, 2014, pp. 339–422. DOI: https://doi.org/10.1016/B978-0-12-396502-8.00007-3.

[91] Christian Achim Hellwig. "Modeling, simulation and experimental investigation of the thermal and electrochemical behavior of a LiFePO4-based lithium-ion battery". PhD thesis. Fakultaet Chemie der Universitaet Stuttgart, 2013. DOI: http://dx.doi.org/10.18419/opus-1400.

[92] Gunter Heppeler, Marcus Sonntag, Uli Wohlhaupter, and Oliver Sawodny. "Predictive planning of optimal velocity and state of charge trajectories for hybrid electric vehicles". In: *Control Engineering Practice* 61 (2017), pp. 229–243. DOI: https://doi.org/10.1016/j.conengprac.2016.07.003.

[93] Kobus Hereijgers, Emilia Silvas, Theo Hofman, and Maarten Steinbuch. "Effects of using Synthesized Driving Cycles on Vehicle Fuel Consumption". In: *IFAC-PapersOnLine* 50.1 (2017). 20th IFAC World Congress, pp. 7505–7510. DOI: https://doi.org/10.1016/j.ifacol.2017.08.1183.

[94] Michael Hess. "Kinetics and stage transitions of graphite for lithium-ion batteries". Doctoral Thesis. ETH Zurich, 2013. DOI: https://doi.org/10.3929/ethz-a-010000442.

[95] Anna-Karin Hjelm and Goeran Lindbergh. "Experimental and theoretical analysis of LiMn2O4 cathodes for use in rechargeable lithium batteries by electrochemical impedance spectroscopy (EIS)". In: *Electrochimica Acta* 47.11 (2002), pp. 1747–1759. DOI: https://doi.org/10.1016/S0013-4686(02)00008-7.

[96] A. Hoke, A. Brissette, K. Smith, A. Pratt, and D. Maksimovic. "Accounting for Lithium-Ion Battery Degradation in Electric Vehicle Charging Optimization". In: *IEEE Journal of Emerging and Selected Topics in Power Electronics* 2.3 (Sept. 2014), pp. 691–700. DOI: 10.1109/JESTPE.2014.2315961.

[97] Joris de Hoog, Jean-Marc Timmermans, Daniel Ioan-Stroe, Maciej Swierczynski, Joris Jaguemont, Shovon Goutam, Noshin Omar, Joeri Van Mierlo, and Peter Van Den Bossche. "Combined cycling and calendar capacity fade modeling of a Nickel-Manganese-Cobalt Oxide Cell with real-life profile validation". In: *Applied Energy* 200 (2017), pp. 47–61. DOI: https://doi.org/10.1016/j.apenergy.2017.05.018.

[98] Boris Houska, Hans Joachim Ferreau, and Moritz Diehl. "ACADO Toolkit – An Open Source Framework for Automatic Control and Dynamic Optimization". In: *Optimal Control Applications and Methods* 32.3 (2011), pp. 298–312. DOI: 10.1002/oca.939.

[99] IEA. *CO2 Emissions from Fuel Combustion 2018 Highlights*. International Energy Agency. 2018. URL: https://webstore.iea.org/co2-emissions-from-fuel-combustion-2018-highlights.

[100] M. Inaba. "Secondary Batteries - Lithium Rechargeable Systems | LITHIUM-ION | Negative Electrodes: Graphite". In: *Encyclopedia of Electrochemical Power Sources*. Ed. by Juergen Garche. Amsterdam: Elsevier, 2009, pp. 198–208. DOI: https://doi.org/10.1016/B978-044452745-5.00189-1.

[101] Thomas M. Jahns. "Flux-Weakening Regime Operation of an Interior Permanent-Magnet Synchronous Motor Drive". In: *IEEE Transactions on Industry Applications* IA-23.4 (1987), pp. 681–689.

[102] K. Jalkanen, J. Karppinen, L. Skogstrom, T. Laurila, M. Nisula, and K. Vuorilehto. "Cycle aging of commercial NMC/graphite pouch cells at different temperatures". In: *Applied Energy* 154 (2015), pp. 160–172. DOI: https://doi.org/10.1016/j.apenergy.2015.04.110.

[103] S. Ji, C. R. Cherry, M.J. Bechle, Y. Wu, and J.D. Marshall. "Electric Vehicles in China: Emissions and Health Impacts". In: *Environmental Science and Technology* 46.4 (Dec. 2011), pp. 2018–2024. DOI: 10.1021/es202347q.

[104] Zhecheng Jing, Guolin Wang, Shupei Zhang, and Chengqun Qiu. "Building Tianjin driving cycle based on linear discriminant analysis". In: *Transportation Research Part D* 53 (2017), pp. 78–87.

[105] Stefan Kaebitz, Jochen Bernhard Gerschler, Madeleine Ecker, Yusuf Yurdagel, Brita Emmermacher, Dave Andre, Tim Mitsch, and Dirk Uwe Sauer. "Cycle and calendar life study of a graphite/LiNi1/3Mn1/3Co1/3O2 Li-ion high energy system. Part A: Full cell characterization". In: *Journal of Power Sources* 239 (2013), pp. 572–583. DOI: https://doi.org/10.1016/j.jpowsour.2013.03.045.

[106] Pallavi Kar and S. Harinipriya. "Modeling of Lithium Ion Batteries Employing Grand Canonical Monte Carlo and Multiscale Simulation". In: *Journal of The Electrochemical Society* 161.5 (2014), A726–A735. DOI: 10.1149/2.021405jes.

[107] M. Kassem, J. Bernard, R. Revel, S. Pelissier, F. Duclaud, and C. Delacourt. "Calendar aging of a graphite/LiFePO4 cell". In: *Journal of Power Sources* 208 (2012), pp. 296–305. DOI: https://doi.org/10.1016/j.jpowsour.2012.02.068.

[108] Marian P. Kazmierkowski and Luigi Malesani. "Current Control Techniques for Three-Phase Voltage-Source PWM Converters: A Survey". In: *IEEE Transactions on Industrial Electronics* 45.5 (Oct. 1998), pp. 691–703.

[109] Peter Keil, Simon F. Schuster, Joern Wilhelm, Julian Travi, Andreas Hauser, Ralph C. Karl, and Andreas Jossen. "Calendar Aging of Lithium-Ion Batteries: I. Impact of the Graphite Anode on Capacity Fade". In: *Journal of The Electrochemical Society* 163.9 (2016), A1872–A1880. DOI: 10.1149/2.0411609jes.

[110] Peter Keil and Andreas Jossen. "Charging protocols for lithium-ion batteries and their impact on cycle life - An experimental study with different 18650 high-power cells". In: *Journal of Energy Storage* 6 (2016), pp. 125–141. DOI: https://doi.org/10.1016/j.est.2016.02.005.

[111] Peter Keil and Andreas Jossen. "Calendar Aging of NCA Lithium-Ion Batteries Investigated by Differential Voltage Analysis and Coulomb Tracking". In: *Journal of The Electrochemical Society* 164.1 (2017), A6066–A6074. DOI: 10.1149/2.0091701jes.

[112] Sven Ludwig Kellner. "Parameteridentifikation bei permanenterregten Synchronmaschinen". PhD thesis. Universität Erlangen-Nürnberg, 2012.

[113] S. Kim, Y. Yoon, S. Sul, and K. Ide. "Maximum Torque per Ampere (MTPA) Control of an IPM Machine Based on Signal Injection Considering Inductance Saturation". In: *IEEE Transactions on Power Electronics* 28.1 (Jan. 2013), pp. 488–497. DOI: 10.1109/TPEL.2012.2195203.

[114] Karoly Pal Kovacs and Istvan Racz. *Transiente Vorgänge in Wechselstrommaschinen*. Vol. 1. Akademiai Kiado, Verlag der Ungarischen Akademie der Wissenschaften, 1959.

[115] Ramu Krishnan. *Electric motor drives: modeling, analysis, and control*. Ed. by Marcia J. Horton. Prentice Hall, 2001.

[116] Ramu Krishnan. *Permanent Magnet Synchronous and Brushless DC Motor Drives*. Vol. 1. CRC Press, 2010.

[117] P. Kurzweil and K. Brandt. "Secondary Batteries - Lithium Rechargeable Systems | Overview". In: *Encyclopedia of Electrochemical Power Sources*. Ed. by Juergen Garche. Amsterdam: Elsevier, 2009, pp. 1–26. DOI: https://doi.org/10.1016/B978-044452745-5.00185-4.

[118] P. Kurzweil and J. Garche. "2 - Overview of batteries for future automobiles". In: *Lead-Acid Batteries for Future Automobiles*. Ed. by Juergen Garche, Eckhard Karden, Patrick T. Moseley, and David A.J. Rand. Amsterdam: Elsevier, 2017, pp. 27–96. DOI: https://doi.org/10.1016/B978-0-444-63700-0.00002-7.

[119] Jinxuan Lai, Lei Yu, Guohua Song, Pei Guo, and Xumei Chen. "Development of City-Specific Driving Cycles for Transit Buses Based on VSP Distributions: Case of Beijing". In: *Journal of Transportation Engineering* 139.7 (2013), pp. 749–757. DOI: 10.1061/(ASCE)TE.1943-5436.0000547.

[120] T.K. Lee, B. Adornato, and Z.S. Filipi. "Synthesis of real-world driving cycles and their use for estimating PHEV energy consumption and charging opportunities: case study for Midwest/U.S." In: *IEEE Transaction on Vehicular Technology* 60.9 (Oct. 2011), pp. 4153–4163.

[121] Meinert Lewerenz, Jens Muennix, Johannes Schmalstieg, Stefan Kaebitz, Marcus Knips, and Dirk Uwe Sauer. "Systematic aging of commercial LiFePO4|Graphite cylindrical cells including a theory explaining rise of capacity during aging". In: *Journal of Power Sources* 345 (2017), pp. 254–263. DOI: https://doi.org/10.1016/j.jpowsour.2017.01.133.

[122] Meinert Lewerenz, Andrea Marongiu, Alexander Warnecke, and Dirk Uwe Sauer. "Differential voltage analysis as a tool for analyzing inhomogeneous aging: A case study for LiFePO4 Graphite cylindrical cells". In: *Journal of Power Sources* 368 (2017), pp. 57–67. DOI: https://doi.org/10.1016/j.jpowsour.2017.09.059.

[123] C. Li, C. Liu, K. Deng, X. Yu, and T. Huang. "Data-Driven Charging Strategy of PEVs Under Transformer Aging Risk". In: *IEEE Transactions on Control Systems Technology* 26.4 (July 2018), pp. 1386–1399. DOI: 10.1109/TCST.2017.2713321.

[124] Xueyan Li, Song-Yul Choe, and Won Tae Joe. "A reduced order electrochemical and thermal model for a pouch type lithium ion polymer battery with LiNixMnyCo1-x-yO2/LiFePO4 blended cathode". In: *Journal of Power Sources* 294 (2015), pp. 545–555. DOI: https://doi.org/10.1016/j.jpowsour.2015.06.090.

[125] Yi Li, Mohamed Abdel-Monem, Rahul Gopalakrishnan, Maitane Berecibar, Elise Nanini-Maury, Noshin Omar, Peter van den Bossche, and Joeri Van Mierlo. "A quick on-line state of health estimation method for Li-ion battery with incremental capacity curves processed by Gaussian filter". In: *Journal of Power Sources* 373 (Jan. 2018), pp. 40–53. DOI: 10.1016/j.jpowsour.2017.10.092.

[126] Yuecheng Li, Jiankun Peng, Hongwen He, and Shanshan Xie. "The Study on Multi-scale Prediction of Future Driving Cycle Based on Markov Chain". In: *Energy Procedia* 105 (2017), pp. 3219–3224.

[127] Zhe Li, Jun Huang, Bor Yann Liaw, Viktor Metzler, and Jianbo Zhang. "A review of lithium deposition in lithium-ion and lithium metal secondary batteries". In: *Journal of Power Sources* 254 (2014), pp. 168–182. DOI: https://doi.org/10.1016/j.jpowsour.2013.12.099.

[128] B. Y. Liaw and M. Dubarry. "From driving cycle analysis to understanding battery performance in real-life electric hybrid vehicle operation". In: *Journal of Power Sources* 174.1 (Nov. 2007), pp. 76–88.

[129] D. W. Limoge, P. Y. Bi, A. M. Annaswamy, and A. Krupadanam. "A Reduced-Order Model of a Lithium-Ion Cell Using the Absolute Nodal Coordinate Formulation Approach". In: *IEEE Transactions on Control Systems Technology* 26.3 (May 2018), pp. 1001–1014. DOI: 10.1109/TCST.2017.2692743.

[130] Xianke Lin, Jonghyun Park, Lin Liu, Yoonkoo Lee, A. M. Sastry, and Wei Lua. "A Comprehensive Capacity Fade Model and Analysis for Li-Ion Batteries". In: *Journal of The Electrochemical Society* 160.10 (2013), A1701–A1710.

[131] Kailong Liu, Kang Li, Zhile Yang, Cheng Zhang, and Jing Deng. "An advanced Lithium-ion battery optimal charging strategy based on a coupled thermoelectric model". In: *Electrochimica Acta* 225 (2017), pp. 330–344. DOI: https://doi.org/10.1016/j.electacta.2016.12.129.

[132] Qianqian Liu, C Du, Bin Shen, Pengjian Zuo, Xinqun Cheng, Yulin Ma, Geping Yin, and Yunzhi Gao. "Understanding undesirable anode lithium plating issues in lithium-ion batteries". In: *RSC Adv.* 6 (Sept. 2016), pp. 88683–88700. DOI: 10.1039/C6RA19482F.

[133] Xinhua Liu, Weilong Ai, Max Naylor Marlow, Yatish Patel, and Billy Wu. "The effect of cell-to-cell variations and thermal gradients on the performance and degradation of lithium-ion battery packs". In: *Applied Energy* 248 (2019), pp. 489–499. DOI: https://doi.org/10.1016/j.apenergy.2019.04.108.

[134] N. Lotfi, R. G. Landers, J. Li, and J. Park. "Reduced-Order Electrochemical Model-Based SOC Observer With Output Model Uncertainty Estimation". In: *IEEE Transactions on Control Systems Technology* 25.4 (July 2017), pp. 1217–1230. DOI: 10.1109/TCST.2016.2598764.

[135] W. Naranjo Lourido, L. E. Munoz, and J. E. Pereda. "A Methodology to Obtain a Synthetic Driving Cycle through GPS Data for Energy Analysis". In: *2015 IEEE Vehicle Power and Propulsion Conference (VPPC)*. Oct. 2015, pp. 1–5. DOI: 10.1109/VPPC.2015.7352876.

[136] Christian von Lueders, Jonas Keil, Markus Webersberger, and Andreas Jossen. "Modeling of lithium plating and lithium stripping in lithium-ion batteries". In: *Journal of Power Sources* 414 (2019), pp. 41–47. DOI: https://doi.org/10.1016/j.jpowsour.2018.12.084.

[137] Ruoyun Ma, Xiaoyi He, Yali Zheng, Boya Zhou, Sheng Lu, and Ye Wu. "Real-world driving cycles and energy consumption informed by large-sized vehicle trajectory data". In: *Journal of Cleaner Production* 223 (2019), pp. 564–574. DOI: https://doi.org/10.1016/j.jclepro.2019.03.002.

[138] Arpit Maheshwari, Michael Heck, and Massimo Santarelli. "Cycle aging studies of lithium nickel manganese cobalt oxide-based batteries using electrochemical impedance spectroscopy". In: *Electrochimica Acta* 273 (2018), pp. 335–348. DOI: https://doi.org/10.1016/j.electacta.2018.04.045.

[139] Zhiyu Mao. "Mathematical Model and Calendar Aging Study of Commercial Blended-Cathode Li-ion Batteries". PhD thesis. UWSpace, 2016.

[140] James Marcicki, Marcello Canova, A. Terrence Conlisk, and Giorgio Rizzoni. "Design and parametrization analysis of a reduced-order electrochemical model of graphite/$LiFePO_4$ cells for SOC/SOH estimation". In: *Journal of Power Sources* 237 (2013), pp. 310–324. DOI: https://doi.org/10.1016/j.jpowsour.2012.12.120.

[141] James Marcicki, Alex Bartlett, Marcello Canova, A. Terrence Conlisk, Giorgio Rizzoni, Yann Guezennec, Xiao Guang Yang, and Ted Miller. "Characterization of Cycle-Life Aging in Automotive Lithium-Ion Pouch Cells". In: *ECS Transactions* 50.26 (2013), pp. 235–247. DOI: 10.1149/05026.0235ecst.

[142] Andrea Marongiu, Marco Roscher, and Dirk Uwe Sauer. "Influence of the vehicle-to-grid strategy on the aging behavior of lithium battery electric vehicles". In: *Applied Energy* 137 (2015), pp. 899–912. DOI: https://doi.org/10.1016/j.apenergy.2014.06.063.

[143] MathWorks. *MATLAB Documentation - MathWorks Deutschland*. The MathWorks, Inc. Sept. 2019. URL: https://de.mathworks.com/help/matlab/.

[144] MathWorks. *Simulink Documentation - MathWorks Deutschland*. The MathWorks, Inc. Sept. 2019. URL: https://de.mathworks.com/help/simulink/.

[145] Ravi N. Methekar, Paul W. C. Northrop, Kejia Chen, Richard D. Braatz, and Venkat R. Subramanian. "Kinetic Monte Carlo Simulation of Surface Heterogeneity in Graphite Anodes for Lithium-Ion Batteries: Passive Layer Formation". In: *Journal of The Electrochemical Society* 158.4 (2011), A363–A370. DOI: 10.1149/1.3548526.

[146] Florent Morel, Xuefang Lin-Shi, Jean-Marie Retif, and Cyril Buttay. "A Comparative Study of Predictive Current Control Schemes for a Permanent-Magnet Synchronous Machine Drive". In: *IEEE Transactions on Industrial Electronics* 56.7 (July 2009), pp. 2715–2728.

[147] Shigeo Morimoto, Yoji Takeda, Takao Hirasa, and Katsunori Taniguchi. "Expansion of Operating Limits for Permanent Magnet Motor by Current Vector Control Considering Inverter Capacity". In: *IEEE Transactions on Industry Applications* 26.5 (1990), pp. 866–871.

[148] F. Morlock, G. Heppeler, U. Wohlhaupter, and O. Sawodny. "Range extension for electric vehicles by optimal velocity planning considering different driver types". In: *2017 IEEE Conference on Control Technology and Applications (CCTA)*. Aug. 2017, pp. 554–559. DOI: 10.1109/CCTA.2017.8062520.

[149] T. Muneer, M. Kolhe, and A. Doyle. *Electric Vehicles: Prospects and Challenges*. Elsevier Science, 2017.

[150] Maik Naumann, Michael Schimpe, Peter Keil, Holger C. Hesse, and Andreas Jossen. "Analysis and modeling of calendar aging of a commercial LiFePO4/ graphite cell". In: *Journal of Energy Storage* 17 (2018), pp. 153–169. DOI: https://doi.org/10.1016/j.est.2018.01.019.

[151] Navigant Research. *Electric Bicycles – Li-Ion and SLA E-Bikes: Drivetrain, Motor, and Battery Technology Trends, Competitive Landscape, and Global Market Forecasts*. Navigant Consulting, Inc. Feb. 2016. URL: https://www.pedegoelectricbikes.com/wp-content/uploads/2016/07/MF-EBIKE-16-Executive-Summary-w-Pedego.pdf.

[152] Alexandros Nikolian, Joris Jaguemont, Joris de Hoog, Shovon Goutam, Noshin Omar, Peter Van Den Bossche, and Joeri Van Mierlo. "Complete cell-level lithium-ion electrical ECM model for different chemistries (NMC, LFP, LTO) and temperatures (-5 C to 45 C) - Optimized modelling techniques". In: *International Journal of Electrical Power & Energy Systems* 98 (2018), pp. 133–146. DOI: https://doi.org/10.1016/j.ijepes.2017.11.031.

[153] Naoki Nitta, Feixiang Wu, Jung Lee, and Gleb Yushin. "Li ion Battery Materials: Present and Future". In: *Materials Today* 18 (Nov. 2014).

[154] German National Platform for Electric Mobility NPE. *The German Standardisation Roadmap for Electromobility - Version 3.0*. Tech. rep. The Federal Government's Joint Office for Electric Mobility (GGEMO), 2014.

[155] German National Platform for Electric Mobility NPE. *The German Standardisation Roadmap Electric Mobility 2020*. Tech. rep. The Federal Government's Joint Office for Electric Mobility (GGEMO), 2017.

[156] Adnan Nuhic, Tarik Terzimehic, Thomas Soczka-Guth, Michael Buchholz, and Klaus Dietmayer. "Health diagnosis and remaining useful life prognostics of lithium-ion batteries using data-driven methods". In: *Journal of Power Sources* 239 (2013), pp. 680–688. DOI: https://doi.org/10.1016/j.jpowsour.2012.11.146.

[157] Office of energy efficiency & renewable energy. *Vehicle Technologies Office - Department of Energy*. (accesed on 19. December 2018). 2018. URL: https://www.energy.gov/eere/vehicles/vehicle-technologies-office.

[158] Tsutomu Ohzuku, Masaki Kitagawa, and Taketsugu Hirai. "Electrochemistry of Manganese Dioxide in Lithium Nonaqueous Cell: I . X-Ray Diffractional Study on the Reduction of Electrolytic Manganese Dioxide". In: *Journal of The Electrochemical Society* 136.11 (1989), pp. 3169–3174. DOI: 10.1149/1.2096421.

[159] Tsutomu Ohzuku, Masaki Kitagawa, and Taketsugu Hirai. "Electrochemistry of Manganese Dioxide in Lithium Nonaqueous Cell: II . X-Ray Diffractional and Electrochemical Characterization on Deep Discharge Products of Electrolytic Manganese Dioxide". In: *Journal of The Electrochemical Society* 137.1 (1990), pp. 40–46. DOI: 10.1149/1.2086435.

[160] Tsutomu Ohzuku, Masaki Kitagawa, and Taketsugu Hirai. "Electrochemistry of Manganese Dioxide in Lithium Nonaqueous Cell: III . X-Ray Diffractional Study on the Reduction of Spinel-Related Manganese Dioxide". In: *Journal of The Electrochemical Society* 137.3 (1990), pp. 769–775. DOI: 10.1149/1.2086552.

[161] Noshin Omar, Mohamed Abdel Monem, Yousef Firouz, Justin Salminen, Jelle Smekens, Omar Hegazy, Hamid Gaulous, Grietus Mulder, Peter Van den Bossche, Thierry Coosemans, and Joeri Van Mierlo. "Lithium iron phosphate based battery - Assessment of the aging parameters and development of cycle life model". In: *Applied Energy* 113 (2014), pp. 1575–1585. DOI: https://doi.org/10.1016/j.apenergy.2013.09.003.

[162] Randall J. Osczevski. "The Basis of Wind Chill". In: *Arctic* 48.4 (1995), pp. 372–382.

[163] M. Rosa Palacin. "Understanding ageing in Li-ion batteries: a chemical issue". In: *Chem. Soc. Rev.* 47 (13 2018), pp. 4924–4933. DOI: 10.1039/C7CS00889A.

[164] Joonam Park, Williams Agyei Appiah, Seoungwoo Byun, Dahee Jin, Myung-Hyun Ryou, and Yong Min Lee. "Semi-empirical long-term cycle life model coupled with an electrolyte depletion function for large-format graphite/LiFePO4 lithium-ion batteries". In: *Journal of Power Sources* 365 (2017), pp. 257–265. DOI: https://doi.org/10.1016/j.jpowsour.2017.08.094.

[165] E. Peled. "The Electrochemical Behavior of Alkali and Alkaline Earth Metals in Nonaqueous Battery Systems: The Solid Electrolyte Interphase Model". In: *Journal of The Electrochemical Society* 126.12 (1979), pp. 2047–2051. DOI: 10.1149/1.2128859.

[166] E. Peled and S. Menkin. "Review - SEI: Past, Present and Future". In: *Journal of The Electrochemical Society* 164.7 (2017), A1703–A1719. DOI: 10.1149/2.1441707jes.

[167] Xiongbin Peng, Chong Ma, Akhil Garg, Nengsheng Bao, and Xiangping Liao. "Thermal performance investigation of an air-cooled lithium-ion battery pack considering the inconsistency of battery cells". In: *Applied Thermal Engineering* 153 (2019), pp. 596–603. DOI: https://doi.org/10.1016/j.applthermaleng.2019.03.042.

[168] Alexis Perea, Andrea Paolella, Joel Dube, Dominique Champagne, Alain Mauger, and Karim Zaghib. "State of charge influence on thermal reactions and abuse tests in commercial lithium-ion cells". In: *Journal of Power Sources* 399 (2018), pp. 392–397. DOI: https://doi.org/10.1016/j.jpowsour.2018.07.112.

[169] A. Perner and J. Vetter. "8 - Lithium-ion batteries for hybrid electric vehicles and battery electric vehicles". In: *Advances in Battery Technologies for Electric Vehicles*. Ed. by Bruno Scrosati, Juegen Garche, and Werner Tillmetz. Woodhead Publishing Series in Energy. Woodhead Publishing, 2015, pp. 173–190. DOI: https://doi.org/10.1016/B978-1-78242-377-5.00008-X.

[170] Martin Petit, Eric Prada, and Valerie Sauvant-Moynot. "Development of an empirical aging model for Li-ion batteries and application to assess the impact of Vehicle-to-Grid strategies on battery lifetime". In: *Applied Energy* 172 (2016), pp. 398–407. DOI: https://doi.org/10.1016/j.apenergy.2016.03.119.

[171] Phylion. *Xinheng dianyuan gufen youxian gongsi*. Phylion Battery Co.,Ltd. June 2018. URL: http://www.phylion.com.

[172] Pragasan Pillay and R. Krishnan. "Modeling of Permanent Magnet Motor Drives". In: *IEEE Transactions on Industrial Electronics* 35.4 (1988), pp. 537–541.

[173] Matthew B. Pinson and Martin Z. Bazant. "Theory of SEI Formation in Rechargeable Batteries: Capacity Fade, Accelerated Aging and Lifetime Prediction". In: *Journal of The Electrochemical Society* 160.2 (2013), A243–A250. DOI: 10.1149/2.044302jes.

[174] Harry J. Ploehn, Premanand Ramadass, and Ralph E. White. "Solvent Diffusion Model for Aging of Lithium-Ion Battery Cells". In: *Journal of The Electrochemical Society* 151.3 (2004), A456–A462. DOI: 10.1149/1.1644601.

[175] E. Prada, D. Di Domenico, Y. Creff, J. Bernard, V. Sauvant-Moynot, and F. Huet. "Simplified Electrochemical and Thermal Model of LiFePO4-Graphite Li-Ion Batteries for Fast Charge Applications". In: *Journal of The Electrochemical Society* 159.9 (2012), A1508–A1519. DOI: 10.1149/2.064209jes.

[176] E. Prada, D. Di Domenico, Y. Creff, J. Bernard, V. Sauvant-Moynot, and F. Huet. "A Simplified Electrochemical and Thermal Aging Model of LiFePO4-Graphite Li-ion Batteries: Power and Capacity Fade Simulations". In: *Journal of The Electrochemical Society* 160.4 (2013), A616–A628. DOI: 10.1149/2.053304jes.

[177] Maxwell D. Radin, Sunny Hy, Mahsa Sina, Chengcheng Fang, Haodong Liu, Julija Vinckeviciute, Minghao Zhang, M. Stanley Whittingham, Y. Shirley Meng, and Anton Van der Ven. "Narrowing the Gap between Theoretical and Practical Capacities in Li-Ion Layered Oxide Cathode Materials". In: *Advanced Energy Materials* 7.20 (2017), p. 1602888. DOI: 10.1002/aenm.201602888.

[178] P. Ramadass, Bala Haran, Ralph White, and Branko N. Popov. "Mathematical modeling of the capacity fade of Li-ion cells". In: *Journal of Power Sources* 123.2 (2003), pp. 230–240. DOI: https://doi.org/10.1016/S0378-7753(03)00531-7.

[179] P. Ramadass, Bala Haran, Parthasarathy M. Gomadam, Ralph White, and Branko N. Popov. "Development of First Principles Capacity Fade Model for Li-Ion Cells". In: *Journal of The Electrochemical Society* 151.2 (2004), A196–A203. DOI: 10.1149/1.1634273.

[180] Venkatasailanathan Ramadesigan, Paul W. C. Northrop, Sumitava De, Shriram Santhanagopalan, Richard D. Braatz, and Venkat R. Subramanian. "Modeling and Simulation of Lithium-Ion Batteries from a Systems Engineering Perspective". In: *Journal of The Electrochemical Society* 159.3 (2012), R31–R45. DOI: 10.1149/2.018203jes.

[181] J. E. B. Randles. "Kinetics of rapid electrode reactions". In: *Discussions of the Faraday Society* 1 (1947), pp. 11–19. DOI: http://dx.doi.org/10.1039/DF9470100011.

[182] S. K. Rechkemmer, B. Czech, X. Zang, W. Zhang, and O. Sawodny. "Adaptability of Li-Ion Single Particle Model for Lifetime Simulation Using LFP and LMO Cells". In: *2018 IEEE Conference on Control Technology and Applications (CCTA)*. Aug. 2018, pp. 1415–1420. DOI: 10.1109/CCTA.2018.8511388.

[183] S. K. Rechkemmer, X. Zang, W. Zhang, and O. Sawodny. "Towards a Shanghai electric two-wheeler cycle (SE2WC)". In: *2019 12th Asian Control Conference (ASCC)*. June 2019, pp. 319–324.

[184] Sabrina K. Rechkemmer, Weimin Zhang, and Oliver Sawodny. "Modeling of a Permanent Magnet Synchronous Motor of an E-Scooter for Simulation with Battery Aging Model". In: *IFAC-PapersOnLine* 50.1 (July 2017). 20th IFAC World Congress, pp. 4769–4774. DOI: 10.1016/j.ifacol.2017.08.956.

[185] Sabrina K. Rechkemmer, Xiaoyun Zang, Alexander Boronka, Weimin Zhang, and Oliver Sawodny. "Utilization of Smartphone Data for Driving Cycle Synthesis based on Electric Two-Wheelers in Shanghai". In: *IEEE Transactions on Intelligent Transportation Systems* (2020), pp. 1–11. DOI: 10.1109/tits.2019.2961179.

[186] Sabrina Kathrin Rechkemmer, Xiaoyun Zang, Weimin Zhang, and Oliver Sawodny. "Empirical Li-ion aging model derived from single particle model". In: *Journal of Energy Storage* 21 (Feb. 2019), pp. 773–786. DOI: 10.1016/j.est.2019.01.005.

[187] Sabrina Kathrin Rechkemmer, Xiaoyun Zang, Weimin Zhang, and Oliver Sawodny. "Lifetime optimized charging strategy of Li-ion cells based on daily driving cycle of electric two-wheelers". In: *Applied Energy* 251 (Oct. 2019), p. 113415. DOI: 10.1016/j.apenergy.2019.113415.

[188] Sabrina Kathrin Rechkemmer, Xiaoyun Zang, Weimin Zhang, and Oliver Sawodny. "Calendar and cycle aging study of a commercial LiMn2O4 cell under consideration of influences by cell progress". In: *Journal of Energy Storage* 30 (Aug. 2020), p. 101547. DOI: 10.1016/j.est.2020.101547.

[189] Y. Reynier, R. Yazami, and B. Fultz. "The entropy and enthalpy of lithium intercalation into graphite". In: *Journal of Power Sources* 119-121 (2003), pp. 850–855. DOI: https://doi.org/10.1016/S0378-7753(03)00285-4.

[190] Frank Richter, Preben J.S. Vie, Signe Kjelstrup, and Odne Stokke Burheim. "Measurements of ageing and thermal conductivity in a secondary NMC-hard carbon Li-ion battery and the impact on internal temperature profiles". In: *Electrochimica Acta* 250 (2017), pp. 228–237. DOI: https://doi.org/10.1016/j.electacta.2017.07.173.

[191] Fridolin Roeder, Richard D. Braatz, and Ulrike Krewer. "Direct coupling of continuum and kinetic Monte Carlo models for multiscale simulation of electrochemical systems". In: *Computers & Chemical Engineering* 121 (2019), pp. 722–735. DOI: https://doi.org/10.1016/j.compchemeng.2018.12.016.

[192] Björn Rumberg, Bernd Epding, Ina Stradtmann, and Arno Kwade. "Identification of Li ion battery cell aging mechanisms by half-cell and full-cell open-circuit-voltage characteristic analysis". In: *Journal of Energy Storage* 25 (2019), p. 100890. DOI: https://doi.org/10.1016/j.est.2019.100890.

[193] SAC. *Electric Bicycles - General Technical Requirements (GB-17761-1999)*. Standardization Administration of China. 1999.

[194] SAC. *City driving cycle for vehicle testing (QC/T 759-2006)*. Standardization Administration of China. 2006.

[195] SAC. *Electric Motorcycles and electric mopeds (GB/T-24158)*. Standardization Administration of China. 2009.

[196] SAC. *Safety specifications for power-driven vehicles operating on roads (GB-7258)*. Standardization Administration of China. 2012.

[197] SAC. *Technical Specifications of Remote Service and Management System for Electric Vehicles (GB/T 32960)*. Standardization Administration of China, 2016.

[198] SAC. *Safety technical specification for electric bicycle (GB 17761-20xx)*. Draft Standard accessed on 19.01.2018. Standardization Administration of China. 2018. URL: http://www.miit.gov.cn/n1146285/n1146352/n3054355/n3057497/n3057502/c6014728/part/6014732.pdf.

[199] M. Safari, M. Morcrette, A. Teyssot, and C. Delacourt. "Multimodal Physics-Based Aging Model for Life Prediction of Li-Ion Batteries". In: *Journal of The Electrochemical Society* 156.3 (2009), A145–A153. DOI: 10.1149/1.3043429.

[200] M. Safari and C. Delacourt. "Mathematical Modeling of Lithium Iron Phosphate Electrode: Galvanostatic Charge/Discharge and Path Dependence". In: *Journal of The Electrochemical Society* 158.2 (2011), A63–A73.

[201] E. Sarasketa-Zabala, I. Gandiaga, E. Martinez-Laserna, L.M. Rodriguez-Martinez, and I. Villarreal. "Cycle ageing analysis of a LiFePO4 graphite cell with dynamic model validations: Towards realistic lifetime predictions". In: *Journal of Power Sources* 275 (2015), pp. 573–587. DOI: https://doi.org/10.1016/j.jpowsour.2014.10.153.

[202] Samveg Saxena, Anand Gopal, and Amol Phadke. "Electrical consumption of two-, three- and four-wheel light-duty electric vehicles in India". In: *Applied Energy* 115 (2014), pp. 582–590. DOI: https://doi.org/10.1016/j.apenergy.2013.10.043.

[203] M. Schimpe, M. E. von Kuepach, M. Naumann, H. C. Hesse, K. Smith, and A. Jossen. "Comprehensive Modeling of Temperature-Dependent Degradation Mechanisms in Lithium Iron Phosphate Batteries". In: *Journal of The Electrochemical Society* 165.2 (2018), A181–A193. DOI: 10.1149/2.1181714jes.

[204] C. Schlasza, P. Ostertag, D. Chrenko, R. Kriesten, and D. Bouquain. "Review on the aging mechanisms in Li-ion batteries for electric vehicles based on the FMEA method". In: *2014 IEEE Transportation Electrification Conference and Expo (ITEC)*. June 2014, pp. 1–6. DOI: 10.1109/ITEC.2014.6861811.

[205] Johannes Schmalstieg, Stefan Kaebitz, Madeleine Ecker, and Dirk Uwe Sauer. "A holistic aging model for Li(NiMnCo)O2 based 18650 lithium-ion batteries". In: *Journal of Power Sources* 257 (2014), pp. 325–334. DOI: https://doi.org/10.1016/j.jpowsour.2014.02.012.

[206] Alexander Uwe Schmid, Moritz Kurka, and Kai Peter Birke. "Reproducibility of Li-ion cell reassembling processes and their influence on coin cell aging". In: *Journal of Energy Storage* 24 (2019), p. 100732. DOI: https://doi.org/10.1016/j.est.2019.04.006.

[207] Julius Schmitt, Arpit Maheshwari, Michael Heck, Stephan Lux, and Matthias Vetter. "Impedance change and capacity fade of lithium nickel manganese cobalt oxide-based batteries during calendar aging". In: *Journal of Power Sources* 353 (2017), pp. 183–194. DOI: https://doi.org/10.1016/j.jpowsour.2017.03.090.

[208] A. Schuller, B. Dietz, C. M. Flath, and C. Weinhardt. "Charging Strategies for Battery Electric Vehicles: Economic Benchmark and V2G Potential". In: *IEEE Transactions on Power Systems* 29.5 (Sept. 2014), pp. 2014–2022. DOI: 10.1109/TPWRS.2014.2301024.

[209] Simon F. Schuster, Tobias Bach, Elena Fleder, Jana Mueller, Martin Brand, Gerhard Sextl, and Andreas Jossen. "Nonlinear aging characteristics of lithium-ion cells under different operational conditions". In: *Journal of Energy Storage* 1 (2015), pp. 44–53. DOI: https://doi.org/10.1016/j.est.2015.05.003.

[210] V. Schwarzer and R. Ghorbani. "Drive Cycle Generation for Design Optimization of Electric Vehicles". In: *IEEE Transactions on Vehicular Technology* 62.1 (Jan. 2013), pp. 89–97. DOI: 10.1109/TVT.2012.2219889.

[211] Ming Shen and Qing Gao. "A review on battery management system from the modeling efforts to its multiapplication and integration". In: *International Journal of Energy Research* 43.10 (2019), pp. 5042–5075. DOI: 10.1002/er.4433.

[212] Shuming Shi, Nan Lin, Yan Zhang, Jingmin Cheng, Chaosheng Huang, Li Liu, and Bingwu Lu. "Research on Markov property analysis of driving cycles and its application". In: *Transportation Research Part D: Transport and Environment* 47 (2016), pp. 171–181. DOI: https://doi.org/10.1016/j.trd.2016.05.013.

[213] E. Silvas, K. Hereijgers, H. Peng, T. Hofman, and M. Steinbuch. "Synthesis of Realistic Driving Cycles With High Accuracy and Computational Speed, Including Slope Information". In: *IEEE Transactions on Vehicular Technology* 65.6 (June 2016), pp. 4118–4128. DOI: 10.1109/TVT.2016.2546338.

[214] Gordon R. Slemon and Xian Liu. "Modeling and Design Optimization Of Permanent Magnet Motors". In: *Electric Machines & Power Systems* 20.2 (1992), pp. 71–92. DOI: 10.1080/07313569208909572.

[215] A. J. Smith, J. C. Burns, Xuemei Zhao, Deijun Xiong, and J. R. Dahn. "A High Precision Coulometry Study of the SEI Growth in Li/Graphite Cells". In: *Journal of The Electrochemical Society* 158.5 (2011), A447–A452. DOI: 10.1149/1.3557892.

[216] Wenji Song, Mingbiao Chen, Fanfei Bai, Shili Lin, Yongzhen Chen, and Ziping Feng. "Non-uniform effect on the thermal/aging performance of Lithium-ion pouch battery". In: *Applied Thermal Engineering* 128 (2018), pp. 1165–1174. DOI: https://doi.org/10.1016/j.applthermaleng.2017.09.090.

[217] R. Spotnitz. "Simulation of capacity fade in lithium-ion batteries". In: *Journal of Power Sources* 113.1 (2003), pp. 72–80. DOI: https://doi.org/10.1016/S0378-7753(02)00490-1.

[218] Barbara Stiaszny, Joerg C. Ziegler, Elke E. Krauss, Mengjia Zhang, Jan P. Schmidt, and Ellen Ivers-Tiffee. "Electrochemical characterization and post-mortem analysis of aged LiMn2O4-NMC/graphite lithium ion batteries part II: Calendar aging". In: *Journal of Power Sources* 258 (2014), pp. 61–75. DOI: https://doi.org/10.1016/j.jpowsour.2014.02.019.

[219] Barbara Stiaszny, Joerg C. Ziegler, Elke E. Krauss, Jan P. Schmidt, and Ellen Ivers-Tiffee. "Electrochemical characterization and post-mortem analysis of aged LiMn2O4/Li(Ni0.5Mn0.3Co0.2)O2/graphite lithium ion batteries. Part I: Cycle aging". In: *Journal of Power Sources* 251 (2014), pp. 439–450. DOI: https://doi.org/10.1016/j.jpowsour.2013.11.080.

[220] Jillian Strauss and Luis F. Miranda-Moreno. "Speed, travel time and delay for intersections and road segments in the Montreal network using cyclist Smartphone GPS data". In: *Transportation Research Part D: Transport and Environment* 57 (2017), pp. 155–171. DOI: https://doi.org/10.1016/j.trd.2017.09.001.

[221] D. Stroe, M. Swierczynski, A. Stan, R. Teodorescu, and S. J. Andreasen. "Accelerated Lifetime Testing Methodology for Lifetime Estimation of Lithium-Ion Batteries Used in Augmented Wind Power Plants". In: *IEEE Transactions on Industry Applications* 50.6 (Nov. 2014), pp. 4006–4017. DOI: 10.1109/TIA.2014.2321028.

[222] X. Su, H. Caceres, H. Tong, and Q. He. "Online Travel Mode Identification Using Smartphones With Battery Saving Considerations". In: *IEEE Transactions on Intelligent Transportation Systems* 17.10 (Oct. 2016), pp. 2921–2934. DOI: 10.1109/TITS.2016.2530999.

[223] T. Sun, J. Wang, and X. Chen. "Maximum Torque Per Ampere (MTPA) Control for Interior Permanent Magnet Synchronous Machine Drives Based on Virtual Signal Injection". In: *IEEE Transactions on Power Electronics* 30.9 (Sept. 2015), pp. 5036–5045. DOI: 10.1109/TPEL.2014.2365814.

[224] M. Swierczynski, D. Stroe, A. Stan, R. Teodorescu, and S. K. Kaer. "Lifetime Estimation of the Nanophosphate $LiFePO_4$/C Battery Chemistry Used in Fully Electric Vehicles". In: *IEEE Transactions on Industry Applications* 51.4 (July 2015), pp. 3453–3461. DOI: 10.1109/TIA.2015.2405500.

[225] Daichun Tang, Yang Sun, Zhenzhong Yang, Liubin Ben, Lin Gu, and Xuejie Huang. "Surface Structure Evolution of LiMn2O4 Cathode Material upon Charge/Discharge". In: *Chemistry of Materials* 26.11 (2014), pp. 3535–3543. DOI: 10.1021/cm501125e.

[226] L. Tang, G. Rizzoni, and A. Cordoba-Arenas. "Battery Life Extending Charging Strategy for Plug-in Hybrid Electric Vehicles and Battery Electric Vehicles". In: *IFAC-PapersOnLine* 49.11 (2016). 8th IFAC Symposium on Advances in Automotive Control AAC 2016, pp. 70–76. DOI: https://doi.org/10.1016/j.ifacol.2016.08.011.

[227] H. Tanji. "Secondary Batteries - Lithium Rechargeable Systems | LI-ION: Separators". In: *Encyclopedia of Electrochemical Power Sources*. Ed. by Juergen Garche. Amsterdam: Elsevier, 2009, pp. 51–70. DOI: https://doi.org/10.1016/B978-044452745-5.00206-9.

[228] Farid Tazerart, Zahra Mokrani, Djamila Rekioua, and Toufik Rekioua. "Direct torque control implementation with losses minimization of induction motor for electric vehicle applications with high operating life of the battery". In: *International Journal of Hydrogen Energy* 40.39 (Oct. 2015), pp. 13827–13838.

[229] J. Tian, R. Xiong, and Q. Yu. "Fractional-Order Model-Based Incremental Capacity Analysis for Degradation State Recognition of Lithium-Ion Batteries". In: *IEEE Transactions on Industrial Electronics* 66.2 (Feb. 2019), pp. 1576–1584. DOI: 10.1109/TIE.2018.2798606.

[230] J.H. Tong, H.D. Tung, W.T. Hung, and H.V. Nguyen. "Development of driving cycles for motorcycles and light-duty vehicles in Vietnam". In: *Atmospheric Environment* 45.29 (Sept. 2011), pp. 5191–5199.

[231] Jiun-Horng Tsai, Hung-Lung Chiang, Yi-Chun Hsu, Bo-Jun Peng, and Rong-Fang Hung. "Development of a local real world driving cycle for motorcycles for emission factor measurements". In: *Atmospheric Environment* 39.35 (Nov. 2007), pp. 6631–6641.

[232] Gwo-Hshiung Tzeng and June-Jye Chen. "Developing a Taipei motorcycle driving cycle for emissions and fuel economy". In: *Transportation Research Part D* 3.1 (Jan. 1998), pp. 19–27.

[233] M. Nasir Uddin, Tawfik S. Radwan, and M. Azizur Rahman. "Performance of Interior Permanent Magnet Motor Drive Over Wide Speed Range". In: *IEEE Transactions on Energy Conversion* 17.1 (2002), pp. 79–84.

[234] UNECE. *New European Driving Cycle (NEDC)*. United Nations Economic Commission for Europe, 1997.

[235] UNECE. *Worldwide harmonized motorcycle emissions vertification/test procedure (WMTC)*. (revised 2011). United Nations Economic Commission for Europe, 2003.

[236] UNECE. *Worldwide harmonized Light vehicles Test Procedure (WLTP)*. United Nations Economic Commission for Europe, 2015.

[237] US EPA. *EPA Federal Test Procedure (FTP-75)*. US Environmental Protection Agency, 2008.

[238] Pallavi Verma, Pascal Maire, and Petr Novak. "A review of the features and analyses of the solid electrolyte interphase in Li-ion batteries". In: *Electrochimica Acta* 55.22 (2010), pp. 6332–6341. DOI: https://doi.org/10.1016/j.electacta.2010.05.072.

[239] J. Vetter, P. Novak, M.R. Wagner, C. Veit, K.-C. Moeller, J.O. Besenhard, M. Winter, M. Wohlfahrt-Mehrens, C. Vogler, and A. Hammouche. "Ageing mechanisms in lithium-ion batteries". In: *Journal of Power Sources* 147.1 (2005), pp. 269–281. DOI: https://doi.org/10.1016/j.jpowsour.2005.01.006.

[240] J. Vetter, M. Winter, and M. Wohlfahrt-Mehrens. "Secondary Batteries - Lithium Rechargeable Systems | LITHIUM-ION | Aging Mechanisms". In: *Encyclopedia of Electrochemical Power Sources*. Ed. by Juergen Garche. Amsterdam: Elsevier, 2009, pp. 393–403. DOI: https://doi.org/10.1016/B978-044452745-5.00922-9.

[241] Tyrone L. Vincent, Peter J. Weddle, and Gongguo Tang. "System theoretic analysis of battery charging optimization". In: *Journal of Energy Storage* 14 (2017), pp. 168–178. DOI: https://doi.org/10.1016/j.est.2017.09.009.

[242] B. Wang, L. Gao, and Z. Juan. "Travel Mode Detection Using GPS Data and Socioeconomic Attributes Based on a Random Forest Classifier". In: *IEEE Transactions on Intelligent Transportation Systems* 19.5 (May 2018), pp. 1547–1558. DOI: 10.1109/TITS.2017.2723523.

[243] Li-Fang Wang, Chin-Ching Ou, Kathryn A. Striebel, and Jenn-Shing Chen. "Study of Mn Dissolution from LiMn2O4 Spinel Electrodes Using Rotating Ring-Disk Collection Experiments". In: *Journal of The Electrochemical Society* 150.7 (2003), A905–A911. DOI: 10.1149/1.1577543.

[244] Li-Fang Wang, Bor-Jian Fang, and Jenn-Shing Chen. "Rotating ring-disc electrode measurements of manganese dissolution and capacity loss of Li1xMn2xO4 and LixAlyMn2x spinel electrodes for lithium-ion batteries". In: *Journal of Power Sources* 150 (2005), pp. 1–10. DOI: https://doi.org/10.1016/j.jpowsour.2005.01.043.

[245] John Wang, Ping Liu, Jocelyn Hicks-Garner, Elena Sherman, Souren Soukiazian, Mark Verbrugge, Harshad Tataria, James Musser, and Peter Finamore. "Cycle-life model for graphite-LiFePO4 cells". In: *Journal of Power Sources* 196.8 (2011), pp. 3942–3948. DOI: https://doi.org/10.1016/j.jpowsour.2010.11.134.

[246] Jonathan Weinert, Joan Ogden, Dan Sperling, and Andrew Burke. "The future of electric two-wheelers and electric vehicles in China". In: *Energy Policy* 36.7 (2008), pp. 2544–2555. DOI: https://doi.org/10.1016/j.enpol.2008.03.008.

[247] World Bank. *China | Data*. online [accessed 14.05.2019]. World Bank. 2019. URL: https://data.worldbank.org/country/china.

[248] She-Huang Wu and Po-Han Lee. "Storage fading of a commercial 18650 cell comprised with NMC/LMO cathode and graphite anode". In: *Journal of Power Sources* 349 (2017), pp. 27–36. DOI: https://doi.org/10.1016/j.jpowsour.2017.03.002.

[249] Y. Wu and D. Zhu. "Bicycle Sharing Based on PSS-EPR Coupling Model: Exemplified by Bicycle sharing in China". In: *Procedia CIRP*. Vol. 64. 2017, pp. 423–428.

[250] Hui Xia, Zhentao Luo, and Jianping Xie. "Nanostructured LiMn2O4 and their composites as high-performance cathodes for lithium-ion batteries". In: *Progress in Natural Science* 22 (Dec. 2012), pp. 572–584. DOI: 10.1016/j.pnsc.2012.11.014.

[251] Quan Xia, Zili Wang, Yi Ren, Laifa Tao, Chen Lu, Jun Tian, Daozhong Hu, Yituo Wang, Yuzhuan Su, Jin Chong, Haizu Jin, and Yongshou Lin. "A modified reliability model for lithium-ion battery packs based on the stochastic capacity degradation and dynamic response impedance". In: *Journal of Power Sources* 423 (2019), pp. 40–51. DOI: https://doi.org/10.1016/j.jpowsour.2019.03.042.

[252] K. Xu. "Secondary Batteries - Lithium Rechargeable Systems | Electrolytes: Overview". In: *Encyclopedia of Electrochemical Power Sources*. Ed. by Juergen Garche. Amsterdam: Elsevier, 2009, pp. 51–70. DOI: https://doi.org/10.1016/B978-044452745-5.00206-9.

[253] Kang Xu. "Electrolytes and Interphases in Li-Ion Batteries and Beyond". In: *Chemical Reviews* 114.23 (2014). PMID: 25351820, pp. 11503–11618. DOI: 10.1021/cr500003w.

[254] Mengqing Xu, Weishan Li, and Brett L. Lucht. "Effect of propane sultone on elevated temperature performance of anode and cathode materials in lithium-ion batteries". In: *Journal of Power Sources* 193.2 (2009), pp. 804–809. DOI: https://doi.org/10.1016/j.jpowsour.2009.03.067.

[255] Yadea. *Yadea | Green Life Starts Here | electric bike | electric motorcycle | electric scooter | electric tricycle*. accessed on 08.01.2018. Wuxi Yadea export-import co.,ltd. 2017. URL: http://www.globalyadea.com/en/index.html.

[256] J. Yamaki. "Secondary Batteries - Lithium Rechargeable Systems | LI-ION: Overview". In: *Encyclopedia of Electrochemical Power Sources*. Ed. by Juergen Garche. Amsterdam: Elsevier, 2009, pp. 51–70. DOI: https://doi.org/10.1016/B978-044452745-5.00206-9.

[257] Xiao-Guang Yang, Yongjun Leng, Guangsheng Zhang, Shanhai Ge, and Chao-Yang Wang. "Modeling of lithium plating induced aging of lithium-ion batteries: Transition from linear to nonlinear aging". In: *Journal of Power Sources* 360 (2017), pp. 28–40. DOI: https://doi.org/10.1016/j.jpowsour.2017.05.110.

[258] Yang Yang, Tiezhu Li, Hongfei Hu, Tao Zhang, Xianhua Cai, Shuyan Chen, and Fengxiang Qiao. "Development and emissions performance analysis of local driving cycle for small-sized passenger cars in Nanjing, China". In: *Atmospheric Pollution Research* (2019). DOI: https://doi.org/10.1016/j.apr.2019.04.009.

[259] H. A. Yavasoglu, J. Shen, C. Shi, M. Gokasan, and A. Khaligh. "Power Split Control Strategy for an EV Powertrain With Two Propulsion Machines". In: *IEEE Transactions on Transportation Electrification* 1.4 (Dec. 2015), pp. 382–390. DOI: 10.1109/TTE.2015.2504406.

[260] Jaeshin Yi, Boram Koo, Chee Burm Shin, Taeyoung Han, and Seongyong Park. "Modeling the effect of aging on the electrical and thermal behaviors of a lithium-ion battery during constant current charge and discharge cycling". In: *Computers & Chemical Engineering* 99 (2017), pp. 31–39. DOI: https://doi.org/10.1016/j.compchemeng.2017.01.006.

[261] K. Yoon and B. Kwon. "Optimal Design of a New Interior Permanent Magnet Motor Using a Flared-Shape Arrangement of Ferrite Magnets". In: *IEEE Transactions on Magnetics* 52.7 (July 2016), pp. 1–4. DOI: 10.1109/TMAG.2016.2524505.

[262] Toshihiro Yoshida, Michio Takahashi, Satoshi Morikawa, Chikashi Ihara, Hiroyuki Katsukawa, Tomoyuki Shiratsuchi, and Jun-ichi Yamaki. "Degradation Mechanism and Life Prediction of Lithium-Ion Batteries". In: *Journal of The Electrochemical Society* 153.3 (2006), A576–A582. DOI: 10.1149/1.2162467.

[263] K. Zaghib, A. Mauger, F. Gendron, C.M. Julien, and J.B. Goodenough. "Secondary Batteries - Lithium Rechargeable Systems | LITHIUM-ION | Positive Electrode: Lithium Iron Phosphate". In: *Encyclopedia of Electrochemical Power Sources*. Ed. by Juergen Garche. Amsterdam: Elsevier, 2009, pp. 264–296. DOI: https://doi.org/10.1016/B978-044452745-5.00204-5.

[264] Caiping Zhang, Jiuchun Jiang, Yang Gao, Weige Zhang, Qiujiang Liu, and Xiaosong Hu. "Charging optimization in lithium-ion batteries based on temperature rise and charge time". In: *Applied Energy* 194 (2017), pp. 569–577. DOI: https://doi.org/10.1016/j.apenergy.2016.10.059.

[265] Fei Zhang, Fen Guo, and Hong Huang. "A Study of Driving Cycle for Electric Special-purpose Vehicle in Beijing". In: *Energy Procedia* 105 (2017), pp. 4884–4889.

[266] Hua Zhang, Susan A. Shasheen, and Xingpeng Chen. "Bicycle Evolution in China: From the 1900s to the Present". In: *International Journal of Sustainable Transportation* 8.5 (Oct. 2014), pp. 317–335.

[267] Jin Zhang, Zhenpo Wang, Peng Liu, Zhaosheng Zhang, Xiaoyu Li, and Changhui Qu. "Driving cycles construction for electric vehicles considering road environment: A case study in Beijing". In: *Applied Energy* 253 (2019), p. 113514. DOI: https://doi.org/10.1016/j.apenergy.2019.113514.

[268] Linling Zhang, Ruyin Long, Hong Chen, and Jichao Geng. "A review of China's road traffic carbon emissions". In: *Journal of Cleaner Production* 207 (2019), pp. 569–581. DOI: https://doi.org/10.1016/j.jclepro.2018.10.003.

[269] Ruifeng Zhang, Bizhong Xia, Baohua Li, Libo Cao, Yongzhi Lai, Weiwei Zheng, Huawen Wang, and Wei Wang. "State of the Art of Lithium-Ion Battery SOC Estimation for Electrical Vehicles". In: *Energies* 11.7 (2018). DOI: 10.3390/en11071820.

[270] C. Zhou, H. Jia, Z. Juan, X. Fu, and G. Xiao. "A Data-Driven Method for Trip Ends Identification Using Large-Scale Smartphone-Based GPS Tracking Data". In: *IEEE Transactions on Intelligent Transportation Systems* 18.8 (Aug. 2017), pp. 2096–2110. DOI: 10.1109/TITS.2016.2630733.

[271] Wenyu Zhou, Ke Xu, Ying Yang, and Jiahuan Lu. "Driving cycle development for electric vehicle application using principle component analysis and k-means cluster: with the case of Shenyang, China". In: *Energy Procedia* 105 (2017), pp. 2831–2836.

[272] Dennis Zuev. *Introduction: Towards an Understanding of E-bike Mobility in China*. Springer International Publishing, 2018, pp. 1–13. DOI: https://doi.org/10.1007/978-3-319-76590-7.

[273] Dennis Zuev, David Tyfield, and John Urry. "Where is the politics? E-bike mobility in urban China and civilizational government". In: *Environmental Innovation and Societal Transitions* 30 (2019). Low-carbon China: Emerging phenomena and Implications for innovation governance, pp. 19–32. DOI: https://doi.org/10.1016/j.eist.2018.07.002.